UNIVERSITAT POLITÈCNICA DE CATALUNYA

DOCTORAL THESIS

Ultrafast optoelectronics in 2D materials and their heterostructures

Author:
Mathieu MASSICOTTE

Supervisor:
Dr. Prof. Frank H. L. KOPPENS

A thesis submitted in fulfillment of the requirements for the degree of Doctor of Philosophy

in the

Quantum Nano-Optoelectronic group
ICFO - The Institute of Photonic Sciences

May 25, 2017

Abstract

Understanding and improving how light is converted into electricity in materials is one of the central goals in the field of optoelectronics. This basic physical process lies at the heart of several major technologies, including solar cells and ultrafast optical communication systems, which have pervaded and shaped the world we live in. As technological performance approaches the limit of conventional materials, the need for optoelectronic platforms presenting novel properties and superior characteristics, in terms of speed, efficiency and wavelength range, is rapidly growing.

Two-dimensional (2D) layered materials, such as graphene and transition metal dichalcogenides (TMDs), have recently emerged as prime candidates for photonic and optoelectronic applications. This new class of one-atom-thick materials has sparked tremendous interest due to their exceptional electrical and optical properties, which can be drastically different from those of their bulk counterpart. Since the first isolation of graphene in 2004, the library of 2D materials has expanded considerably and now comprises many other crystals covering a wide range of complementary properties. Assembling these 2D building blocks into vertical heterostructures opens up exciting possibilities for designing artificial materials with atomic-layer precision. The resulting van der Waals heterostructures (vdWH), in addition to combining the properties of their constituent layers, provide a rich playground for studying photophysical phenomena and implementing novel photodetection schemes.

The goal of this thesis is to explore the optoelectronic response of devices based on 2D materials and their heterostructures in order to understand the dynamic processes governing their photocurrent generation mechanisms, and thereby facilitate the design of photodetectors with higher performances. From the broad library of 2D materials, we focus our attention on the three that have attracted the most interest: graphene, TMDs and hexagonal boron nitride (hBN). These materials possess entirely distinct optoelectronic properties. For instance, graphene, a semimetal, displays a broadband photoresponse dominated by hot carriers, whereas the optical response of semiconducting TMDs is governed by strong excitonic effects. Studying how these light-matter interactions induce an electric signal in actual devices poses many experimental challenges. Besides the fabrication of high-quality devices, one of the main difficulties is to assess the ultrafast electronic processes involved in the photocurrent generation. To this end, we apply and further develop a versatile time-resolved photocurrent measurement technique (TRPC) which combines electronic detection with sub-picosecond optical excitation.

Contents

Abstract iii

Introduction 1

1 Properties of 2D materials and their heterostructures 7

1.1 Graphene 8

1.1.1 Electronic properties 8

Band structure 8

Transport properties 9

Electronic heat capacity 11

1.1.2 Optical properties 11

1.1.3 Photocarrier dynamics 13

Carrier heating 13

Carrier cooling 16

1.2 Transition metal dichalcogenides 17

1.2.1 Electronic properties 17

1.2.2 Optical properties 19

Excitons 20

Light absorption and emission 22

1.2.3 Photocarrier dynamics 22

Exciton formation 24

Exciton recombination 24

1.3 Hexagonal boron nitride 25
1.4 Van der Waals heterostructures 26
1.4.1 Structural properties 28
1.4.2 Electronic properties 29
Interlayer transport 30
1.4.3 Optical properties 32

2 Photocurrent generation and measurement in 2D materials 33

2.1 Introduction 34
2.2 Photodetection terminology 35
2.3 Photodetection enabled by photoexcited carriers 36
2.3.1 Carrier dynamics and transport in semiconductors 36
2.3.2 Photoconductive effect 37
Intrinsic photoconductor 38
Extrinsic photoconductor 39
2.3.3 Photovoltaic effect 41
2.3.4 Internal photoemission 43
2.4 Photodetection enabled by hot carriers 44
2.4.1 Dynamics and transport of electronic heat 45
2.4.2 Photo-thermoelectric effect 45
PTE photodetectors 46
Graphene-based PTE photodetectors 47
2.4.3 Photo-bolometeric effect 50
2.5 Photocurrent measurement techniques 51
2.5.1 Scanning photocurrent microscopy 53
2.5.2 Photocurrent spectroscopy 54

2.5.3 Time-resolved photocurrent measurement 55

3 Fabrication and characterization of van der Waals heterostructures 61

3.1 Introduction 62

3.2 Device fabrication 63

3.2.1 Exfoliation and characterization of 2D materials 64

3.2.2 Mechanical layer assembly technique 66

3.2.3 One-dimensional edge-contacts and wire-bonding 68

3.3 Characterization of the heterostructure 70

3.4 Conclusion 73

4 Hot-carrier photocurrent in lateral graphene junctions 75

4.1 Introduction 76

4.2 Devices 77

4.3 Photovoltage generation on a femtosecond timescale 79

4.4 Efficient photo-induced carrier heating 81

4.5 Photo-thermoelectric effect at graphene-metal interfaces 84

4.5.1 Time-resolved photocurrent 85

4.5.2 Spectrally-resolved photocurrent 86

4.5.3 Gate-tunable photoresponse 88

4.5.4 Polarization-controlled photoresponse 90

4.6 Conclusion and outlook 93

5 Interlayer photocurrent in graphene-based heterostructures 95

5.1 Photo-thermionic effect in G/WSe_2/G heterostructures 97

5.1.1 Introduction 97

5.1.2 Devices 99

5.1.3 Experimental signature of photo-thermionic effect 100
5.1.4 Electrical tuning of the PTI effect 102
5.1.5 Theoretical model of the PTI effect 104
5.1.6 Discussion on the PTI efficiency 106
5.2 Tuning ultrafast electron thermalization pathways in G/hBN/G heterostructures 107
5.2.1 Devices 107
5.2.2 Photo-thermionic emission versus photon-assisted tunneling 109
5.2.3 Time-resolved photocurrent measurements 110
5.2.4 Fowler-Nordheim tunneling and thermalization time . . . 111
5.3 Conclusions and outlook 113

6 Picosecond photoresponse in TMD-based heterostructures 115
6.1 Introduction 116
6.2 Graphene/WSe_2/Graphene devices 117
6.3 Measurement of the photoresponse time 118
6.4 Photocarrier dynamics in TMD-based heterostructures 122
6.5 Efficiency of G/WSe_2/G photodetectors 124
6.6 Conclusion and outlook 125

7 Tunnel ionization of 2D excitons in monolayer WSe_2 127
7.1 Introduction 128
7.2 Monolayer WSe_2 p-n junctions 131
7.3 Field-dependent photocurrent spectroscopy 131
7.4 Measurement of the photoresponse time 134
7.4.1 Nonlinear photoresponse 134
7.4.2 Time-resolved photocurrent 135

7.5 Exciton dissociation and photocurrent dynamics in monolayer WSe_2 136
7.6 Conclusion and outlook 138

Conclusion **139**

A Fabrication recipes **145**

A.1 Layer assembly procedure 145
A.2 Laser writer 149

B Complement: Photo-thermionic effect in G/WSe_2/G heterostructures **151**

B.1 Cooling pathways of thermalized hot carriers in graphene 151
B.2 Devices with different WSe_2 thicknesses 153
B.3 Internal photoemission in Au/WSe_2/Au heterostructures 155
B.4 PTI model 157
B.5 Measurements at different ambient temperatures 158

C Complement: Picosecond photoresponse in TMD-based heterostructures **161**

C.1 Steady-state photocurrent and IQE model 161
C.2 Electrostatic model for a G/WSe_2/G heterostructure 162
C.3 Real-time photoresponse and RC-time constant 165
C.4 Photoluminesence quenching 166
C.5 Characterization of the photodetectors 168

D Complement: Tunnel ionization of 2D excitons in monolayer WSe_2 **171**

D.1 Device characterization 171
D.2 Calculations of the electric field distribution 174
D.3 Wannier-Mott exciton model 174
D.4 Nonlinear photoresponse model 176

D.4.1 Power dependence of the photocurrent 176
D.4.2 Time-resolved photocurrent 177
D.5 Linear photoresponse model 180
D.6 Collection efficiency 181
Experimental estimation of the collection efficiency . . . 182
D.6.1 Numerical estimation of the collection efficiency 183

Publications **185**

Bibliography **187**

List of Figures

1 History of scientific publications on 2D materials 2

2 Overview of the optoelectronic properties of 2D materials and their heterostructures 4

3 Schematics of the main 2D material systems studied in this thesis 6

1.1 Structural and electronic properties of graphene 10

1.2 Optical absorption of graphene 12

1.3 Photocarrier dynamics in graphene 14

1.4 Structural and electronic properties of TMDs 18

1.5 Exciton and optical properties of TMDs 21

1.6 Photocarrier dynamics in TMDs 23

1.7 Structural and electronic properties of hBN 26

1.8 Structural and optoelectronic properties of vdWHs 27

2.1 Main classes of photodetection mechanisms 34

2.2 Intrinsic and extrinsic photoconduction 39

2.3 Planar and vertical photovoltaic photodetector 42

2.4 Internal photoemission and photovoltaic effect in a Schottky photodiode 44

2.5 Photo-thermoelectric effect and comparison with other photodetection mechanims 49

2.6 Experimental setup 52

2.7 Schematic view of the optical and electrical setup 54

2.8 Characterization of the quasi-CW supercontinuum laser source . . 56

2.9 Time-resolved photocurrent measurement and analysis 58

2.10 Characterization of the ultrashort pulse laser source 60

3.1 Main steps involved in the fabrication of 2D material-based electronic devices 63

3.2 Characterization of various exfoliated flakes 66

3.3 Layer assembly process 68

3.4 One-dimensional edge-contacts 69

3.5 Wire-bonding and chip carrier mounting 70

3.6 Characterization of vdWH by AFM and electrical measurements . 72

4.1 Hot-electron photocurrent and devices 78

4.2 Femtosecond sensing of hot electrons 81

4.3 Spectral dependence of the PTE response 82

4.4 Electron heating efficiency in graphene 84

4.5 Hot-electron dynamics at p-n junction and graphene-metal contact 85

4.6 Effect of photon energy on photocurrent 87

4.7 Effect of the Fermi energy on the photocurrent 89

4.8 Effect of light polarization on photocurrent 92

5.1 Internal photoemission vs photo-thermionic emission 98

5.2 The photo-thermionic device 99

5.3 Experimental signatures of photo-thermionic emission 101

5.4 Tunable photo-thermionic response 103

5.5 Comparison between data and photo-thermionic model 105

5.6 IQE vs. laser-induced temperature change ΔT. 107

5.7 Interlayer photocurrent of a G/hBN/G device 108

5.8 Two different regimes of interlayer photocurrent in a G/hBN/G device . . . 110

5.9 Two-pulse correlation of interlayer photocurrent in a G/hBN/G device . . . 111

5.10 Experimental signatures of direct Fowler-Nordheim carrier tunneling 113

6.1 Photocurrent generation in G/WSe2/G heterostructure . . . 117

6.2 Characterization of a G/WSe_2/G device . . . 118

6.3 Extraction of the photoresponse time of a G/2.2-nm WSe_2/G heterostructure by time-resolved photocurrent measurements . . . 119

6.4 Tuning of the photoresponse time by variation of the WSe_2 layer thickness and bias voltage . . . 121

6.5 Dynamic processes governing the photoresponse of G/WSe_2/G heterostructures . . . 123

6.6 Internal Quantum Efficiency of G/WSe_2/G heterostructures . . . 124

7.1 Schematic of the exciton under high electric field and experimental concept . . . 129

7.2 Photocurrent generation in a monolayer WSe_2 p-n junction . . . 130

7.3 Field-dependent photocurrent spectroscopy in a monolayer WSe_2 p-n junction . . . 132

7.4 DC Stack shift in a monolayer WSe_2 . . . 133

7.5 Analysis of the nonlinear photoresponse due to exciton-exciton annihilation . . . 135

7.6 Determination of the photoresponse τ by time-resolved photocurrent measurements . . . 136

7.7 Dynamic processes governing the photoresponse of monolayer WSe_2 p-n junctions . . . 137

7.8 Comparison of the performances of 2D materials and vdWHs for ultrafast photodetection . . . 142

A.1 Flowchart of the layer assembly process and description of transfer setup . . . 146

B.1 Heating and cooling pathways of hot carriers in graphene 153

B.2 PTI photocurrent in G/2.2 nm WSe_2/G heterostructure 154

B.3 PTI photocurrent in G/7.4 nm WSe_2/G heterostructure 155

B.4 Photocurrent measurements in Au/20-nm-thick WSe_2/Au heterostructure 157

B.5 PTI response at different ambient temperature 159

C.1 Schematic of the heterostructure and its band alignment 162

C.2 Comparison between measured and modelled photocurrent in a G/WSe_2/G heterostructure 164

C.3 Real-time photocurrent response of G/WSe_2/G photodetectors . . 166

C.4 Photoluminescence quenching at G/WSe_2 interfaces 167

C.5 Performance of the G/7.4 nm WSe_2/G photodetector 169

D.1 Characterization of device 1 172

D.2 Characterization of Devices 2 and 3 173

D.3 Finite-element calculations of the electric field at the p-n junction 174

D.4 Calculated stark shifts and ionization rate for different dielectric encapsulations 176

D.5 Additional analysis of the nonlinear and time-resolve photocurrent measurements 179

D.6 Experimental and numerical estimations of the collection efficiency 183

Introduction

“What could we do with layered structures with just the right layers?”, asked Richard P. Feynman in 1959 during his famous lecture entitled *There’s Plenty of Room at the Bottom* [1]. “What would the properties of materials be if we could really arrange the atoms the way we want them?”. The idea of designing materials at the atomic level is very appealing, but almost 60 years after Feynman’s talk, its implementation remains a major goal of materials science. One of the most successful approaches to date arose in the 70s with the development of multilayer (III-V) heterostructures grown by molecular beam epitaxy [2, 3]. This key technology has led to many important optoelectronic applications, including semiconductor lasers, solar cells, and high-speed photodetectors, which have transformed our daily lives. Yet, various material constraints (e.g., lattice matching conditions) severely limit the quality and variety of these heterostructures [4], which calls for a new material design strategy.

2D materials and their heterostructures

Two-dimensional (2D) layered materials have recently emerged as a promising platform for the creation of a new type of heterostructure that overcomes the limitations of conventional materials. For the past decade, this class of one-atom-thick materials has been a major topic in a wide range of fields, from particle physics to biology. The first isolation of graphene in 2004 [5] and of other 2D crystals in 2005 [6] by Geim and Novoselov triggered enormous interest for these materials [7]. In their bulk form, these materials are formed by atoms with strong in-plane covalent bonds, while each layer is weakly bound to neighbouring layers by van der Waals interactions. This weak interlayer interaction makes it possible to mechanically exfoliate individual layers from the bulk. Driven by the simplicity of this isolation method (the so-called “scotch-tape method”), a large research effort ensued that revealed the truly fascinating properties of graphene, including its high electronic mobility [8, 9], large tensile strength [10] and superior thermal conductivity [11]. The rapid development of this field of research is reflected by the dramatic increase of publications on graphene after 2004 (Fig. 1).

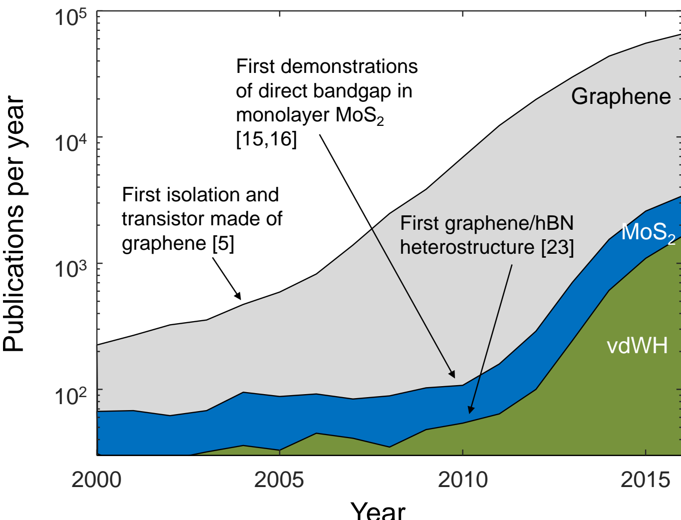

FIGURE 1: **History of scientific publications on 2D materials.** Number of publications on graphene (grey), Mos_2 (blue) and vdWHs (green) in recent years. The data was obtained by a keyword search with the name of each material in SCOPUS. Some of the most important breakthroughs in the field of 2D materials are indicated by the black arrows.

After several years of intensive research on graphene, the attention gradually shifted towards other 2D materials (Fig. 1), notably hexagonal boron nitride (hBN) and transition metal dichalcogenides (TMDs). These crystals display a wide range of properties which complement those of gapless graphene. For instance, hBN is a transparent insulator [12, 13], while TMDs (group-V) [14–17], like MoS_2, are semiconductors with bandgaps in the near-infrared to visible region (Fig. 2). Moreover, due to important changes in their electronic band structure, 2D materials typically display properties that are very different from those of their bulk counterparts. TMDs, for example, exhibit a crossover from indirect to direct bandgap in the monolayer limit [15, 16]. The collection of 2D materials is growing day by day and the latest additions include: anisotropic semiconductors (black phosphorus) [18, 19], superconductors ($NbSe_2$) [20], topological semimetals (WTe_2) [21] and ferromagnets (CrL_3) [22].

This extensive library of materials with diverse properties opens up exciting possibilities for the creation of hybrid systems with predetermined attributes and multiple functionalities. The fabrication of such artificial materials has recently been made possible by the development of techniques which allow 2D crystals to be stacked on top of one another in an atomically precise sequence [23, 24] (Fig. 1). The artificial materials resulting from this process are called van der Waals (vdW) heterostructures in reference to the force that holds the layers together [25–27]. This weak interlayer coupling allows the integration of different 2D crystals without the constraints of lattice matching imposed on conventional

heterostructures. This ability makes it possible to engineer and create a quasi-infinite number of different heterostructures[1] with unfathomable properties.

Optoelectronic prospects

In recent years, the potential of 2D materials and their heterostructures for photonic and optoelectronic applications have become increasingly evident [31–35]. A wide range of optoelectronic devices based on 2D materials have indeed been successfully demonstrated, including optical modulators [36], light-emitting diodes (LEDs) [37] and plasmonic devices [38]. Among these, photodetectors have undoubtedly attracted the most attention, as illustrated by the many review articles published on this topic [31, 33–35, 39–43]. This intense research has been prompted by the prospects of photodetectors with superior performance in terms of efficiency, detection speed, as well as wavelength range and mechanical flexibility.

Indeed, 2D materials, in particular graphene and TMDs, are appealing for photodetection applications. Due to its gapless nature, graphene has a broadband [44] (Fig. 2) and ultrafast photoresponse dominated by hot carriers [45], making it promising for high-speed photodetection [46–48]. In contrast, the optical response of semiconducting TMDs exhibits strong light-exciton interactions [15, 49], advantageous for applications requiring high light absorption [50]. Combining these complementary properties in a single heterostructure is promising approach for creating multi-functional, high-performance optoelectronic materials.

Over the last decade, a large number of prototype photodetectors have been developed that exploit the distinct properties and advantages of these materials. In many cases, the performance parameters of the photodetectors have been shown to match or even surpass current technologies [31]. However, while the potential of these photodetectors has been demonstrated, many of the intrinsic physical processes governing their performance have remained elusive. The general objective of this thesis is to explore and understand how light is converted into electricity in optoelectronic devices made of 2D materials and vdWHs. More specifically, the goal is to identify their dominant photodetection (or photocurrent generation) mechanisms and to unravel the dynamic processes governing their photoresponse in order to facilitate the design of photodetectors with superior performance. Ultimately, the aim is to bridge the gap between the fundamental studies of carrier dynamics in 2D materials and the research on photodetection applications.

From the vast library of 2D materials, we focused our attention on the three most common, i.e., graphene, TMDs and hBN, and investigated four types of

[1]Considering that there are an estimated ~ 100 stable monolayers [28–30], the number of possible 4-layers heterostructure (with repetition) is $\binom{103}{4} \sim 4.4$ millions. For 10-layers heterostructures, this number goes up to ~ 42 trillions

optoelectronic devices made of these materials (Fig. 3). These devices can be characterized by their photoactive material (graphene or TMD) and by the direction of the photocurrent with respect to the 2D layer (in-plane or out-of-plane). Depending on the light-absorbing material, different forms of electronic energy (excess heat or photocarriers) can drive the photodetection mechanism. Changing the photodetection geometry, on the other hand, has important implication on the charge carrier transport (interlayer vs. intralayer) and the photon collection efficiency.

Studying how light-matter interactions induce an electric signal in these devices poses many experimental challenges. Besides the fabrication of high-quality devices, one of the main difficulties is to assess the ultrafast electronic processes responsible for the photocurrent generation. To this end, we employed and further developed a versatile time-resolved photocurrent (TRPC) measurement technique which combines electronic detection with subpicosecond optical excitation. Compared to all-optical ultrafast techniques [51], TRPC allows us to isolate the processes responsible for the generation of photocurrent in actual devices.

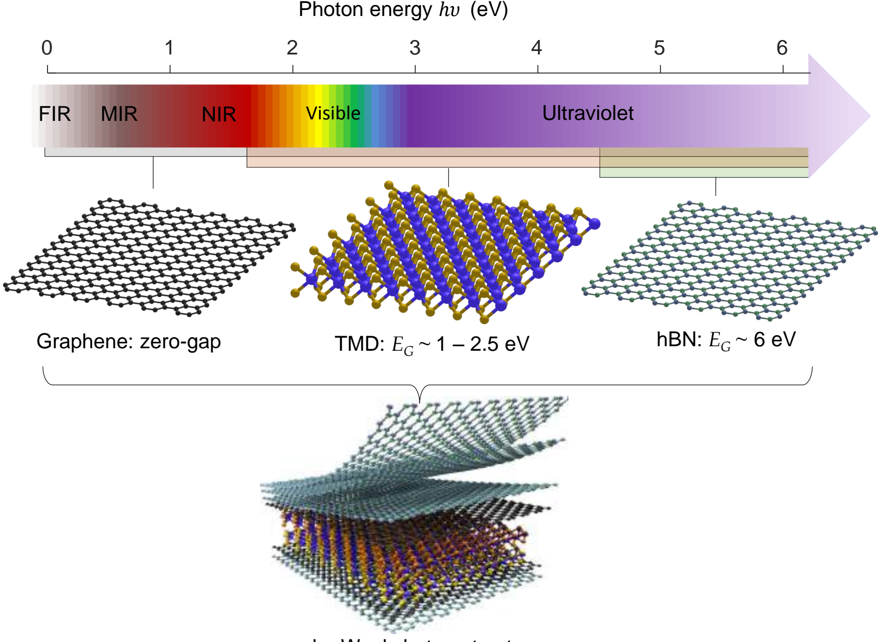

FIGURE 2: **Overview of the optoelectronic properties of 2D materials and their heterostructures.** The electromagnetic spectrum is shown in the top portion of the panel. Different spectral regions are identified, where NIR, MIR and FIR indicate near-, mid- and far-infrared, respectively. The atomic structures of graphene, WSe_2 (a TMD) and hBN are presented below the spectrum, together with their bandgap E_G and their absorption range. A schematic of a vdWH is shown in the lower portion of the panel.

Thesis outline

This thesis is organized as follows:

- Chapter 1 gives an overview of the remarkable optoelectronic properties of graphene, TMDs, hBN and their heterostructures, with an emphasis on the dynamics of their photocarriers.

- Chapter 2 presents the basic photodetection concepts and measurement techniques that are relevant for this thesis, along with a review of the main photocurrent generation mechanisms observed in 2D materials.

- Chapter 3 describes the techniques employed to fabricate high-quality, state-of-the-art devices based on 2D materials and vdWHs.

- Chapter 4 presents an in-depth study on the photocurrents generated laterally in various graphene devices and investigates the ultrafast heating dynamics of the hot carriers which drive this process.

- Chapter 5 explores the photon-induced interlayer transport in graphene-based heterostructures and introduces two novel photodetection mechanisms: thermionic emission and photon-assisted tunneling.

- Chapter 6 demonstrates that heterostructures made of thin TMD crystals can possess both a high efficiency and a fast photoresponse on the order of a few picoseconds, and examines the dynamic processes that limit their performance.

- Chapter 7 reports on the tunnel ionization of excitons under high in-plane electric fields in monolayer TMDs, and on the concomitant Stark and Franz-Keldysh effects.

- Finally, in the Conclusion, a summary of the main achievements of thesis is presented, along with a discussion on the potential of 2D materials for ultrafast optoelectronic applications.

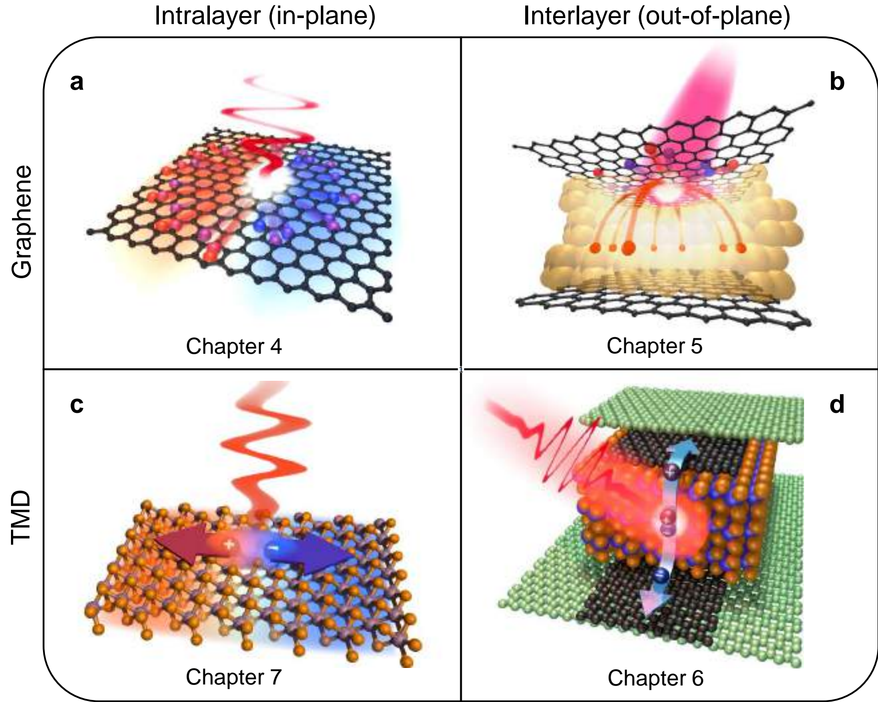

FIGURE 3: **Schematics of the main 2D material systems studied in this thesis.** The devices are arranged according to their photoactive material (graphene or TMD) and the direction of the photocurrent they produce with respect to the 2D layer (in-plane or out-of-plane). The chapter in which each device is studied is indicated below them. **a)** in-plane graphene p-n junction. **b)** graphene/TMD/graphene heterostructure with light absorption in graphene. **c)** in-plane p-n junction made of monolayer TMD. **d)** hBN/graphene/TMD/graphene/hBN. Here, light is absorbed in the TMD layer.

Chapter 1

Properties of 2D materials and their heterostructures

In this chapter we review the electronic and optical properties of the 2D materials that are examined in this thesis, e.i., graphene, TMDs and hBN. We describe the band structure of each material and discuss its implications on their optical response. We also highlight the dynamics of the photoexcited carriers in graphene and TMDs, and introduce the concepts of hot carriers and exctions. Finally, we give an overview of the main physical properties of van der Waals heterostructures, with an emphasis on the interlayer transport mechanisms.

1.1 Graphene

Graphene is the first and by far the most prominent 2D material. The concept of graphene dates back from the middle of the 20th century, when this one-atom thick sheet of carbon atoms was theoretically studied to understand the properties of graphite and other carbon allotropes [52]. For a long time, the mere existence of graphene was in doubt since according to Mermin-Wagner's theorem, no long-range order can exist in two-dimensions [53]. This situation changed drastically in 2004, when Geim and Novoselov managed to isolate micrometer-size graphene flakes and probed their electrical properties [5]. This groundbreaking experiment attracted tremendous scientific interest and earned them the 2010 Nobel prize in physics [54, 55].

The large research effort triggered by Geim and Novoselov's seminal work revealed the fascinating and unique properties of graphene [56–58], such as its high carrier mobility ($> 1 \times 10^6$ cm^2/Vs) [9, 59], great tensile strength [54, 55] and broadband light absorption determined by the fine structure constant [44, 60]. All these properties are a direct or indirect consequence of the 2D nature of graphene. In the following sections, we focus on the electronic and optical properties of graphene, most of which can be derived from its band structure.

1.1.1 Electronic properties

Graphene is a single layer of sp^2-hybridized carbon atoms arranged in a two-dimensional hexagonal lattice, with a nearest-neighbour distance of 1.42 Å (Fig. 1.1a). Each atom shares an in-plane σ bond with its three nearest neighbour, while the remaining valence electron forms a delocalized, out-of-plane π-bond. These bonds give rise to the valence π-band and conduction π^*-bands and are responsible for the most of the intriguing electronic properties of graphene.

Band structure

As Wallace first demonstrated in 1947 [52], the band structure of graphene can be obtained by dividing the honeycomb structure into two triangular sublattices (A and B in Fig. 1.1a) and using a tight-binding approximation. The resulting band structure (Fig. 1.1b), which describes relationship between the energy and momentum of the electrons, displays particular features at the K and K' points of the Brillouin zone. At these points, also called Dirac points, the conduction and valence band meet, thus making graphene a zero-band gap semimetal. Under ideal conditions (no doping, zero temperature), the Fermi energy E_{F} is exactly at the Dirac points. The two sets of Dirac points (K and K'), corresponding to the two sublattices, give graphene a valley degeneracy of $g_{\mathrm{v}} = 2$. Close to the Dirac points ($|E| \lesssim 1$ eV), the valence and conduction bands form a conical structure

(Fig. 1.1b), which is well described by a linear dispersion relation:

$$E(\mathbf{k}) = \pm\hbar v_{\mathrm{F}}|\mathbf{k}|, \tag{1.1}$$

where $\hbar$ is the reduced Planck constant, $v_{\mathrm{F}} \approx c/300 \approx 10^6$ m/s is the Fermi velocity and **k** is the wave vector measured from the Dirac point. Interestingly, this corresponds to the spectrum of the Dirac-like Hamiltonian for massless Dirac fermions with a velocity v_{F} [61, 62]. This resemblance attracted a lot of attention in the early days of graphene [63]. In contrast, charge carriers in conventional semiconductors and bilayer graphene are described by a non-relativistic, parabolic dispersion.

The linear dispersion of graphene leads to a density of state that is proportional to the energy:

$$D(E) = \frac{g_{\mathrm{s}}g_{\mathrm{v}}}{2\pi(\hbar v_{\mathrm{F}})^2}|E|, \tag{1.2}$$

where $g_{\mathrm{s}} = 2$ is the spin degeneracy. The relationship between the charge carrier density n and the Fermi energy E_{F} is obtained by integrating $D(E)$ up to E_{F}:

$$E_{\mathrm{F}} = \mathrm{sgn}(n)\hbar v_{\mathrm{F}}\sqrt{\pi|n|}. \tag{1.3}$$

Hence, due to the gapless nature, the carrier density can be tune continuously from electrons ($n > 0$) to holes ($n < 0$) by varying E_{F}, and vice-versa.

Transport properties

A common and convenient way to modulate the charge carrier density in graphene (and in 2D materials in general) is to apply a potential difference between graphene and a metallic gate, separated by an insulator. This electrostatic effect, also called field effect, is often use to tune and study the electrical properties of graphene. For instance, the electrical conductivity σ of graphene increases with the number of electrons and holes, showing a minimum at the so-called charge neutrality point when the Fermi energy is at the Dirac point (Fig. 1.1c). However, due to thermal effects and local variations in the Fermi level (so-called electron-hole puddles), the charge carrier density, and therefore the conductivity, never vanish completely.

Studying the relation of $\sigma(n)$ provides insight into the electrical transport properties such as the charge carrier mobility. In the diffusive regime, the mobility μ is defined as the ratio between the conductivity σ and the charge density $\rho = e_0 n$, where e_0 is the elementary charge. Due to the massless nature of its carriers and their low scattering rate with intrinsic phonons, graphene can exhibit a room temperature mobility that surpasses by far the one of conventional semiconductors or 2DEGs. Room temperature mobilities of up to 140 000 cm^2/Vs have been demonstrated in clean graphene samples encapsulated between two

layers of hBN [9]. Since the mobility usually reflects the quality of the graphene, measuring this quantity allows us to verify the quality of our samples (see section 3.3). The transport properties of graphene have been studied in great detail over the last decade and we refer the interested reader to the excellent review articles published on this topic [56–58].

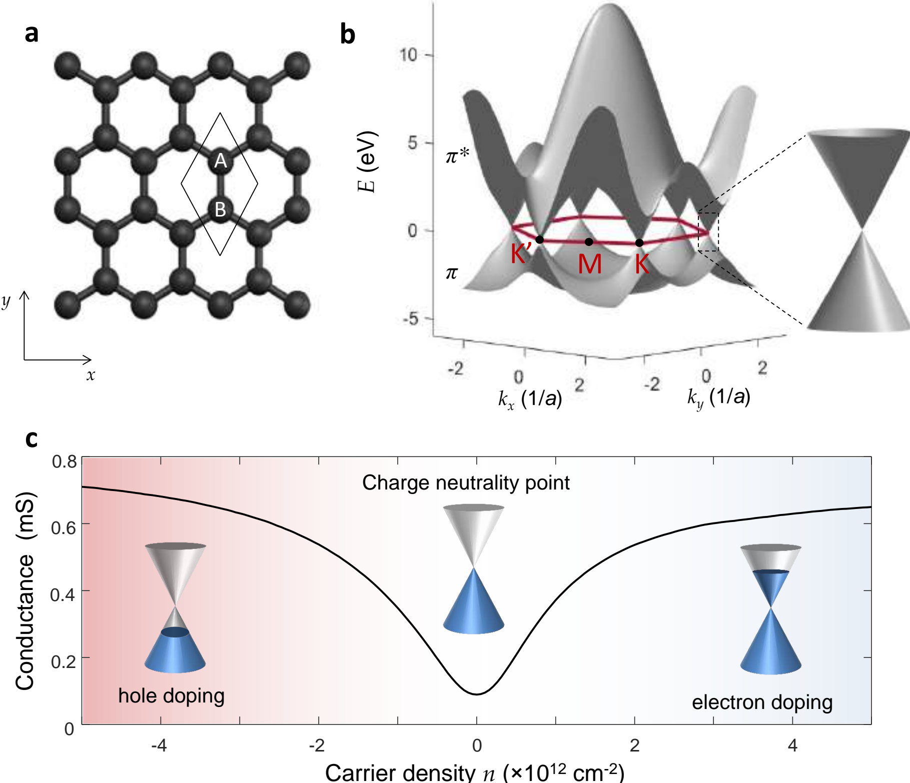

FIGURE 1.1: **Structural and electronic properties of graphene. a)** The hexagonal lattice of graphene. The elementary cell (solid black line) contains two carbon atoms belonging to sublattices A and B. Each atom in sublattice A has 3 nearest neighbours in sublattice B, and vice-versa. **b)** Band structure of graphene. Left: Electronic dispersion of the valence π-band and conduction π^*-bands calculated using the tight-binding approximation [56]. The k_x and k_y are normalized by the lattice constant a. The Brillouin zone and the high symmetry points are shown in red. Right: Zoom on the linear dispersion (Dirac cone) close to one of the Dirac points. **c)** Ambipolar conductance of a graphene device as a function of the charge carrier density n. Inset: Dirac cones with different doping levels. The blue region corresponds to the states filled by electrons.

Electronic heat capacity

As we explain in Section 1.1.3, the electronic heat capacity C_e is another important electronic property since it governs the carrier heating and cooling processes in graphene. The electronic heat capacity at constant Fermi energy E_F is given by

$$C_\mathrm{e} = \frac{\partial U}{\partial T_\mathrm{e}} = \frac{\partial}{\partial T_\mathrm{e}} \int_{-\infty}^{\infty} D(E) f(E, E_\mathrm{F}, T_\mathrm{e}) E \mathrm{d}E, \tag{1.4}$$

where U represents the total internal energy of the material, $D(E)$ is the density of state (see Eq. 1.2) and f, the Fermi-Dirac distribution is defined as

$$f = \frac{1}{\exp\left(\frac{E - E_\mathrm{F}}{k_\mathrm{B} T_\mathrm{e}}\right) + 1}, \tag{1.5}$$

with T_e representing the electronic temperature and k_B, the Boltzmann constant. For doped graphene, in the limit where $k_\mathrm{B} T_\mathrm{e} \ll E_\mathrm{F}$, the Sommerfeld expansion can be employed to evaluate 1.4 and we obtain:

$$C_\mathrm{e} = \frac{2\pi}{3} \left(\frac{k_\mathrm{B}}{\hbar v_\mathrm{F}}\right)^2 E_\mathrm{F} T_\mathrm{e} = \alpha_\mathrm{C} T_\mathrm{e}, \tag{1.6}$$

which corresponds to the heat capacity C_e of a degenerate 2D electron gas.

1.1.2 Optical properties

The unique band structure of graphene leads to distinct optical properties and various types of light-matter interaction [32, 39, 60]. In particular, its gapless nature gives rise to a very broad absorption spectrum, which makes it an attractive material for optoelectronic applications.

The intrinsic optical absorption of 2D layers A_abs is determined by the real part of their optical conductivity σ, i.e.,

$$A_\mathrm{abs} = \frac{\mathrm{Re}[\sigma]}{\epsilon_0 c}, \tag{1.7}$$

where ϵ_0 is the vaccum permittivity and c is the speed of light. In graphene, the optical conductivity is governed by two type of processes: the interband and intraband optical transitions (Fig. 1.2a) [60]. The relative contribution of both processes depends on the Fermi energy of graphene E_F and the photon energy $E_\mathrm{photon} = h\nu$, where ν is the photon frequency. When $E_\mathrm{F} > h\nu/2$, only intraband transitions are allowed since interband transitions are prohibited by Pauli blocking. For realistic doping level (E_F = 0.1 to 0.3 eV), this corresponds to the spectral range below the mid- to near- infrared regions. In this regime,

the intraband absorption is due to the free-carrier response and can therefore be well described by the Drude model, which takes into account the scattering time of the free carriers [64, 65].

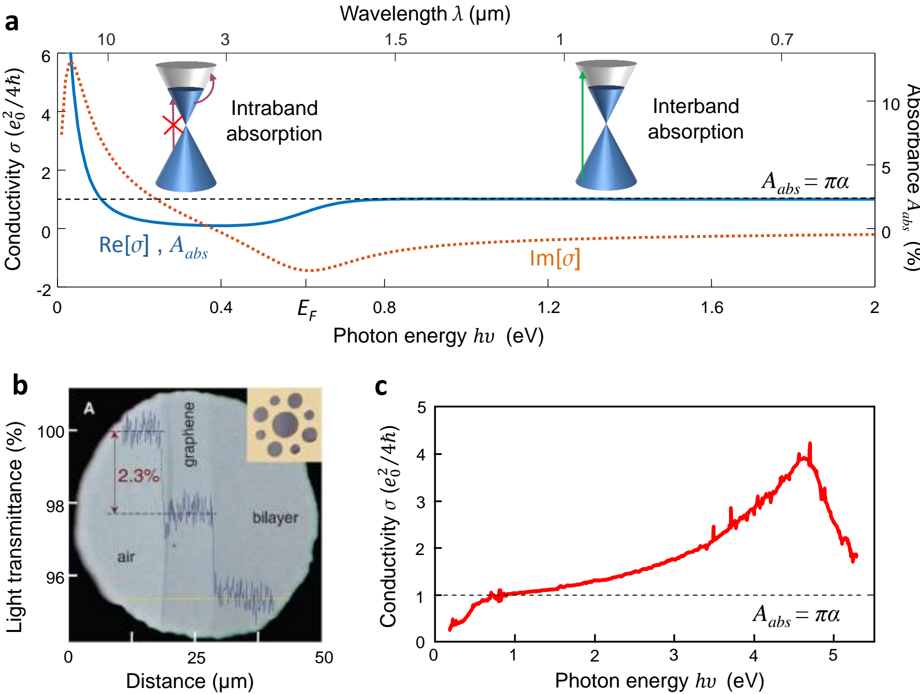

FIGURE 1.2: **Optical absorption of graphene. a)** Real (solid blue line) and imaginery (dashed orange line) part of the theoretical optical conductivity of graphene (left axis) and the corresponding absorbance (right axis) as a function of the photon energy $h\nu$. The conductivity is calculated according to Falkovsky *et al.* [66] in the local limit ($k = 0$), for a temperature $T = 300$ K, Fermi energy $E_F = 0.3$ eV and a scattering time $\tau = 20$ fs. The dashed black line corresponds to the "universal" absorbance value of $\pi\alpha$. Inset: Dirac cones showing the interband transition process allowed at $h\nu > 2E_F$, but forbidden (red cross) at $h\nu < 2E_F$ due to Pauli blocking. In this regime, only intraband transitions (curved arrow) are allowed. **b** Image of an aperture partially covered by graphene and bilayer graphene (also shown at lower magnification in the inset) taken from Nair *et al.* [44]. The transmitted white light measured along the yellow line shows clear steps of 2.3%, as predicted. **c)** Experimental optical conductivity (solid red line) spectrum measured by Mak *et al.* [67]. The dotted black line indicates the universal absorbance value.

Passed this energy threshold, when $E_F < h\nu/2$, interband transitions are no longer forbidden and they dominate the optical response. Interestingly, in the linear dispersion regime of graphene, the theoretical interband absorption does not dependent on the photon energy, nor even on the specific material parameters of

graphene. It is entirely determined by universal constants: $A_{\rm abs} = \pi\alpha \approx 2.3\%$, where $\alpha = e_0^2/4\pi\epsilon_0\hbar c$ is the fine-structure constant [44] (Fig. 1.2b). To a large extent, this "universal" absorbance value is a consequence of the 2D nature of graphene, and has also been observed in other 2D systems, such as InAs thin films [68]. In practice, the measured absorbance agrees quite well with $\pi\alpha$ for photon energies ranging between $\sim$ 0.5 to 2 eV [44, 64], which is the spectral region relevant for this thesis. However, the absorbance deviates from the universal values in the ultraviolet region as interband transitions depart from the linear dispersion regime and approach the saddle-point singularity at the M point of the Brillouin zone. In this range, excitonic effects lead to a pronounced Fano resonance at $h\nu = 4.6$ eV [67] (Fig. 1.2c).

The fact that many applications operate in this spectral range raises an important question: is an absorbance of 2.3% large or small? In fact, both answer are correct. It is indeed remarkable that a single atomic layer can absorbed 2.3% of light. In comparison, about 25 nm of Si ($\sim$ 50 atomic layers) are needed to obtain a similar absorbance in the visible[1]. On the other hand, the small absolute absorbance value is a serious issue for many applications, such as photodetectors and solar cells, requiring near perfect absorption. For this reason, various approaches have been developed to enhance light-matter in 2D materials, such as plasmonic effects, integrated Si waveguides, reflector microcavities and photonic crystals [33, 39, 69].

Finally, we note that the presence of a substrate can have a large impact on the absorption spectrum of 2D materials as it may cause multiple light reflections and interferences (see Section 4.5.2). This effect can also be exploited to enhance the contrast of 2D materials, making them more easily identifiable (see Section 3.2.1) [70]. In the simplest case of a 2D layer on an infinitely thick substrate, the actual optical absorption is $A_{\rm abs}(\frac{2}{1+n_{\rm s}})^2$, where $n_{\rm s}$ is the refractive index of the substrate.

1.1.3 Photocarrier dynamics

Photons absorbed in graphene by interband transitions create photoexcited electron-hole pairs, also called photocarriers. The energy relaxation dynamics of these photocarriers has been the subject of intense investigation [71–94]. Here, we give an overview of the main relaxation processes that have been proposed and demonstrated in the literature (Fig. 1.3).

Carrier heating

As we discussed in the previous section, photons with an energy larger than twice the graphene Fermi level ($E_{\rm photon} = h\nu > 2E_{\rm F}$) are absorbed in graphene due

[1] In the visible, the absorption coefficient of Si is $\sim 1 \times 10^4$ cm^{-1}

to interband transitions. The photon energy is transferred to an electron-hole pair, both with energies $E = h\nu/2$ with respect to the Dirac point (Fig. 1.3a). In general, photoexcited carriers can either lose their excess energy by redistributing it amongst the other carriers (i.e. thermalization) via carrier-carrier Coulomb interactions, or by emitting massless bosons such as photons or phonons. Several experiments have shown that the thermalization (or carrier heating) process is the dominant relaxation pathway, as it occurs within only a few tens of femtoseconds [71, 75, 78, 95].

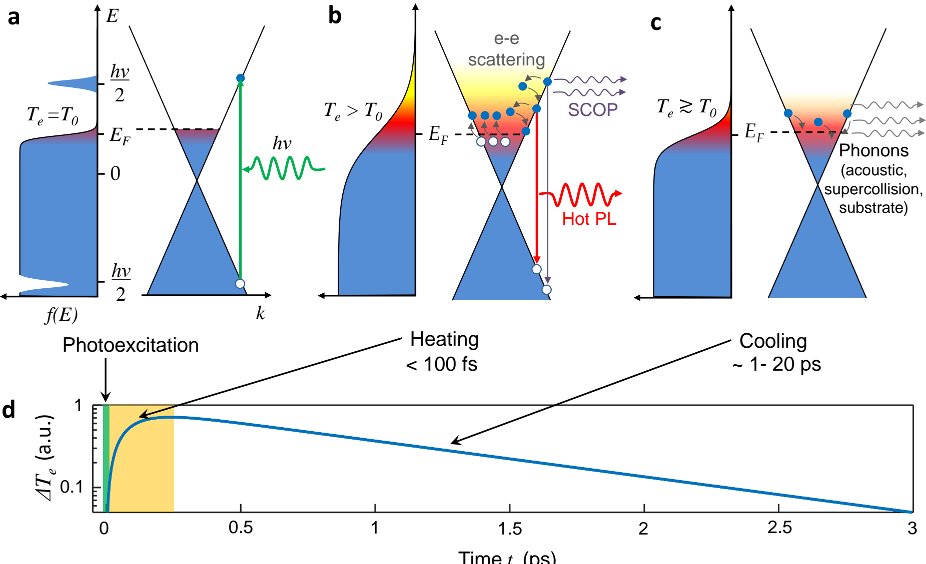

FIGURE 1.3: **Photocarrier dynamics in graphene. a)** A photoexcited electon-hole pair is created by the absorption of a photon with energy $h\nu$. This process drives the carrier distribution $f(E)$ (orginally at a temperature $T_\mathrm{e} = T_0$) out of equilibrium. **b)** The photoexcited electron energy ($h\nu/2$) is rapidly ($\tau_\mathrm{heat} < 50$ fs) transferred to the electronic bath via various e-e scattering processes, which results in the formation a hot carrier distribution with temperature $T_\mathrm{e} > T_0$. Part of the energy is also lost through the emission of optical phonons (SCOPs) and photons (hot photoluminescence). **c)** The hot carrier distribution slowly cools down through various phonon emission processes and return to ambient temperature T_0 on a picosecond timescale (τ_cool). **d)** Schematic time dependence of the carrier temperature increase $\Delta T_\mathrm{e} = T_\mathrm{e} - T_0$ illustrating the heating (yellow area) and cooling of carriers after photoexcitation (green area). Here, ΔT_e is simply modelled by two exponentials, i.e., $\Delta T_\mathrm{e} = (T_{\mathrm{e},0} - T_0)\,[1 - \exp(-t/\tau_\mathrm{heat})]\,\exp(-t/\tau_\mathrm{cool})$.

To understand the origin of the ultrafast carrier-carrier scattering in graphene, it is enlightening to compare the energy of Coulomb interactions between carriers to their kinetic energy [72, 96]. The ratio between these two quantities is given by the so-called graphene's fine structure constant $\alpha_\mathrm{G} = e_0^2/4\pi\epsilon_0\epsilon_\mathrm{r}\hbar v_\mathrm{F} = 2.19/\epsilon_\mathrm{r}$, which is analogous to the QED fine structure constant α discussed in the previous

section. Interestingly, this value is independent of the charge carrier density, but depends on the relative permittivity of the dielectric environment ϵ_r. In most cases, α_G is close to unity, which indicates strong Coulomb interactions and, therefore, rapid carrier-carrier (e-e) scattering.

Depending on the doping and photoexcitation conditions, different types of e-e scattering processes can take place, including intraband and interband scattering [85, 97], impact ionization (also called carrier multiplication) and Auger recombination [92, 93]. The last two (Auger-type) processes have been predicted and shown to be particularly efficient in undoped graphene [81, 94]. In doped graphene, intraband scattering dominates the photocarrier relaxation dynamics and can lead to the generation of multiple electron-hole excitations by a single absorbed photon, a process called hot-carrier multiplication [85, 89]. Through these scattering events, photoexcited carriers distribute their energy to ambient carriers in the Fermi sea, leading to the rapid ($\tau_{\text{heat}} \lesssim 50$ fs) formation of a hot carrier distribution characterized by a temperature T_e larger than the ambient temperature T_0 (Fig. 1.3b). In Chapter 4 we investigate this carrier heating process by measuring the photocurrent driven by the hot carrier distribution, while in Chapter 5, we indirectly probe the timescale of this process by comparing it to the tunnelling time in graphene/hBN/graphene heterostructures.

As carriers thermalize among themselves, they also partially equilibrate with strongly coupled optical phonons (SCOPs), and therefore a fraction of the carrier energy is transferred to the lattice [80]. This process, which occurs within 200 fs, leads to a reduction of the heating efficiency η_{heat}, defined as the ratio between the energy contained in the electron bath versus the total absorbed energy. Since carrier thermalization occurs on a faster time scale than SCOP emission, the heating efficiency can exceed 50%, depending on the carrier temperature [89]. However, since SCOPs have a high energy ($E_{\text{op}} \approx 200$ meV ≈ 2300 K/k_B), their coupling with hot carriers becomes dominant when $T_e \gtrsim 2000$ K. At this carrier temperature, light (black-body) emission also becomes observable [80].

Such a high carrier temperature can be reached by exciting carriers with an ultrashort light pulse of fluence F. The increase in carrier temperature created by this energy impulse is governed by the heat capacity C_e (Eq. 1.6) and the rate at which heat Q (per area) is transferred to the electronic bath, i.e.,

$$C_e \frac{\mathrm{d}T_e}{\mathrm{d}t} = \frac{\mathrm{d}Q}{\mathrm{d}t}. \tag{1.8}$$

Assuming that the heating of the carriers is instantaneous ($\mathrm{d}Q/\mathrm{d}t = F\delta(t)$), the initial temperature $T_{e,0}$ of the electron gas after photoexciation is

$$T_{e,0} = \sqrt{T_0^2 + \frac{2FA_{\text{abs}}\eta_{\text{heat}}}{\alpha_C}}, \tag{1.9}$$

where A_{abs} is the absorption of graphene (Section 1.1.2) and $\alpha_{\mathrm{C}} = C_{\mathrm{e}}/T_{\mathrm{e}}$.

Carrier cooling

Fig. 1.3d illustrates the increase in carrier temperature ΔT resulting from a pulsed excitation. Once the hot carrier distribution is formed (within $\sim$ 50 fs) and has equilibrated with high-energy optical phonons (within $\sim$ 200 fs), carriers slowly thermalize with the lattice and the surrounding environment (within $\sim$ 1 to 20 ps), and cool down to ambient temperature T_0. Experiment and theory show that carriers mainly dissipate their excess heat through acoustic phonon emission (Fig. 1.3c), disorder-enhanced electron-phonon scattering (supercollision) and coupling to the remote polar (SPP) or hyperbolic phonons of the substrate.

Acoustic phonon emission (also called "normal collision") is the dominant cooling pathway predicted for pristine, suspended graphene [90, 98]. In this ideal system, carriers with energy below the optical phonon energy E_{op} can only relax via scattering with acoustic phonons. These phonons have a linear dispersion characterized by a sound velocity $v_{\mathrm{s}} \approx 20$ km/s which is much smaller than the carrier Fermi velocity v_{F}. Due to this velocity mismatch and moment conservation constraints, every phonon emitted E_{ac} only releases a small fraction of the hot carrier energy $E_{\mathrm{ac}}/k_{\mathrm{B}}T_{\mathrm{e}} \lesssim 0.04$. Hence, multiple acoustic phonons are required to cool down a single hot electron. In the doped regime, this mechanism gives a heat loss rate $H \propto T_{\mathrm{e}} - T_0$. Although, it has never been measured experimentally, this very slow relaxation pathways is expected a cooling bottleneck with characteristic cooling time $\tau_{\mathrm{cool}} \sim 1$ ns.

Disorder-enhanced supercollision describes the simultaneous emission of an acoustic phonon with the recoil of a carrier due to impurity scattering [83]. This disorder-assisted scattering effectively relaxes the momentum conservation restrictions of normal acoustic phonon emission, and therefore allows for the emission of acoustic phonons with large momentum and energy ($\sim k_{\mathrm{B}}T_{\mathrm{e}}$). Hence, in disordered graphene, supercollision leads to much faster carrier cooling than in pristine graphene, with cooling time $\tau_{\mathrm{cool}} \sim 1$ to 10 ps. The heat loss rate predicted for this cooling mechanism is $H \propto T_{\mathrm{e}}^3 - T_0^3$. Experiments have shown that supercollision is the dominant relaxation pathway for hot carriers in SiO_2-supported graphene devices [76, 99, 100].

Direct coupling to substrate phonons provides an additional energy relaxation pathway for supported graphene. Two coupling mechanisms between hot electrons and substrate phonons have been proposed. The first one occurs via the remote surface phonon modes (SPP) of polar substrates such as SiO_2 and hBN. This effect was found to affect mobility of charge carriers in SiO_2 supported graphene [101, 102]. The heat loss rate due to SPPs was calculated by Low *et al.* [79], who predicted an effective thermal conductance $\Gamma = H/\Delta T$

ranging between 1 and 10 MW/Km^2 for SiO_2 and hBN at room temperature, corresponding to a cooling time $\tau_{\rm cool} \sim 1$ ps. Experiments by Freitag *et al.* on SiO_2-supported and suspended graphene suggests that the SPP mechanism is the dominant cooling pathway for supported graphene [73]. Recently, we demonstrated another coupling mechanism between hot electrons and substrate phonons in hBN-supported graphene samples [88]. In this case, hot carriers transfer their energy by launching highly-directional hyperbolic phonon polaritons (Section 1.3). Due to their unusual hyperbolic nature, these phonons have a very high density of optical states, which gives rise to a highly efficient (super-plankian) near-field heat transfer and a cooling time of ~ 1 ps at room temperature [82].

1.2 Transition metal dichalcogenides

As we discussed in the previous section, the linear dispersion relation of graphene leads to unique optical and electrical properties, but the lack of bandgap limits its use for many applications where semiconductors are needed. The search for other 2D materials with a bandgap has led to the discovery of monolayer (group-VI) transition metal dichalcogenides (TMDs), which most notably includes Mos_2, WS_2, $MoSe_2$ and WSe_2. Although TMDs in their layered bulk form have been studied for many decades [103–107], the properties of their mono- and few layers have only been investigated in recent years [14, 40]. In the monolayer limit, TMDs possess a direct bandgap in the visible to near-infrared region [15, 16], which makes them suitable for various electrical and optoelectronic applications. Combined to their relatively high mobility (1 - 100 cm^2/Vs at room temperature) [108], their sizable bandgap makes them attractive as a channel material in logic transistors [6, 17, 109]. TMDs have also aroused great interest due to their unique optical properties [34, 110], which, as we discuss below, are governed by strong light-exciton interactions .

1.2.1 Electronic properties

TMDs (group-VI) encompass all compounds with the formula MX_2, where M is transition metal VI (Mo, W) and X is a chalcogen (S, Se). Each monolayer consists of two planes of chalcogen atoms sandwiching a plane of metal atoms in the trigonal prismatic structure [103] (Fig. 1.4a). Monolayer TMDs have a hexagonal out-of-plane symmetry, but unlike graphene, their in-plane inversion symmetry is broken. In the bulk form, monolayers are usually stacked in the ABAB sequence (2H polytype), which restores the inversion symmetry.

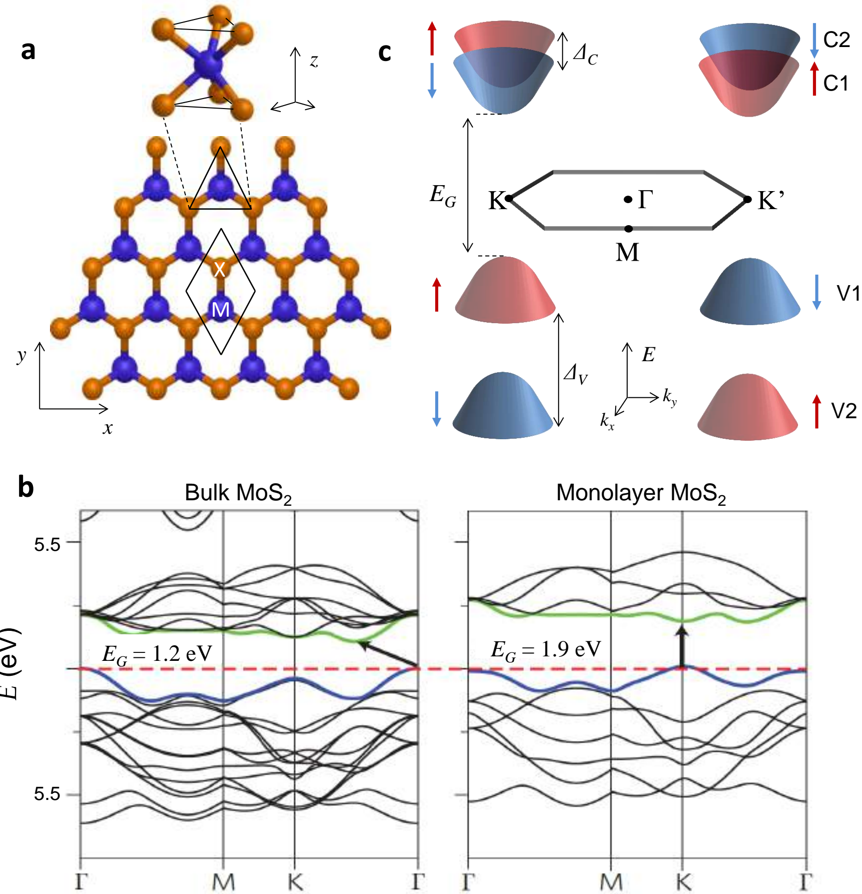

FIGURE 1.4: **Structural and electronic properties of TMDs.** **a)** Crystal structure of a monolayer TMD. The elementary cell (black rhombus) is composed of a transition metal atom (M, blue) and two chalcogen atoms (X, orange). **b)** Band structures of bulk (left) and monolayer (right) MoS_2 calculated using density-functional theory (DFT) by Kuc *et al.* [111]. The top of the valence band and bottom of the conduction band are coloured in blue and green, respectively. The red dash line represents the Fermi level and the arrows indicate fundamental bandgap. **c)** Schematic of the electronic dispersion relation around the K and K' points in monolayer WX_2. Spin-orbit coupling splits the spin degeneracy of the conduction (C1, C2) and valence (V1, V2) bands into spin-up (red) and spin-down (blue) bands. The energy separations Δ_C and Δ_V between the bands depends on the TMD compound [112]. The tilted hexagon represents the Brillouin zone with the high-symmetry points.

Due to their identical atomic structure, these TMDs have a similar band structure and, therefore, electronic and optical properties. The band structure of bulk and monolayer MoS_2 obtained from ab initio calculations is shown in Fig. 1.4b.

Bulk TMDs have an indirect bandgap ($E_{\mathrm{G}} \sim$ 1.1 to 1.4 eV) with a valence-band maximum at the Γ point and a conduction-band minimum between the K and Γ points. As the number of layers decreases, TMDs exhibit a crossover and become direct bandgap semiconductor in the monolayer limit [15, 16, 111, 113, 114]. This effect is a consequence of the change in orbital hybridization due to quantum confinement effects [115]. Indeed, the states near the Γ point are partly localized around the chalcogen atoms (hybridized p_z) and extend in the out-of-plane direction, while the states at the K and K' points are localized in-plane, around metal atoms (d orbital). Hence, changing the number of layers significantly alters the states at the Γ point, while those at the K points remain relatively unaffected, resulting in a larger direct bandgap ($E_{\mathrm{G}} \sim$ 1.7 to 2.1 eV) at the K and K' points for monolayer TMDs.

Close to the Fermi energy (Fig. 1.4c), the band structure of monolayer TMDs can be represented by two sets of degenerate conduction and valence bands around the K and K' points, with parabolic dispersion relations:

$$E(\mathbf{k}) = \pm\frac{\hbar^2|\mathbf{k}|^2}{2m^*}, \tag{1.10}$$

where m^* is the effective electron or hole mass (typically between 0.4m_0 and 0.6m_0, where m_0 is the electron rest mass) [34] and $\mathbf{k}$ is the wave vector measured from the K or K' point. Interestingly, this resembles the spectrum of a 2D Dirac Hamiltonian for massive Dirac fermions, which also describe carriers in gapped graphene [116]. Additionally, the spin-orbit interactions breaks the spin degeneracy in both the conduction and the valence band. The spin splitting is much smaller in the conduction band ($\sim$ 3 to 30 meV) than in the valence band ($\sim$ 150 to 500 meV).

Due to the broken inversion symmetry, carriers in K and K' valleys are subject to opposite orbital magnetic moment and Berry curvatures, which gives rise to the rich valley physics observed in monolayer TMDs. In particular, the contrasting magnetic moment leads to circularly polarized optical selection rules that allows optical control over the valley pseudospin [117]. This unique ability makes monolayer TMDs a promising material for valleytronic applications [118]. However, valley physics falls beyond the scope of this thesis and the interested reader is directed to one of the recent reviews on this topic [112, 119, 120].

1.2.2 Optical properties

Due to their electronic bandgap, TMDs have optical properties radically different than those of graphene. While they are transparent to long wavelengths, TMDs display high optical absorption and emission in the near-infrared and visible spectral region [34]. These strong light-matter interactions are a consequence of the enhanced carrier-carrier interactions, which give rise to prominent excitonic effects [121].

Excitons

An exciton is a neutral quasiparticle consisting of an electron and a hole bound together by their attractive Coulomb interaction [122] (Fig. 1.5a). In 3D bulk semiconductors, the properties of excitons are well described by the hydrogenic model [123] where the attractive electron-hole potential is given by $V(r) = -e_0^2/\epsilon r$. Here, ϵ is the dielectric constant of the material and r is the electron-hole separation. Due to the large dielectric constant ($\epsilon_\mathrm{r} \sim 13$), these Wannier-Mott excitons have a large radius ($a_0 \sim 15$ nm) and small binding energy ($E_\mathrm{B} \sim 5$ meV), which makes them unstable at room temperature [124]. In contrast, monolayer TMDs have been predicted to host excitons with binding energies as high as ~ 1 eV and unusual excitation spectra that deviates from the standard 2D hydrogenic model [125–129]. Despite their large binding energies, these excitons are also of the Wannier-Mott type since their wave functions are localized in k-space and extended in real-space [130]. Experimentally, binding energies between 0.2 and 0.7 eV have been measured using optical and scanning tunnelling spectroscopy [121, 131–135].

These large binding energies originate from two effects that are related to the 2D nature of the excitons: (i) quantum confinement and (ii) reduced dielectric screening. In contrast to conventional bulk semiconductors, excitons in TMDs are strongly confined in the plane of the monolayer and can be treated as 2D. Indeed, since their Bohr radius ($a_0 \sim 1 - 3$ nm) is longer than the layer thickness (0.6 nm), they fulfil the criterion of real two-dimensionally [68]. Due to this quantum confinement effect (i) alone, the exciton binding energy is expected to be four times larger than in 3D [124]. Additionally, the exciton experience reduced Coulomb screening (ii) because the electric field linking the electron and hole extends outside the monolayer (Fig. 1.5a), where the dielectric constant is usually lower than in the TMD. Reducing the screening leads to an enhancement of the electron-hole Coulomb interaction and therefore to an increase of the exciton binding energy. Thus, the dielectric environment surrounding the monolayer strongly influences the exciton, and can be further tuned to control its properties [130, 134, 136].

Another important consequence of this spatially non-uniform dielectric environment is that the effective dielectric screening experienced by the exciton depends on the distance between the electron and hole. Indeed, the dielectric screening decreases as the electron-hole distance increases because a larger portion of the electric field lies outside the monolayer. This "non-local" dielectric screening effect is well described by the screened Keldysh potential [137]:

$$V(r) = \frac{\pi e_0^2}{2r_0}\left[H_0\left(\frac{r}{r_0}\right) - Y_0\left(\frac{r}{r_0}\right)\right], \tag{1.11}$$

where H_0 and Y_0 are the zeroth order Struve and Bessel functions, and r_0 is the screening length. This potential has a $1/r$ behaviour at large distances ($r \gg r_0$) but a weaker $\log(r)$ dependence at small distances ($r \ll r_0$) due to screening

[138]. This difference gives rise to a non-hydrogenic exciton Rydberg series [131], which are schematically depicted in Figs. 1.5b,c. In addition to optically accessible bright excitonic states, the excitation spectra also display spin-forbidden and momentum-forbidden dark states, which can have a strong influence on the exciton dynamics [132, 139].

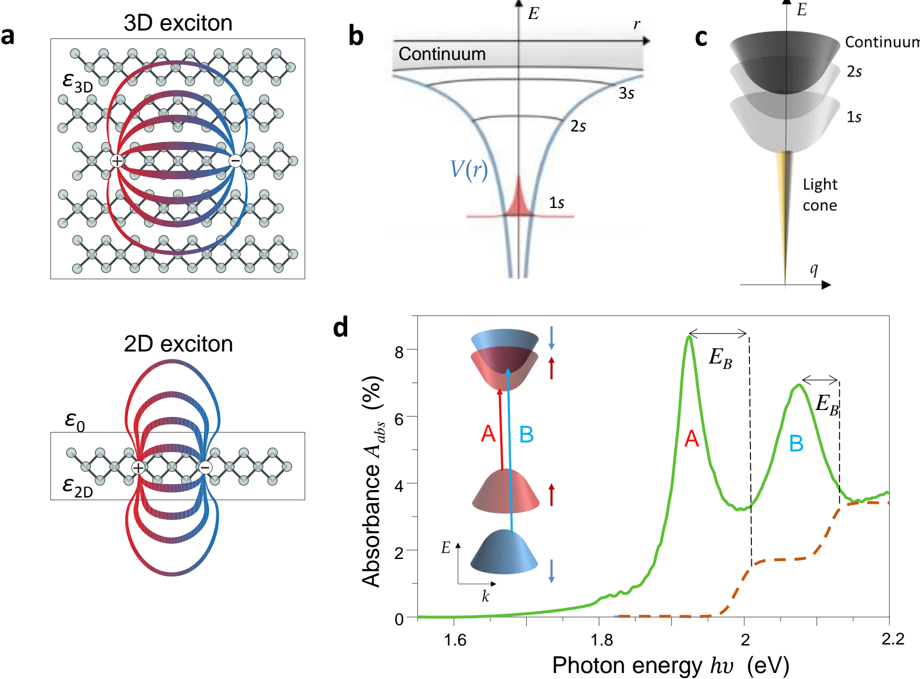

FIGURE 1.5: **Exciton and optical properties of TMDs.** **a)** Schematics of electrons and holes bound into excitons in bulk (3D) and monolayer (2D) TMDs. The coloured lines represents the electric field lines between the electron and hole, and the different dielectric constants ϵ indicate the changes in the dielectric environment. **b)** Schematic of the electron-hole interaction potential $V(r)$ described by Eq. 1.11 (pale blue line) and the eigenenergies (black lines) of various exciton states. The exciton wavefunction is sketched in red. **c)** Depiction of the dispersion relation of different excitonic states, where the q represents the exciton center-of-mass momentum. Excitons inside the light cone can radiatively recombine, while this process is forbidden for (dark) excitons outside the cone. The continuum (in **b** and **c**) represents the free carrier (unbound exciton) states. **d)** Absorbance spectrum of monolayer MoS_2 (green). The A and B excitonic peaks correspond to the interband transitions depicted in the inset. The orange dashed line illustrates the absorption (in arbitrary units) expected in the absence of excitonic effects, where free-particle transitions leads to step-like increases in absorption. The energy difference between these steps and the excitonic peaks corresponds to the binding energy E_B. Adapted from [34].

The large binding energies of excitons in 2D TMDs allow not only for excitons

to survive at room temperature, but also for the formation of higher-order excitonic quasiparticles. To date, trions [140, 141] (quasiparticles of two electrons and one hole, or vice versa) and biexcitons [142] (quasiparticles of two excitons) have been reported in monolayer TMDs. Once again, the binding energy of these quasiparticles is approximately one order of magnitude larger than in conventional semiconductors. We note that excitons in bulk TMDs also have significant binding energies ($\sim$30 – 60 meV), which affects their optical properties even at room temperature [106, 143, 144].

Light absorption and emission

These strong excitonic effects have a large impact on the absorption and emission spectrum of TMDs. As figure indicates, for both bulk and monolayer TMDs, the lowest direct transition between the valence and conduction bands is at the K and K' points. This optical transition therefore governs the absorption in TMDs in the near-infrared and visible region, regardless of their layer number [15, 16, 106, 114]. In the absence of excitonic effects, the absorption spectrum should display a staircase-like function, which is characteristic of 2D semiconductors [124]. Experimental absorption spectrums (Fig. 1.5d), on the other hand, exhibit sharp resonance features, which are clear evidences of strong excitonic effects. Indeed, an excitonic state (with binding energy E_{B}) typically creates an additional absorption peak below the direct free-particle transitions (with energy E_{FP}) at a photon energy $h\nu = E_{\mathrm{FP}} - E_{\mathrm{B}}$. In TMDs, the main excitonic peaks, denoted A and B, correspond to transitions from the two spin-split valence bands to the conduction bands [106, 107]. Due to the transfer of oscillator strength from the band-to-band to the excitonic transition, suspended monolayer TMDs can have an absorbance as high as $A_{\mathrm{abs}} = 15\%$ at the exciton resonances [15, 49], which highlights the strong light-matter interactions in these materials.

These excitonic states also play an important role in photolumincence (PL) of monolayer TMDs. Due to the indirect to direct bandgap crossover, monolayer TMDs displays much higher PL (up to a factor 10^4) than their bulk counterparts [15, 114]. Hence, as we show in Section 3.2.1, monolayer TMDs can be easily identified by measuring the PL. Experiments have shown that in clean and undoped TMDs, the PL spectrum is dominated by emission from the neutral A exciton, while emission from charged A trions prevails in highly doped samples [140, 141]. PL quantum yield close to 100% have recently been reported for chemically-treated MoS_2 samples, demonstrating the potential of TMDs for light emitting applications [145].

1.2.3 Photocarrier dynamics

Interband photon absorption in TMDs leads to the generation of photoexcited electrons and holes, which as we discussed in the previous section, can form

strongly bound excitons. The formation and relaxation dynamics of these excitons and residual free carriers is however a broad and complex issue, which has been mostly address by ultrafast laser spectroscopy studies [51, 146]. Here we provide a short review of the main dynamic processes involved in the life cycle of photocarriers in TMDs.

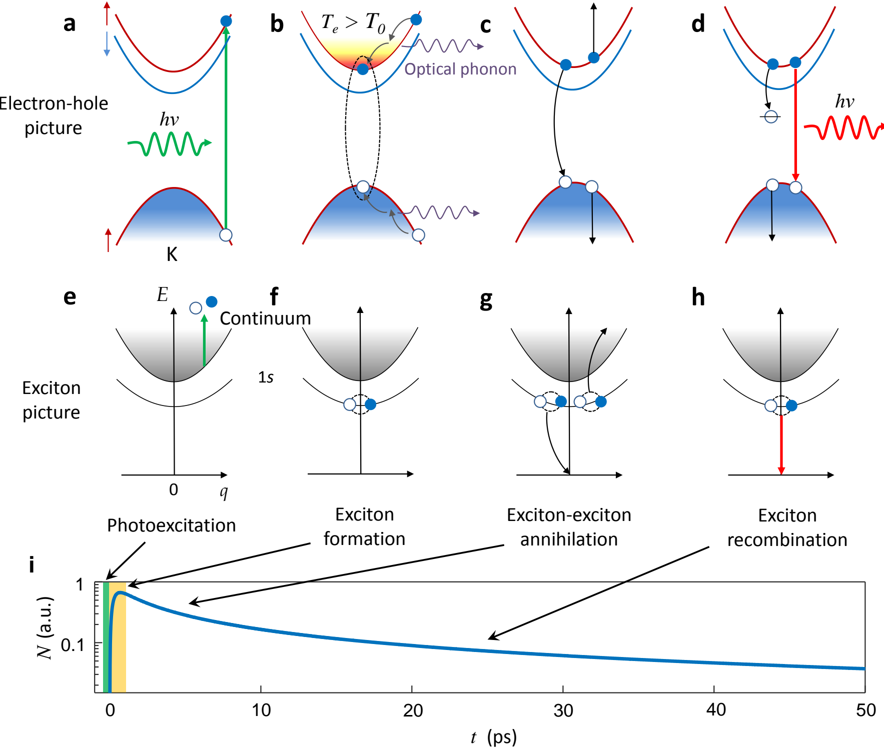

FIGURE 1.6: **Photocarrier dynamics in TMDs.** Schematic representation of the photocarrier dynamics at the K point in the single-particle momentum k-space (**a - d**) and in the exciton momentum q-space (**e - h**). **a,e)** The absorption of a photon with energy $h\nu$ create a free, photoexcited electron-hole pair. **b,f)** Free photocarriers rapidly relax via optical phonon emission and carrier-carrier scattering. This leads to the creation of a hot electron distribution (with temperature T_{e} larger than the ambient temperature T_0) and, subsequently, to the formation of excitons within 1 ps (the dashed black line represents the Coulomb attraction). **c,g** At high exciton density, the exciton decay is dominated by exciton-exciton annihilation. **d,h)** At low density, radiative recombination (red arrow) and defect-assisted recombination (black arrows) are the main exciton relaxation processes and are characterized by an exponential recombination time τ_{r}. **i)** Schematic illustrating the time dependence of the exciton density N after photoexcitation (green area). The exciton formation is represented by an exponential rise (yellow area), followed by a non-exponential exciton decay governed by the equation $\mathrm{d}N/\mathrm{d}T = -N/\tau_{\mathrm{r}} - \gamma N^2$.

Exciton formation

Depending on their energies, photons can either be absorbed through nonresonant band-to-band transitions (Figs. 1.6a,e) or through resonant excitonic transitions. The resonant absorption process instantly generates excitons, while nonresonant excitations create free electron-hole pairs, which subsequently relax toward their respective band extrema and form excitons (Figs. 1.6b,f). The exciton formation process is the result of a complex interplay between various sub-picosecond processes, including carrier-carrier scattering and optical phonon emission [147]. Nie *et al.* [148] have found that due to these processes, carrier thermalization occurs within $\sim$ 100 fs, which is comparable to the fast thermalization observed in graphene (Section 1.1.3). The resulting hot Fermi-Dirac distribution cools down rapidly (within ~ 0.6 ps) via the emission of longitudinal optical phonons [149].

Interestingly, due to the strong Coulomb interactions in monolayer TMDs, carriers start forming excitons within only 1 ps, while they are still at an elevated temperature [150, 151]. Steinleitner *et al.* [151] have indeed shown that more than 60$\%$ of the photoexcited free carriers are bound into excitons after 0.4 ps. This exciton formation time is roughly two orders of magnitude shorter than in conventional semiconductor quantum wells [152]. Importantly, it demonstrates the crucial role that excitons play in the photoresponse of TMDs, even under nonresonant excitation.

Exciton recombination

Once formed, excitons eventually decay by recombining or by dissociating into a free electron-hole pair. As we show in Chapter 7, this latter process can occur in the presence of a large electric field. In the absence of such field, excitons may recombine radiatively or nonradiatively through various processes.

Exciton-exciton annihilation, also called Auger recombination, is a bimolecular process that depends on the exciton density N. As shown in Figs. 1.6c and g, this nonlinear process results from the scattering between two excitons where one exciton recombines non-radiatively and transfers its energy and momentum to a second exciton [153]. This process is generally described by an exciton decay rate $\mathrm{d}N/\mathrm{d}t = -\gamma N^2$, where γ is the exciton-exciton annihilation rate [154]. Due to the strong many-body interactions in TMDs, this process has been found to be very efficient decay process, even at relatively low exciton density ($N \sim 10^{11}$ cm^{-2}). Studies performed on different TMDs have reported exciton-exciton annihilation rate between $\gamma =$ 0.04 and 0.33 cm^{-2}, implying an effective exciton lifetime of $\sim$ 3 - 20 ps at an exciton density of 1×10^{12} cm^{-2} [154–159]. In Chapters 6 and 7, we exploit this nonlinear process to study the photocurrent dynamics in monolayer and bulk WSe_2 devices. We note that other nonlinear phenomena can also occur at high exciton density, including phase space filling and bandgap

renormalization [159, 160]. At very high exciton density ($N \sim 1 \times 10^{14}$cm^{-2}), TMDs can undergo a Mott transition which suppresses excitonic states and gives rise a dense electron-hole plasma [161].

Radiative recombination (Figs. 1.6d,h) limits the intrinsic lifetime of exictons in defect-free TMDs at low exciton density. This process, which is responsible for the photoluminescence observed in most samples, is only allowed for exictons with small center-of-mass momentum $q \sim 0$. Due to the large oscillator strength of excitons in TMDs, an ultrafast intrinsic radiative lifetime (∼ 0.2 ps) is expected for excitons with zero momentum [162, 163]. Poellmann *et al.* [155] experimentally confirmed that excitons within the light cone ($q \sim 0$) radiatively decay within 150 fs. They also showed that because of their interactions with phonons or background carriers, excitons are rapidly scattered to large-momentum states outside the light cone. These dark excitons can recombine non-radiatively via Auger processes, and thereby reduce the photoluminescence quantum yield. Another important consequence of this broad momentum distribution is that it increases the average (or effective) radiative lifetime of excitons. Due to this effect, thermalized exciton populations have an effective radiative lifetime on the order of 1 ns at room temperature, which decreases to ∼ 2 - 5 ps at low temperature (∼ 4 K) [162, 164]. We also note that spin-forbidden, dark exciton states can also significantly affect the effective radiative lifetime [139].

Defect-assisted recombination, also called Auger carrier capture or exciton trapping, has been found to dominate the exciton decay dynamics in disordered TMD samples [165, 166]. This process typically corresponds to the capture of electron (hole) into a defect state due to scattering with a hole (electron), leading to a non-radiative recombination (Fig. 1.6d). Since this process depends strongly on the defect density, it can lead to decay rates that vary greatly from sample to sample. Indeed, carrier capture times between 1 and 100 ps have been reported. Interestingly, the carrier lifetime has been shown to increase drastically with layer number (from $\sim$ 10 ps for monolayer to $>$ 1 ns for 10-layer samples), showing the important role played by surface defects [167].

1.3 Hexagonal boron nitride

Also known as “white graphene”, hBN is a layered material with an atomic structure very similar to that of graphene: boron and nitrogen atoms are arranged in a honeycomb lattice with a lattice constant only 1.8% larger than graphene [13, 168]. Because of the different on-site energies of B and N atoms, few-layer hBN has a large indirect bandgap of $\sim$ 6 eV [12], which makes it electrically insulating. Due to its chemical and mechanical stability, hBN is an ideal material to encapsulate or support other 2D materials, providing an atomically flat surface free of dangling bond and charge traps. Indeed, Dean *et al.* [23] showed that compared to SiO_2, hBN substrates reduces disorder and charge inhomogeneity in graphene and greatly improves its carrier mobility. hBN was also shown to be

an ideal tunnel barrier, with a high dielectric breakdown field (up to 0.8 V/nm) [169, 170] .

Optically, hBN is transparent to all wavelengths below the ultraviolet region and host indirect Wannier excitons with a binding energy of ~ 100 meV [12]. The recent observation of room-temperature single-photon emission from point defects in hBN opens up interesting possibilities for quantum photonics [171]. Phonon-polariton modes in the mid-infrared were also observed in thin hBN flakes [172]. These polaronic waves arise from the hyperbolic character of the hBN dielectric function, which features two Reststrahlen bands at $\sim$ 100 and 180 meV.

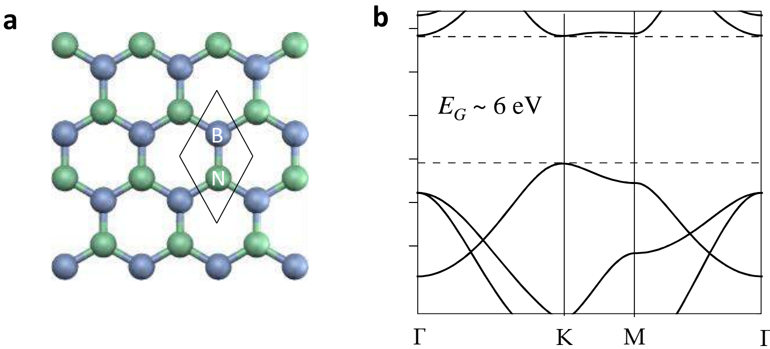

FIGURE 1.7: **Structural and electronic properties of hBN. a)** The hexagonal lattice of monolayer hBN is very similar to that of graphene. The unit cell (solid black line) contains one boron atom and one nitrogen atom. **b)** Band structure of monolayer hBN showing a bandgap E_{G} of 6 eV. Adapted from [33].

1.4 Van der Waals heterostructures

As we discussed in the previous sections, 2D layered materials, such as graphene, TMDs and hBN, display a wide variety of complementary properties. Interestingly, the same weak van der Waals forces that allow exfoliation of these bulk materials into single layers free of dangling bonds can also be used to stack them onto one another in the desired layer order. The resulting van der Waals heterostructures (vdWHs) not only combine the individual properties of the layers that they comprise, but they also present new physical effects and interesting possibilities for engineering their optoelectronic properties. Indeed, the lack of lattice matching constraints introduces several degrees of freedom in the fabrication of these heterostructures, such as the thickness of the layers, their sequence and their rotational alignement. Hence, with so many 2D materials to choose from, it is possible to create a large variety of vdWHs.

Within just a few years, the rapid surge of interest in vdWHs has led to enormous progress in this field, which is documented in several review articles [25–27, 173, 174]. Here we give an overview of the main physical properties of vdWHs with an emphasis on those relevant for this thesis.

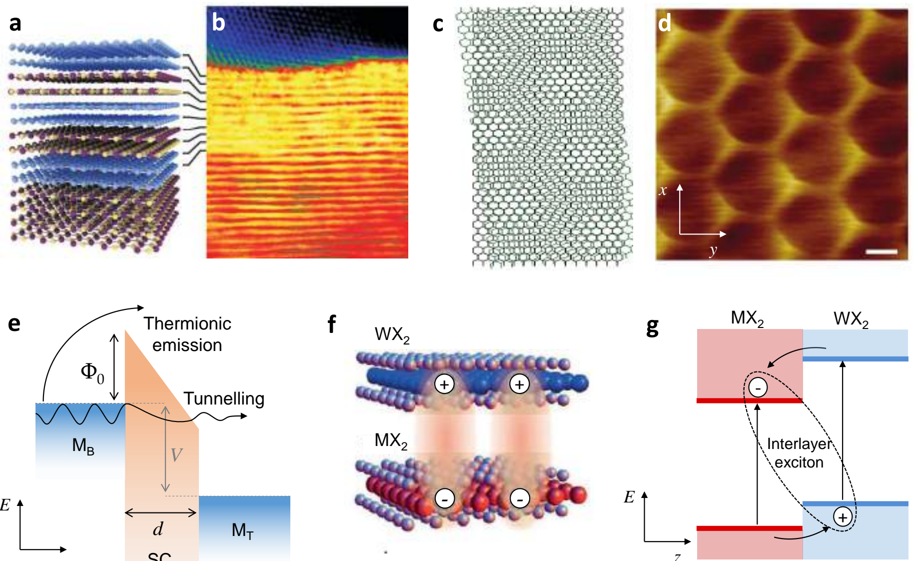

FIGURE 1.8: **Structural and optoelectronic properties of vdWHs. a)** Illustration of a graphene/hBN heterostructure where graphene layers are coloured in blue and hBN layers in yellow and purple. **b)** Cross-sectional TEM image of the heterostructure shown in **a**. **c)** Schematics of Moiré pattern created by stacking a layer of hBN (green honeycomb lattice) over graphene (black honeycomb lattice) with a rotation angle of 0.1 rad. **d)** Scanning tunneling microscope (STM) topography image showing a Moiré pattern with a periodicity of 11.5 nm measured on a graphene/hBN heterostructure with a rotation angle of $\sim 1^\circ$ (the scale bar is 5 nm). **e)** Band diagram of an heterostructure made of a barrier layer (SC) sandwitched between two conducting layers (M_B and M_T). The barrier layer has a thickness d and forms a potential energy barrier Φ_0. A voltage V is applied between the two conducting layers. The two main transport mechanisms are illustrated: electron tunnelling is represented by the wavy arrow, while the arching arrow depicts the thermionic emission of electrons over the barrier. **f)** Schematic of the interlayer excitons in a WX_2/MX_2 TMD heterostructure. The red shadded region represents the Coulomb force binding the electrons and holes in different layers. **g)** Band diagram of a WX_2/MX_2 heterojunction showing a typical type-II band alignment. Electrons or holes created in individual layers (vertical black arrows) are rapidly (within 50 fs) transferred between layers (curved black arrows), which leads to the formation of interlayer excitons (dotted black line). Panels **a** and **b** are adapted from [175], panel **c** is taken from [176], panel **d** is from [177] and panel **f** is adapted from [120].

1.4.1 Structural properties

Van der Waals heterostructures are three-dimensional artificial materials made of different stacked 2D (or few-layer) layered materials. As we showed in the preceding sections, 2D layered materials are atomically thin crystals where atoms are bond in-plane by fully saturated covalent bonds. Due to this particular atomic structure, 2D materials are in principle free of dangling bonds and surface trap states, and they interact with their neighbouring layers via van der Waals forces. Since these forces are relatively weak compared to direct chemical bonds, layers with different atomic structures and rotational orientation can be vertically assembled without compromising the integrity of each layer or degrading their properties.

In contrast, in conventional epitaxial heterostructures (e.g. III-V semiconductors), chemical interactions between layers impose so-called lattice matching conditions, which need to be satisfied in order to avoid the formation of dislocations and other material defects [4]. This constraint is an important bottleneck for the creation of conventional heterostructures as it greatly reduces the choice of compatible materials. In vdWHs, the lattice matching condition is drastically relaxed, allowing for the combination of any 2D layers, even with large lattice mismatch.

Although several techniques to directly grow vdWHs are currently being developed [178, 179], the most versatile method for fabricating vdWHs at the moment consists in mechanically stacking exfoliated layers on top of one another. In Chapter 3, we give a detail description of this assembly technique. Conceptually, fabricating vdWHs is the reverse process of mechanically exfoliating layered materials: in the latter, layers are separated into individual monolayers, while in the former, single layers are assembled to form a heterogeneous 3D material. As the transmission electron microscopy (TEM) image shown in Fig. 1.8b demonstrates, the resulting vdWHs can be made of one-atom thick layers and have sharp interfaces that are free of any contaminations [175]. Comparatively, the layers in conventional heterostructures are at least few-atom thick ($>$ 2 nm) and usually have rough interfaces [4].

This atomically smooth and clean interface is one main features that motivated the early development of vdWHs. In 2010, Dean *et al.* [23] have reported the first vdWHs made of graphene on hBN, and showed that the electrical performances of graphene are greatly enhanced due to the quality of the graphene/hBN interface. Even better results have later been obtained by fully encapsulating graphene between two hBN flakes [9]. Similar strategies have recently been used with TMDs, leading to drastic improvement in the electrical [180] and optical properties of the TMDs [181–183].

Another important structural parameter of vdWHs is the relative orientation of neighbouring layers. The rotational alignment between the two lattices can lead to the formation of moiré patterns [177, 184, 185] (Figs. 1.8c,d) and to

surface reconstruction effects [186], both of which can have a substantial impact on the structural and electronic properties of the two layers. These effects have been most studied in graphene/hBN heterostructures because of their similar lattice parameters. It has been shown that when the lattices of these two crystals is practically aligned (larger moiré periodicity), graphene stretches locally to match with the hBN lattice, resulting in large areas where the two lattices are commensurate separated by regions of incommensurate stacking [186]. For large misorientation angles (small moire periodicity), this surface reconstruction effect disappear. Similar effects have also recently been measured in $MoSe_2$/WSe_2 heterostructures [187].

1.4.2 Electronic properties

Stacking different materials together can have various effects on the electronic properties of individual layers and the vdWH as a whole. These effects mostly depend on the electronic band alignment between the layers and on the strength of the interlayer coupling, which is in part determined by the rotational alignment and lattice mistmatch of the layers.

If the interlayer coupling is weak (which is normally the case for misoriented layers), individual layers largely preserve their 2D properties and interact with their neighbouring layers via electrostatic coupling. In this case, the electronic behaviour of the vdWH is determined by the contribution of the individual layers and by the heterojunctions that they form. Like in conventional heterostructures, these heterojunctions create discontinuities in the band diagram and are classified in different categories, depending on the type of materials forming the junction and their band alignment. Since the surface of layered materials is free of dangling bonds, their alignment generally follows the predictions of simple electrostatic models such as the Schottky-Mott and Anderson's rules [188–190]. For instance, graphene/TMD junctions typically create Schottky metal-semiconductor junctions with a Schottky barrier height approximately given by $\Phi_B = W_G - \chi$, where W_G is the work function of graphene and χ is the electron or hole affinity of the TMD. In contrast, graphene/hBN junctions form metal-insulator interfaces where the Dirac point of graphene is located well above the edge of the hBN valence band ($\Phi_0 \approx 1.3$ eV) [168]. TMD/TMD heterojunctions usually have a staggered (type-II) band alignment, with valence or conduction band offsets of $\sim$ 0.1 - 0.3 eV [185, 187, 191, 192].

While the concepts related to 3D bulk junctions often apply to those made of 2D materials, they also have some limitations. Generally, joining two materials with different work functions produces a transfer of charges between them. In 3D bulk junctions, the internal electric field created by this charge transfer leads to a gradual band bending (or depletion region) which extends away from the junction. In 2D materials, however, the concept of depletion region breaks down since the charges are localized within the two layers. Instead, 2D junctions are

more appropriately described by parallel plate capacitors separated by a small vdW gap. This simple model can indeed explain the significant charge doping and Fermi level shift observed in 2D junctions [185, 193]. Recently, Andersen *et al.* [194] have proposed a generalized model predicting the spatial and dynamical dielectric properties of a given vdWH based on the dielectric properties of its constituent 2D layers and their long-range Coulomb interactions.

We note that in some cases (mostly when the two crystals are rotationally aligned), the interlayer coupling can be strong enough to substantially alter the band structure of the individual layers. This intriguing phenomenon can be caused by various hybridization effects [187, 195] or by the formation of moiré superlattices [177, 184]. In the latter case, a moiré pattern creates a weak but observable electrostatic periodic potential that leads to reconstruction of the electronic spectrum at the wave vectors corresponding to the periodicity of the moiré pattern. In graphene/hBN heterostructures, this effect gives rise to a new set of Dirac points in the valence and conduction band of graphene [177], which enables the study of the Hofstadter butterfly effect. Recently, a similar effect has also been reported in MoS_2/WSe_2 heterostructure, where spatial modulation in the local bandgap lead to the formation of a 2D electronic superlattice [184].

Interlayer transport

Owing to their 3D nature, vdWHs give access to both intralayer (in-plane) and interlayer (out-of-plane) transport geometries. While intralayer transport in 2D layers has been extensively studied [57, 108], interlayer transport remains relatively unexplored and involves drastically different transport processes. Indeed, inside individual layers, transport is generally diffusive and carried out by the delocalized carriers of the band structure. In the out-of-plane direction, however, heterojunctions create a discontinuous band diagram, which result in potential energy barriers. This jagged potential profile combined with the weak interlayer coupling strongly reduces the delocalization of carriers [174], and thus transport between layers occurs via thermionic emission or tunnelling.

To illustrate this point, we consider a simple heterostructure made of two conducting layers (top and bottom) sandwiching an insulator or semiconductor layer of thickness d and potential energy height Φ_0 (Fig. 1.8e). The current flowing above or across such a barrier layer can be described by a model that draws on Landauer's transport theory and Simmons model [196]. This model, which has been successfully applied to various vdWHs [191, 197, 198], predicts that the current depends on the number of electronic states occupied and available in both conducting layers and on the probability T for carriers to cross the barrier layer. It also assumes that tunnelling is elastic, i.e., in-plane momentum is not conserved, which is the case for rotationally misoriented layers. When a voltage V is applied between the two conducting layers, the total current is given by

$$I(V) \propto \int_{-\infty}^{\infty} D_{\mathrm{B}}(E) D_{\mathrm{T}}(E - e_0 V) T(E, V)[f_{\mathrm{T}}(E - e_0 V) - f_{\mathrm{B}}(E)] \mathrm{d}E, \quad (1.12)$$

where E is the energy measured with respect to Fermi level of the bottom layer, $f_{\mathrm{B/T}}(E)$ is the Fermi-dirac distribution (Eq. 1.5) of the bottom and top layers, and $D_{\mathrm{B/T}}(E)$ is their density of states. According to the WKB approximation, the energy-dependent transmission probability function is

$$T(E, V) = \begin{cases} \exp\left[\frac{-2\sqrt{2m^*}}{\hbar} \int_0^d \mathrm{d}x \sqrt{\Phi(x, V) - E}\right] & \text{for } E \leq \Phi_0 \\ 1 & \text{for } E > \Phi_0, \end{cases} \quad (1.13)$$

where m^* is the effective mass of the carrier inside barrier and $\Phi(x, V)$ is the profile of the potential barrier. According to this expression, carriers with an energy lower than Φ_0 rely on quantum tunnelling to cross the barrier, while those with a higher energy (hot carriers) have a unity probability of overcoming barrier, a process called the thermionic emission.

In fact, Eq. 1.12 and 1.13 are a generalization of the more familiar Fowler-Nordheim equation [199] and Richardson's law [200]. Indeed, by using a triangular barrier $\Phi(x, V) = \Phi_0 + e_0 V x/d$ and considering only the carriers at the Fermi level, we obtain:

$$I(V) \propto \exp\left[\frac{-4d\sqrt{2m^*}\Phi_0^{3/2}}{3e_0 \hbar V}\right], \quad (1.14)$$

which is characteristic of Fowler-Nordheim tunneling. Richardson's law is simply recovered by assuming a thick barrier and a relatively low temperature ($\Phi_0 \gg k_{\mathrm{B}} T_{\mathrm{e}}$). Under these assumption, Eq. 1.12 gives

$$I(T_{\mathrm{e}}) \propto \exp\left[\frac{-\Phi_0}{k_{\mathrm{B}} T_{\mathrm{e}}}\right]. \quad (1.15)$$

These transport mechanisms have recently been exploited and studied in the context of vertical transistors, in which layers of hBN or TMDs are employed as potential barriers with graphene serving as one or both electrodes [26, 169, 170, 197, 201–205]. In these devices (sometimes called barristors [206]), the thermionic and tunnelling currents are controlled by modulating the Fermi level of graphene, and thereby the energy barrier height Φ_0. These transistors exhibit large on/off ratio at room temperature ($> 10^6$) [197] and high on-current ($>$ 5 000 A/cm^2) [201]. Remarkably, when the two graphene electrodes are rotationally aligned, resonant tunnelling gives rise to a negative differential resistance that persists up to room temperature [203, 204]. In Chapter 5 we study how

light affects the thermionic and tunnelling transport mechanisms in these vertical vdWHs, while in Chapter 6 we examine the dynamics of carriers generated in a TMD layer and their out-of-plane transport to the graphene contacts.

1.4.3 Optical properties

Due to the weak electronic interactions between layers, the optical properties of vdWHs can be approximately described by a superposition of their individual layers [207]. However, studies reveal that dynamics of the photogenerated charges can be significantly altered by the electronic states of the surrounding layers. One of the most prominent examples of this is found in TMD/TMD hetero-bilayers. Due to their staggered band alignment and large band offset [185, 187, 191], photocarriers created in each layers are rapidly (< 50 fs) transferred [207–209], leading to the accumulation of photoexcited electrons and holes in different layers (Fig. 1.8f,g). These spatially separated electrons and holes can subsequently bind together to form interlayer excitons. When they recombine radiatively, these interlayer excitons emit photons with an energy lower than the intralayer excitons of both layers [185, 210–212]. Importantly, since interlayer excitons are indirect both in real-space and momentum-space (due to the rotational misalignment), their lifetime can be more than one order of magnitude longer (> 30 ns) than the one of intralayer excitons [162, 212]. For this reason, TMD/TMD heterostructures are a promising platform for studying valley physics [212] and observing exciton condensations [213, 214].

Similar charge transfer processes have also been reported in graphene/TMD heterojunctions [215, 216]. He *et al.* [216] showed that photocarriers generated in the TMD are transfered to graphene in picosecond timescale, leading to a strong quenching of the TMD photoluminescence. In addition to charge transfer processes, intralayer photocarriers can also relax through interlayer energy transfer, a process which is often observed in molecular complexes. The mechanisms for this energy transfer can be radiative (annihilation of an exciton in one layer and the creation an exciton in the other) or non-radiative (Forster resonance energy transfer due to dipole-dipole coupling) [217]. The latter has been observed in graphene/quantum dots systems [218] as well as in some TMD/TMD heterostructures [219]. In Chapter 6, we also argue that this near-field energy transfer mechanism can explain the photoluminescence quenching and the photocarriers lifetimes that we measure in graphene/TMD/graphene heterostructures.

Chapter 2

Photocurrent generation and measurement in 2D materials

In this chapter, we introduce the basic photodetection concepts and measurement techniques that are relevant for the rest of the thesis. We begin by defining the principal performance characteristics of photodetectors. We review the main photodetection mechanisms that have been observed in 2D material and derive simple expressions for their photodetection characteristics. This allows us to identify the relevant electronic properties and processes for each photodetection mechanism, and to compare their theoretical perfomances. Finally, we describe the techniques and experimental apparatus that we used in this thesis to generate and measure photocurrent in 2D material-based devices, and to assess their photodetection characteristics.

2.1 Introduction

The conversion of absorbed photons into an electrical signal is the key process on which photodetectors and other optoelectronic applications rely. This process, called photodetection, is driven by the excess energy contained in the electronic system. The photodetection mechanisms are typically divided into two classes, depending whether the excess energy results in excess carriers or in excess electronic heat. The first class of mechanisms relies on the transport of photoexcited carriers (also called photocarriers) created by optical transitions between two separated energy levels (Fig. 2.1a). In the second class of photodetection mechanisms, the electric signal is driven by the rise of the electron bath temperature ΔT_{e} resulting from light absorption (Fig. 2.1b).

In this chapter, we present the main photodetection mechanims that have been reported so far for 2D material-based photodetectors and describe the techniques that we employ to probe these mechanisms. Our goal is to introduce the physical and technical concepts that underpin the photodetection studies presented in the rest of the thesis. We also review the performances of various far-field photodetectors based on 2D materials, leaving aside those involving light-enhancement techniques. For a more exhaustive discussion on 2D material-based photodetectors, we refer the reader to the many review articles published on this topic [31, 33, 34, 41].

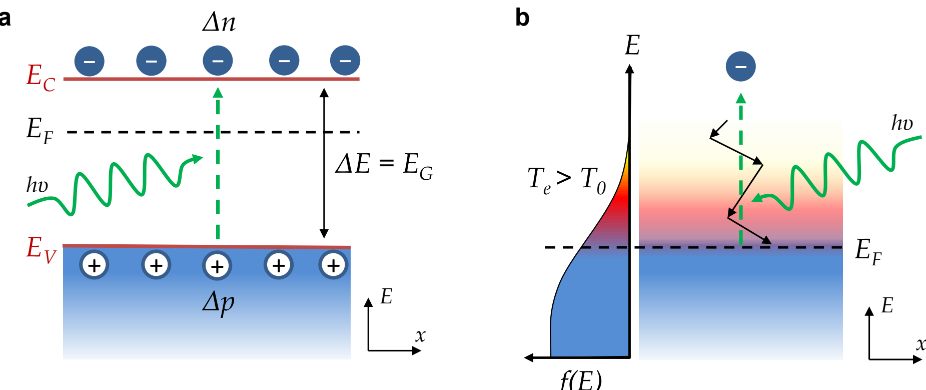

FIGURE 2.1: **Main classes of photodetection mechanisms.** Photodetection can be driven (**a**) by photoexcited carriers (electrons with a density Δn and holes with a density Δp) generated by optical transition (green arrow) between two energy levels (here, the conduction band E_{C} and valence band E_{V} of a semiconductor with bandgap E_{G}), or (**b**) by the excess heat contained in the electronic bath created by the thermalization of photoexcited carriers with the surrounding carriers. This process, depicted by the black arrows, leads to an electronic Fermi-Dirac distribution $f(E)$ with a temperature T_{e} larger than the ambient or lattice temperature T_0.

2.2 Photodetection terminology

To begin, we define some of the important concepts and performance metric associated to photodetection. We consider light incident on a photodetector, with total power P and photon energy $E_{\mathrm{photon}} = h\nu$, corresponding to a photon flux of $\Phi = P/h\nu$. Assuming that the fraction of light absorbed by the photodetector is A_{abs}, the absorbed photon flux is $\Phi_{\mathrm{abs}} = A_{\mathrm{abs}}\Phi$. Depending on the operation mode of the photodetector, the absorbed light produces a *photovoltage* $\Delta V = V_{\mathrm{l}} - V_{\mathrm{d}}$ or a *photocurrent* PC $= I_{\mathrm{l}} - I_{\mathrm{d}}$. The subscripts l and d refer to illuminated and dark states of the photodetector, respectively.

The *responsivity* $\Re$ of the photodetector in photocurrent mode is the ratio between the photocurrent and the incident power $\Re =$PC$/P$, while for the photovoltage mode it is defined as $\Re = \Delta V/P$. The *spectral responsivity* refers to the dependence of $\Re$ on the incident photon energy $h\nu$, and is therefore strongly influenced by the absorption spectrum of the photoactive material.

The *external quantum efficiency*, EQE, is the ratio between the number of photo-induced charges collected per second divided by the number of incident photon per second: $\mathrm{EQE} = (\mathrm{PC}/e_0)/\Phi$, where e_0 represents the elementary charge. The *internal quantum efficiency*, IQE, is calculated by considering the number photons absorbed: $\mathrm{IQE} = (\mathrm{PC}/e_0)/\Phi_{\mathrm{abs}}$. We note that for photodectors with current-gain mechanisms (e.g. phototransistors, extrinsic photodetectors and avalanche photodiode), the IQE is also referred to as *gain*.

We also define the *photoresponse time* (or *photo-switching time*) of a photodetector as the characteristic time τ that the photodetector takes to switch between the illuminated (ON) and dark (OFF) states. Assuming that τ is not limited by the resistance-capacitance time of the circuit ($\tau \gg RC$), the *bandwidth* B of the photodetector is given by the *cutoff frequency* of the photodetector $f_{\mathrm{c}} \approx 0.55/\tau$ [220].

The *noise-equivalent power* (NEP) corresponds to the incident optical power required to produce a signal-to-noise ratio of one in a 1 Hz bandwidth [221]. For most photodetectors, the two main noise contributions are the shot noise and Johnson noise. The shot noise originates from the fluctuations in the background radiation, which produce variations in the dark current I_{d} of the photodetector: $\sigma_{\mathrm{shot}} = \sqrt{2e_0 I_{\mathrm{d}} B}$. The Johnson noise (also called thermal noise) is caused by the random motions of the charge carriers under thermal equilibrium conditions: $\sigma_{\mathrm{thermal}} = \sqrt{4k_{\mathrm{B}}T_0 B/R_{\mathrm{d}}}$, where k_{B} is the Boltzmann constant, T_0 is the ambient temperature, and R_{d} is the equivalent resistance in the dark [222]. Under these assumptions, the NEP (for $B = 1$) can be evaluated as $\mathrm{NEP} = \frac{1}{\Re}\sqrt{\sigma_{\mathrm{shot}}^2 + \sigma_{\mathrm{thermal}}^2}$. Finally, the *specific detectivity* D^* of a photodetector of area A is defined has $D^* = \sqrt{AB}/\mathrm{NEP}$ and is measured in cm $\mathrm{Hz}^{1/2}\mathrm{W}^{-1}$ (= 1 Jones).

2.3 Photodetection enabled by photoexcited carriers

Sereral photodetection mechanisms are driven by photoexcited carriers, including the photoconductive effect, the photovoltaic effect, the photogating effect and the internal photoemission. The operation of photodetectors based on these effects typically includes three steps.

i) *Generation of the photocarriers*. Photocarriers are created when photons absorbed in the photoactive material promote a carrier to a higher energy level. These optical transitions are most commonly interband transitions between the valence and conduction band of a semiconductor, but can also include transitions from a defect states or over an energy potential. Importantly, in order for photocarriers to remain in their photoexcited state, the excited and ground states must be separated by an energy difference ΔE containing no intermediate electronic states. In semiconductors, for instance, ΔE corresponds to the material's bandgap. The presence of ΔE also implies that photocarrier-driven photodetectors have a photon energy threshold (or cutoff): they cannot detect photons with energy $h\nu$ smaller than ΔE.

ii) *Transport or trapping of the photocarriers*. Carriers in the photoexcited state travel through the photoactive materials in the presence of an electric field. If the material contains localized mid-gap states, photocarriers can relax into these states and get trapped.

iii) *Extraction or recombination of the photoexcited carriers*. The photocarriers have two possible fates: they are either collected by the electrical contacts of the photoactive material or they return to their original ground state through some relaxation or recombination mechanism. In the case of trapped photocarriers, a charge-compensating current circulate though the material until the photocarriers returns to their ground state.

2.3.1 Carrier dynamics and transport in semiconductors

Since photocarrier-based mechanisms typically occur in semiconductors, we first consider the general case of a defect-free 2D semiconductor illuminated with above-bandgap photons ($h\nu > E_{\mathrm{G}}$). The photon absorbed by the material generate electron-hole pairs at a rate G which leads to an excess electron density $\Delta n = n - n_0$ and hole density $\Delta p = p - p_0$ (n_0 and p_0 are the carriers density without illumination). These excess charges can recombine through various processes at a rate R. According to the drift-diffusion model and the charge conservation principle, the dynamic and transport of the charge carriers is governed

by the following equations [124]:

$$\frac{\partial n}{\partial t} = \frac{1}{e_0}\nabla \cdot \mathbf{J}_n + G - R \tag{2.1}$$

$$\frac{\partial p}{\partial t} = -\frac{1}{e_0}\nabla \cdot \mathbf{J}_p + G - R, \tag{2.2}$$

where the electrons $\mathbf{J}_n$ and holes $\mathbf{J}_p$ current densities are:

$$\mathbf{J}_n = e_0\mu_n n\mathbf{E} + e_0 D_n \nabla n \tag{2.3}$$

$$\mathbf{J}_p = e_0\mu_p p\mathbf{E} - e_0 D_p \nabla p, \tag{2.4}$$

where μ and D are the mobilities and diffusion coefficients of each carrier types, and $\mathbf{E}$ is the electric field in the semiconductor, which can be calculated by solving Poisson's equation. We also note that since electron and holes are created in pairs, the semiconductor remains electrically neutral, i.e. $\Delta n = \Delta p$. Eqs. 2.2 and 2.4 provide a general framework to understand the various photocarrier-driven mechanisms that are presented below.

2.3.2 Photoconductive effect

The photoconductive effect correspond to the increase of the material electrical conductivity $\Delta\sigma$ due to photo-generated excess carriers. The photocurrent density J_{PC} thus generated is[1]:

$$J_{\mathrm{PC}} = \Delta\sigma E, \tag{2.5}$$

where E is the external electric field created by applying a voltage between two electrical contacts. According to Eq. 2.4, the change in conductivity resulting from the generation of photocarriers is:

$$\Delta\sigma = e_0(\mu_n \Delta n + \mu_p \Delta p) = e_0(\mu_n + \mu_p)\Delta n, \tag{2.6}$$

where Δn can be obtained by solving Eq. 2.2.

Photoconduction has been observed several times in 2D semiconductors, in particular in TMDs [15, 118, 223–229] and black phosphorus [230–233]. Biased graphene devices can also exhibit a small photoconductive response when they are undoped [234]. Very high responsivities ($\sim$ 1000 A/W) have been reported in in-plane TMD photoconductors but the bandwidth of these devices are typically very small, on the order of 1 Hz [227, 229]. The origin of this behaviour has been attributed to extrinsic effects related to impurity and defect state [224, 228]. On the other hand, lower responsivities ($\sim$ 0.1 A/W) and faster response time have been observed in vertical, few-layer TMD devices [50, 235], suggesting an intrinsic photoconductive response. In Chapter 5 we present a detailed study of

[1] For the sake of simplicity, we limit ourselves to a one-dimensional treatment.

this effect in a graphene/WSe_2/graphene heterostructure. In order to highlight the difference between intrinsic and extrinsic photoconduction, we examine the two following cases.

Intrinsic photoconductor

In the first case, we consider an intrinsic (i.e., containing no defect or trap states) 2D semiconductor of length L and width W illuminated uniformly such that the photocarrier density is generated at a rate $G = \Phi_{\mathrm{abs}}/(LW)$ (Fig. 2.2a,b). Two ohmic contacts are placed on each end of the semiconductor and voltage V is applied between them, creating a uniform electric field $E = V/L$ across the semiconductor. According to Eq. 2.2, the photocarriers can either drift-diffuse out of the semiconductor or recombine at a rate R. For this example, we assume that photocarriers recombine with a characteristic lifetime τ_{r} and that the contribution of diffusion is negligible (i.e., the diffusion length, $L_{\mathrm{d}} = \sqrt{D\tau_{\mathrm{r}}}$, is much smaller than L). Finally, we can easily show that the average time that a photocarrier travelling at constant drift velocity $v_{\mathrm{d}} = \mu E$ takes to drift out of the semiconductor is $\tau_{\mathrm{d}} = L/(2\mu E)$. By applying these simplification to Eq. 2.2, we obtain the dynamic equation of the spatially average photocarrier density Δn_{a} :

$$\frac{\mathrm{d}\Delta n_{\mathrm{a}}}{\mathrm{d}t} = G - \frac{\Delta n_{\mathrm{a}}}{\tau_{\mathrm{d}}} - \frac{\Delta n_{\mathrm{a}}}{\tau_{\mathrm{r}}}. \tag{2.7}$$

Under pulsed excitation ($G(t) = \Delta n_{\mathrm{a}}(0)\delta(t)$), the solution to Eq. 2.7 is

$$\Delta n_{\mathrm{a}}(t) = \Delta n_{\mathrm{a}}(0)\exp(-t/\tau_{\mathrm{i}}), \tag{2.8}$$

where $\tau_{\mathrm{i}} = (1/\tau_{\mathrm{r}} + 1/\tau_{\mathrm{d}})^{-1}$ is the characteristic time that photocarriers live in the semiconductor before drifting out of it or recombining. Thus, it represents the photoresponse time of the intrinsic photoconductor.

Under steady-state conditions, Eq. 2.7 yields:

$$\Delta n_{\mathrm{a}} = G\tau_{\mathrm{i}}. \tag{2.9}$$

According to Shockley-Ramo theorem [236], the photocurrent produced by the photoconductive effect is given by :

$$\mathrm{PC} = \frac{1}{L}\iint J_{\mathrm{PC}}\mathrm{d}x\mathrm{d}y = \frac{e_0}{L}(\mu_n + \mu_p)\Phi_{\mathrm{abs}}\tau_{\mathrm{i}}E. \tag{2.10}$$

Assuming that the hole and electron mobility are equal, we obtain

$$\mathrm{PC} = e_0\Phi_{\mathrm{abs}}\frac{\tau_{\mathrm{i}}}{\tau_{\mathrm{d}}} \tag{2.11}$$

and the resulting IQE is simply

$$\text{IQE} = \frac{\tau_\text{i}}{\tau_\text{d}} = \frac{\tau_\text{r}}{\tau_\text{d} + \tau_\text{r}}. \tag{2.12}$$

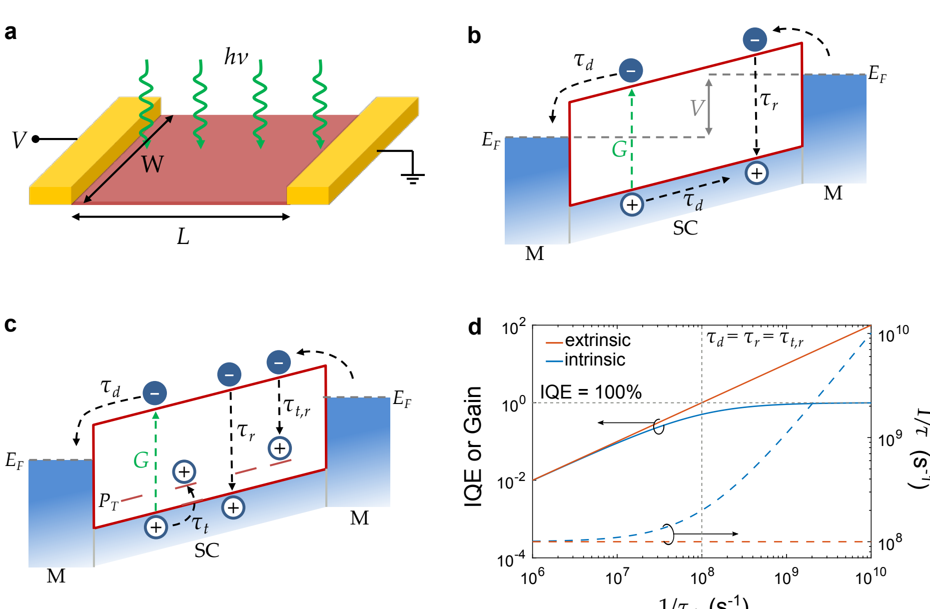

FIGURE 2.2: **Intrinsic and extrinsic photoconduction. a)** Schematic of a photoconductor, which consists of 2D semiconductor (red) with two ohmic contacts (yellow) under illumination. **b)** Band diagram of an intrinsic semiconductor channel (SC) contacted with two metals (M) under an external bias V. Photons absorbed by the semiconductor generate photocarriers (at a rate G), which drift out of the channel (τ_d) or recombine (τ_r). **c)** Band diagram of an extrinsic semiconductor channel containing trap states (P_t). The photogenerated holes are trapped at a rate τ_t and then recombine ($\tau_{\text{t,r}}$). **d)** IQE (or gain) and photoresponse rate $1/\tau$ as a function of the drift rate $1/\tau_\text{d}$ for the intrinsic (blue) and extrinsic (red) photoconductors described in the main text, assuming $\tau_\text{r} = \tau_{\text{t,r}} = 10$ ns. The solid lines correspond to the IQE, while the dotted lines represent the photoresponse rate.

Extrinsic photoconductor

We can generally distinguish two type of extrinsic photoconductors. In the first case (*normal*), light is absorbed in a photoactive semiconductor and one of the photocarrier types (electrons or holes) get trapped in localized states of the semiconductor (for example, mid-gap or surface states) or in a nearby molecule or nanomaterial. In the second case (*hybrid*), light is first absorbed in a molecule or nanomaterial (for example, quantum dots). Then, one of the photocarrier types is transferred to a biased conductor and contribute to the photocurrent while the

other photocarrier remains trapped. This photocurrent generation mechanism is also called the *photogating effect*.

To illustrate the effect of charge trapping on the photoconductive effect, we present a model of *normal* extrinsic photoconductivity similar to the one presented by Furchi *et al.* [224]. We start by assuming that the 2D semiconductor examined in the previous case now contains trap states with a density P_t close to the valence band (Fig. 2.2c). Photoexcited holes that get trapped at a rate $1/\tau_\mathrm{t}$ can only escape the trap by recombining at a rate $1/\tau_\mathrm{t,r}$. To preserve charge neutrality, electrons with a density equal to the trapped hole density p_t must be injected from the electrical contacts. Eq. 2.6 thus becomes

$$\Delta\sigma = e_0(\mu_n + \mu_p)\Delta n + e_0\mu_n p_\mathrm{t}. \tag{2.13}$$

The differential equations describing the dynamics of the average photocarrier density Δn_a and trapped hole density p_t are:

$$\frac{\mathrm{d}\Delta n_\mathrm{a}}{\mathrm{d}t} = G - \frac{\Delta n_\mathrm{a}}{\tau_\mathrm{d}} - \frac{\Delta n_\mathrm{a}}{\tau_\mathrm{r}} - \frac{\Delta n_\mathrm{a}}{\tau_\mathrm{t}}\left(1 - \frac{p_\mathrm{t}}{P_\mathrm{t}}\right) \tag{2.14}$$

$$\frac{\mathrm{d}p_\mathrm{t}}{\mathrm{d}t} = \frac{\Delta n_\mathrm{a}}{\tau_\mathrm{t}}\left(1 - \frac{p_\mathrm{t}}{P_\mathrm{t}}\right) - \frac{p_\mathrm{t}}{\tau_\mathrm{t,r}}. \tag{2.15}$$

The steady-state solution under low-illumination conditions is

$$\Delta n_\mathrm{a} = G\tau_\mathrm{e} \tag{2.16}$$

$$p_\mathrm{t} = G\tau_\mathrm{e}\left(\frac{\tau_\mathrm{t,r}}{\tau_\mathrm{t}}\right), \tag{2.17}$$

where $1/\tau_\mathrm{e} = 1/\tau_\mathrm{d} + 1/\tau_\mathrm{r} + 1/\tau_\mathrm{t}$. Assuming that trapping is the fastest process (i.e., $1/\tau_\mathrm{t} > 1/\tau_\mathrm{d} + 1/\tau_\mathrm{r}$), it is straightforward to show that the right term of Eq. 2.13 is larger than the left one and therefore

$$\mathrm{IQE} = \frac{\tau_\mathrm{t,r}}{\tau_\mathrm{d}} \tag{2.18}$$

and that the dominant photoresponse time is governed by $\tau_\mathrm{t,r}$.

To understand the advantage of the intrinsic and extrinsic photoconductors, we compare their IQE and photoresponse time as function of the drift rate ($1/\tau_\mathrm{d}$) for a given recombination rate ($\tau_\mathrm{r} = \tau_\mathrm{t,r} = 10$ ns, Fig. 2.2d). At larger drift rate, almost all photocarriers are swept out of the intrinsic photoconductor before they recombine, which leads to an IQE approaching 100%. Conversely, the IQE of the extrinsic photoconductor is not limited to 100% and can reach arbitrary large values. This photoconductive gain originates from the fact that once an electron is trapped, multiple charge-compensating holes can travel across the semiconductor before the electron recombines.

However, a large gain usually implies a slow photoresponse time. As Fig. 2.2d shows, the photoresponse rate ($1/\tau$) of the exctrinsic photoconductor is determined by the recombination time of the trapped electron $\tau_{\mathrm{t,r}}$, while the one of intrinsic photoconductor increases with the drift rate. This result explains why photodetectors with large gains usually have very slow response times [227, 229], and vice versa. Due to this trade-off, intrinsic photoconductors are better suited for applications requiring fast photoresponses, whereas extrinsic photodetectors are more advantageous for technologies demanding high detectivities. In fact, we can easily demonstrate that the product $\mathrm{IQE} \times 1/\tau = 1/\tau_{\mathrm{d}}$ is identical for both intrinsic and extrinsic photodetectors. From this relation, we conclude that both the IQE and τ can be increased by reducing the drift time of the carriers. In chapter 6, we apply this conclusion to vertical TMD photodetectors by exploiting their very short channel length and demonstrate both high IQE and fast photoresponse.

2.3.3 Photovoltaic effect

In the photovoltaic (PV) effect, the separation and transport of the photocarriers is due to the presence of an internal (built-in) electric field inside the photoactive material[2]. This internal electric field can be created, for instance, at the interface between semiconductors with different doping level (p-n junction) or at the interface between a metal and a semiconductor (Schottky junction). Generally, these devices can operate both in the photovoltaic and photoconductive mode.

In the PV mode, the device is unbiased, i.e., the external voltage applied is null. Under illumination and short-circuit condition, the photocurrent generated is similar to that of an intrinsic photoconductor presented above, except that E corresponds to the internal electric field. The photocurrent measured in this configuration is also called short-circuit current I_{sc}. In the open-circuit configuration, photocarriers with different polarities accumulate to counterbalance the internal electric field, thus generating a photovoltage. The forward bias voltage required to compensate this photovoltage is called open-circuit V_{oc}. The PV effect is used in solar cells to generate electrical power.

The photoconductive mode is activated when an external bias is applied to the device. Increasing the reverse bias of a p-n or Schottky junctions leads to an increase of the photocurrent since photocarriers are swept out of the junction more rapidely. Hence, photodetectors operated in the photoconductive mode have the advantages of having a shorter photoresponse time and higher responsivity than the photovoltaic mode. However, since the dark current is lower in the photovoltaic mode, photovoltaic detectors typically have a lower NEP and higher specific detectivity.

[2]In contrast, the photoconductive effect is caused by the application of an external electric field on the material.

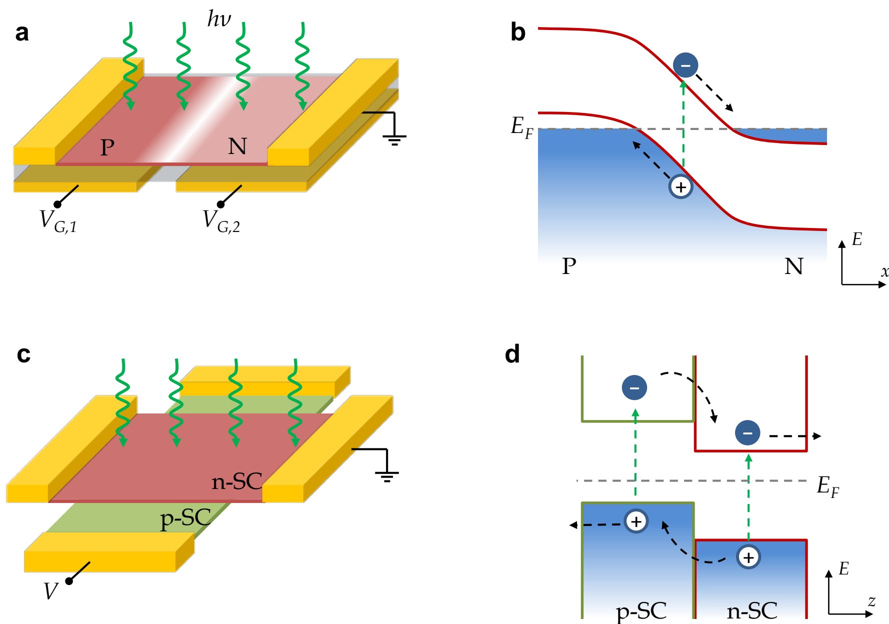

FIGURE 2.3: **Planar and vertical photovoltaic photodetector. a)** Schematic of a planar p-n junction achieved by locally doping the semiconductor channel (red) with split gates $V_{G,1}$ and $V_{G,2}$. **b)** Band diagram of the p-n junction under illumination depicting the photocurrent generation process. **c)** Schematic of a vertical p-n junction made by stacking two different layered semiconductors (p- and n-SC). **d** Band diagram illustrating the charge transfer process between the two semiconductors under illumination.

The PV effect has been observed in various planar and vertical 2D material devices, including metal- and graphene-TMD Schottky junctions [50, 235, 237], as well as TMD- and black phosphorus-based p-n junctions [238–242]. In-plane p-n junctions can be realized by doping the semiconductor with local split-gates, which allows controlling of the built-in electric field across the depletion region (Figs. 2.3a,b) . Typically, the width of the depletion region is on the order of $\sim$ 200 nm. This device architecture has been used to study the PV effect in monolayer WSe_2 [238, 239, 241] and few-layer black phosphorus [243]. In Chapter 7 we present an in-depth study of the photocurrent generation mechanism in a monolayer Wse_2 p-n junction. The zero-bias responsivity of these devices is on the order of 1-10 mA/W, corresponding to an IQE of 3 to 30%. These relatively low efficiencies result from the difficulty of realizing, at the same time, a large depletion width to capture photogenerated charges (or excitons) and a large field to separate (dissociate) them. Hence, a substantial fraction of the photocarriers recombine before they diffuse to the p-n junction.

One way to circumvent this limitation is to use a vertical geometry where

the junction extends over the entire surface of the stacked 2D materials. Out-of-plane p-n junctions (typically, type-II band alignment) can be made by stacking two semiconducting TMD layers with opposite doping polarity (Figs. 2.3c,d). Due to the small interlayer separation, very high electric field ($\sim$ 1 V/nm) can form at the interface, ensuring efficient charge (exciton) separation. Schottky junctions made of graphene-TMDs can also host large built-in fields, which, as we show in Chapter 6, can be further tuned using external gates. In both cases (Schottky and p-n junctions), the responsivity ranges from $\sim$ 10 mA/W to $>$ 0.1 A/W, depending on the thickness of the semiconductor. IQEs between 30 and 85% have been reported. The superior IQE of out-of-plane photodetectors (compared with in-plane devices) is in most part due to their larger active area.

2.3.4 Internal photoemission

Internal photoemission (IPE) corresponds to injection (or emission) of photoexcited carriers over a Schottky barrier, which is typically formed between a metal and a semiconductor (Fig. 2.4a). This process is similar to the photoelectric effect first observed by Heinrich Hertz in 1887 [244] and explained by Albert Einstein in 1905 [245]. The process of internal photoemission involves the following steps [124, 246]: i) A photon absorbed in the metal promotes a carrier to an energy superior to the Schottky barrier height Φ_B. ii) If the carrier has a momentum perpendicular to the metal/semiconductor interface, it can be injected into one of the band of the semiconductor and iii) swept away by the internal electric field of the semiconductor. Hence, due to step i), IPE photodetector have a photon energy threshold corresponding to $E_\mathrm{photon} = \Phi_\mathrm{B}$. According to Fowler's law [247], the efficiency of internal photoemission for a 3D metal (with a density of state $\propto \sqrt{E}$) is given by:

$$\mathrm{IQE} = \frac{1}{8E_\mathrm{F}h\nu}(h\nu - \Phi_\mathrm{B})^2, \tag{2.19}$$

where E_F is the Fermi energy of the metal.

As Eq. 2.19 indicates, the efficiency of this process is relatively low. For instance, the IQE of a Schottky junction made of gold ($E_\mathrm{F} = 5.5$ eV) at photon energy 10% larger than the energy threshold (i.e., $h\nu = 1.1\Phi_\mathrm{B}$) is only $\sim$ 0.2%. Moreover, given the short ballistic mean free path ($\sim$ 0.1 nm) and fast relaxation time ($\sim$ 100 fs) of photocarriers in metals, the EQE is typically an order of magnitude smaller than the IQE. Nevertheless, these photodetectors have attracted interest due to their ease of fabrication and because they offer a simple way to extend the spectral range of semiconducting photodetectors. Indeed, since Φ_B is necessarily smaller than the semiconductor bandgap, IPE photodetectors allows for sub-bandgap photodetection (Fig. 2.4b). Conversely, IPE spectroscopy can also be used to determine Φ_B [248, 249]. Although IPE is a rather common effect in bulk materials, it has not often been reported in 2D materials. A

few studies attributed the infrared photoresponse observed in graphene-Si junctions to IPE [250–252], but despite their impressive results (responsivities up to 0.14 A/W), the role of IPE in this devices remains elusive. In Chapter 5 we introduce a new photocurrent generation mechanism in graphene-TMD junctions, the photo-thermionic effect, that outcompetes the IPE observed in conventional metal-semiconductors junctions. We also demonstrate that a process similar to IPE, involving the emission of photoexcited carriers through a tunnelling barrier, takes place in graphene/hBN/graphene heterostructures.

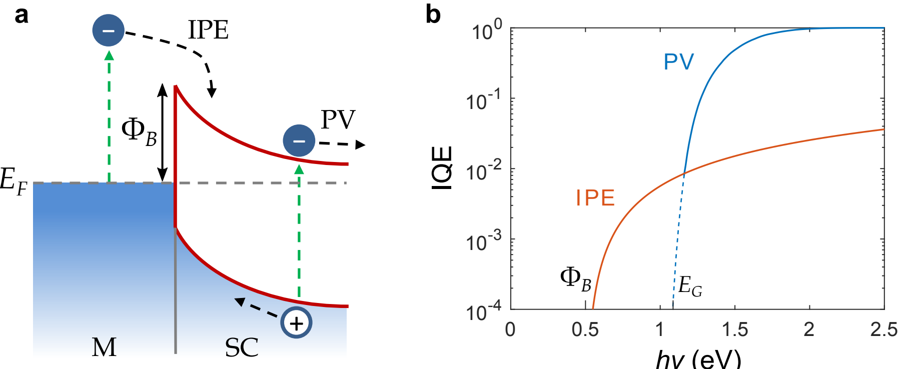

FIGURE 2.4: **Internal photoemission and photovoltaic effect in a Schottky photodiode. a)** Band diagram of a Schottky barrier (with height Φ_B) formed at a metal-semiconductor interface. Photoexcitations in the metal and semiconductor can generate a photocurrent via the IPE and PV effects, respectively. **b)** Spectral dependence of IQE for a Schottky diode made of a semiconductor with $E_G = 1.1$ eV and a Au contact with $\Phi_B = 0.5$ eV. The contributions of the IPE and PV effects are represented by the red and blue solid lines, respectively.

2.4 Photodetection enabled by hot carriers

One of the possible relaxation path of photoexcited carriers is to redistribute their energy among other carriers, which leads to an increase of the electron bath temperature T_e. In photovoltaic cells, this process transforms the excess photon energy into electronic heat and leads to a loss of power conversion efficiency. However, the rise in the average carrier temperature can in turn drive a photocurrent or photovoltage via two main processes: the thermoelectric (or Seebeck) effect and the bolometric effect. These photodetection mechanisms can be divided in three steps:

i) *Generation of photocarriers*. Photocarriers are generated upon photon absorption in the photoactive material via optical transitions. Unlike photocarrier-driven detectors, thermally-driven detectors do not require the excited and ground states of the optical transition to be separated by an energy gap

ΔE. In other words, both intraband and interband transitions can contribute to the photodetection process. Due to this absence of photon energy threshold, thermal photodetectors usually have a broad spectral responsivity.

ii) *Generation of a hot-carrier distribution*. Photocarriers then thermalize with the surrounding carriers, typically through carrier-carrier scattering. Once carriers have reached thermal equilibrium (with themselves, not necessarily with the lattice), they form a so-called hot carrier distribution, which can be well described by a Fermi-Dirac distribution with an elevated temperature T_{e}.

iii) Tr*ansport and cooling of the hot carriers*. The creation of a local or global hot carrier distribution can have several effects on carrier transport. The temperature gradient resulting from local heating may lead to the generation of photocurrent or photovoltage through the thermoelectric effect. Homogenous heating can also modify the resistance of the photoactive material (bolometric effect), resulting in a change in voltage or current. The electric signal persists until the hot carrier distribution cools back to the ambient (lattice) temperature.

2.4.1 Dynamics and transport of electronic heat

Since the photodetection mechanisms described in this section rely on the heat contained in the electronic bath, we first consider the general thermoelectric equations governing the energy flux and current density $\mathbf{J}$ in electronic systems [253]:

$$C_{\mathrm{e}}\frac{\partial T_{\mathrm{e}}}{\partial t} = \kappa\nabla^2 T_{\mathrm{e}} - \nabla\cdot(V+\Pi)\mathbf{J} + \dot{Q}_{\mathrm{ext}} \tag{2.20}$$

$$\mathbf{J} = \sigma(-\nabla V - S\nabla T), \tag{2.21}$$

where T_{e} is the local carrier temperature, S is the local Seebeck coefficient of material, V is the local voltage, C_{e} is the electronic heat capacity, κ is the thermal conductivity, Π is the local Peltier coefficient of the material and $\dot{Q}_{\mathrm{ext}}$ is rate at which heat added (or removed) by an external source (cooling channel). The first term of Eq. 2.20 corresponds to Fourier's law, while the second term is the energy carried by the electric current density. Since $\mathbf{J}$ is usually small in practice, this term can be neglected.

2.4.2 Photo-thermoelectric effect

In the photo-thermoelectric (PTE) effect, light absorbed in a region of the photoactive material heats up the local carrier temperature T_{e}, which generates a temperature gradient ∇T_{e} between the two ends of the material. Due to variations in the carrier drift velocity and chemical potential with temperature, the

thermal diffusion of carriers creates a net charge imbalance, and therefore a potential gradient ∇V between the hot and cold ends. According to Eq.2.21, the conversion of ∇T_e into ∇V is proportional to the Seebeck coefficient, or thermopower, S:

$$\nabla V = S\nabla T_\mathrm{e}. \tag{2.22}$$

In metals, the Seebeck coefficient can be evaluated by using the well-know Mott formula:

$$S = -\frac{\pi^2 k_\mathrm{B}^2 T_\mathrm{e}}{3e_0}\frac{1}{\sigma(E_\mathrm{F})}\frac{\partial\sigma(E)}{\partial E}\Big|_{E=E_\mathrm{F}}, \tag{2.23}$$

where $\sigma(E)$ is the energy-dependent conductivity. We note that this formula is derived using the Sommerfeld expansion, which is only valid for $T_\mathrm{e} \ll E_\mathrm{F}/k_\mathrm{B}$.

The PTE effect has been shown to contribute to the zero-bias photoresponse of several 2D materials, such as graphene [45, 46, 48, 73, 254, 255], WSe_2 [242], MoS_2 [256] and black phosphorus [257]. This effect, which is particularly pronounced in graphene, was first observed at the interface of single layer and bilayer graphene [255]. Gabor *et al.* [45] later confirmed that this effect also takes place at the interface of graphene with different Fermi energies, in agreement with theoretical predictions [84]. In Chapter 4, we show that the PTE effect also dominates the photoresponse measured at graphene-metal interfaces. Relatively high PTE responsivities ($\sim$ 10 mA/W) were measured in suspended graphene devices [73], corresponding to an IQE of $\sim$ 40%. Fast photo-switching speed was also demonstrated in graphene-based PTE photodetectors [31, 46–48, 258–260], with a demonstrated bandwidth as high as 65 GHz [48]. In order to identify the properties and physical parameters relevant to the PTE effect, we present below a simple model of a PTE photodetector and discuss its implications in the specific case of graphene.

PTE photodetectors

In PTE photodetectors, photovoltage (or photocurrent) is generated by shining light at the junction of regions with different Seebeck coefficients (S_1 and S_2), which can be made by using two different materials or by changing the doping level in two distinct regions of the same material (Fig. 2.5a). In the short-circuit configuration, the total photovoltage generated by the PTE effect is given by

$$\Delta V = \frac{1}{W}\iint S\nabla T_\mathrm{e}\mathrm{d}x\mathrm{d}y \tag{2.24}$$

$$= (S_2 - S_1)(T_\mathrm{e,hot} - T_\mathrm{e,0}) = \Delta S\Delta T_\mathrm{e}, \tag{2.25}$$

where W is the width of the $T_\mathrm{e,hot}$ is the increased carrier temperature at the junction and $T_\mathrm{e,0}$ is the carrier temperature without illumination (normally equal to the ambient temperature). In the short-circuit configuration, the photovoltage

acts as an electromotive force and generates a photocurrent

$$\mathrm{PC} = \frac{\Delta S \Delta T_{\mathrm{e}}}{R}, \tag{2.26}$$

where R is the total resistance of the device.

The efficiency and response time of PTE detectors are strongly influenced by the heat transport in the device which governs ΔT. To illustrate this, we consider the simplest case where a light beam (with power P and area A) heats carriers at a rate corresponding to the optical power absorbed in the material, while heat is lost at a rate $\Gamma \Delta T_{\mathrm{e}}$. We also assume that heat conduction in the material is negligible. In this case, Eq. 2.20 becomes

$$C_{\mathrm{e}} \frac{\mathrm{d}T_{\mathrm{e}}}{\mathrm{d}t} = P_{\mathrm{in}} - \Gamma \Delta T_{\mathrm{e}}, \tag{2.27}$$

where $P_{\mathrm{in}} = P_{\mathrm{abs}}/A$ is the absorbed power density.

Under pulsed excitation, and assuming that C_{e} and Γ are constant, the solution to this equation is

$$\Delta T_{\mathrm{e}}(t) = \Delta T_{\mathrm{e}}(0) \exp(-t/\tau_{\mathrm{cool}}), \tag{2.28}$$

where $\Delta T_{\mathrm{e}}(0)$ is the intial raise in carrier temperature and $\tau_{\mathrm{cool}} = C_{\mathrm{e}}/\Gamma$ is the characteristic carrier cooling time. Since photocurrent generation is driven by ΔT_{e}, τ_{cool} determines the photoresponse time of the photodetector.

Under steady-state conditions, Eq. 2.27 yields:

$$\Delta T_{\mathrm{e}} = \frac{P_{\mathrm{in}}}{\Gamma} = \frac{P_{\mathrm{in}} \tau_{\mathrm{cool}}}{C_{\mathrm{e}}}. \tag{2.29}$$

By combining Eqs. 2.26 and 2.29, we obtain

$$\mathrm{PC} = \frac{\Delta S}{R} \frac{P_{\mathrm{in}} \tau_{\mathrm{cool}}}{C_{\mathrm{e}}}. \tag{2.30}$$

and

$$\mathrm{IQE} = \frac{h\nu}{e_0} \frac{\Delta S}{AR} \frac{\tau_{\mathrm{cool}}}{C_{\mathrm{e}}}. \tag{2.31}$$

Graphene-based PTE photodetectors

Several conclusions can be drawn from this simple PTE model, in particular with respect to graphene-based photodetectors. First, it shows that the PTE effciency depends directly on two important electronics properties of the photoactive materials: the electron heat capacity C_{e} and the seebeck coefficient S. Graphene is

an excellent PTE material since it combines both a small C_e (see Section 1.1.1) and a large S, in particular close to the Dirac point. Assuming that the carrier mobility is independent of E_F (which is the case when charged impurity scattering is the dominant process), Mott formula (Eq. 2.23) gives

$$S = -\frac{2\pi^2 k_\mathrm{B}^2 T_\mathrm{e}}{3e_0 E_\mathrm{F}}. \tag{2.32}$$

This equation and Eq. 1.6 indeed show that S increases and C_e decreases as E_F approaches the charge neutrality point. However, both equations are invalid in the limit where $E_\mathrm{F}/k_\mathrm{B} \ll T_\mathrm{e}$ and a more detailed theory is required in this regime [84, 261]. It is also interesting to note that $S = C_\mathrm{e}/(e_0 n)$, where n is the charge carrier density. This illustrates the fact that Seebeck coefficients describe the flow of entropy per unit charge across a junction [262].

The difference in Seebeck coefficient ΔS also gives rise to a distinct six-fold pattern in the PTE photocurrent when the Fermi level of both regions are varied (Fig. 2.5b). Indeed, Song *et al.* [84] first predicted that the PTE photocurrent should vanish when the Fermi energies of both regions are equal ($E_{\mathrm{F},1} = E_{\mathrm{F},2}$) and when they satisfy the relation $E_{\mathrm{F},1}E_{\mathrm{F},2} = \Delta^2$, where Δ represents the width of the charge neutrality point, also known as charge-puddle width. The last condition is due to the fact that both electrons and holes contribute to the PTE effect and cancel each other. This is in stark contrast with the photovoltaic (PV) effect discussed in Section 2.3.3, where the polarity of the photocurrent depends on the direction of the electric field (Fig. 2.5c). In this case, the PV photocurrent dependence on the Fermi enegies changes polarity only once, when $E_{\mathrm{F},1} = E_{\mathrm{F},2}$. Hence, measuring the photocurrent as a function of both Fermi energies provides a clear and simple way to distinguish between the PV and PTE effect and identify the dominant photocurrent generation mechanism [45].

The PTE model presented above also highlights the important effect of the cooling time τ_cool on the IQE and photoresponse time of the photodetector. As previously observed in photoconductors (Section 2.3.2), a trade-off exists between these two performance metrics. In the case of PTE, a long cooling time leads to a large IQE but results in a slow photoresponse time, and vice versa. In graphene, the cooling time of hot carriers depends on various carrier relaxation processes (see Section 1.1.3), depending on the experimental conditions (defects, substrate, temperature, etc). In general, its cooling time at room temperature is on the order of $\sim$ 1 ps, which implies a large theoretical bandwidth ($\sim$ 500 GHz [258]) but leads to moderate IQE values (1 to 20%) [31, 260].

Finally, it is instructive to compare the spectral response of PTE and PV photodetectors (Fig. 2.5d). As we previously noted, PV (and IPE) detectors have photon energy threshold corresponding to bandgap of the material (or Φ_B), while PTE detectors do not require such a threshold to operate. Hence, they can detect light over a larger spectral range and are only limited by the absorption spectrum of the photoactive material. Again, graphene is particularly well-suited for

PTE detectors with its nearly constant absorption from the mid-IR to the near-UV (Section 1.1.2).

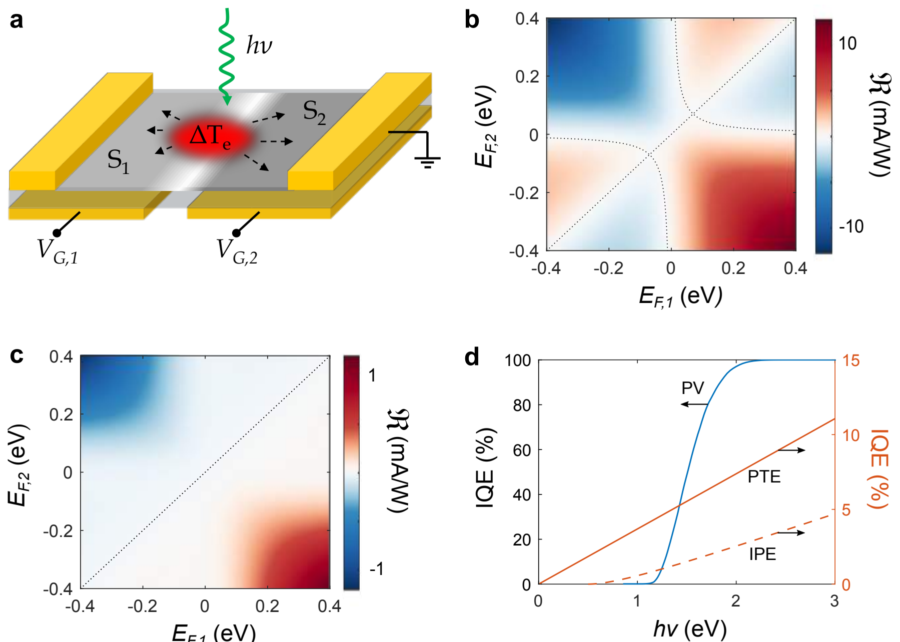

FIGURE 2.5: **Photo-thermoelectric effect and comparison with other photodetection mechanims. a)** Schematic of a PTE photodetector. Photocurrent or photovoltage is generated by locally heating (ΔT_e, red region) the interface between regions with different Seebeck coefficients (S_1 and S_2). Here, this interface is created by locally doping each region with split gates ($V_{\mathrm{G},1,2}$). **b)** PTE responsivity $\Re$ of graphene calculated as a function of the Fermi energies $E_{\mathrm{F},1,2}$ in the two regions shown in **a**. Calculations are performed using a conductivity model similar to the one presented by Song *et al.* [84], with a constant temperature difference $\Delta T_\mathrm{e} = 4$ K and charge-puddle width $\Delta = 70$ meV. The dotted lines indicate where the responsivity vanishes. The PTE response displays a six-fold pattern, whereas the PV response (shown in **c**) only shows two regions with different polarities. The PV response of graphene was calculated using the same conductivity model as in **b**, assuming a mobility $\mu = 1000$ cm^2/Vs and photocarrier lifetime of 1 ps. **d)** Spectral dependence of the IQE for different photodetections mechanisms. The PV efficiency (solid blue line) is calculated for a semiconductor with $E_\mathrm{G} = 1.1$ eV, assuming 100% efficiency for above-bandgap photons. The PTE efficiency (solid red line) is calculated using $E_\mathrm{F} = 0.2$ eV, $\tau_\mathrm{cool} = 2$ ps, $\Delta S = 20$ μV/K and $R = 1$ kΩ. The IPE efficiency (dotted red line) is calculated using the same parameters as in Fig. 2.4b.

Finally, it is instructive to compare the spectral response of PTE and PV photodetectors (Fig. 2.5d). As we previously noted, PV (and IPE) detectors have photon energy threshold corresponding to bandgap of the material (or Φ_B), while PTE detectors do not require such a threshold to operate. Hence, they can detect

light over a larger spectral range and are only limited by the absorption spectrum of the photoactive material. Again, graphene is particularly well-suited for PTE detectors with its nearly constant absorption from the mid-IR to the near-UV (Section 1.1.2).

Moreover, since the PV effect depends on the number of photocarriers, the IQE of this process is, in principle, independent of the photon energy and limited to 100% (Fig. 2.5d). In other words, photons with an energy larger than the bandgap contribute equally to the IQE. This means that the energy in excess of the bandgap is lost via thermalization and that the responsivity of the photodetectors decreases with photon energy. On the other hand, the PTE effect depends on the thermal energy contained in the electron bath. Assuming that the energy of the absorbed photon is completely converted into carrier heat, the PTE efficiency is expected to increase linearly with photon energy (Eq. 2.31): the larger the energy of the photon is, the more it generates photocurrent. For this reason, the PTE efficiency is not limited to 100% and can reach arbitrarily large values. In Chapter 4, we show that the conversion of photon energy into carrier heat is indeed a very fast and efficient process in graphene, which leads to a linear increase of the IQE with photon energy.

2.4.3 Photo-bolometeric effect

The photo-bolometric (PB) effect occurs when the transport conductance G_e of a material changes due to heating induced by photon absorption. The photocurrent generated via this process is therefore given by

$$\mathrm{PC} = \frac{\partial G_\mathrm{e}}{\partial T} V \Delta T_\mathrm{e} \tag{2.33}$$

In most materials, the change in conductance is due to the carrier mobility dependence on temperature. Since this effect relies on a change in the transport properties of the material (as opposed to the transport of charges), photo-bolometers cannot drive a photocurrent and require an external bias (V) to operate. Unlike the PTE effect, the PB effect can take place in a homogeneous photoactive material and do not require any type of junction. However, the photoresponse time of photo-bolometers is similar to that of PTE photodetectors because in both cases, it relies on the cooling time of the hot carriers.

The photo-bolometric effect has been measured several times in graphene [48, 234, 263] and black phosphorus [257, 264]. Since both PTE and PB photodetectors rely on the photo-induced heating of carriers, many of their photodetection metrics are similar. The responsivity reported for graphene devices at room temperature is however relatively low, on the order of 0.2 mA/W [234].

2.5 Photocurrent measurement techniques

Having described the main photodetection mechanisms in conventional and 2D materials, we now present the experimental techniques that we employ in the rest of the thesis to investigate these mechanisms and to probe the optoelectronic processes on which they rely.

Studying 2D materials poses many experimental challenges. The first and maybe main difficulty consists in fabricating high-quality electronic devices based on these new materials. Chapter 3 explains how state-of-the-art device fabrication is accomplished. Once a device is produced, measuring its optoelectronic response requires specific capabilities:

Broadband and wavelength-tunable light sources are necessary in order to measure the spectral response of the device. In our experimental setup (Fig. 2.6a), a quasi-CW (continuous wave) supercontinuum laser provides a wide spectral light source, ranging from $\lambda = 500$ to 1500 nm. We also use CW diode lasers with fixed wavelength at $\lambda =$705, 730, 785 and 1500 nm.

High temporal resolution is required to probe the photoresponse time of the device. As we explained in more detailed in Section 2.5.3, this can be achieved by using pulsed laser with ultrashort pulse duration (in our case, a Ti:Sapphire laser with $\sim$ 200-fs pulse duration) in combination with a variable optical delay line.

Controlling the properties of light, such as its polarization and intensity, is achieved using different optical components on an optical table (Fig. 2.6b). Important information can be obtained by monitoring the effect of these parameters on the device photoresponse.

Controlling the ambient conditions under which the sample is measured, such as temperature and pressure, is often necessary in order to ensure the device stability and study the dependence of the photoresponse in different conditions. For these reasons, all our devices are measured under vacuum inside a cryostat (Fig. 2.6c) with a controllable temperature ranging between 30 and 340 K.

High-spatial-resolution mapping allows for local probing the photoresponse in different regions of the device. As we explain in the next section, mapping the photoresponse of the device provides a wealth of information on the origin the photodetection process. Since 2D material-based devices are usually very small, on the order of $\sim$ 10 μm, it is crucial to use a probe with even smaller dimensions. We accomplish this by focusing light close to its diffraction limit with a microscope objective, resulting in a laser spot size (full width at half maximum, FWHM) of $\sim$ 1.5 μm. A set of piezoelectric positioning stages (Fig. 2.6d) allows us to translate the sample in all directions and thereby to scan the laser over the sample.

Sensitive electrical measuring instruments (Fig. 2.6e) are required in order to acquire the small electrical signals generated by the photoactive device. Lock-in detection is a particularly useful technique for this purpose as it allows to isolate the signal induced by the modulated laser from the noise produced by the ambient light and the dark current.

In the following sections, we describe the main photocurrent measurement techniques that we use throughout this thesis: scanning photocurrent microscopy, photocurrent spectroscopy and time-resolved photocurrent measurements. The experimental setup that we employ to perform these techniques is illustrated in Figs. 2.6 and 2.7.

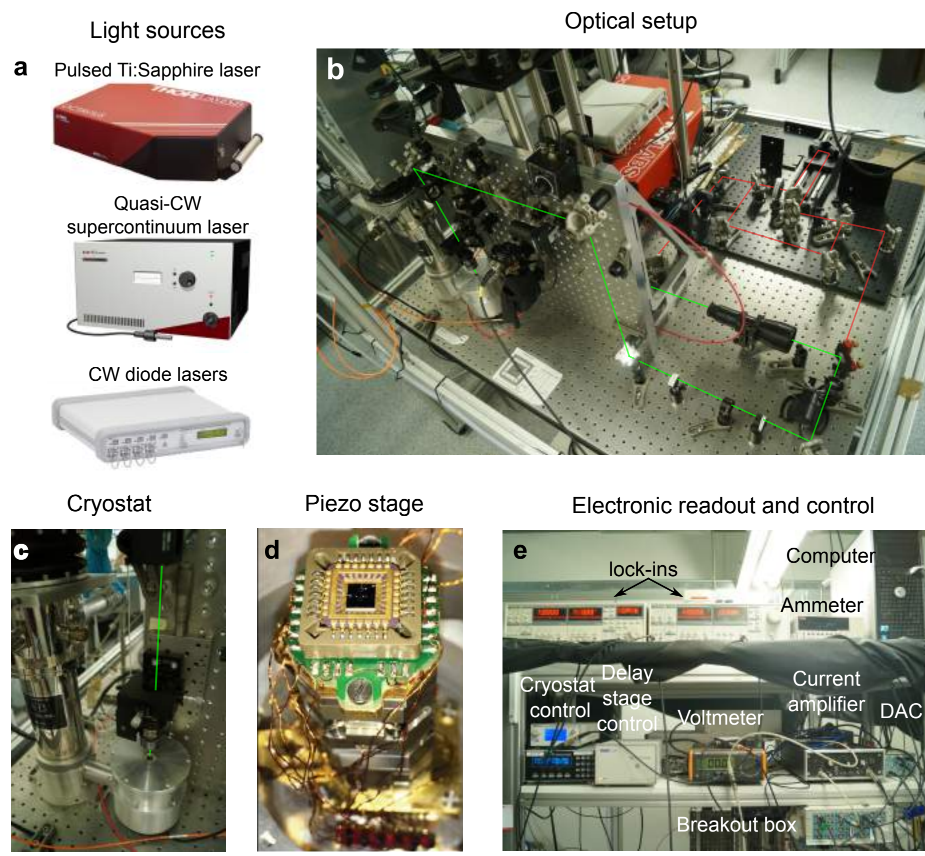

FIGURE 2.6: **Experimental setup. a)** Laser light sources. Top: Thorlabs Octavius 85M. Middle: SuperK Extreme. Bottom: Thorlabs diode laser. **b)** Photograph of the optical setup. The green line represents the optical path of the supercontinuum laser beam, while the red line shows the optical path of the pulsed laser beam. **c)** Photograph of the cryostat containing the measured device. The green line shows the laser beam focused on the device by the microscope objective. **d)** Photograph of a device mounted on the piezoelectric stage inside the cryostat (credit: Niels Hesp). **e)** Photograph of the electronic instruments employed to measure the device or control the apparatus of the setup.

2.5.1 Scanning photocurrent microscopy

Scanning photocurrent microscopy (SPCM) is a technique that consists in scanning a focused laser beam over the surface of a sample and measuring the resulting photocurrent (or sometimes, photovoltage) as a function of the laser position [265]. The concept of SPCM is hardly new, as it was first introduced by Haynes and Shockley in 1949 [266]. The method has now become very well established and is commonly used to study nanomaterials such as 2D materials, nanowires, carbon nanotubes and colloidal semiconductor quantum dots.

Spatial photocurrent maps provide a wealth of information on the optoelectronic properties of the photoactive material. First of all, knowing the position where the photoresponse is maximum can help identify the dominant photocurrent generation mechanism of the photodetector. For instance, by observing a strong photoresponse at monolayer-bilayer graphene interfaces, Xu *et al.* [255] were able to demonstrate the photo-thermoelectric origin of the photocurrent in graphene. In PTE-based devices, SPCM can also provide information on the spatial variation of the Seebeck coefficient and on the carrier cooling length, which, according to Eqs. 2.20 and 2.27, corresponds to $L_{\mathrm{cool}} = \sqrt{\kappa/\Gamma}$. In graphene, for example, Garbor *et al.* [45] measured $L_{\mathrm{cool}} \sim 2$ μm at low temperature. Similarly, in photocarrier-driven photodetectors, SPCM can help determining the electric field distribution as well as the minority carrier diffusion length L_{d}. Using Eqs. 2.2 and 2.7 , we can easily show that $L_{\mathrm{d}} = \sqrt{D\tau_{\mathrm{r}}}$. Diffusion lengths on the order of 500 nm have been measured in few-layer TMDs using SPCM [267].

Most of the SPCM experiments shown in thesis are performed using the setup shown in Fig. 2.7. A laser beam, generated by one of the laser sources shown in Fig. 2.6, is modulated by a mechanical chopper at a frequency of $\sim$ 100 Hz and focused onto the device by a microscope objective (Olympus LUCPlanFLN-40x for the visible light and Olympus LCPLN-50x for the near-IR light). The device is mounted on a piezoelectric positioning stage (Attocube ANC300), which allows us to control the xyz-position of our device with an accuracy of $\sim$ 10 nm (in x-y). The photocurrent generated by the modulated laser beam is measured with a preamplifier (Ithaco 1211) and a lock-in amplifier (Stanford Research SR830) synchronized with the mechanical chopper.

The device and piezoelectric stage are placed inside a closed-cycle cryostat (Janis CCS-XG-M/204N) with a base temperature of 30 K and a base pressure of $\sim 3{\times}10^{-5}$ mbar. The device temperature can be varied between 30 and 340 K by controlling a resistive heater placed below the device holder. The light reflected or emitted by the device can be measured using a photodiode (Thorlabs DET36A) connected to a lock-in amplifier or by a spectrometer (Andor Shamrock 193i). Measuring the reflected light allows us to correlate the photocurrent map with the device geometry, while spectroscopy can provide information on the material under study. All the data are acquired by a computer via the measurement software QTLab. This software also allows us to control the voltages applied on the device via a digital-to-analogue converter (DAC, National Instrument).

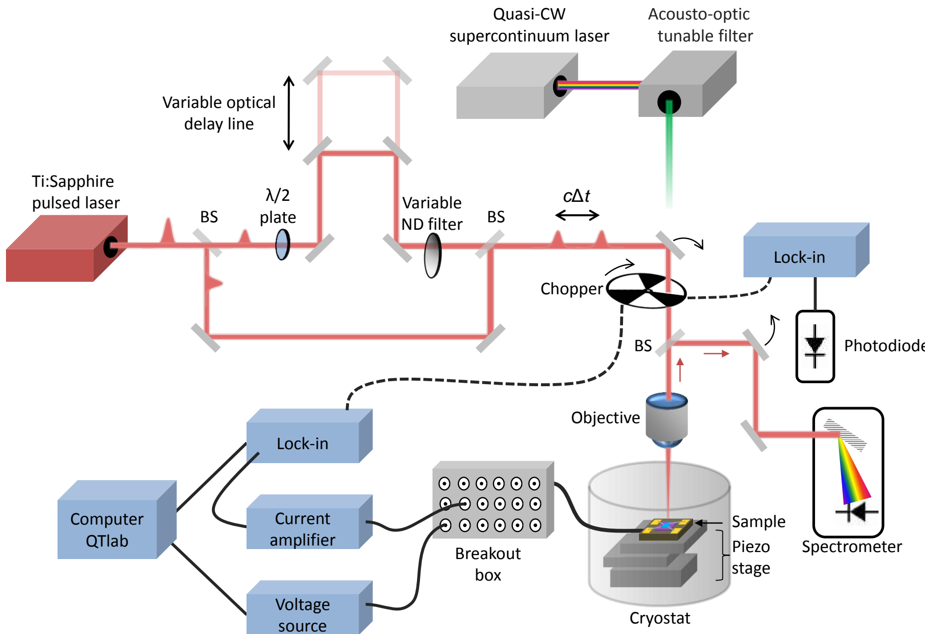

FIGURE 2.7: **Schematic view of the optical and electrical setup.** The laser pulses (red) of the Ti:Sapphire laser are split by a beam splitter (BS) into two arms, one of which contains a variable delay line controlling the time delay Δt between the pulse pair. One arm also contains a half-wave ($\lambda/2$) plate to make the pulses orthogonal to each other, and a variable neutral density filter to control the pulse intensity. A flip mirror (black curved arrows) allows to switch the pulsed laser source for a wavelength-tunable, quasi-CW laser source. Both laser beams are modulated by a mechanical chopper and focused on a sample by a microscope objective.The light reflected or emitted from the sample can either be directed to a spectrometer or a photodiode, measured with a lock-in synchronized with the chopper. The device is mounted on a xyz-piezo stage inside a cryostat. The photocurrent generated by the focused laser beam is detected using a preamplifier and a lock-in amplifier in referenced to the mechanical chopper. Data are acquired by a computer using the software QTlab.

2.5.2 Photocurrent spectroscopy

Photocurrent spectroscopy is performed by measuring the photocurrent produced by a material as a function of the energy (or wavelength) of the incident photons. This technique can give information on the absorption spectrum of the photoactive material and on the energy-dependence of the electronic processes involved in the generation of photocurrent. Depending on the photoresponsity of the device under study, PC spectroscopy can be simpler and more sensitive than the more conventional absorption spectroscopy [228]. It also allows for selective

measurement of the absorption in regions where PC is generated . In Chapter 7, for instance, we use this feature to probe changes in the absorption spectrum caused by the presence of an in-plane electric field in a monolayer WSe_2.

PC spectroscopy can be easily implemented by combining our SPCM setup with a broadband, wavelength-tunable source. To this end, we use a supercontinuum laser (SuperK Extreme NKT Photonics) with a repetition rate of 40 MHz and a broad emission spectrum (Fig. 2.8a) ranging from λ = 500 to 1500 nm ($E_{\mathrm{photon}} \sim$ 0.8 to 2.5 eV) . The laser is coupled to a computer-controlled acousto-optic tunable filter (AOTF, SpectraK Dual NTK Photonics) that allows us to tune the wavelength of the output laser beam with a resolution varying from 4 to 14 nm (Fig. 2.8b). We characterize the temporal shape of the laser pulse using an ultrafast photodetector (Fig. 2.8c) and measure the focused laser beam profile using a technique similar to the knife-edge method (Fig. 2.8d). This measurements show that the focused laser pulse can be well approximated by a Gaussian function:

$$P(x, y, t) = \frac{P_{\mathrm{tot}}}{(2\pi)^{3/2}\sigma_x\sigma_y\sigma_t} \exp\left(-\frac{x^2}{2\sigma_x^2} - \frac{y^2}{2\sigma_y^2} - \frac{t^2}{2\sigma_t^2}\right), \tag{2.34}$$

where P_{tot} is the total laser power, and $\sigma_{x,y,t}$ are the standard deviations of the Gaussian function in the spatial and temporal domains. We measure a FWHM pulse duration of $\tau_{\mathrm{pulse}} = 2\sqrt{2\ln 2}\sigma_t = 100$ ps. Similarly, assuming that the profile is circular (i.e., $\sigma = \sigma_x = \sigma_y$), we obtain a laser spot size of $L_{\mathrm{spot}} = 2\sqrt{2\ln 2}\sigma = 1.8\ \mu$m. Moreover, measurements of the laser profile for different wavelengths show that the laser spot size is nearly independent of λ (Fig. 2.8e).

2.5.3 Time-resolved photocurrent measurement

Time-resolved photocurrent (TRPC) measurements are techniques that allow for the assessment of the photoresponse time of a photosensitive device. As we have shown in Section 2.3, the photoresponse time is determined by the dynamics of the various electronic processes involved in the photocurrent generation. Hence, TPRC measurements not only assess the photodetector intrinsic bandwidth, but they also give insight into the microscopic processes governing the photoresponse. We note that in contrast to all-optical pump-probe measurements, which are also employed to probe fast electronic processes, TRPC techniques selectively isolate the electronic processes involved in the generation of photocurrent.

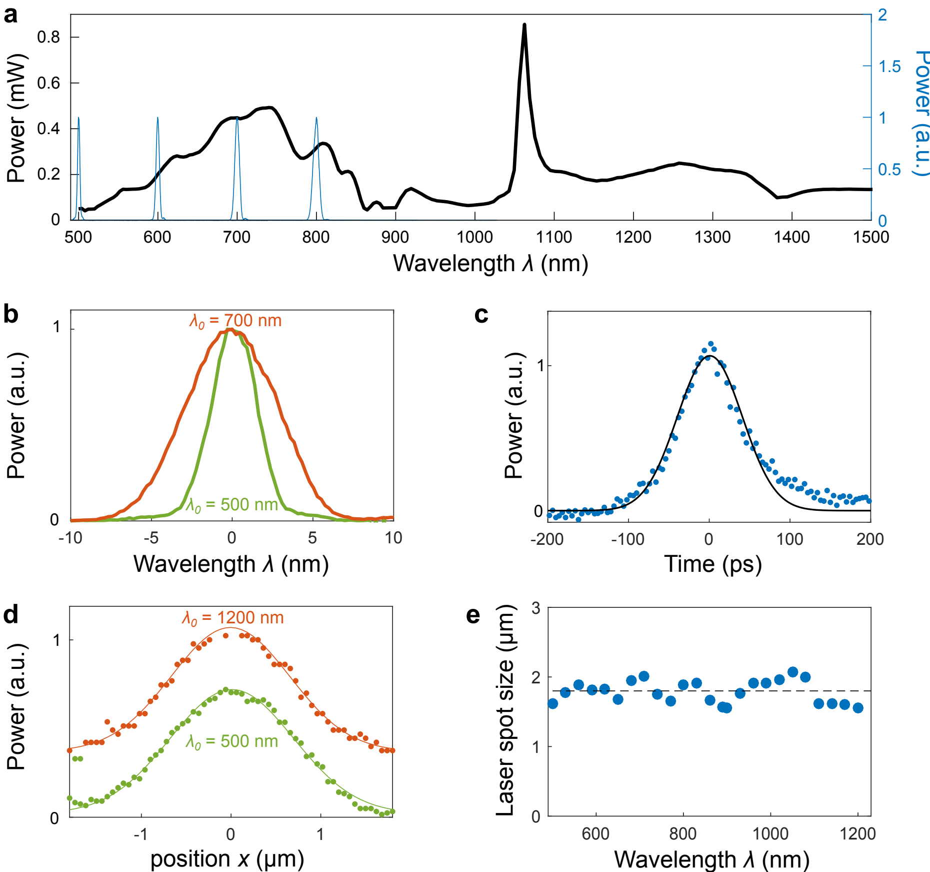

FIGURE 2.8: **Characterization of the quasi-CW supercontinuum laser source. a)** Power spectrum of the supercontinuum laser measured at the sample position (solid black line, left axis) and power spectrum of the laser for various wavelengths ($\lambda_0 = 500$, 600, 700 and 800 nm) selected by the AOTF (solid blue line, right axis). **b)** Same power spectrum (centered around λ_0) for $\lambda_0 = 500$ (green) and 700 nm (red). **c)** Temporal intensity profile of the quasi-CW source (blue dots) fitted with a Gaussian function (solid black line) with $\sigma_t = 44$ ps, corresponding to a pulse duration of $\tau_{\text{pulse}} = 100$ ps. **d)** Spatial profile of the focused laser beam measured for $\lambda_0 = 500$ (green) and 1200 nm (red, offset for clarity). The solid lines are Gaussian fits yielding $\sigma \sim 0.75$ μm. **e)** Laser spot size L_{spot} measured as a function of the laser wavelength λ, showing a nearly constant size of ~ 1.8 μm.

Measuring the generation of photocurrent in the time domain can be performed through various ways. The most direct method consists in measuring the photocurrent produced by an ultrashort laser pulse in real time. However, the temporal resolution of this technique is limited by the bandwidth of the electronic measuring equipment or by the response time of the high-frequency circuit connecting the photoactive material to measuring instruments [47, 48]. These restrictions typically lead to a temporal resolution of ~ 10 ps, which is often much

longer than the time scale of the electronic processes that we want to study.

One way to overcome this limitation is to perform photocurrent autocorrelation measurements, a technique that exploits the nonlinear response of photodetectors and the high temporal resolution of optical pump-probe experiments. This method consists in exciting a photodetector, which has a nonlinear power-dependent response, with a pair of ultrashort laser pulses (pump and probe) separated in time by a controllable time delay Δt. By measuring the total photocurrent produced by these two pulses as a function of Δt, it is possible to extract the photoresponse time of the device and to obtain information on processes involved in the photoreponse. In this case, the temporal resolution is only limited by the pulse duration of the laser, which is typically on the order of 100 fs. This TRPC technique has been employed to study several electronic processes in 1D and 2D materials, including the cooling of hot electrons in graphene [76, 254, 268], the drift of photocarriers in carbon nanotubes [269, 270] and the trapping of photocarriers in MoS_2 [271].

To illustrate this measurement technique, we consider a photodetector with a sublinear power dependence (Fig. 2.9a) excited by two pulses with the same power P. When the time delay between each pulses is very long, the total photocurrent is simply the sum of two independent pulses $\mathrm{PC}(\Delta t \to \infty) = 2\mathrm{PC}(P)$. At $\Delta t = 0$, the two overlapping pulses form a single pulse of power $2P$ and the total photocurrent is $\mathrm{PC}(\Delta t = 0) = \mathrm{PC}(2P)$. Due to the sublinear power dependence of the photodetector, the total photocurrent is smaller when the pulses coincide in time than when they are separated $(\mathrm{PC}(2P) < 2\mathrm{PC}(P))$. Hence, in this case, the photocurrent autocorrelation measurement will display a symmetric dip around $\Delta t = 0$ as the one shown in Fig. 2.9b.

This photocurrent dip indicates the time that the photodetector takes to return to its equilibrium (dark) state. It therefore yields the intrinsic photoresponse time of the device, which, in turn, contains valuable information on the photocarrier dynamics. In first approximation, the photoresponse time τ of the device can be obtained by modelling the Δt-dependence of the dip with an exponential decay [268, 270]. We employ similar models to extract the photoresponse time of the devices presented in Chapter 5 and 6. However, this simple analysis is usually only valid for near-equilibrium measurements since it ignores the effect of the laser power on the measured response time.

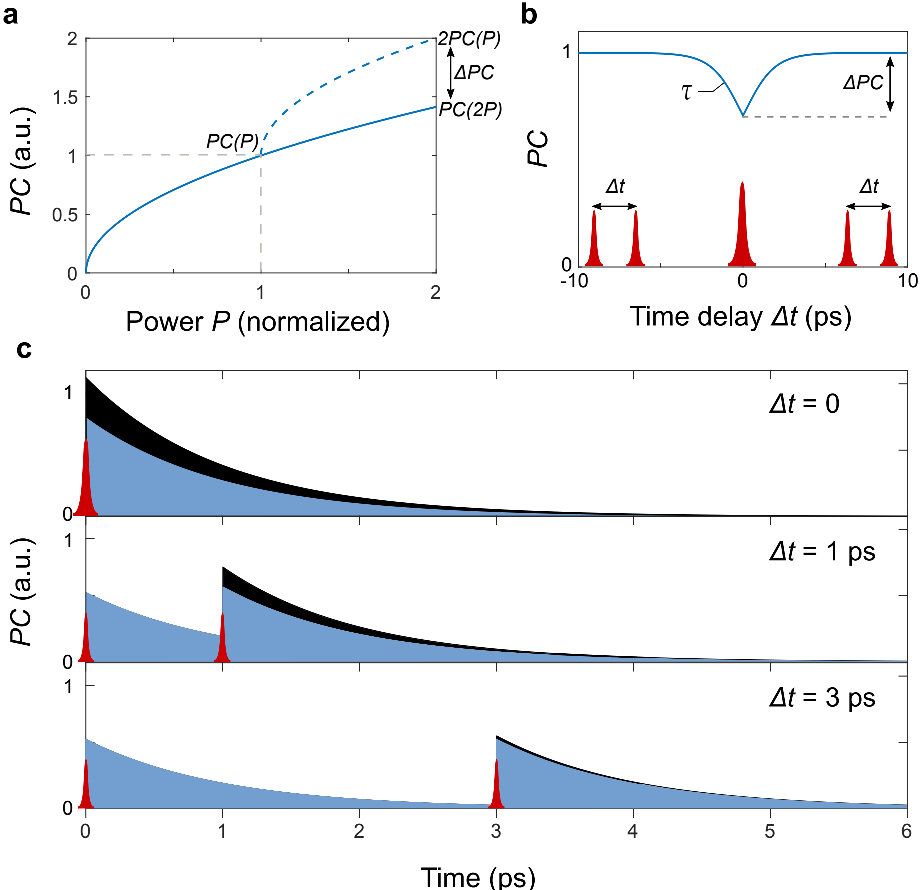

FIGURE 2.9: **Time-resolved photocurrent measurement and analysis.** Photocurrent autocorrelation measurements rely on the non-linear power dependence of the photocurrent, which is illustrated in **a** by the sublinear ($\mathrm{PC} = \sqrt{P}$) solid blue curve. The photocurrent generated for a single pulse $\mathrm{PC}(P)$ is indicated by the gray dotted lines. When the time between the two pulses is very long, the total photocurrent is simply $\mathrm{PC}(\Delta t \to \infty) = 2\mathrm{PC}(P)$, which, graphically, corresponds to the end of the dotted blue line. The photocurrent generated when both pulses are overlapping in time is $\mathrm{PC}(\Delta t = 0) = \mathrm{PC}(2P)$, which is smaller than $2\mathrm{PC}(P)$. The difference between these two photocurrent values is denoted $\Delta\mathrm{PC}$. **b)** The decrease in photocurrent at $\Delta t = 0$ gives rise to a characteristic dip (with a depth equal to $\Delta\mathrm{PC}$) when the photocurrent is measured as function of Δt. The photoresponse time of the device τ can be extracted from the Δt-dependence of the dip. **c)** Illustration of the time-dependent photocurrent $\mathrm{PC}(\xi)$ (with a characteristic decay time $\tau = 1$ ps) for different time delays Δt. The blue area represents the outcome of Eq. 2.35 for a sublinear parameter $\xi(P)$, while the black area corresponds to the photocurrent generated by two independent pulses (i.e., for a linear ξ). At $\Delta t = 3$ ps, the first photocurrent pulse has almost vanished when the second laser pulse arrives, resulting in nearly independent photocurrent pulses (i.e., the blue and black areas are very similar). As Δt approaches zero, the contribution due to second pulse becomes smaller due to the sublinearity (i.e., the blue area is smaller the black area), which produces the photocurrent dip shown in **b**.

To account for these second-order effects, one needs to model the nonlinear photoresponse and photoresponse time in a self-consistent manner. A common approach [76] to this problem is to consider that the photocurrent is dependent on a time-dependent nonlinear parameter $\xi(P, \xi_0, t)$, where P is the laser pulse power and ξ_0 is its initial condition. This parameter represents, for instance, the electronic temperature T_e or the photocarrier (or exciton) density Δn. While this approach is far more thorough than the exponential decay analysis, it relies on the development of quantitative models to describe $\xi(P, \xi_0, t)$ and its relationship with PC. The former requires detailed insights into the dynamics of photocarriers governing ξ, while the latter implies a precise knowledge of the photocurrent generation mechanism at play.

In general, under instantaneous excitation (i.e., when the pulse duration is much shorter than the photocurrent dynamics), the total photocurrent at a given time delay Δt is obtained by integrating the piecewise, time-dependent photocurrent $\mathrm{PC}[\xi(P, \xi_0, t)]$:

$$\mathrm{PC}(\Delta t) = \int_0^{\Delta t} \mathrm{PC}\left[\xi\left(P, \xi_0, t\right)\right] \mathrm{d}t + \int_{\Delta t}^{\infty} \mathrm{PC}\left[\xi\left(P, \xi(\Delta t), t\right)\right] \mathrm{d}t. \tag{2.35}$$

Fig. 2.9c illustrates the outcome of this calculation for different values of Δt. The blue area corresponds to the time-integrated photocurrent for a sublinear $\xi(P)$, while the black area represents the photocurrent expected for independent pulses (i.e., a linear ξ). As Δt approaches zero, the second photocurrent pulse becomes smaller (i.e., the black area becomes larger than the blue one) due to the sublinear ξ, which creates a dip in the calculated PC(Δt) (Fig. 2.9b). Hence, by comparing the prediction of Eq. 2.35 with photocurrent autocorrelation measurements, one can extract the photoresponse time of the device and obtain information on the microscopic processes governing ξ. In Chapters 4 and 7, we apply this approach to analyse the photoresponse of graphene- and WSe_2-based photodetectors, respectively.

Most of the TRPC studies presented in this thesis are realized via photocurrent autocorrelation measurements, using the optical setup shown in Fig. 2.7. A mode-locked Ti:Sapphire laser (Thorlabs Octavius 85M) generates ultrashort (pulse duration < 8 fs) pulses with a large spectral bandwidth (> 200 nm, Fig. 2.10a), centered at 800 nm, and with a repetition rate of 85 MHz. The pulses broaden as they travel through various dispersive optical elements of the setup and have a duration of ~ 200 fs when they reach the sample (Fig. 2.10b). To obtain a pair of pulses, the laser beam is split into two arms and recombined using 50/50 beamsplitters. The time delay Δt between the two pulses is varied by changing the path length of one of the two arms, which is achieved by placing a motorized translation stage in one of the arms and controlling its position by computer.

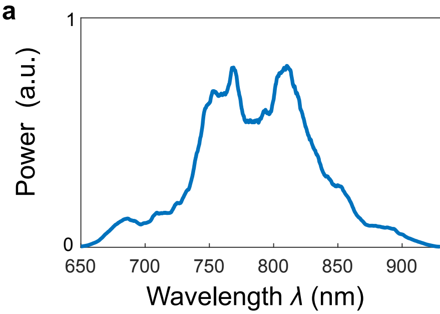

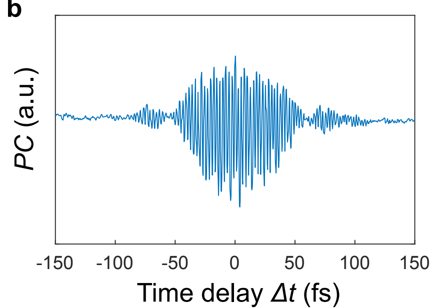

FIGURE 2.10: **Characterization of the ultrashort pulse laser source. a)** Power spectrum of the pulsed laser measured at the exit of the laser by a spectrometer. **b)** Characterization of the pulse duration by field autocorrelation: the photocurrent produced by two pulses with the same polarization is measured as a function of their time delay Δt.

Chapter 3

Fabrication and characterization of van der Waals heterostructures

In this chapter we describe the main processes involved in fabrication of high-quality, state-of-the-art devices based on 2D materials and their van der Waals heterostructures (vdWHs). We also present several techniques that we use to characterize the resulting devices, such as Raman and photoluminescence spectroscopy, atomic force microscopy, and electrical measurements.

3.1 Introduction

Progress in the field of solid states physics is often driven by improvement in material quality. Investigating clean samples gives access to the intrinsic properties of the material and can sometimes lead to the discovery of new physical phenomena. The fractional quantum Hall effect, which was first observed in extremely clean two-dimensional electron gas [272], is a good example.

Similarly, important advances in the field of graphene and other 2D materials have been achieved by developing new ways to produce high-quality samples. Following the demonstration of the first graphene transistor by Geim and Novoselov [273], many post-process cleaning methods have been proposed such as chemical [274] and mechanical cleaning [275], as well as thermal [276] and current-induced annealing [277]. However, it rapidly became obvious that the device quality was mainly limited by the dielectric environment surrounding the graphene sheet such as the substrate and encapsulating material. Indeed, it was established that the quality of graphene on SiO_2, the most common substrate at the time, was impaired by charged surface states, impurities, phonons and roughness in the SiO_2 [102]. Suspending the graphene above the substrate circumvents this issue [278], but this geometry restricts the device architecture.

Ultimately, hexagonal boron nitride (hBN, see Section 1.3) emerged as an ideal dielectric since it provides an atomically flat, dangling bond-free surface on which to deposit or encapsulate graphene and other 2D materials [23]. The superior quality of these devices was demonstrated by their extremely high mobility and the observation of exotic phenomena such as the fraction quantum Hall effect [279]. In addition to identifying hBN as an excellent substrate, the work of Dean *et al*. [23] initiated the development of deterministic stacking methods necessary to assemble 2D materials into van der Waals heterostructures (vdWHs, see Section 1.4). Soon after, several other stacking techniques were proposed and heterostructures more complex than graphene on hBN were assembled. A crucial step towards the fabrication of cleaner heterostructures was taken by Wang *et al.* [9] who introduced a method to make one-dimensional side contacts to graphene. With this edge-contact geometry, the heterostructure can be entirely assembled before the contact metallization step. Thus the active layers of the heterostructure can be fully encapsulated in clean hBN without being in contact with the polymer used in the layer assembly.

Today, most vdWHs are made by mechanical stacking of individual exfoliated flakes. This method offers flexibility in layer sequence and clean interfaces, but it is rather slow and tedious. For this reason, current research efforts now aim at developing techniques for the large-scale synthesis of vdWHs [178]. These methods typically involve the direct growth of heterostructures by CVD or vdW epitaxy, or the assembly of heterostructures from CVD-grown or liquid-phase-exfoliated 2D materials [27]. Since they are still in their infancy, mechanical assembly remains most suitable for exploring the science of vdWHs.

3.2 Device fabrication

Most of the devices investigated in this thesis are fabricated using a technique inspired by the one proposed by Wang *et al.* [9], which so far has yielded the best results in terms of cleanliness, ease and reproducibility. In this section, we describe the procedure we developed to fabricate and characterize clean, state-of-the-art vdWHs. Appendix A contains a detail description of the main processes.

Fig. 3.1 summarizes the main steps involved in the manufacture of the 2D material-based devices. The fabrication starts by exfoliating 2D crystals on a substrate. Layers of various materials are then mechanically stacked on top of another using a polymer-free assembly method to produce a vdWH. The resulting heterostructure is then electrically contacted via 1D contacts and can be subsequently shaped to fit the needs of the experiment. Finally, the device is wire-bonded to a chip carrier in order to be connected with the electronics of the experimental setup. The fabrication of devices made of a single 2D material, as those presented in Chapter 4, follows a very similar procedure except that the layer assembly step is omitted and the material is contacted by deposition of standard metal electrodes.

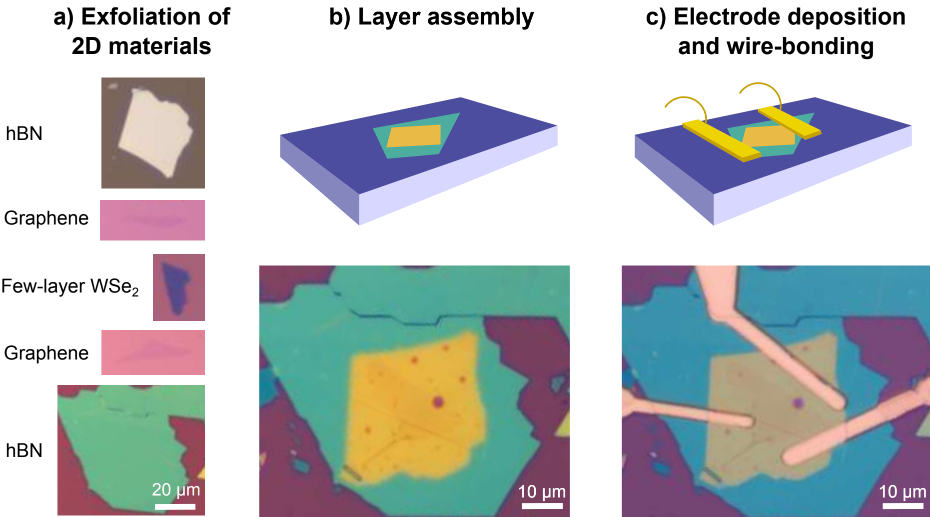

FIGURE 3.1: **Main steps involved in the fabrication of 2D material-based electronic devices. a)** Optical microscope images of various exfoliated flakes. The top hBN is exfolied on a transparent polymer, while the other layers are exfoliaded on SiO_2/Si. All images have the same scale bar shown in the lower image. **b)** Bottom: Optical image of an heterostructure made by assembling the flakes shown in **a** on top of one another, and Top: Sketch of the heterostruture (green/orange) on a SiO_2/Si (dark/light purple) substrate. **c)** Bottom: Same heterostructure as in **b** edge-contacted with gold electrodes. Top: Sketch representing the deposition of electrical contacts (yellow rectangles) on a heterostructure and the subsequent wire-bonding of the device (yellow lines).

3.2.1 Exfoliation and characterization of 2D materials

Since the first isolation of graphene [273] and other 2D crystals [6] by Geim and Novoselov using the famous Scotch-tape technique, many methods have been developed to produce 2D materials. These processes, which include most notably chemical vapor deposition (CVD) [280] and liquid-phase exfoliation [281], have shown great promise for large-scale production. Yet, mechanical exfoliation remains the only way to obtain the highest quality materials[1].

For these reasons, the devices presented in this thesis are mainly made of flakes obtained by mechanical exfoliation. The exfoliation procedure is similar for every material, only the starting bulk material varies. Graphene is obtained from highly ordered pyrolytic graphite (Graphenium flakes) from NGS Naturgraphit GmbH, bulk TMDs crystals are purchased from HQ Graphene, and hBN crystals are provided by Kenji Watanabe and Takashi Taniguchi from the National Institute for Materials Science (Tsukuba, Japan). Bulk flakes are exfoliated by placing them on the sticky surface of a tape, and folding and unfolding the tape until the tape is covered by small flakes with the desired thickness (approximately). Although exfoliation can be achieved with standard Scotch Tape, we prefer using tapes that leave less glue residue behind (e.g. R1011 from Ultron Systems or SPV 224PR from Nitto). Thin sheets of commercial PMDS sheet (Gel-Pak®, retention level 4) can also be used to get clean exfoliated flakes. Exfoliated flakes of various thicknesses are then randomly transferred by pressing the flake-covered tape on a chosen substrate. Flakes are typically deposited onto a highly doped Si wafer with a thermally grown oxide layer of 285 nm. At this thickness, interference effects increase the optical contrast of the flakes such that even monolayers of graphene and other 2D crystals can be detected with an optical microscope. The final and most critical step of this process is the removal of the tape from the substrate. In general, a good yield of monolayers can be achieved by slowly peeling the tape. However, we found that for graphene, larger flakes could be obtained by quickly removing the tape perpendicularly to the substrate. Hence, exfoliating appears to be less a science than an art.

The deposited flakes are then inspected visually using an optical microscope (ZEISS Axio Scope A1). Since the apparent color of thin flakes (1 to 3-4 layers) changes quite drastically with layer thickness, it is often possible to accurately determine their layer number [282, 283]. Alternatively, one can characterize flakes by Raman spectroscopy, atomic force microscope (AFM) or photoluminescence (PL) spectroscopy. Depending on the material and the characterization technique employed, various properties can be probed such as the layer number, cleanliness, charge doping, defect density, etc. Fig. 3.2 shows the characterization of the different layered materials using various techniques.

[1] Luckily, it is also the easiest one, as some high school students and teachers can attest (www.icfo.eu/newsroom/news/article/2258).

Raman spectroscopy is a particularly useful tool to probe the characteristics of graphene, such as its number of layer, intrinsic doping, and defect density [284]. This non-invasive technique relies on the inelastic (Raman) scattering of light, which is associated with optical phonons. The Raman spectrum of graphene typically has three main peaks located at $\sim$ 2700 cm^{-1} (2D peak), $\sim$ 1580 cm^{-1} (G peak) and $\sim$ 1350 cm^{-1} (D peak) [285]. The G peak corresponds to the optical phonon at the Γ point ($q = 0$). Information on the doping of graphene can be obtained from the position and width of the G peak. The D peak is activated by the presence of defects in the graphene lattice. Hence, a large ratio between the D and G peak implies a large defect density. The absence of D peak in the Raman spectrum of Fig. 3.2b therefore indicates that the graphene flakes contains very few defects. Finally, the 2D peak, which involves double phonon scattering, is particularly useful for determining the number of layers because its shape and intensity varies with the layer number (Fig. 3.2c). Indeed, for monolayer graphene, the 2D peak has a characteristic Lorentzian line-shape (with a full width at half maximum (FWHM) of $\sim$ 15 to 30 cm^{-1} [286]) and higher intensity compared to the G peak. The peak broadens (multiple components appear) and the 2D/G ratio decreases as the number of layer increases.

Photoluminescence spectroscopy is the technique of choice for identifying monolayer flakes of semiconducting TMDs. Indeed, due to confinement effects, these materials exhibit an indirect-to-direct band gap transition when exfoliated from bulk to monolayer [15, 114]. Since this crossover occurs at the monolayer limit, the photoluminescence (PL) efficiency of single layer flakes is much larger ($\sim$ 1 or 2 orders of magnitude) than that of bilayer and multilayer flakes. For the same reason, the position of the maximum PL peak shifts toward longer wavelength as the number of layer increases. Hence, by illuminating a flake with high energy photons (larger than the energy of the optical bandgap) and monitoring the intensity and position of the PL peak, one can easily determine the number of layers (Fig. 3.2e). A second peak at lower energy, attributed to trion emission [140, 141], can also be observed for doped monolayer flakes. The presence and position of this peak can therefore help to estimate the doping density of the flake.

AFM is a convenient tool for determining the cleanliness and thickness of exfoliated flakes. By measuring the topography of a flake with nanometer resolution, one can easily detect the presence of polymer residues introduced during the exfoliation and invisible under the optical microscope. Hence, to make the cleanest heterostructures, all flakes should be inspected with the AFM before being stacked. AFM is also the best technique to measure the thickness of flakes that have no distinct Raman or PL signature, such as hBN and multilayer graphene and TMD flakes. Fig. 3.2g shows a topographic AFM image of a thick hBN flake.

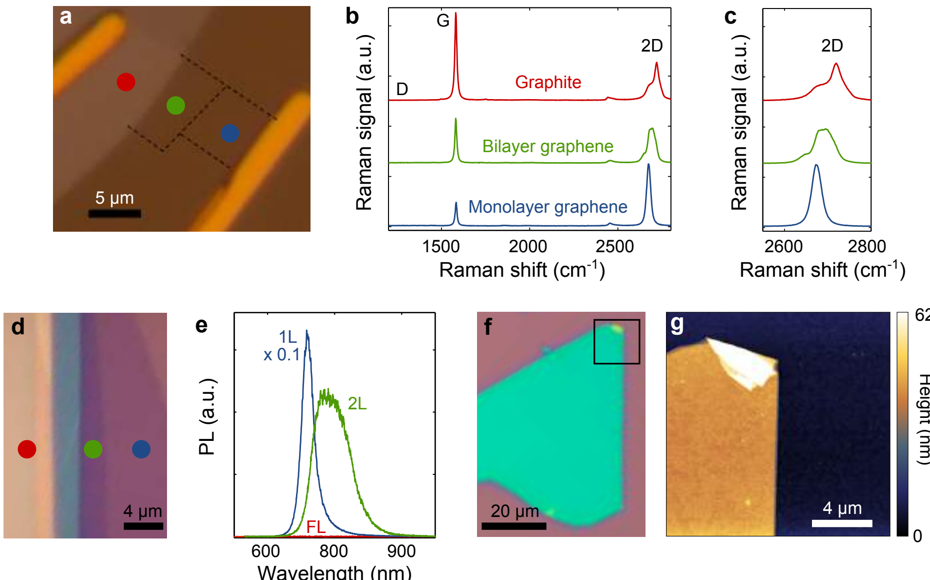

FIGURE 3.2: **Characterization of various exfoliated flakes. a)** Optical microscope image of a device containing an exfoliated flake with monolayer graphene(blue dot), bilayer graphene (green dot) and graphite (red dot) regions. The flake is on a transparent substrate (1 mm thick crystal of SiO_2) and connected by two electrodes. The dashed lines indicate the monolayer and bilayer graphene regions. **b)** Raman spectra measured at three different locations on the flake shown in **a** (coloured dots), indicating the presence of monolayer graphene (blue), bilayer graphene (green) and graphite (red). **c)** Zoom on the 2D peaks. **d)** Optical microscope image of a WSe_2 flake with monolayer (blue dot), bilayer (green dot) and multilayer (red dot) regions. **e)** PL spectra measured at three different locations on the flake shown in **d** (coloured dots), indicating the presence of monolayer (blue), bilayer (green) and multilayer (red) WSe_2. **f)** Optical microscope image of a multilayer hBN flake. The black square indicates the region where the AFM topographic map shown in **g** was measured.

3.2.2 Mechanical layer assembly technique

Once all flakes required for a given vdWH have been exfoliated and identified, the next step consists in stacking them on top of each other. The main concerns in this step are producing heterostructures with clean interfaces, undamaged and precisely aligned layers (both in terms of position and rotation). The early assembly method demonstrated by Dean *et al.* [23] is based on preparing a flake of 2D material on a sacrificial film, aligning and depositing it on another flake, and then removing the film. Additional flakes are stacked by repeating the process. This process was shown to give good results for two-layer heterostructures, but since the flakes are exposed to the sacrificial film and solvents, contamination often gets trapped under the additional flakes. An effective way to circumvent this problem, which was introduced by Wang *et al.* [9], takes advantage of the strong

vdW interaction between layered materials. When two flakes are brought into contact, they preferentially stick to each other rather than to the substrate. By lifting up the top flake, the second one is therefore likely to follow and be lifted up from the substrate. By repeating the process, multi-layer heterostructures with clean interfaces can be assembled.

More concretely, this method, also called the "pick-up technique", begins by making a transparent polymer stamp that serves as a substrate for the flakes and a handle during the assembly process. The stamp consists of a thin ($\sim 1\ \mu$m) layer of poly-propylene carbonate (PPC) placed onto a transparent elastomer (poly dimethyl siloxane, PDMS), which is put onto a microscope slide (Fig. 3.3a). The first, top flake can be either exfoliated directly on top of the PPC (using a PDMS sheet for exfoliation) or picked up from a substrate. To achieve the latter option, the microscope slide is attached to a $x-y-z$ micromanipulator with the polymer stamp facing down, while the substrate supporting the desired flake is secured on top of a stage with rotation and coarse $x-y$ adjustment. Importantly, the stage can also be heated up by a temperature-controlled heater. Our mechanical layer assembly setup is very similar to the one described by Castellano-Gomez *et al.* [287] and details can be found in Section A.1.

The flake and polymer stamp are aligned on top of each other with the help of a zoom lens camera, and brought into contact. The sample stage is then heated to about 35°C, a temperature close to the glass temperature of PPC. The stage is cooled back to room temperature and the polymer stamp is slowly lifted from the substrate. In most cases, the flake adheres preferentially to the stamps and is successfully picked-up. If not, the process is repeated until it succeed. Typically, the first flake is the most difficult one to pick-up. It can therefore be preferable to exfoliate the flake directly onto the PPC in order to avoid that problem.

Once the first flake is on the polymer stamp, the following flakes can be picked up using the same process. In this case, the pick-up success rate is much higher, above $\sim$ 90%. As the number of stacked layers increases on the stamp, the alignment of the flakes usually becomes the main challenge. Once the desired heterostructure is assembled, it is released onto a final substrate by depositing the stamp on the substrate and heating the stage to 90°C. At this temperature, the PPC softens and adheres to the substrate, which allows the PDMS and microscope slide to be removed. The PPC is finally removed in acetone and isopropanol, leaving the heterostructure on the substrate. Fig. 3.3 (and the video attached to the QR code on the right of Fig. 3.3) illustrates this assembly process for a hBN/Graphene/hBN heterostructure.

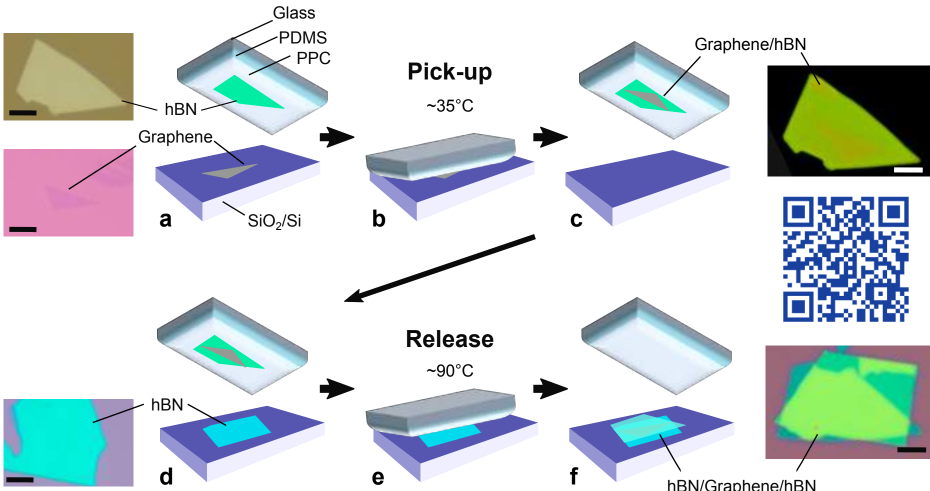

FIGURE 3.3: **Layer assembly process.** Figure **a** to **f** illustrates the main steps involved in the assembly of a hBN/Graphene/hBN heterostructure. **a)** A hBN flake is placed on a polymer stamp made of PPC/PDMS on a glass slide and aligned with a graphene layer exfoliated on a SiO_2/Si substrate. Left: optical microscope images of a hBN and graphene flake. **b)** The two flakes are brought into contact, the stage is heated to $\sim 35°$C and cooled back to room temperature. The stamp is then slowly lifted in order to pick up the graphene flake from the substrate. **c** The graphene flake is now located on the hBN flake. Right: Optical microscope image of the Graphene/hBN stack on the polymer stamp. **d)** A second hBN flake is exfoliated on a SiO_2/Si substrate and aligned with the Graphene/hBN stack on the stamp. Left: Optical image of the hBN flake. **e)** The Graphene/hBN stack is released on the hBN flake by pressing the stamp and heating the polymer to $\sim 90°$C. **f)** A hBN/Graphene/hBN stack is thus obtained. Right: Optical microscope image of the final stack. All scale bars are 10 μm. The Quick Response (QR) code on the right leads to a short video showing and explaining the assembly of vdWHs (https://youtu.be/0QVvna4Nyp0).

3.2.3 One-dimensional edge-contacts and wire-bonding

In order to avoid direct contact between the active layers of the heterostructure and the polymer stamp, flakes of hBN are commonly used as top and bottom encapsulation layers. While they protect the active layers from the dirty environment, the hBN flakes prevent one to make electrical contact to the inner layers. Wang *et al.* showed that this problem can be solved by metallizing the 1D edge of a monolayer graphene. The contact resistance of these edge contacts can be as low as 35 $\Omega \cdot \mu$m for graphene, but to date, edge contacting TMDs has yet not been successfully demonstrated [288]. Instead, the best strategy so far to contact encapsulated TMDs is to use graphene as an intermediate between the metal electrode and the TMD [180].

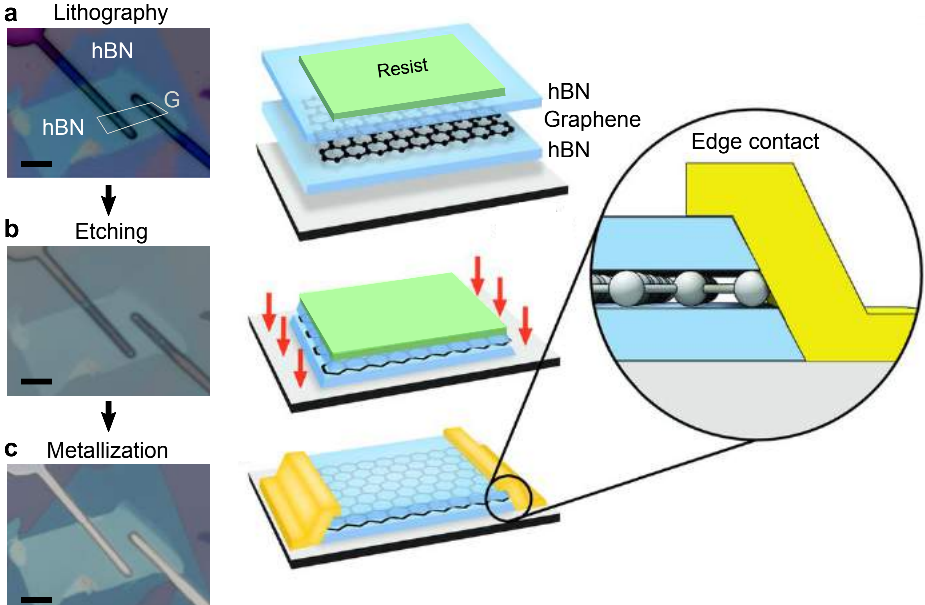

FIGURE 3.4: **One-dimensional edge-contact.** Left: Optical microscope images illustrating the fabrication of edge-contacts on a hBN/Graphene/hBN heterostructure. The graphene flake is outlined for clarity. Right: Schematics depicting the fabrication process of edge-contacts. **a)** First, the heterostructure is spin-coated with a thin resist film. Contacts are defined by patterning (via lithography) and developing the resist. **b)** The edge of the graphene are exposed by etching the resist-free area of the heterostructure using RIE. **c)** Electrodes are deposited by evaporating a thin metal film on the sample. All scale bars are 5 μm.

Following the recipe of Wang *et al.*, we developed a reliable process to make 1D edge-contacts to graphene (Fig. 3.4). First, the geometry of the contacts is defined by a lithographic process such as electron beam lithography, UV-mask lithography or laser writing. The later, performed with a Microtech LW405B system, is particularly useful for this task (see Section A.2). It allows the user to visualize the heterostructure and to draw the desired contacts in situ, making it a remarkably flexible and user-friendly tool. The laser writer can achieve feature sizes down to $\sim$ 1 μm, which is usually sufficient to contact flakes with typical dimensions of the order of 10 μm.

After photoresist development, the edge of the encapsulated graphene are exposed by etching the resist-free area of the heterostructure. This is performed in an Reactive Ion Etching (RIE) system (Oxford Instruments Plasmalab Symtem 100), using a gas mixture of O_2 and CHF_3 with flow rates of 4 standard cubic centimeters per minute (sccm) and 40 sccm, respectively. By setting the RF power to 60 W and the chamber pressure to 90 mTorr, we obtain an etch rate of 10-15 nm/min for hBN and 7-12 nm/min for SiO_2.

Once the top hBN layer is completely etched through, a thin metal layer is deposited over the entire substrate with an evaporator (Leybold Univex 350). The remaining photoresist is dissolved in acetone and the metal on top is lifted-off, leaving only the lithographically-defined metal electrodes behind. Typically, electrodes in our samples are made of 2 nm of titanium, deposited with electron beam evaporation, and 100 nm of gold, deposited with thermal evaporation. We note that other combinations of metal can give even better contacts.

Finally, the device is glued on a 28-pin chip carrier (Kyocera C-QFJ) using a drop of epoxy, silver paste or PMMA, and the electrodes of the heterostructure are connected to the chip carrier via wire-bonding (Fig. 3.5). A wire-bonder (West bond Luxury II) with aluminium wire is used for this purpose.

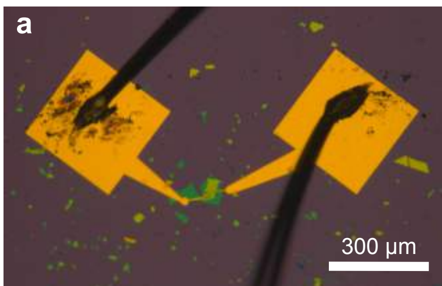

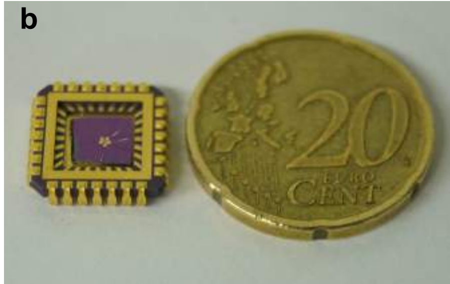

FIGURE 3.5: **Wire-bonding and chip carrier mounting. a)** Optical microscope image of a wire-bonded device. **b)** Photograph of a device mounted on a chip carrier.

3.3 Characterization of the heterostructure

After fabrication, the final device can be characterized by electrical measurements or using the same techniques employed for inspecting individual flakes, such as AFM, Raman and PL spectroscopy. Generally, AFM and electrical measurements are sufficient to ensure the quality and proper functioning of the device.

AFM provides information on the structural quality and the cleanliness of the stack by detecting the presence of dirt between the layers. Indeed, despite our best effort to select clean flakes, contamination can hardly be avoided. When stacked, dirt is trapped between flakes and aggregates in "bubbles", which are easily revealed by AFM (Fig. 3.6b). Interestingly, Kretinin *et al.* [289] showed that these bubbles are the result of a self-cleansing mechanism that is intrinsic to certain layered materials. When the affinity between two 2D materials is larger than their affinity with the contaminants, the materials tend to maximize their common interface. Contaminants are thereby pushed away and coalesce to forms bubbles. Although these pockets of contaminations can be detrimental to

the device operation, the area between them is presumably free of any contamination. Transmission electron microscopy (TEM) studies indeed showed that in bubble-free areas, interfaces between 2D materials are clean and atomically flat [27]. Recently, it was shown that the formation of contamination bubbles could be prevented by assembling layers at high temperature [290].

Electrical characterization is essential to ensure the good functioning of the device and to quantify the electronic properties of the electrically active material. Graphene-based devices are a prime example since many relevant physical parameters can be extracted by measuring its resistance R as a function of its charge carrier density. As we discussed in Section 1.1.1, the latter can be electrostatically controlled by applying a voltage V_{G} to a capacitive gate. The relation between the applied voltage and the gate-induced carrier density (n_{V}) is simply

$$n_{\mathrm{V}}(V_{\mathrm{G}}) = p - n = -\frac{C}{e_0}(V_{\mathrm{G}} - V_{\mathrm{D}}), \tag{3.1}$$

where p and n are respectively the hole and electron density, $C = \epsilon_0 \epsilon_{\mathrm{r}}/d$ is the capacitance, ϵ_0 is the vacuum permittivity, ϵ_{r} is the relative permittivity of the gate dielectric, d is the thickness of the dielectric, and V_{D} is the gate voltage corresponding to the charge neutrality (Dirac) point. At the Dirac point, the charge density should theoretically vanish, but in reality, impurities, disorder and thermal effects generate a residual charge density n_0, which affects the electrical behaviour to the Dirac point. In order to account for this residual charge density, the total carrier density can be written as follows [291, 292]:

$$n_{\mathrm{t}}(V_{\mathrm{G}}) = p + n = \sqrt{n_{\mathrm{V}}^2 + 4n_0^2} \tag{3.2}$$

Considering the contribution of both electron and holes (with mobility μ_n and μ_p, respectively) to the conductance σ of the graphene sheet, the total resistance of a two-terminal graphene device can be calculted as

$$R(V_{\mathrm{G}}) = \frac{L}{W}\frac{1}{\sigma} + 2R_{\mathrm{c}} = \frac{L}{W}\frac{1}{e_0\,(\mu_n n + \mu_p p)} + 2R_{\mathrm{c}}, \tag{3.3}$$

where R_{c} is the contact resistance of one of the two electrodes, and L and W are the length and width of the graphene flake, respectively.

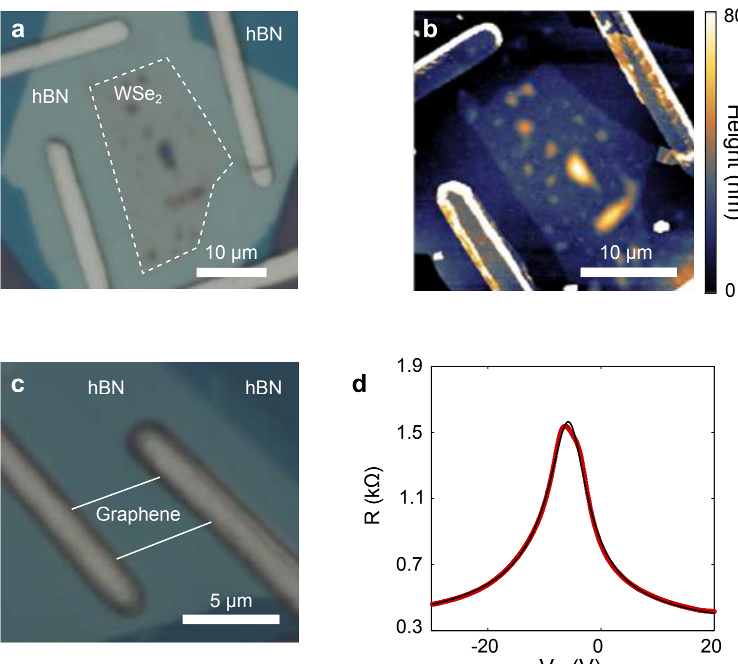

FIGURE 3.6: **Characterization of vdWHs by AFM and electrical measurements. a)** Optical microscope image and **(b)** AFM topographic map of a hBN/WSe_2/hBN heterostructure. "Bubbles" of aggregated dirt are clearly visible in the AFM image. **c)** Optical microscope image of a hBN/Graphene/hBN device and **(d)** its measured gate-dependant resistance (red dots). The solid black line is a fit to the data using the model presented in the main text. The WSe_2 and graphene flakes are outlined in **a** and **c**, respectively.

We apply, for instance, this model to characterize the hBN/G/hBN device shown in Fig. 3.6c. The heterostructure is deposited on a SiO_2/Si substrate where the heavily doped Si is used a back gate, and the SiO_2 layer and bottom hBN flakes, respectively 285 and 20 nm, act as gate dielectrics. The measured gate-dependant resistance of the device and the fit of Eq. 3.3 are presented in Fig 3.6d. From the fit, we extract a contact resistance R_c = 270 Ω (which corresponds to $\sim$ 1.3 kΩ $\cdot$ μm), a residual density $n_0 = 1 \times 10^{11}$ cm^{-2}, and an electron and hole mobility of 27 000 and 20 000 cm^2/Vs, respectively. These values compare well with those of the best devices reported so far. Indeed, state-of-the-art encapsulated graphene devices have mobilities ranging from 30 000 to 140 000 cm^2/Vs, with typical contact resistance on the order of 100 to 1000 Ω $\cdot$ μm [9]. Moreover, most of the residual density can be accounted for by the density of thermally generated carriers, which, for graphene at temperature T, is $n_{\text{th}} = \frac{\pi}{6}\left(\frac{k_B T}{\hbar v_F}\right)^2$. Hence, at room temperature, we find $n_{\text{th}} = 8.1 \times 10^{10}$ cm^{-2}, a value close to the extracted n_0. We note that for a more precise characterization of the electrical properties can be obtained by performing Hall measurements.

3.4 Conclusion

To summarise, the layer assembly method presented in this chapter is a reliable and efficient way to fabricate high-quality vdWH-based devices with chosen layer sequences and thicknesses. The remarkable electrical characteristics obtained for hBN-encapuslated graphene devices demonstrate the cleanliness of the interfaces, as well as the quality of the edge contacts. The fabrication can also be quite fast : complex heterostructures containing more than 5 flakes can be assembled within a day, and electrically contacted on the next day. The assembly method also allows for different layers to be rotationally aligned with quite high precision (within $\sim$ 1-2°). Control over the sequence, thickness and rotational alignment of layers are key ingredients for exploring and designing the properties of vdWHs.

Chapter 4

Hot-carrier photocurrent in lateral graphene junctions

Graphene is a promising material for ultrafast and broadband photodetection. In this chapter we present a study on the photocurrent generated at different interfaces in in-plane graphene devices. First we investigate the photovoltage generation time in graphene-based photo-thermoelectric devices and find it to be faster than 50 fs. The observation that carrier heating is ultrafast suggests that energy from absorbed photons can be efficiently transferred to carrier heat. To study this, we next examine the spectral response and find a constant spectral responsivity between 500 and 1500 nm, consistent with efficient electron heating. Finally, we examine the photocurrent at the graphene-metal interface and show that all experimental results can be explained within the general framework of photo-thermoelectric current generation.

This chapter is based on:

- Tielrooij, K. J.*, **Massicotte, M.***, Piatkowski, Woessner, A., Ma, Q., Jarillo-Herrero, P.,Van Hulst, N. F., and Koppens, F. H. L. *Hot-carrier photocurrent effects at graphene–metal interfaces*. J. Phys. Condens. Matter, 27, 16, 164207 (2015)
- Tielrooij, K. J., Piatkowski, L.*, **Massicotte, M.***, Woessner, A., Ma, Q., Lee, Y., Myhro, K. S.,Lau, C. N., Jarillo-Herrero, P., van Hulst, N. F. and Koppens, F. H. L. *Generation of Photovoltage in Graphene on a Femtosecond Timescale through Efficient Carrier Heating.* Nature Nanotech. 10, 5, 437–443 (2015)

* These authors contributed equally to this work

4.1 Introduction

Over the last decade, graphene has attracted much attention for photodetection because of its unique optical and electronic properties (see Chapter 1), making it a prime candidate for high-speed light detection [31, 46–48, 258–260]. In early studies, the photocurrent generation mechanism was ascribed to the photovoltaic effect [293–295], but it was later revealed that the photocurrent is in most cases driven by hot carriers through the photo-thermoelectric effect (PTE, see Section 2.4.2). This effect was established for photocurrent generated at the junction between monolayer-bilayer graphene [255] and at the interface between graphene regions with different Fermi energy E_F, such as a p-n junction [45, 255]. In such PTE graphene devices, the local electronic temperature gradient created by the absorbed light, in combination with the difference in Seebeck coefficients between the two graphene regions, gives rise to a photo-thermoelectric voltage $\Delta V = (S_2 - S_1)(T_e - T_0)$. Here S_1 and S_2 are the Seebeck coefficients of regions 1 and 2, respectively, T_e is the temperature of the hot carrier distribution, and T_0 the ambient temperature.

The performance of PTE graphene devices is intimately connected to the dynamics of the photoexcited electrons and holes, which have mainly been studied in graphene samples through ultrafast optical pump-probe measurements [71, 74, 75, 77, 78, 80, 89, 95]. As explained in Section 1.1.3, the dynamics start with *i)* photon absorption and electron-hole pair generation; followed by *ii)* electron heating through carrier-carrier scattering, in competition with optical phonon emission, which both take place on a $\lesssim$ 100 fs time scale; and finally *iii)* electron cooling by thermal equilibration with the lattice, which takes place on a picosecond time scale. The effect of the picosecond cooling step *iii)* on the switching speed of graphene devices has been studied using time-resolved photovoltage scanning experiments with $\sim$ 200 fs time resolution [76, 254, 268]. These studies showed that the picosecond electron cooling time limits the intrinsic photo-switching rate of these devices to a few hundred GHz, because faster switching would reduce the switching contrast, as the system does not have time to return its equilibrium. Indeed, GHz switching speeds have been demonstrated in graphene-based devices [46, 47, 258, 259, 296].

However, the most crucial aspects of the photo-thermoelectric response are captured by the heating dynamics, as electron heating leads to photovoltage generation. Additionally, these dynamics determine the ultimate intrinsic carrier heating efficiency and the resulting spectral response. In the first half of this chapter, we measure of the photovoltage generation time τ_{heat} with an unprecedented time resolution of $\sim$ 30 fs and find τ_{heat} to be on the order of 50 fs. We further assess the effect of this ultrafast heating time on the heating efficiency through spectral responsivity measurements. In an ideal photo-thermoelectric detector, all the absorbed photon energy is transferred rapidly to electron heat (before energy is lost through other channels). In this case, and as we indeed observe, doubling the photon energy leads to doubling of the photovoltage and

results in a flat spectral responsivity $\Re = \mathrm{PC}/P$, where PC is the generated photocurrent and P is the excitation power. In strong contrast, and has we discussed in Section 2.3, the spectral response of photovoltaic semiconductor detectors is not flat at all, since it is determined by the band gap: Photons with an energy below the band gap are not absorbed, i.e. $\Re = 0$, and the excess energy above the band gap typically does not lead to an additional photoresponse, i.e. a decreasing $\Re$ with photon energy [221].

In the last section of this chapter, we investigate in detail the photocurrent produced at the graphene-metal interface in order to address its generation mechanism. We show that using the PTE framework we can explain: the time-resolved photocurrent dynamics that we observe at the graphene-metal interface, the dependence of the photocurrent on the photon energy, the effect of the Fermi energy on the photocurrent, and finally the influence of the polarization of the incident light on the generated photocurrent. These results are useful for assessing the potential and limitations of device performance parameters, such as the photodetection speed, photoconversion efficiency, and spectral response, among others.

4.2 Devices

To study photocurrent generation in graphene, we use three different samples that contain - besides graphene–metal interfaces - other interfaces, where the photocurrent generation mechanism has been established to be dominated by the PTE effect. This enables us first to study in more depth the PTE response at these interfaces and second, to compare it to the response at the graphene-metal interface.

The first device is a *dual-gated device* (Fig. 4.1a) that consists of graphene on a substrate with a doped silicon backgate (separated from the graphene sheet by 300 nm of SiO_2) and a local metal top gate (separated by 10-20 nm of hexagonal boron nitride). Both gates can be used to change the Fermi energy of the exfoliated graphene flake. A scanning photocurrent image is shown in the lower part of Fig. 4.1a, where the top gate and bottom gate voltages are such that a p-n junction is formed at the edge of the top gate. Fig. 4.1b shows the photocurrent generated with the laser focused at this position, as a function of backgate and top-gate voltages. The multiple sign reversals indicate that the photovoltage is generated through the PTE effect [45, 84]. This device also contains two metal contacts and thus two graphene-metal interfaces. More details on the fabrication of this device can be found in Ref. [45].

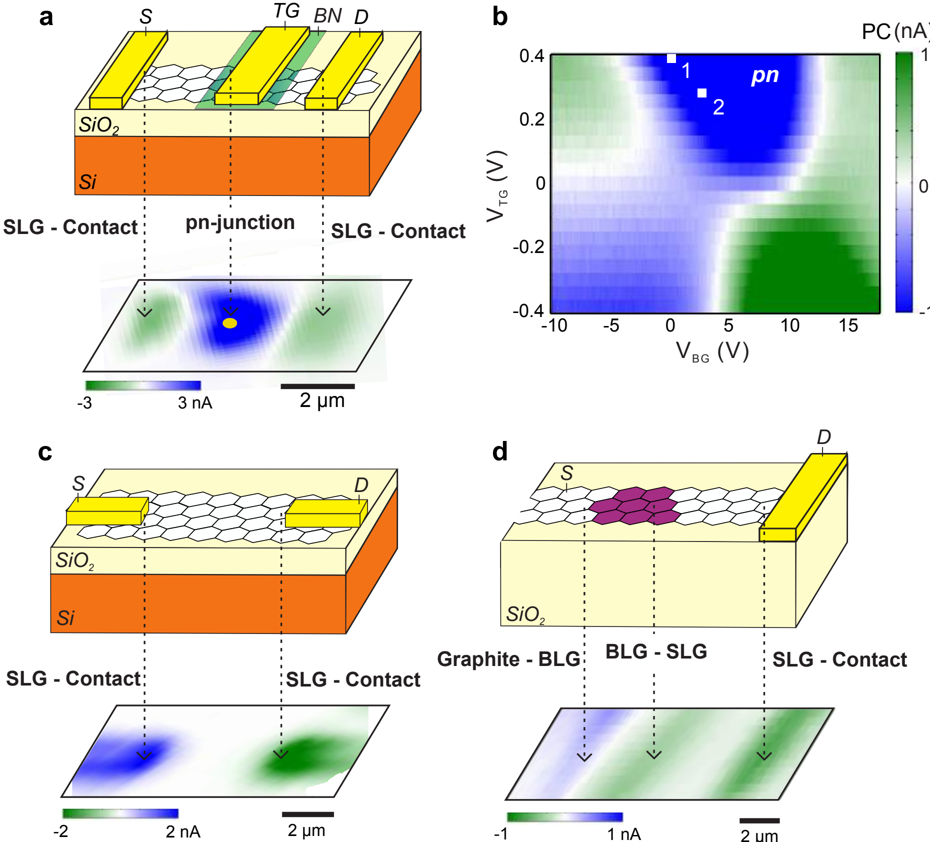

FIGURE 4.1: **Hot-electron photocurrent and devices.** **a)** Device layout and photocurrent scanning microscopy image of the *dual-gated device*, with a silicon backgate separated by 300 nm SiO_2, and a top gate (*TG*) separated by hexagonal BN. The graphene (atomic structure not to scale) is contacted by source (*S*) and drain (*D*) contacts, through which photocurrent is measured.**b)** The photocurrent as a function of gate voltages at the position of the yellow dot in panel **a**, showing clear multiple sign reversals that are indicative of PTE current generation [45, 84]. **c)** Device layout and photocurrent scanning microscopy image of the *globally gated device*, with a silicon backgate separated by 285 nm SiO_2 and graphene contacted by source (*S*) and drain (*D*) contacts. **d)** Device layout and photocurrent scanning microscopy image of the *transparent substrate device*, with a flake that contains adjacent regions of single layer graphene (SLG), bilayer graphene (BLG) and graphite.

Our second device is a *globally gated device* in the most common field-effect transistor geometry (see Fig. 4.1c). This device contains an exfoliated graphene flake, with two metal contacts. The backgate is formed by doped silicon, separated from the graphene sheet by 285 nm of SiO_2. Photocurrent is created when light is focused at the interface of graphene and the metal contacts.

Finally, the third device is a *transparent substrate device*. It consists of a graphene flake exfoliated onto a 1 mm-thick SiO_2 substrate (see Fig. 4.1d). In this case, the Fermi energy of the graphene is not tunable. However, the device offers three different interfaces to study photocurrent generation: a graphene-metal interface, an interface of single layer graphene (SLG) and bilayer graphene (BLG) and an interface between bilayer graphene and multilayer graphene. In the case of the SLG-BLG interface, the photocurrent mechanism has been established to be PTE [255].

4.3 Photovoltage generation on a femtosecond timescale

In order to capture the time scale of photovoltage generation, we perform time-resolved photocurrent measurements (also called photocurrent autocorrelation measurements) with the highest time resolution to date of $\sim$ 30 fs. We achieve this by using a setup similar [1] to the one presented in Section 2.5.3, except that it contains a pulse shaper that corrects for any dispersion (and thus pulse stretching) that the pulses pick up on their way from the laser to the device [297].

As we explain in detail in Section 2.5.3, this technique relies on the nonlinear photoresponse of the device under investigation and consists in recording the photocurrent, averaged over a large number of pulse pairs, as a function of delay Δt between two ultrashort laser pulses. In graphene devices, the nonlinearity originates from the sublinear relation between the amount of heat transferred to the electronic bath and the rise in electron temperature ΔT_{e} under pulsed excitation. Indeed, as we show in Section 1.1.3, the temperature dependence of the electronic heat capacity C_{e} leads to a square root dependence of the initial electron temperature $T_{\mathrm{e},0}$ on the laser power P, which is reflected in the measured photocurrent (Fig. 4.2a).

We apply our femtosecond photovoltage sensing technique to the *dual-gated device*. We show the photocurrent generated in this device as a function of Δt in Fig. 4.2b, which clearly shows a dip around $\Delta t = 0$. In Figs.4.2c,d, we show the normalized photocurrent dip $\Delta\mathrm{PC}$ for two combinations of gate voltages, both in the p-n regime. The decays on both sides of $\Delta t = 0$ reflect the cooling dynamics with a picosecond time scale, as observed in Refs. [76, 254, 268]. Around $\Delta t = 0$ we notice that the photocurrent dip $\Delta\mathrm{PC}$ is remarkably sharp, which is only possible when the time resolution of the complete system (i.e., the

[1] We use a broadband Ti:Sapphire laser (Octavius 85M, Menlo Systems) tuned to a central wavelength of $\sim$ 800 nm with a bandwidth of $\sim$ 120 nm combined with a liquid crystal based spatial light modulator (SLM) pulse shaper arranged in a 4f-configuration. After propagating through the shaper, the laser beam is spectrally split using a dichroic filter (Semrock, 830 nm Edge Basic) into two parts: the pump ($<$ 800 nm) and the probe ($>$ 800 nm), each with a bandwidth of $\sim$ 55 nm. Due to this spectral separation, the two pulses do not show any coherent artefact when they overlap in time.

laser pulses and the graphene photoresponse) is sufficiently high. Any decrease of time resolution, either because of longer pulses or due to a slower generation of the photovoltage in graphene, would lead to a broadening of the apex of the inverted v-shape.

To quantitatively determine the time scale of photovoltage creation, we develop a model for the photocurrent as a function of Δt, based on heating dynamics induced by the pulse-pair excitation and including nonlinear heating. As discussed in the introduction (step *ii*), we assumed that the energy contained E in the photoexcited carriers is either converted into electronic heat at a rate $1/\tau_{\mathrm{heat}}$, or lost via optical phonon emission or other loss mechanisms at a rate $1/\tau_{\mathrm{loso}}$. Hence the carrier heating dynamics is governed by

$$\frac{\mathrm{d}E}{\mathrm{d}t} = P_{\mathrm{in}} - \frac{E}{\tau_{\mathrm{heat}}} - \frac{E}{\tau_{\mathrm{loss}}}, \tag{4.1}$$

where P_{in} is the optical power density absorbed by graphene converted into photoexcited carriers. From this equation, we define the heating efficiency as $\eta_{\mathrm{heat}} = \tau_{\mathrm{loss}}/(\tau_{\mathrm{loss}} + \tau_{\mathrm{heat}})$, which represents ratio between the energy converted into electronic heat and the total absorbed energy.

To describe the dynamics of the electronic bath temperature T_{e} (step *iii* in the introduction), we use a model similar to the one presented in Section 2.4.2:

$$C_{\mathrm{e}}\frac{\mathrm{d}T_{\mathrm{e}}}{\mathrm{d}t} = \frac{E}{\tau_{\mathrm{heat}}} - \Gamma\Delta T_{\mathrm{e}}, \tag{4.2}$$

where Γ represents the thermal conductance (due to phonon emission) and C_{e} is the temperature-dependent electron heat capacity of graphene. We further assume that the electron cooling time $\tau_{\mathrm{cool}} = C_{\mathrm{e}}/\Gamma$ is a constant, which, along with τ_{heat}, we use as a fitting parameters to model our time-resolved photocurrent measurements. We note that the value of τ_{loss} does not influence the photocurrent dynamics, but only its efficiency η_{heat}, which we address in the next section.

Photocurrent is calculated (up to a constant) by integrating $\Delta T_{\mathrm{e}}(t)$, assuming instantaneous excitation. We note that for $\tau_{\mathrm{heat}} \ll \tau_{\mathrm{cool}}$ the numerical solution of the initial electron temperature $T_{\mathrm{e},0}$ corresponds well with the analytical solution found for instantaneous heating shown in Eq. 1.9 (Fig. 4.2a). In Fig. 4.2b(c), we show the time-resolved measurements for the first (second) gate voltage combination, together with the modelled photocurrent change $\Delta\mathrm{PC}(\Delta t)$. We find excellent agreement between data and model for $\tau_{\mathrm{heat}} = 50$ (80) fs and a cooling time of $\tau_{\mathrm{cool}} = 1.3$ (1.5) ps. As an illustration we show the model for $\tau_{\mathrm{heat}} = 250$ fs, which is clearly in strong disagreement with the data. We thus conclude that for the p-n junction configuration, photovoltage generation occurs within 50 fs.

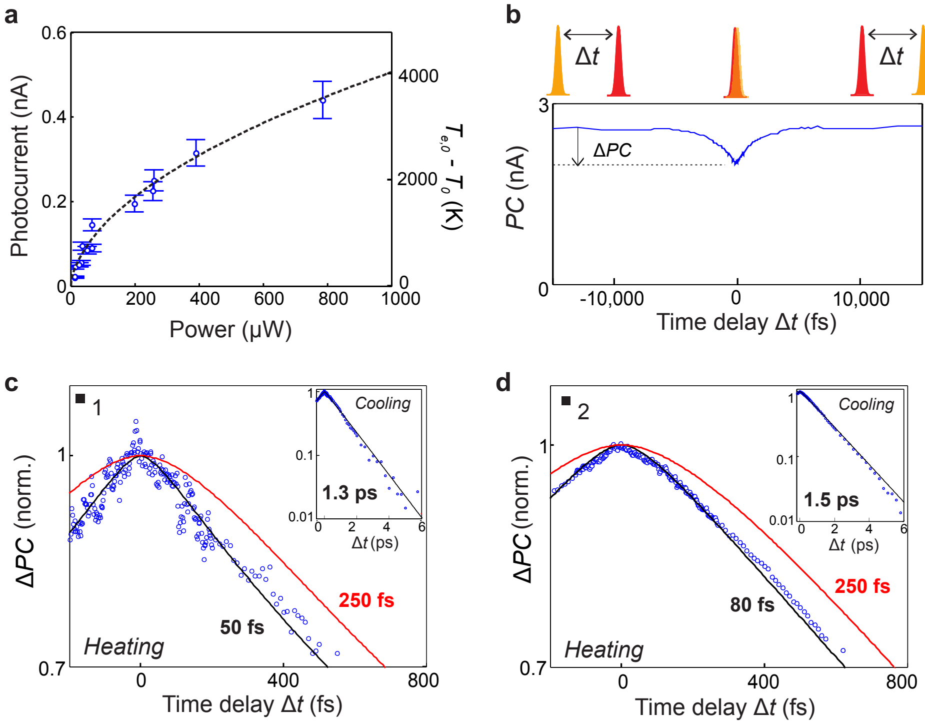

FIGURE 4.2: **Femtosecond sensing of hot electrons. a)** Photocurrent PC (left vertical axis) as a function of power, showing the nonlinear dependence. The solid black line is a fit obtained from the model, assuming $E_F = 0.3$ eV, $\eta_{\text{heat}} = 1$ and 1% absorption. The initial electron temperature increase $T_{e,0} - T_0$ predicted by this model is indicted on the right vertical axis. **b)** The photocurrent as a function of delay time Δt shows a dip ΔPC when the two pulses overlap and recovers with dynamics that correpond to the hot electron dynamics. We show the dynamics of the (normalized) time-resolved photocurrent dip ΔPC around $\Delta t = 0$ (blue circles) for gate configurations 1 **(c)** and 2 **(d)**, both in the p-n junction regime (squares in Fig. 4.1b). The solid black lines describe the model results, using a heating time of 50 (80) fs and a cooling time of 1.3 (1.5) ps for gate configuration 1 (2). The red lines show the modelled dip with a slower heating time scale of 250 fs, which is incompatible with the data. The insets show the data and model results over a larger time range.

4.4 Efficient photo-induced carrier heating

Having established that carrier heating and PTE photovoltage generation occur on a femtosecond time scale, we now address how this step affects the energy conversion efficiency η_{heat} of graphene PTE devices. The main question is if the carrier heating is fast enough to out-compete energy loss processes ($\tau_{\text{heat}} \ll \tau_{\text{loss}}$), such as optical phonon emission (Fig. 1.3b). To this end, we study the photoresponse for a wide range of photon energies, from 0.8 (1500 nm) to 2.5

eV (500 nm). We use a laser source (quasi-CW, since the pulse duration of 100 ps is larger than the cooling time of $\sim$ 1 ps) with a controllable wavelength and a constant excitation power P (see Section 2.5.2).

To avoid the strongly wavelength-dependent absorption [70], we use the *transparent substrate device* and measure the PTE photocurrent at the monolayer-bilayer graphene interface [255]. Fig. 4.3a shows the responsivity $\Re$ spectrum of this device, together with the measured graphene absorption on a similar device. These data are obtained from spatially resolved measurements, which show that the spatial extent of the photoresponse does not change with wavelength. The spectral response (for constant excitation power) of the device is strikingly constant over this broad range of excitation wavelengths. The flat $\Re$ shows that decreasing the number of incident photons (by increasing the photon energy) does not lead to a decrease in photovoltage: thus a higher photon energy gives a larger photovoltage. This is in stark contrast with photovoltaic detectors based on semiconductors , where the photovoltage generally decreases for increasing photon energy, meaning that excess energy is lost [221]. The flat $\Re$ at the monolayer-bilayer interface is therefore consistent with photo-thermoelectric current generation.

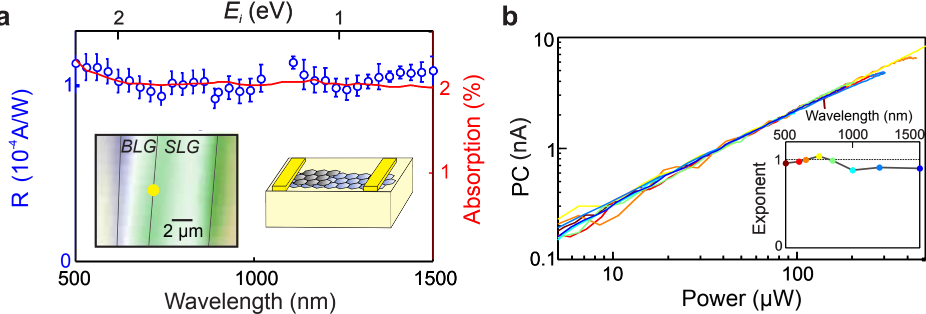

FIGURE 4.3: **Spectral dependence of the PTE response. a)** Responsivity as a function of excitation wavelength (blue data points, left axis) and measured absorption spectrum (red line, right axis) for the *transparent substrate device* at the monolayer-bilayer graphene interface (P $\sim$ 50 μW). Error bars are calculated from independent measurement scans and represent the 68% confidence interval. The left inset shows a scanning photovoltage image with photovoltage generation at the monolayer-bilayer (SLG-BLG) interface. The right inset shows the device layout, with a 1 mm thick SiO_2 substrate. The agreement between the responsivity and absorption curve shows that a lower number of absorbed photons (shorter wavelength, higher photon energy) does not lead to a lower responsivity, consistent with PTE current generation [84]. **b)** Power dependence of the photovoltage with the laser focused at the SLG-BLG interface (yellow dot in the inset of **b**) for a range of wavelengths (see inset for the wavelength corresponding to each color), showing linear scaling, which corresponds to the *weak heating* regime, where $\Delta T_e < T_0$. The inset shows the fitted power exponent as a function of wavelength.

To understand the flat, broadband $\Re$ for constant absorbed power, we examine what this result means for the electron heating $\Delta T_e = T_e - T_0$ as a function

of photon energy. First we note that the photovoltage scales linearly with power for all wavelengths (see Fig. 4.3b), which means that we are in the *weak heating* regime where $\Delta T_\mathrm{e} < T_0$ and the electronic heat capacity is constant (in contrast to the *strong heating* regime in the ultrafast experiment, where the scaling is sublinear). The reason for the small heating is that we use more than 10 times lower power and quasi-CW laser excitation with $\sim$ 100 ps laser pulses, which is longer than the cooling time of $\sim$ 1 ps (leading to a peak power that is 3 orders of magnitude smaller than for ultrafast excitation). In this *weak heating* regime, the cooling rate is constant [76], which means that the conversion efficiency is not affected by the lifetime of the hot electrons. Furthermore, the Seebeck coefficients S_1 and S_2 do not change with excitation wavelength. Therefore, from the flat $\Re$ we conclude that the light-induced increase in electron temperature ΔT_e at constant power is the same for all photon energies.

This result enables us to assess the efficiency of the electron heating (in the *weak heating* regime). We examine two alternative ultrafast energy relaxation pathways for photo-excited electrons and holes: carrier-carrier scattering and optical phonon emission (see Fig. 4.4a). Graphene optical phonons have an energy of $\sim$ 0.2 eV and therefore photoexcited carriers above 0.2 eV can in principle relax by emitting a phonon. The faster process of these two competing processes will dominate the ultrafast energy relaxation. We have determined the time scale of carrier-carrier scattering (through the photovoltage generation in the *dual-gated device*) to be $<$50 fs. The time scale of phonon emission is typically $<$150 fs [71, 80], and therefore this does not give a definite answer about which ultrafast relaxation process dominates. However, from the measured spectral responsivity we can extract the heating efficiency.

We illustrate this by considering two contrasting cases (Fig. 4.4a): *(i)* dominant coupling of photo-excited electrons to optical phonons, with a small fraction of the absorbed photon energy converted into hot electrons and *(ii)* dominant carrier-carrier scattering [85, 93] with a large fraction of the energy converted into hot electrons. In case *(i)*, the energy loss rate $\mathrm{d}E/\mathrm{d}t$ through optical phonon emission increases linearly with initial electron energy E_i, since it is governed by a constant electron-phonon coupling, and an energy-momentum scattering phase space that increases linearly with energy [89]. Thus in case *(i)*, a larger E_i leads to more energy loss to phonons. On the other hand, in case *(ii)*, the electron temperature scales linearly with E_i, because the energy of the photoexcited electron is fully transferred to the electron gas. Thus, the role of optical phonon emission can be measured by studying the scaling of ΔT_e with E_i.

This relationship, extracted from the photovoltage measurements, is shown in Fig. 4.4b, where we plot the internal quantum efficiency (IQE), which represents the generated photocurrent normalized by the number of absorbed photons. We find (nearly perfect) linear scaling of the IQE with E_i, as the linear fits go nearly trough the origin. This means that a higher photon energy corresponds to a larger photovoltage and thus to a larger ΔT_e, which is consistent with terahertz photoconductivity measurements [77, 85, 89], where a terahertz probe

provided a measurement of the carrier temperature. We therefore conclude that the generated photovoltage comes from ultrafast, efficient photon-to-electron-heat conversion and an unmeasurably small loss to optical phonons.

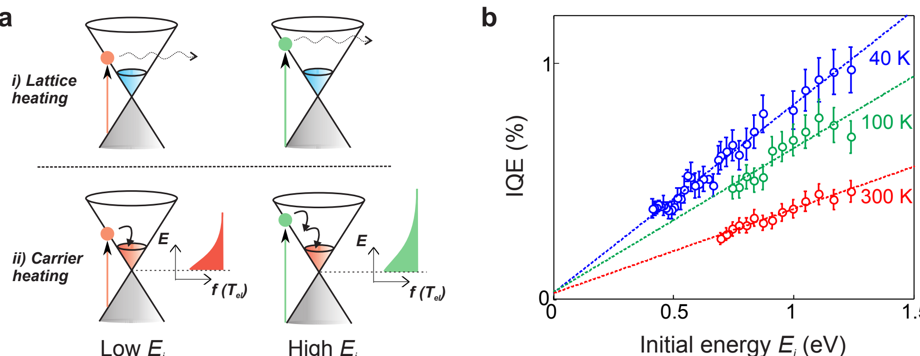

FIGURE 4.4: **Electron heating efficiency in graphene. a)** Schematic representation of ultrafast energy relaxation after photoexcitation, through phonon emission, which leads to lattice heating (top), and through carrier-carrier scattering, which leads to carrier heating (bottom). In the case of lattice heating, a larger photon energy leads to a larger phase space to scatter to and therefore more energy is transferred to the phonon bath, predicting sub-linear scaling of the IQE with photon energy. In the case of carrier heating, a larger photon energy leads to a hotter electron distribution (see the smeared Fermi-Dirac distributions next to the Dirac cones), predicting linear scaling of the IQE with photon energy (in the *weak heating* regime). **b)** The internal quantum efficiency (IQE) as a function of initial electron energy after photoexcitation for ambient temperatures $T_0 = 40$, 100 and 300 K. Error bars are calculated from independent measurement scans and represent the 68% confidence interval. The linear scaling through the origin shows that heating dominates the ultrafast energy relaxation and therefore that electron heating is efficient.

Finally, we also demonstrate that the efficiency of electron heating is independent of lattice temperature, as we obtain the same linear scaling through the origin for a lattice temperature of 40, 100 and 300 K. We note that the overall photovoltage is larger for lower lattice temperatures. This is caused by the longer cooling time τ_{cool} at low temperatures, due to a lower coupling between electrons and acoustic phonons [76, 84, 298]. The Seebeck coefficient decreases with temperature, meaning that the overall generated photovoltage is about a factor two larger [76].

4.5 Photo-thermoelectric effect at graphene-metal interfaces

In this section we extend our investigation of the photocurrent generated in graphene to the case of graphene-metal interfaces. While the PTE effect has

been shown to be the dominant photocurrent generation mechanism at p-n junctions and monolayer-bilayer graphene interfaces, the origin of the photocurrent at the graphene-metal interfaces remain elusive and a subject of debate. In the following section, we examine the dependence of the photocurrent on many important experimental parameters (time, photon energy, Fermi energy, incident light polarization) and show that the photo-thermoelectric effect can account for all experimental results.

4.5.1 Time-resolved photocurrent

To establish a better understanding of the mechanism and dynamics of the photoresponse near contacts, we compare the photovoltage dynamics for the two regions (at the contact and at the p-n junction). We apply ultrafast time-resolved photocurrent scanning microscopy measurements to our *dual-gated device* and compare the dynamics at the p-n junction with the dynamics at the graphene-metal interface. Figure 4.5a shows the results for the PTE photocurrent that is generated at the p-n junction, together with a numerical fit of Δt-dependent photocurrent (see Section 4.3). The dynamics correspond to a photocurrent generation time $<$ 200 fs (our time resolution in this experiment) and a relaxation time of 1.4 ps.

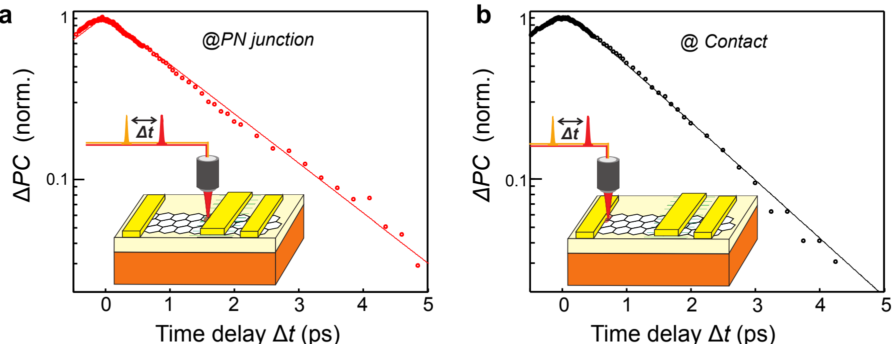

FIGURE 4.5: **Hot-electron dynamics at p-n junction and graphene-metal contact. a)** Experimental results (dots) of time-resolved photocurrent microscopy measurements at the p-n junction of the *dual-gated device*, where a pulse pair with the pulses separated by a time Δt, create a dip in the photocurrent. The photon wavelength is 800 nm. The photocurrent dip as a function of delay time represents the electron temperature dynamics. The line describes the numerically calculated photocurrent dip, based on electron heating with a time scale $<$ 200 fs and an exponential cooling time of 1.4 ps. The inset shows the device and measurement configuration. **b)** The experimental results (dots) of the same measurement as in **a**, now with the laser pulse-pair focused at the graphene-contact interface. The line describes the numerically calculated photocurrent dip, based on electron heating with a time scale $<$ 200 fs and an exponential cooling time of 1.2 ps.

The time-resolved photocurrent measurements on the same device, under the same conditions, but with the laser focused at the graphene-metal interface is shown in Fig. 4.5b. These dynamics, with a photocurrent generation time below 200 fs and a relaxation time of 1.2 ps, are strikingly similar to the dynamics at the p-n junction. For the p-n junction, it is well established that the photocurrent is generated through the PTE effect [45, 76, 84]. Therefore the observation of a similar photocurrent dip and similar dynamics at the graphene-metal interface suggest that the same intrinsic nonlinearity due to electron heating and the same hot electron dynamics give rise to the observed time-resolved signal at the graphene-metal interface. Thus for both the p-n junction and the graphene-metal interface the temporal dynamics are in agreement with PTE photocurrent generation, corresponding to femtosecond carrier heating [71, 75, 85, 89], and relaxation corresponding to picosecond supercollision cooling [76, 83, 236, 298].

4.5.2 Spectrally-resolved photocurrent

As we explained in Section 4.4, the spectral response of PTE-based photodetectors is an important device characteristic since it provides information on the carrier heating efficiency. Here, we compare the spectral response at the p-n junction (Fig. 4.6a) with the one at the graphene-metal interface (Fig. 4.6b). The inset in Fig. 4.6c schematically shows the spectrally-resolved measurement technique. The photoresponse at the p-n junction is wavelength-dependent in a non-monotonous fashion. The reason for this response is that the graphene absorption $A_{\mathrm{abs}}(\lambda)$ depends on wavelength λ due to reflections at the SiO_2/Si interface [89] - an effect that is very similar to the one that makes graphene visible when using a similar substrate [70]. Indeed, the photocurrent has a very similar wavelength dependence as the absorption that was calculated using numerical software (Lumerical FDTD Solutions software), taking into account the multi-layer substrate. The responsivitity is thus wavelength-dependent, as a result of the substrate that is used.

In Section 4.4 we demonstrated that the intrinsic responsivity (without substrate effects) of PTE-based graphene devices is spectrally flat [89]. Considering that the PTE photocurrent generated at the p-n junction is spectrally modulated by substrate effects, we can divide out these effects by taking the ratio between the photocurrent generated at the contact and the one measured at the p-n junction. This ratio, shown in Fig. 4.6c, therefore reflects the intrinsic wavelength dependence of the photocurrent generated at the contact. We find that the response is almost flat above $\sim$ 600 nm and increases below 600 nm.

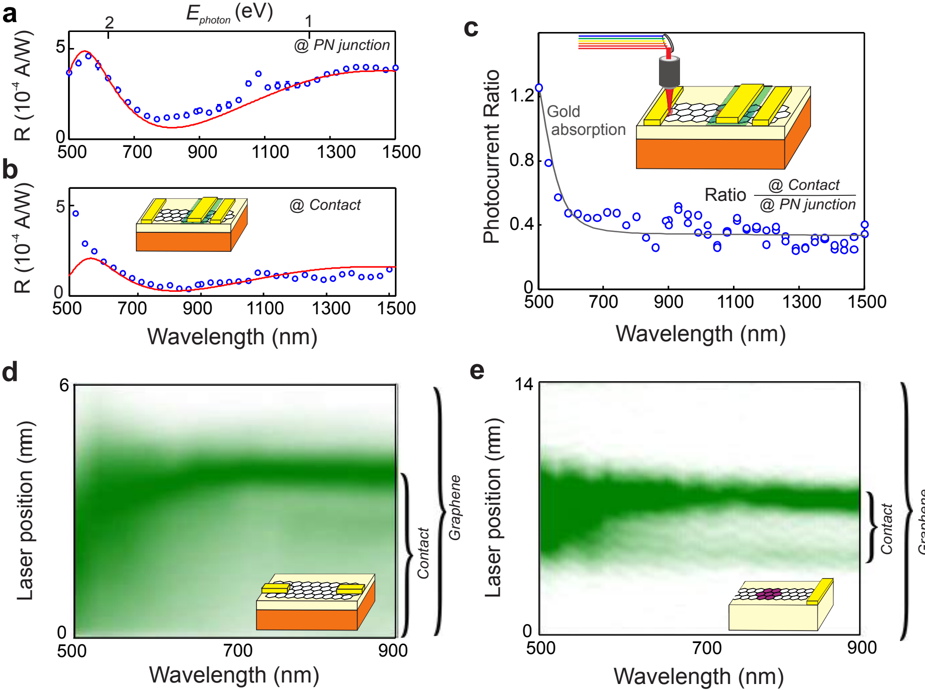

FIGURE 4.6: **Effect of photon energy on photocurrent.** Responsivity with the laser focused at the p-n junction **(a)** and the graphene-metal interface **(b)** of the *dual-gated device*, as a function of wavelength, together with numerical simulations of the wavelength-dependent absorption of the multilayer structure with reflections at the SiO_2/Si interface and a SiO_2 layer thickness of 300 nm (red line). **c)** Ratio of the photocurrent with the laser focused at the graphene-contact interface divided by the photocurrent with the laser focused at the p-n junction for the *dual-gated device*. This ratio reflects the photocurrent that is generated at the graphene-metal interface, compared to the p-n junction. The laser excitation has a power of $\sim$ 20 μW. Above 600 nm, the ratio is almost flat, indicating that the spectral response at the contact is very similar to the spectral response at the p-n junction, where it is dominated by the PTE effect [45, 89]. Below 600 nm, the ratio increases, which suggests that the photocurrent at the graphene-metal interface is a sum of two photocurrent generation mechanisms: PTE photocurrent that gives a flat spectral response [89] and thermoelectric photocurrent due to gold heating, which is proportional to the gold absorption (grey line). The inset shows the measurement configuration, where the laser excites the device with a variable photon wavelength. **d)** Spatially-resolved photocurrent as a function of wavelength for the *globally gated device*. **e)** Spatially-resolved photocurrent as a function of wavelength for the *transparent substrate device*.

The flat response above 600 nm indicates that for this wavelength range, PTE effect is the dominant photocurrent generation mechanism at the graphene-metal interface. As discussed in section, this flat response implies that a high energy photon leads to a proportionally higher electron temperature than a low energy photon. From a microscopic standpoint, this effect is explained by the fact that a

higher energy photon lead to a proportionally larger number of intraband carrier-carrier scattering events, which in turn lead to a higher electron temperature and thus a larger photovoltage [85, 89, 236] (Fig. 4.4a). We previously argued that a flat spectral response denotes a highly efficient carrier heating process, and that this efficiency is due to the ultrafast timescale associated with carrier-carrier scattering, which dominates over alternative energy relaxation pathways, such as acoustic and optical phonon emission [77]. Hence, from the wavelength-independent PC ratio shown in Fig. 4.4c we conclude that the energy transfer from absorbed photons to hot electrons is also efficient at the graphene-metal contact.

Below $\sim$ 600 nm, we observe that the photocurrent ratio increases quite strongly. Interestingly, this increase corresponds well with the wavelength-dependent absorption of the gold contacts, calculated using the complex refractive index of gold from Ref. [299]. This correspondence was also observed in Ref. [300] and can be understood by taking into account the contact-heating-induced thermoelectric effect: absorbed light and subsequent heat dissipation in a gold contact lead to local heating of the graphene sheet, generating a photocurrent. An analogous effect was observed recently by resonantly exciting SiO_2 substrate phonons with mid-infrared light, which also leads to photocurrent enhancement [301, 302]. Thus, the photocurrent at the graphene–metal interface is a combination of the PTE effect due to light absorption in graphene and in the metal contact, where the former dominates above 600 nm.

In the regime where photocurrent is dominated by light absorption in the contact, we note that photocurrent is not only generated at the graphene-metal interface. Rather, the photocurrent extends spatially into the contacts, as shown in Figs. 4.6d. Indeed, this occurs mainly for wavelengths that correspond to significant gold absorption. In the case of direct absorption in graphene (for excitation wavelengths above 600 nm) the spatial extent of the photocurrent corresponds to longest of the following lengths: the cooling length, which is determined by a trade-off between hot carrier cooling and carrier mobility [84, 298], and the laser spot size. In our case, the cooling length of $\sim$ 100 nm is smaller than the laser spot size of $\sim 1\ \mu$m . In the case of indirect heating by gold absorption (for excitation wavelengths below 600 nm), the extent of the photocurrent is determined by heat diffusion and cooling in the gold-graphene-substrate structure. These processes lead to a significantly larger spatial extent of the photocurrent.

4.5.3 Gate-tunable photoresponse

Due to the E_{F}-dependent Seebeck coefficient, the PTE photocurrent response is strongly gate-tunable [303], which is an interesting feature for optoelectronic devices that would require an electrically controllable photoresponse. We now examine the gate-response at the p-n junction of the *dual-gated device* and at

the metal-graphene interface of the *globally gated device* and evaluate the results within the framework of PTE photovoltage creation. In Fig. 4.7a we show that the *dual-gated device* at the p-n junction shows two sign changes as a function of backgate voltage. It has been shown that PTE photocurrent in such a device should indeed result in two sign changes: one when the two chemical potentials are equal and another one when the graphene whose carrier density is determined by the backgate, is tuned close to the Dirac point [45, 76, 84].

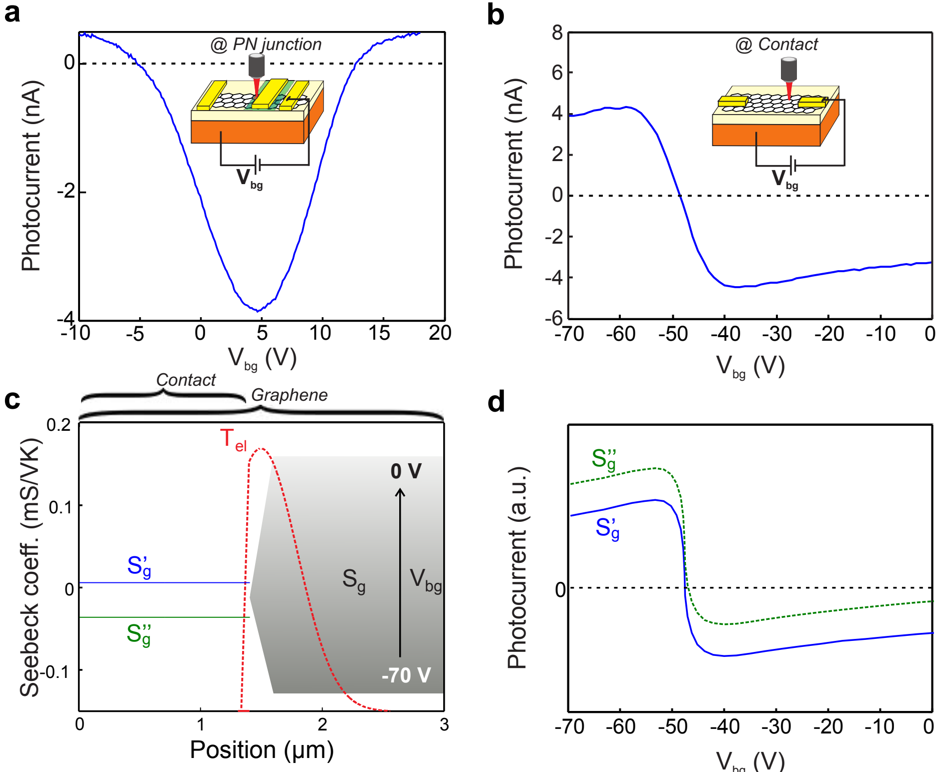

FIGURE 4.7: **Effect of Fermi energy on photocurrent.** **a)** Photocurrent as a function of backgate voltage V_{bg} for the *dual-gated device*. The multiple sign crossings and asymmetric gate effect clearly indicate PTE photocurrent generation [45, 84, 303]. The inset shows the measurement and device configuration, where the laser is fixed at 630 nm and the graphene carrier density is controlled by changing the backgate voltage, while the top gate is fixed at 0.4 V. **b)** Photocurrent as a function of V_{bg} for the *globally gated device*. The response is symmetric with one sign reversal at the Dirac point. **c)** Details of the numerical simulation of the PTE photocurrent as a function of V_{bg}. There are three regions with different Seebeck coefficients: the graphene underneath the gold contact with S'_{g} or S''_{g}, a transition region, and the graphene sheet with the gate-dependent S_{g}. The red dashed line represents the extent of the laser pulse and thus the region where the hot electrons are generated. **d)** Simulation results for the gate-dependent PTE photocurrent using the Seebeck coefficient profile and hot electron profile as in **c**, for the two distinct Seebeck coefficients for the graphene underneath the metal contact.

The photocurrent for the *globally gated device* as a function of backgate voltage (for 630 nm excitation) shows a symmetric signal with a single sign change around the Dirac point (Fig. 4.7b), similar to what has been reported earlier [293]. While the double sign change is a clear signature of the PTE effect, we now argue that PTE can also give rise to a symmetrical gate response near the contacts. In the most simple approach, the photovoltage is given by $V_{\mathrm{PTE}} = (S_2 - S_1)(T_{\mathrm{el,hot}} - T_{\mathrm{el,0}})$. If S_2 represents the Seebeck coefficient of the graphene underneath the metal contact and there would be very little metal-induced doping, the photocurrent would only depend on the gate dependence of S_1. This then leads to a symmetric gate response as in Fig. 4.7b, assuming that photoexcitation is similar in both graphene regions outside and underneath the metal contact.

In a more realistic approach, where we take into account the high reflectivity of the metal contact, we numerically simulate the PTE photocurrent response at the graphene-metal interface using a spatial profile of the Seebeck coefficient $S(x)$ and a spatial profile of the electron temperature $T_{\mathrm{e}}(x)$. This will generate a local photovoltage $V_{\mathrm{PTE}} = \int S(x)\nabla T_{\mathrm{e}}(x)dx$. For the Seebeck coefficient profile we use three regions: the first region corresponds to graphene underneath the gold contact, with a Fermi energy that is pinned at $S'_{\mathrm{g}} = 5$ μV/K or at $S''_{\mathrm{g}} = -30$ μV/K; the next region is a transition region between graphene that is pinned by the contact and the gate-tunable graphene sheet; and finally we have the gate-tunable graphene region with $S_{\mathrm{g}}(V_{\mathrm{bg}})$. For the spatial profile of the hot electrons we take into account the Gaussian beam profile of the laser focus and the strong reflection of incident light at the gold contact. We note that the width of the Seebeck regions, their numerical values, and the shape of the hot electron profile do not influence the qualitative shape of the gate-dependent PTE photocurrent. However, it is essential to include the transition region between pinned graphene underneath the metal and gate-tunable graphene.

Using $S(x)$ and $T_{\mathrm{e}}(x)$ we find the gate-dependent photocurrent traces in Fig. 4.7d. This reproduces the symmetric dependence with a sign change close to the Dirac point, for the case of low metal-induced doping (S'_{g}). By changing the metal-induced doping of the graphene underneath the contact to S''_{g} (see Figs. 4.7c,d), we can also create a less symmetric gate response, with a sign change that occurs at a higher or lower voltage than the voltage that corresponds to the Dirac point, as observed for instance in Refs. [293, 304]. Whereas this model reproduces the experimentally observed trends, it merely serves as an example to demonstrate that the observations can be explained by PTE-generated photocurrent at the graphene-metal contact.

4.5.4 Polarization-controlled photoresponse

We complete our study of the PTE photocurrent generated at graphene-metal interfaces by investigating its dependence on the polarization of the incident

light, an experimental variable which is known to influence the dynamics of photoexcited charges. It has indeed been predicted [305] and shown experimentally [306] that linearly polarized light generates a very short-lived (~ 150 fs) anisotropic carrier distribution in momentum space. We now investigate the effect of this anisotropy on the photoresponse. In Fig. 4.8a we compare the polarization dependence of the photocurrent generated at the three different interfaces of the *transparent substrate device*. The light polarization appears to have no effect on the photocurrent at the SLG-BLG and BLG-graphite interfaces, from which we conclude that the initial anisotropic carrier distribution directly after photon absorption does not affect the photocurrent magnitude. The reason for this is that the PTE photocurrent response depends on the temperature of the carrier distribution, rather than on its momentum distribution. Furthermore, the PTE photocurrent is generated during the time interval that carriers are hot, which is 1-2 picoseconds (see Section 4.5.1) and thus much longer than the lifetime of the anisotropic carrier distribution. Therefore, light polarization does not have an effect on the intrinsic PTE response.

In contrast, the photocurrent at the graphene-metal interface for 630 nm excitation displays a strong dependence on polarization, with a maximum (minimum) photocurrent when the polarization is perpendicular (parallel) to the metal contact edge. We observe this effect at the graphene-metal interface of every one of the ~ 10 devices that we have measured. This effect is reduced for excitation with 1500 nm light, compared to 630 nm excitation. Fig. 4.8b shows a polarization-resolved photocurrent map of the metal-graphene interface (of the *globally gated device*) which is obtained by measuring the photocurrent as a function of polarization at many different positions (630 nm excitation). This vector map clearly reveals that the photocurrent is enhanced when light polarization is perpendicular to the contact edge. A similar effect was observed in Ref. [300], whereas Ref. [307] reports the opposite effect, i.e., a maximum photocurrent for polarization parallel to the metal contact edge.

The observation of a polarization-dependent photocurrent at the graphene-metal interface, together with the absence of polarization effect at the SLG-BLG interface, suggests that an extrinsic factor affects the photoresponse at the graphene-metal interface. The extrinsic factor we consider is the effect of the metal contacts on the electrical field intensity and thereby the light absorption in the graphene sheet. We perform simulations using a 2D Maxwell equations solver (Lumerical FDTD Solutions software) for 630 nm and 1500 nm excitation, and find that for perpendicular polarization (with respect to the metal contact edge) the electric field is enhanced and confined at the graphene-metal interface (Fig. 4.8d). This is a phenomenon known in photonics as the lightning-rod effect. Due to this photonic effect, the energy absorbed by graphene close to a metal edge varies with polarization $A_{\text{abs}}(\angle)$, reaching a maximum when the polarization is perpendicular to the contact edge $A_{\text{abs}}(\perp)$.

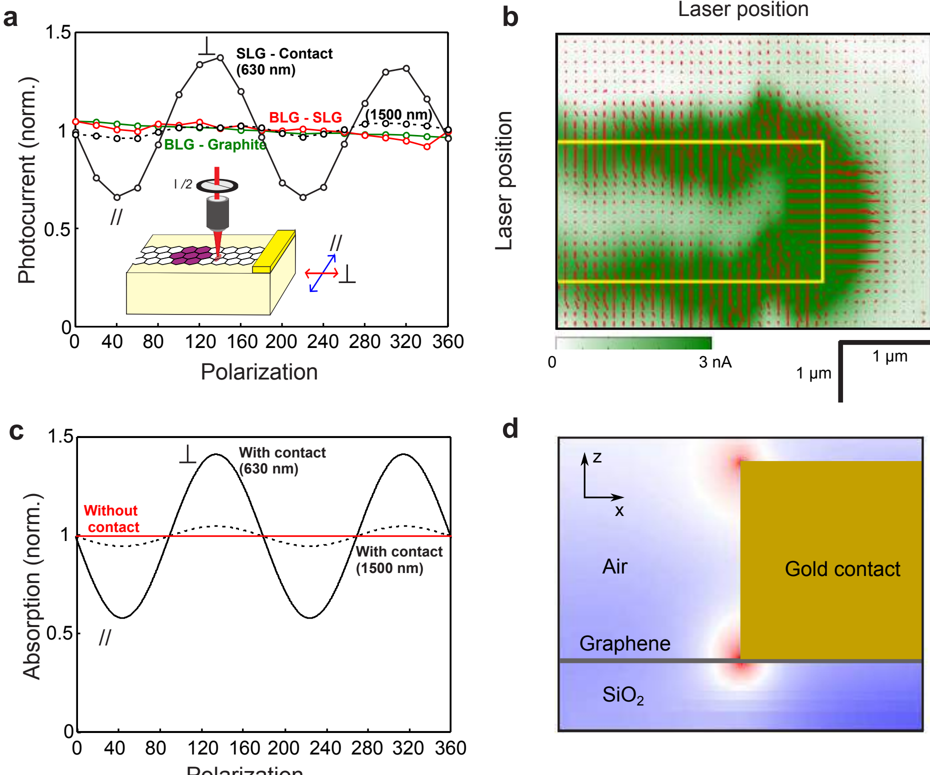

FIGURE 4.8: **Effect of light polarization on photocurrent. a)** Photocurrent as a function of polarization for the *transparent substrate device*. When light is focused at the BLG-SLG interface (red line) and the BLG-graphite interface (green line), there is no polarization dependence, whereas there is a strong polarization dependence for 630 nm excitation at the contact-graphene interface (black solid line) with increased (decreased) signal for light perpendicular (parallel) to the metal contact edge. Excitation with 1500 nm (black dashed line) leads to a lower contrast. The inset shows the device and measurement configuration, where a half wave plate is used to change the polarization of the incident light. **b)** Photocurrent scanning microscopy image (green color scale) for the *globally gated device*. The yellow line indicates the position of the metal contact. The red lines indicate the direction of maximum photocurrent, while their length indicates the magnitude of the photocurrent. The photocurrent is enhanced when the light is polarized perpendicular to the metal contact edge. **c)** Results of numerical simulations (using Lumerical FDTD Solutions software), showing the polarization-dependent graphene absorption without metal contact (red line) and with metal contact for 630 nm excitation (black solid line) and 1500 nm excitation (black dashed line). The inset shows a side view of the field confinement that leads to the absorption enhancement for polarization perpendicular to the metal contact edge. **d)** Side view of the field confinement that leads to the absorption enhancement for polarization perpendicular to the metal contact edge.

In Fig. 4.8c we show the normalized light absorption in the graphene sheet with and without the presence of a gold contact (for 630 and 1500 nm light).

We observe no polarization contrast when there is no gold contact, whereas the presence of a contact leads to polarization contrast, which is stronger for 630 nm excitation than for 1500 nm excitation. Thus, we observe very similar behavior for the light absorption in graphene (Fig. 4.8c) and for the photocurrent at the graphene-metal contact (Fig. 4.8a) as a function of polarization. These similarities arise, because the PTE photocurrent depends on the power absorbed in graphene, which is subsequently converted into electron heat. A polarization-dependent graphene absorption $A_{\mathrm{abs}}(\angle)$ will therefore give rise to a corresponding dependence of the PTE photocurrent.

4.6 Conclusion and outlook

In summary, the results presented in this chapter demonstrate that graphene PTE devices exhibit ultrafast, efficient and broadband photoresponse. The extremely short photovoltage generation time ($<$ 50 fs) indicates that photoexcited carriers rapidly thermalize with, and thereby heat up, the electron bath. From the flat spectral responsivity measured over a broad wavelength range, we infer that the carrier heating is fast enough to outcompete energy loss processes (e.g. optical phonon emission) and that it is therefore a very efficient process. Finally, we find that the photocurrent produced at the graphene-metal interface exhibits similar carrier dynamics and spectral response as in PTE devices. Moreover, the gate and polarization dependence can be understood within the framework of the PTE effect.

The high efficiency of the carrier heating process is very encouraging for PTE photodetectors. It implies that a large fraction of the absorbed photon energy is converted into hot carriers, which drive the PTE photocurrent. However, the efficiency of the PTE effect is mainly limited by the subsequent cooling of the hot carrier distribution, which typically leads to IQE of $\sim$ 1 to 20%. Although the cooling mechanism is still a topic of debate, it is clear that a longer cooling time (or equivalently, a smaller electronic thermal conductance) results in a higher (time-averaged) hot carrier temperature, and therefore a higher photodetection responsivity and efficiency. It was for instance shown that high responsivity ($\sim$ 10 mA/W, which translate into an IQE of $\sim$ 40%) can be obtained in suspended graphene samples, where the electronic cooling channel provided by substrate phonons is eliminated [73]. Future work should therefore aim at investigating substrates where phonons couple weakly to hot carriers in graphene, such as nonpolar materials (e.g. Si) or other layered materials (e.g. TMDs).

On the other hand, increasing the hot carrier cooling time reduces intrinsic photo-switching rate and thus the bandwidth of the photodetector. One way to improve the PTE efficiency without affecting the response time is to increase the Seebeck factor ($S_2 - S_1$). This can be done by using cleaner devices where the width of the charge neutrality region is smaller. Gabor *et al.* [45], for instance, reported responsivity of up to 8 mA/W at low temperature (IQE $\sim$ 6%) owing,

in part, to the quality of their hBN-covered device. For this reason, clean hBN-encapsulated graphene appears to be a promising device architecture. However, recent a recent study revealed that hyperbolic phonons in hBN provide an efficient cooling channel for hot electrons in graphene, and therefore limit the photodetection efficiency [88]. Nonetheless, vdW heterostructures provide a way to engineer the optical and thermal properties of graphene, and thereby improve its photodetection performance. Indeed, Wu *et al.* [308] showed that Moiré minibands in hBN-encapsulated graphene can greatly enhance the thermoelectric coefficient of the device, leading to the collection of multiple hot carriers per absorbed photons (IQE above 100%). This impressive result is a consequence of the efficient carrier heating observed in Section 4.4 and in THz measurements [89]. However, we note that multiple hot-carrier collection has only been demonstrated at low temperature and under small magnetic field.

Finally, another interesting approach to improve the collection efficiency of hot carrier is to explore photocurrent generation mechanisms other than the PTE effect. The bolometric effect, for instance, has been investigate but the weak temperature dependence of the conductance in graphene limits the performance of this type of photodetector [263]. Both the PTE and bolometer effects allow for in-plane collection of hot carriers in graphene. In the next chapter, we demonstrate and study a new photocurrent generation mechanism, the photothermionic effect, where hot carriers in graphene are vertically extracted.

Chapter 5

Interlayer photocurrent in graphene-based heterostructures

Van der Waals heterostructures provide new opportunities for photodetection and light harvesting. In this chapter we report on the photon-induced interlayer transport of carriers in graphene-based heterostructures. We show that in G/WSe_2/G devices, photocurrent is generated through the photo-thermionic effect: the absorbed photon energy in graphene is efficiently transferred to the electron bath, leading to a thermalized hot carrier distribution. Carriers with energy higher than the Schottky barrier between graphene and WSe_2 can be emitted over the barrier, thus creating photocurrent. We further demonstrate that this process is at work in G/hBN/G devices, and that it competes with photon-assisted tunneling of photoexcited carriers. Studying the competition between these two mechanisms provides a way to estimate the thermalization time of photoexcited carriers in graphene and demonstrate the possibility to control the energy transport in these heterostructures.

This chapter is based on:

- Ma, Q.*, Andersen, T.*, Nair, N.*, Gabor, N., **Massicotte, M.**, Lui, C. H., Young, A., Fang, W., Watanabe, K., Taniguchi, T., Kong, J., Gedik, N., Koppens F. H. L. and Jarillo-Herrero, P. *Ultrafast electron thermalization pathways in a van der Waals heterostructure.* Nature Phys. 12, 455-459 (2015)
- **Massicotte, M.**, Schmidt, P., Vialla, Watanabe, K., Taniguchi, T., Tielrooij, K. J. and Koppens, F. H. L. *Photo-thermionic effect in vertical graphene heterostructures*. Nat. Commun. 7, 12174 (2016)

* These authors contributed equally to this work

As we demonstrated in the Chapter 4, broadband absorption, efficient carrier heating and ultrafast carrier dynamics make graphene a very appealing material for next-generation optoelectronics. Over the last decade, much effort has been devoted to understand and improve devices based on intralayer photocurrent in lateral graphene photodetectors. In this device geometry, photocurrent is typically produced at 1D interfaces (graphene p-n junctions or graphene-metal interface) which severely restricts the size of the photoactive area and, consequently, the photon harvesting efficiency

Recent advances in the development of van der Waals heterostructures (vdWHs, Section 1.4) have opened up new possible ways of exploiting the unique properties of graphene for photodetection. Rather than collecting photocarriers laterally within the same graphene layer (*intra*layer), these novel vertical heterostructures enable the out-of-plane (*inter*layer) extraction of photocarriers. Hence, compared to lateral devices, the vdWH geometry provides a large active area, which maximizes the collection of photocarriers. However, while this photodetection scheme has been proposed by several theoretical studies [309–312], it has not yet been experimentally demonstrated and, in general, the interlayer transport of photocarriers in graphene-based heterostructures remain largely unexplored.

In this chapter, we investigate the photon-induced interlayer transport processes in photoexcited G/X/G heterostructures, where G denotes graphene and X represents a semiconducting (WSe_2) or insulating (hBN) layer of various thickness. As discussed in Section 1.4.2, this layer provides a potential energy barrier that governs the transport of carriers (photoexcited or not) from one graphene layer to the other. In the first section of this chapter, we report on the near-infrared photoresponse of G/WSe_2/G heterostructures. Due to strong electron-electron interactions in graphene, photoexcited carriers redistribute their energy among other carriers leading to the build-up of a hot thermalized distribution. This enables a significant fraction of hot carriers to be thermionically emitted over the energy barrier at the graphene/WSe_2 planar interface, thus generating a photocurrent. We study this photo-thermionic effect over a wide range of optical (wavelength, power, time delay) and electrical (bias voltage, gate voltage) parameters, and obtain good quantitative agreement with a model based on the theory presented in Section 1.4.2. From these results, we identify clear strategies for optimizing the efficiency of the PTI effect. This opens up a promising avenue for optoelectronic applications that require sub-bandgap photodetection, size-scalable active area, electrical tunability, broadband and ultrafast response.

In the second section of this chapter, we extend our study of interlayer transport processes to G/hBN/G heterostructures. In collaboration with the group of Pablo Jarillo-Herrero at MIT, we show that despite the large potential energy barrier between graphene and hBN, the photo-thermionic also takes place, albeit weakly, in those heterostructures. Most remarkably, by tuning the interlayer potential and the photon energy, we observe a new photocurrent generation mechanism whereby photoexcited carriers tunnel through the hBN layer

before they thermalize with the electronic bath. By examining the competition between this photon-assisted tunnelling process and the photo-thermionic effect, we demonstrate the possibility to control the interlayer charge and energy transport mechanism in graphene-based heterostructures. Moreover, our analysis of these transport processes reveals that the *intra*layer thermalization time of photoexcited carriers in graphene is on ther order of 10 fs, which is consistent with the results presented in Chapter 4.

5.1 Photo-thermionic effect in G/WSe_2/G heterostructures

5.1.1 Introduction

Since the discovery of the photoelectric effect in the late 19th century [244], a great number of photodetectors that rely on the emission of photoexcited charge carriers have been proposed. These carriers – sometimes referred to as hot carriers although they are not thermalized with the electron bath – are typically injected over a Schottky barrier between a metal and a semiconductor, allowing detection of photons with energy lower than the semiconductor bandgap (see Fig. 5.1a). This process, called internal photoemission (see Section 2.3.4), has led to the development of visible and near-infrared photodetectors [246, 313], which have recently been combined with plasmonic enhancement schemes [250, 314–317]. However, the efficiency of this mechanism drops for photon energy lower than the Schottky barrier height Φ_B [247] and is limited by the ability to extract the carriers before they lose their initial energy, which in metals typically occurs on a timescale of approximately 100 fs [318].

A promising way to overcome these limitations is to make use of the excess thermal energy contained in the electron bath. This energy arises from the thermalization of photoexcited carriers with other carriers, which results in a hot carrier distribution with a well-defined temperature T_e. For increasing T_e, a larger fraction of carriers can overcome the Schottky barrier, creating a current via thermionic emission (Fig. 5.1b). In this scheme, even photons with energies below Φ_B can lead to an increase in T_e and subsequently to carrier emission. However, in order to reach high T_e, the hot carriers must be weakly coupled to the surrounding phonon bath [319].

Graphene, which has recently emerged as an excellent platform for converting photons into hot carriers [320], has the ideal properties to implement this scheme. As we demonstrated in Chapter 4, graphene presents strong electron-electron interactions leading to carrier thermalization within less than 50 fs [71, 95, 321], where a large fraction (larger than 50%) of the initial energy of photoexcited carriers is transferred to the electronic system [89]. This efficient carrier heating creates a thermalized hot carrier state that is relatively long-lived

(longer than 1 ps) [76], owing to weak coupling to the lattice and the environment. These thermalized carriers can thus reach temperatures significantly higher than the phonon bath temperature ($T_e > T_{ph}$) even under continuous-wave (CW) excitation [45] (see Section B.1). Moreover, the tunability of the graphene Fermi energy gives control over the height of the Schottky barrier. For these reasons, graphene was recently proposed as a promising material for efficient and tunable thermionic emission of hot carriers [309, 311, 312].

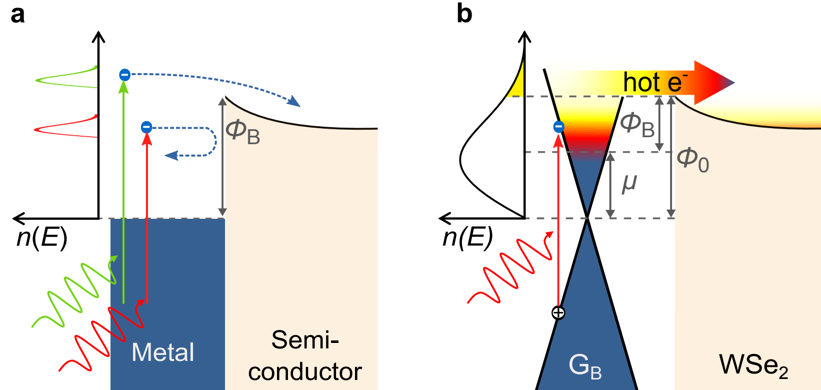

FIGURE 5.1: **Internal photoemission vs photo-thermionic emission a)** Simplified band diagram illustrating the internal photoemission process taking place at a metal-semiconductor interface. Non-thermalized photoexcited carriers in metal with sufficient energy to overcome the Schottky barrier Φ_B can be injected into the semiconductor before they lose their initial energy (within 100 fs for conventional metals [318]). The portion of the energy band filled by electrons and the bandgap of the semiconductor are shaded in blue and pale orange, respectively. Low (high) energy photon and the electronic transition following their absorption are represented by red (green) sinusoidal and vertical arrows. The out-of-equilibrium electron distributions $n(E)$ resulting from these processes are illustrated on the left hand side with the corresponding colours. Photoexcited electrons are depicted by blue dots and their possible transfer path is represented by blue dashed arrows. **b)** Simplified band diagram of the PTI effect at a G/WSe_2 interface. The ultrafast thermalization of photoexcited carriers in graphene gives rise to a hot-electron distribution $n(E)$ with a lifetime longer than 1 ps. As the number of electrons in the hot tail (yellow shaded area) of $n(E)$ increases, more electrons are emitted over the Schottky barrier Φ_B, which generates a larger thermionic current (represented by the horizontal arrow). The colour gradient from blue to yellow illustrates the heat contained in the electron distribution. The offset between the graphene neutrality point and WSe_2 conduction edge is denoted by Φ_0 and was experimentally determined to be 0.54 eV [322].

In this section of the Chapter, we use G/WSe_2/G heterostructures to detect low-energy photons (with a wavelength up to 1.5 μm) through photo-thermionic (PTI) emission. Fig. 5.1b shows in detail how the PTI photocurrent is generated: Photons are absorbed by graphene, creating electron-hole pairs, which then rapidly equilibrate into a thermalized carrier distribution with an elevated electron temperature T_e compared to the temperature of the lattice T_{ph} and the environment T_0; carriers within this distribution with an energy larger than the

Schottky barrier height Φ_B at the graphene/WSe_2 interface can be injected into the WSe_2 and travel to the other graphene layer. The number of carriers with sufficient energy scales with $\exp(-\Phi_B/k_B T_e)$, where k_B is the Boltzmann constant.

5.1.2 Devices

In our device, WSe_2 provides an energy barrier between the two graphene sheets with low interfacial defects and reduced Fermi-level pinning. The active device (depicted schematically in Fig. 5.2a) is encapsulated between layers of hexagonal boron nitride (hBN) which provides a clean, charge-free environment for the graphene and WSe_2 flakes (see Section 3.2 for details on fabrication). The device is equipped with an electrostatic bottom gate (V_G) that enables control of the Fermi energy μ and thereby Φ_B of (mainly) the bottom graphene. All measurements presented in this this section are obtained from one particular device comprising a 28-nm-thick WSe_2 flake (see Fig. 5.2d) and are performed at room temperature with a quasi-CW laser source, unless otherwise mentioned (see Section 2.5.1). We have studied devices with WSe_2 flakes of various thicknesses (L = 2.2 to 40 nm) and obtained similar results, consistent with the PTI effect (see Section B.2).

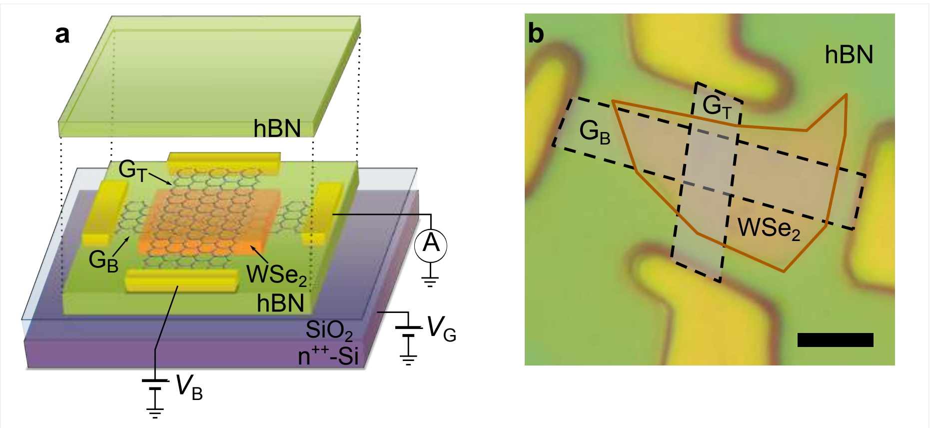

FIGURE 5.2: **The photo-thermionic device a)** Schematic of the heterostructure on a 285-nm-thick SiO_2/Si substrate, to which a gate voltage (V_G) is applied to modify the Fermi level μ of the bottom graphene. An interlayer bias voltage (V_B) between the top (G_T) and bottom (G_B) graphene flakes can be applied, and current or photocurrent flowing through G_B is measured. **b)** Optical image of a heterostructure composed of a 28-nm-thick WSe_2 flake. The top and bottom hBN flakes are 10 and 70 nm thick, respectively. For clarity, graphene flakes are shaded in grey and outlined by a black dashed line, whereas WSe_2 is coloured in orange and outlined by an orange line. The scale bar is 5 μm.

5.1.3 Experimental signature of photo-thermionic effect

The PTI process is driven by the light-induced increase of the thermal energy of the electron gas ($k_\mathrm{B}T_\mathrm{e}$). Signatures of this mechanism are readily visible in the data presented in Fig. 5.3. First, the photocurrent spectrum of Fig. 5.3a shows a sizable, spectrally flat response for photon energies ($E_\mathrm{photon} = h\nu$) well below the band gap of WSe_2 ($h\nu < E_\mathrm{G} \sim 1.3$ eV). That is expected from a thermally driven photocurrent, given the uniform absorption of graphene in the visible, near-infrared range and the fact that $k_\mathrm{B}T_\mathrm{e}$ is independent of $h\nu$ for constant power [89, 321]. Furthermore, the photocurrent generated in this sub-bandgap regime exhibits a striking superlinear dependence on laser power P (Figs. 5.3b,c). This is a direct consequence of the thermal activation of carriers over the Schottky barrier, which, in first approximation, scales exponentially with P. In contrast, the photocurrent in the above-bandgap regime ($h\nu > E_\mathrm{G}$) varies strongly with $h\nu$ and scales linearly with P. This photoresponse is characteristic of light absorption in WSe_2 and transfer of photoexcited carriers to the graphene electrodes, a process driven by the potential drop across the WSe_2 layer [50, 235, 323] (see Chapter 6).

Alternative photocurrent generation mechanisms are less likely to contribute to the observed sub-bandgap photocurrent. To verify this, we measured a device with a Au/WSe_2 interface, where photocurrent is generated by internal photoemission of non-thermalized photoexcited carriers (see Section B.3). This device shows a strong dependence on $h\nu$ along with a cut-off energy at $h\nu = \Phi_\mathrm{B}$, and a linear power dependence – clearly at odds with our observations for G/WSe_2/G devices. We note that multi-photon absorption followed by charge transfer could also lead to a superlinear power dependence, but the laser intensity required to induce significant two-photon absorption in either graphene or WSe_2 is at least 1-2 orders of magnitude higher than the one used in our experiment (smaller than 1 GWcm^{-2}) [324, 325]. Similarly, the photo-thermoelectric and bolometric effects could generate sub-bandgap photocurrent, but both would have a sublinear – rather than the observed superlinear – power dependence [76, 263].

To further verify that the sub-bandgap photocurrent stems from the PTI effect, we perform time-resolved photocurrent measurements by varying the time delay Δt between two sub-picosecond laser pulses generated by a Ti:Sapphire laser (see Section 2.5.3). From the dynamics of the positive correlation signal (due to the superlinear power dependence) in Fig. 5.3d, we extract a characteristic decay time τ_cool of 1.3 ps, which is on the order of the cooling time of hot carriers in graphene observed in Chapter 4 [76, 321]. All together the observations presented in Fig. 5.3 suggest that the sub-bandgap, superlinear, picosecond photocurrent is governed by the PTI effect.

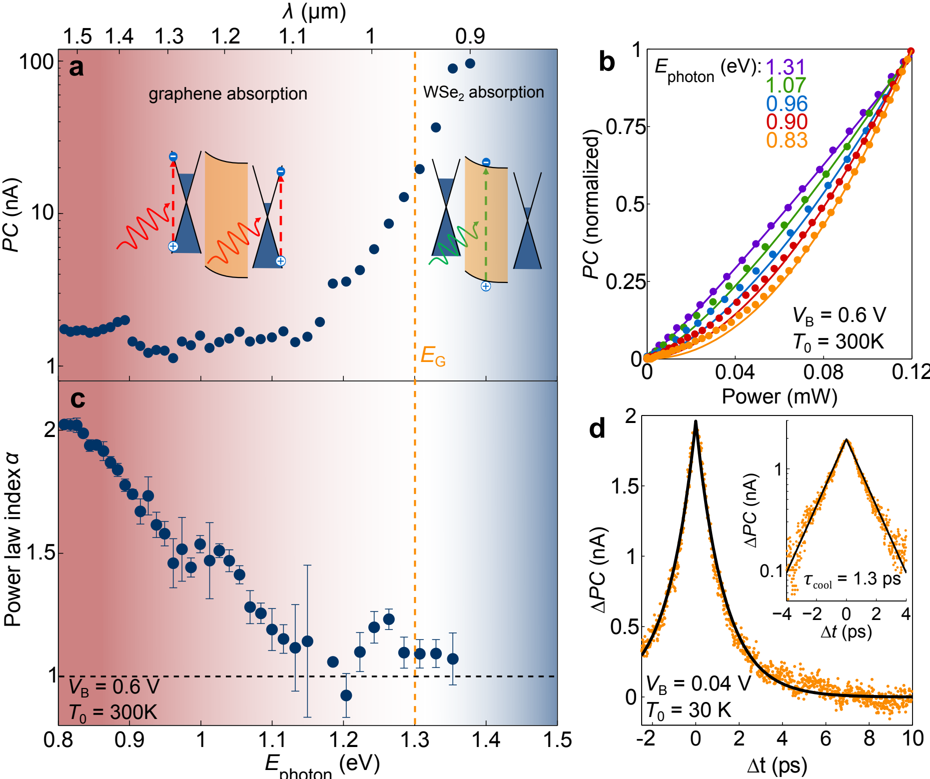

FIGURE 5.3: **Experimental signatures of photo-thermionic emissiona)** Photocurrent (PC) spectrum measured at room temperature in the G/WSe_2/G region with laser power P = 90 μW, V_B = 0.6 V and V_G = 0 V (same conditions for **b** and **c**). The insets illustrate the absorption process taking place in the different photoresponse regimes: absorption in WSe_2 for $h\nu > E_G$ and absorption in graphene for $h\nu < E_G$. The transition between these two regimes is represented by the background color gradient, where red (blue) corresponds to the graphene (WSe_2) absorption regimes. The vertical orange dashed line corresponds to the energy of the bulk WSe_2 bandgap. **b)** Power dependence of the photocurrent for various values of photon energy $h\nu$. The dots represent experimental data and the solid lines are power law fits (PC $\propto P^\alpha$) obtained with a fit range P = 70 to 120 μW . **c)** Fitted power law index α vs. E_{photon}, showing the transition from linear to superlinear power dependence. This transition occurs around $h\nu = E_G$, the indirect bandgap of WSe_2. The error bars correspond to the standard deviation obtained from the linear fit. **d)** Time-resolved photocurrent change ΔPC(Δt) = PC(Δt) - PC($\Delta t \to \infty$), measured using the setup and technique described in Chapter 2.5.3 with an average laser power of 260 μW (wavelength 800 nm), at low temperature (30 K) and bias (V_B = 0.04 V) in order to suppress the contribution of the photocurrent originating from WSe_2 absorption. Experimental data are represented by orange dots and the solid black line is a decaying exponential fit with time constant τ_{cool} = 1.3 ps. Inset: Same data and fit in logarithmic scale.

5.1.4 Electrical tuning of the PTI effect

In contrast to bulk metal-semiconductor systems, this graphene-based heterostructure offers the possibility to tune the Schottky barrier, and therefore the magnitude of the PTI photocurrent, using the interlayer bias voltage (V_B) and gate voltage (V_G). Applying these voltages is necessary in order to generate a finite photocurrent, as it breaks the symmetry of our device which is composed of two G/WSe_2 Schottky barriers with opposite polarity. As the IR photocurrent maps ($h\nu$ = 0.8 eV) in Fig. 5.4a and b indicate, the interlayer voltage V_B essentially controls over which of the two Schottky barriers hot carriers are injected: for V_B = - 0.6 V (Fig. 5.4a), the photoactive region corresponds to the area where the top graphene overlaps with the WSe_2 layer (G_T/WSe_2), whereas the interface with the bottom graphene (G_B/WSe_2) is photoactive for V_B = 0.6 V (Fig. 5.4b). In Figs. 5.4c,d we examine the photocurrent originating from regions containing a single G/WSe_2 interface, thus allowing us to assess each Schottky barrier individually. To create a current, hot carriers need to be emitted over the G/WSe_2 interface and subsequently transported along the WSe_2 layer and collected by the other graphene electrode, as illustrated in the insets of Figs. 5.4c,d. When the interlayer bias V_B makes this process energetically favorable, each Schottky barrier gives rise to a photocurrent with a specific sign. The photocurrent generated in the G/WSe_2/G region (Fig. 5.4e) exhibits both signs as it stems from charge injection over both top and bottom Schottky barriers. From the photocurrent sign associated with each layer, we deduce that hot electrons, rather than holes, are predominantly emitted over both Schottky barriers. This is expected given the work functions of graphene and electron affinity of WSe_2 [322].

One of the hallmarks of thermionic emission is its exponential dependence on the Schottky barrier height. In our device, the gate voltage V_G provides a crucial way of enhancing the photocurrent by controlling the height of the G_B/WSe_2 Schottky barrier via the tuning of the Fermi energy of G_B. As Fig. 5.4f demonstrates, doping the bottom graphene layer with electrons by applying a positive gate voltage V_G effectively lowers Φ_B and results in a strong increase in photocurrent. At high V_G (low Φ_B), the device reaches a responsivity of up to 0.12 mAW^{-1} at wavelength λ = 1500 nm, which, for 0.5% light absorption in graphene [326], translates into an internal quantum efficiency (IQE) of 2%. These figures of merit are similar to those obtained in devices using the in-plane photo-thermoelectric effect [73] and can be further improved by adjusting the relevant physical parameters as discussed below.

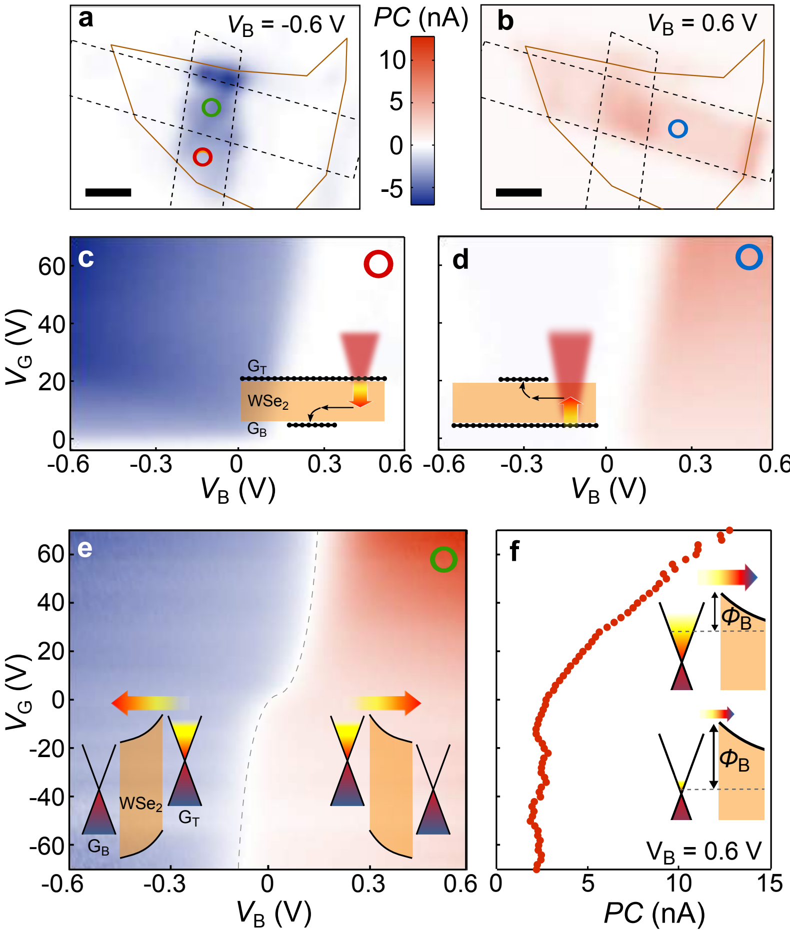

FIGURE 5.4: **Tunable photo-thermionic response a,b)** PC maps of the device shown in Fig. 5.2d measured with an interlayer bias voltage V_B of (**a**) - 0.6 V and (**b**) 0.6 V, and V_G = 0 V. The graphene flakes are outlined by black dotted lines and the WSe_2 flake by solid orange lines, as in Fig. 5.2d. The scale bars are 3 μm. **c,d,e)** PC vs. V_B and V_G measured on single Schottky barriers formed by (**c**) top or (**d**) bottom graphene and WSe_2, as well as (**e**) double G/WSe_2/G interfaces. The coloured circle (green, red and blue) in the upper right corner of each measurement corresponds to the position of the focused laser beam which are indicated on the PC maps **a** and **b**. The black dashed line in **e** indicates where PC is null. All measurements are scaled to the same colour bar. Insets of **c** and **d**: Side view of the heterostructure illustrating the generation and transport of hot carriers from one graphene flake to the other. Insets of **e**: Band diagrams depicting the PTI effect in G/WSe_2/G for $V_B < 0$ (left) and $V_B > 0$ (right). **f)** PC vs. V_G taken from **e** at V_B = 0.6 V. Inset: Band diagrams of the G_B/WSe_2 Schottky barrier at low (bottom) and high (top) V_G illustrating the increase of PTI emission resulting from the lowering of Φ_B. All measurements are performed at room temperature, with $h\nu$ = 0.8 eV and P = 110 μW.

5.1.5 Theoretical model of the PTI effect

The gate tunability of the PTI process and its distinct power dependence allow for a quantitative comparison of our measurements with a Schottky barrier model based on the the one proposed by Sinha *et al.* [327]. In the reverse-bias regime, this model (see Section B.4) predicts that the current density J thermionically emitted over a Schottky barrier of height Φ_B at temperature T is

$$J = \frac{2}{\pi}\frac{e_0}{\tau_{\rm inj}}\left(\frac{k_B T}{\hbar v_F}\right)^2\left(\frac{\Phi_0}{k_B T}+1\right)\exp\left(\frac{-\Phi_B}{k_B T}\right) \tag{5.1}$$

where e_0 is the elementary charge, k_B is the Boltzmann's constant, $\hbar$ is the reduced Planck's constant, v_F is the graphene Fermi velocity, Φ_0 is the band offset at the G/WSe_2 interface (0.54 eV) and $\tau_{\rm inj}$ is the charge injection time. In our experiment, the thermionic photocurrent (PC) we measure is produced by the increase of electronic temperature ΔT = T_e - T_0 upon illumination of the device with a quasi-CW laser at λ = 1500 nm. Hence, it follows that the photocurrent is

$$\mathrm{PC} = AD\left[J\left(T_0+\Delta T\right) - J\left(T_0\right)\right] \tag{5.2}$$

where A is the area of the laser beam (laser spot size of 1.75 μm), D is the duty cycle (D = $dt \cdot f$ = 0.004) and T_0 is the ambient temperature.

To compare our measurements with the model, we use the values for $\Phi_B(V_G)$ that are extracted from temperature-dependent dark current measurements (Fig. 5.5a), which are consistent with a band offset Φ_0 of 0.54 eV [322]. For simplicity, we assume that heat in the electronic system dissipates through a single, rate-limiting cooling pathway characterized by a thermal conductance Γ, such that under steady-state conditions the increase in temperature is

$$\Delta T = \frac{\alpha \eta_{\rm heat} P}{AD\Gamma} \tag{5.3}$$

where $\alpha = 0.5\%$ is the light absorption in graphene, $\eta_{\rm heat}$ is the fraction of absorbed energy that is transferred to the electron bath ($\sim$ 70%) [89], P is the average power of the laser (see Section B.1).

Fig. 5.5b compares the measured and fitted PC as a function of $\Phi_B(V_G)$ and laser power. This two-dimensional fit yields a carrier injection time $\tau_{\rm inj}$ = 47 $\pm$ 10 ps and a thermal conductance Γ= 0.5 $\pm$ 0.3 $MWm^{-2}K^{-1}$. This value of $\tau_{\rm inj}$ is almost identical to the one found for ideal G/Si Schottky barriers [327], while the one obtained for Γ matches the predicted thermal conductance of G/hBN interfaces due to electron coupling with SPP phonons [79] and is also consistent

with disorder-enhanced supercollisions with acoustic phonons [76]. The excellent agreement between model and experiment is clearly visible in Figs. 5.5c,d. We note that the same measurements were performed at other ambient temperatures (T_0 = 230 and 330 K) and the analysis yields very similar results (see Section B.5).

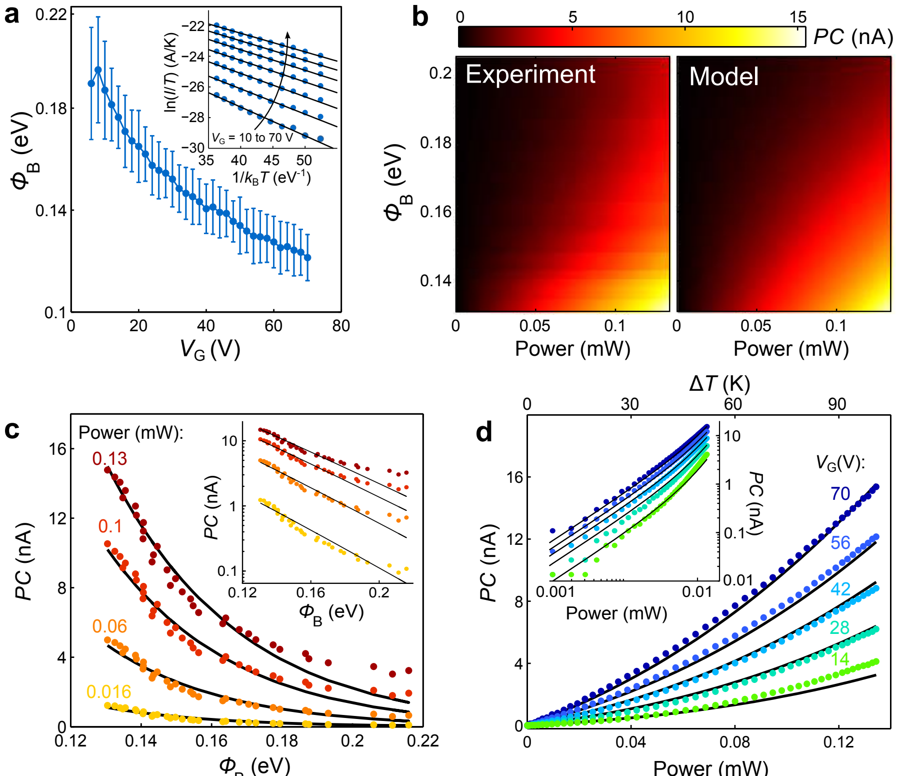

FIGURE 5.5: **Comparison between data and photo-thermionic model a)** Schottky barrier height Φ_B vs. V_G extracted from the temperature-dependence of dark current measurements. Inset: Arrhenius plot of the dark current at different V_G and V_B = 0.36 V. Experimental data are represented by blue dots and the solid black lines are linear fits. The error bars in the main panel correspond to the standard deviation obtained from these fits. **b)** PC vs. Φ_B and laser power P, measured (left plot) and according to our PTI model (right plot). PC is measured at room temperature, with $h\nu$ = 0.8 eV and V_B = 0.36 V. **c)** PC vs. Φ_B for different values of P and **d)** PC vs. P for various values of Φ_B taken from **b**. The data points correspond to the experiment and the solid black lines to the model. The upper horizontal axis shows the rise in electronic temperature ΔT = T_e - T_0 (extracted from the fit of the model to the experiment). Insets of **c** and **d**: Same experimental data and theoretical curves in logarithmic scale.

5.1.6 Discussion on the PTI efficiency

The device modeling and extracted physical parameters provide important insights into how to improve the efficiency of the PTI process. They also explain why this mechanism dominates the photoresponse of graphene/semiconductor heterostructures, while being absent for metal/semiconductor devices. The reason is that the thermal conductance Γ of our graphene-based device is more than 2 orders of magnitude smaller than the thermal conductance due to electron-phonon coupling in thin (approximately 10 nm) metal films [318] (see Section B.3). Hence, thermalized hot carriers in metals do not reach a sufficiently high temperature to generate significant PTI photocurrent. Strategies to substantially increase the device efficiency include further reduction of the thermal conductance in graphene-based devices, for example, by using a non-polar encapsulating material [79]. Likewise, the efficiency of the process can be readily improved by lowering $\Phi_{\rm B}$. Indeed, using the PTI model described above, we find that the PTI efficiency increases by one order of magnitude (up to 20 %) by extrapolating the IQE to higher $T_{\rm e}$ (approximately 1000 K) or lower $\Phi_{\rm B}$ (approximately 0.06 eV, see Fig. 5.6). Moreover, our model suggests that the efficiency can be greatly enhanced by reducing the carrier injection time $\tau_{\rm inj}$, which is related to the coupling energy between adjacent layers. The long $\tau_{\rm inj}$ obtained from our fit appears to be one of the main factors limiting the observed IQE and is presumably due to momentum mismatch between electronic states in the two adjacent materials. The interlayer transfer of charge carriers and heat in van der Waals heterostructures is currently not well understood and further studies are needed in order to unveil the limits of the PTI efficiency.

We finally note that the PTI effect shows some similarities to photon-enhanced thermionic emission (PETE), with the important differences that for PETE the photoexcited carriers are in thermal equilibrium with the lattice of a hot semiconductor and are emitted over a vacuum energy barrier [328, 329]. There are also important resemblances between the PTI mechanism and the concept of hot-carrier solar cells, since both require decoupling of the electron and phonon baths and energy-selective contacts [328, 329]. Both PETE devices and hot-solar cells have an interesting potential for power conversion, but harvesting low-energy photons is limited by the bandgap of the semiconducting absorber. Interestingly, in our PTI device, which has a very simple geometry and operates at room temperature, we also find a gate-dependent open-circuit voltage (of the photocurrent) of up to 0.17 V with a fill factor of 38%. This effect, observable in Fig. 5.4e, opens up a promising avenue for infrared energy harvesting using graphene as the active material [330].

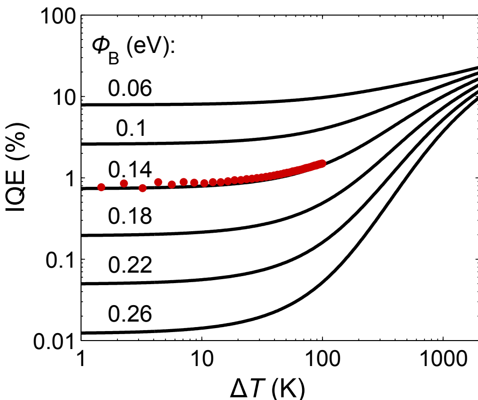

FIGURE 5.6: **IQE vs. laser-induced temperature change ΔT.** The solid lines are theoretical IQE calculated with the PTI model with τ_{inj} = 47 ps and Γ = 0.5 MWm^{-2}K^{-1}, at T_0 = 300 K and at different values of Φ_{B} (indicated on top of each line). The data points are taken from the measurements presented in Fig. 5.5b, at Φ_{B} = 0.14 eV.

5.2 Tuning ultrafast electron thermalization pathways in G/hBN/G heterostructures

In the second section of this chapter, we show that PTI emission also takes place in G/hBN/G heterostructures (Fig. 5.7a) under certain bias and excitation conditions. Remarkably, by adjusting the interlayer bias voltage or the excitation photon energy, a new energy transport channel which competes with the PTI process is observed (Fig. 5.7b). We identify this additional pathway as photon-assisted tunnelling, a process where photoexcited carriers in graphene tunnel through the hBN barrier before they thermalize with other carriers. Hence, by tuning the experimental conditions, we can effectively control the *inter*layer charge transport to occur slower or faster than the *intra*layer thermalization, thus tuning the thermalization process. Our experiments not only provide a way to estimate the thermalization time of carriers in graphene, but also demonstrate a means to manipulate electron thermalization in low-dimensional materials.

5.2.1 Devices

The G/hBN/G heterostructure devices are fabricated on Si/SiO_2 substrates by mechanically assembling the graphene sheets and hBN flakes with 5 - 30 nm thickness (Figs. 5.7a,d). In our experiment, we apply a bias voltage V_{b} between the top and bottom graphene and measured the corresponding interlayer current *PC* under optical excitation with broadband quasi-CW laser. We have measured

four G/hBN/G devices with monolayer graphene and two devices with few-layer ($\leq$ four layers) graphene, and found similar results. The device characteristics are therefore insensitive to a slight change of graphene layer thickness.

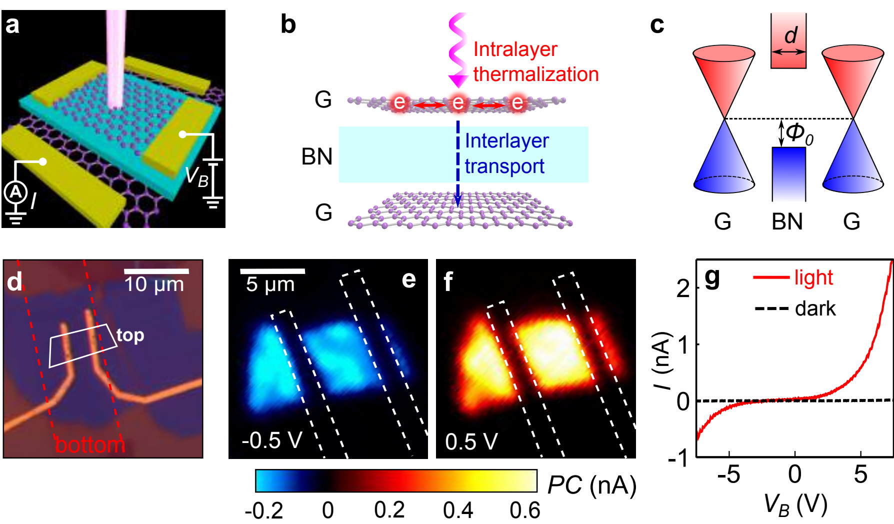

FIGURE 5.7: **Interlayer photocurrent of a G/hBN/G device a)** Schematic of a G/hBN/G device under optical excitation. **b)** Schematic of intralayer thermalization and interlayer transport of the optically excited carriers. **c)** Band alignment between graphene and hBN. hBN has a band gap of 5.9 eV, and the Dirac point of graphene is located $\sim$ 1.3 eV (Δ) above the edge of the hBN valence band [168]. **d)** Optical image of a G/hBN/G device, which consists of a top exfoliated graphene layer (white line), a 14-nm-thick hBN flake, and a bottom graphene layer grown by chemical vapor deposition (dashed red line). **e-f)** Scanning images of interlayer photocurrent at interlayer bias V_{B} = -0.5 and 0.5 V. **g)** Interlayer current I as a function of V_{B} with and without light illumination. All measurements were carried out with 600-nm optical excitation from a supercontinuum laser at T_0 = 100 K. The incident laser power is 500 μW for (**e-f**) and 100 μW for (**g**).

Figs. 5.7d-f show the optical image of a G/hBN/G device and the corresponding device characterization using scanning photocurrent microscopy. PC maps at interlayer bias voltages V_{B} = -0.5 and 0.5 V under 600-nm laser excitation show that photocurrent appears only in the area where the two graphene layers overlap with each other. The photocurrent magnitude increases significantly with V_{B}, and its direction flips with the sign of bias voltage (Fig. 5.7g). We do not observe any current I in the absence of illumination, indicating that optical excitation is necessary to generate a measurable interlayer current in our G/hBN/G devices. Based on recent first-principle calculations [168], the graphene Dirac point is located at $\Phi_0 \sim$ 1.3 eV above the BN valence band edge, and $\sim$ 4.5 eV below the conduction band edge (shown schematically in Fig. 5.7c), in agreement with

dark tunneling measurements [169, 198]. This suggests that, since the potential energy barrier Φ_0 is much smaller for positive charge carriers (holes) than for electrons, the interlayer current is mediated predominantly by holes.

5.2.2 Photo-thermionic emission versus photon-assisted tunneling

The photocurrent in our G/hBN/G devices exhibits complex dependence on excitation laser power P, interlayer bias V_{B} and excitation photon energy $h\nu$ (Fig. 5.8). While the photocurrent generally increases with laser power, it exhibits both linear and superlinear power dependence, depending sensitively on bias voltage and photon energy. If we keep a constant bias $V_{\mathrm{B}} = 5$ V, PC increases superlinearly with P at $h\nu = 1.75$ eV (red dots in the left panel of Fig. 5.8a), yet gradually becomes linear as the photon energy increases to $h\nu = 2.43$ eV (purple squares). If we instead keep a constant photon energy $h\nu$= 2.10 eV, the photocurrent increases superlinearly with P at $V_{\mathrm{B}} = 1.5$ V (red dots in the right panel of Fig. 5.8a), then gradually becomes linear as the bias increases to $V_{\mathrm{B}} =$ 10 V (purple squares).

The complexity of the photocurrent variations can be efficiently captured by a single fitting parameter α, which we obtained by fitting all photocurrent vs. power data with a simple power law $\mathrm{PC} \propto P^{\alpha}$. Fig. 5.8b, our main result, shows α over a wide range of bias voltage and photon energy. The data is separated into several distinct regions, labeled A and B, highlighting the superlinear ($\alpha >$ 1, red-yellow color) and linear ($\alpha = 1 \pm 0.02$, blue) power dependence of the photocurrent, respectively. The value of α demonstrates a clear and gradual transition from roughly three at low bias and photon energy (regime A) to $\alpha \sim 1$ at high bias voltage and photon energy (regime B).

We attribute the complex photocurrent behavior to the transition between two distinct processes, photo-thermionic (PTI) emission and photon-assisted tunneling, both of which mediate charge carrier transit through the G/hBN/G heterostructure (Fig. 5.8c). As we have shown in Section 5.1, PTI emission occurs when photoexcited carriers remain in the graphene, scatter with one another, and quickly reach thermal equilibrium among themselves. High-energy carriers in the hot tails of the resultant thermal distribution that have sufficient energy to overcome the potential energy barrier Φ_0 can then travel to the other graphene layer. This process is characterized by a superlinear dependence of the photocurrent on the laser power, which matches well with our observation at low $V_{\mathrm{B}}/h\nu$ (Regime A in Figs. 5.8b,c).

In contrast, at high $V_{\mathrm{B}}/h\nu$, the effective hBN barrier is reduced, allowing the excited carriers to tunnel from one graphene layer to the other before they scatter with other carriers. Given the energy height and thickness of the hBN potential energy barrier, optical excitation is necessary to assist the tunneling process [169,

198]. Photon-assisted tunneling current then scales with the number of initial photoexcited carriers and therefore increases linearly with laser power. This behavior matches well with the observed linear power dependence of photocurrent at high $V_B/h\nu$ (Regime B in Figs. 5.8b,c).

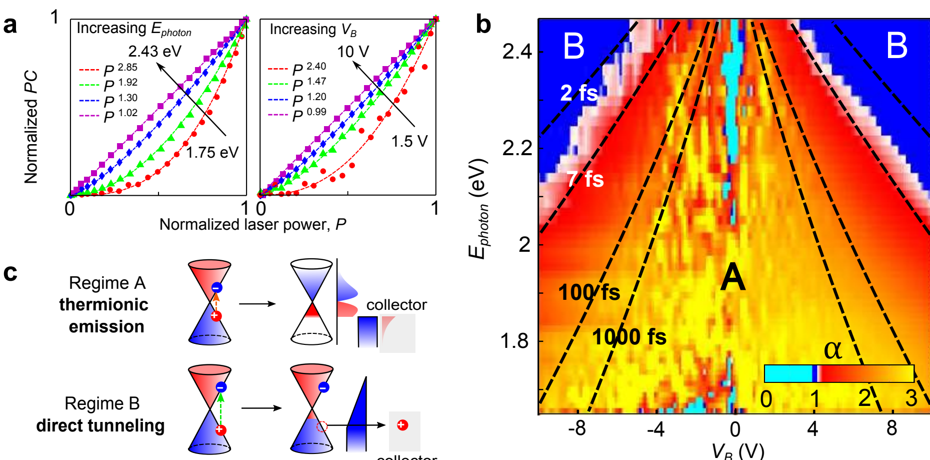

FIGURE 5.8: **Two different regimes of interlayer photocurrent in a G/hBN/G device** **a)** PC as a function of excitation laser power P, at constant interlayer bias $V_B = 5$ V but increasing photon energies $h\nu = 1.75$, 2.10, 2.25 and 2.43 eV (left panel), and at constant $h\nu = 2.10$ eV but increasing bias $V_B = 1.5$, 3.75, 5 and 10 V (right panel). For better comparison, the current and laser power are normalized, and the data are fitted with a power law PC $\propto P^{\alpha}$. **b)** A color map of α as a function of V_B and $h\nu$. The color scale is customized to make the area with $\alpha > 1$ (Region A) and $\alpha = 1 \pm 0.02$ (Region B) appear red-yellow and blue, respectively. The black dashed lines are contours corresponding to tunneling time of 2, 7, 100 and 1000 fs, predicted by our model described in the text. **c)** Schematics depicting the thermionic emission and the direct carrier tunneling as the dominant photocurrent mechanism for Region A and B in (**b**), respectively. All measurements were carried out with a supercontinuum laser at $T_0 = 100$ K.

5.2.3 Time-resolved photocurrent measurements

To confirm that electron thermalization dominates the photocurrent response in the thermionic regime, we performed time-resolved photocurrent measurements (TRPC) using a Ti:Sapphire femtosecond laser[1] at low $V_B/h\nu$. At a photon energy of 1.55 eV, photoexcitation with short pulses (90-fs duration) produces photocurrent that is orders of magnitude higher than that with a supercontinuum laser (pulse duration $\sim$ 90 ps) at the same fluence, indicating that shorter pulses produce higher transient electronic temperature. We observed strong positive

[1]TRPC measurements have been performed with a setup similar to the one presented in Section 2.5.3 . In this case, a 80-MHz Ti:Sapphire oscillator (Tsunami) generates 90-fs-long laser pulses centered at $\lambda = 800$ nm.

two-pulse correlation in the photocurrent signal, which exhibits a short component (< 100 fs) and a long component (~ 1 ps, Fig 5.9). The long timescale matches well the cooling time of hot carriers in graphene observed in vertical G/WSe_2/G devices (Fig. 5.3d) and in-plane graphene devices (Fig. 4.5). The short timescale, on the other hand, can be attributed to cooling of hot carriers by optical phonon emission, a thermalization process which only occurs at very high carrier temperature ($k_B T_e >$ optical phonon energy). We note that these results are similar to the previously reported two-pulse correlation of hot photoluminescence [80], a phenomenon that arises from hot carriers at the high-energy tail of the thermal distribution in graphene. Moreover, positive correlation in the two-pulse photocurrent measurement immediately excludes direct carrier tunneling with a linear P-dependence as the major photocurrent mechanism at low V_B. We thus conclude that the observed photocurrent at low $V_B/h\nu$ arises from high-energy thermalized carriers in graphene.

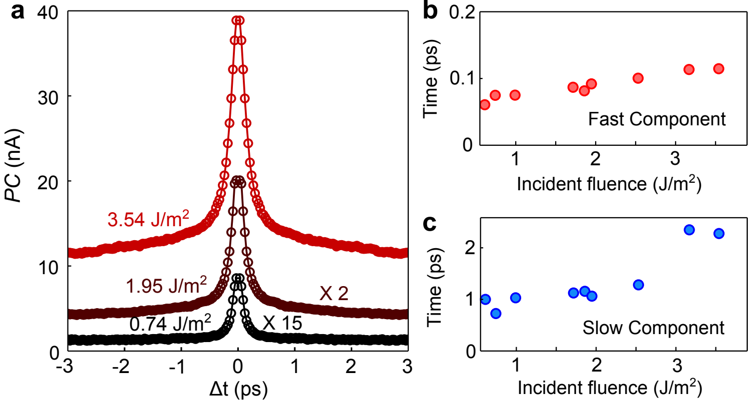

FIGURE 5.9: **Two-pulse correlation of interlayer photocurrent in a G/hBN/G device.** **a)** Photocurrent at $V_B = 0.1$ V, as a function of temporal separation between two identical but cross-polarized excitation pulses Δt. The incident fluences of each beam are 0.74, 1.95 and 3.54 J/cm^2. The pulse duration is 90 fs and the photon energy is 1.55 eV. **b,c)** The time constants of the fast and slow components at different incident fluences. They are extracted by fitting the correlation data with a symmetric biexponential function convoluted with a Gaussian function of width 130 fs. All measurements were carried out with a Ti:Sapphire laser at $T_0 = 300$ K.

5.2.4 Fowler-Nordheim tunneling and thermalization time

In the photon-assisted tunneling regime (high bias voltage and photon energy), electron tunneling is described by the Fowler-Nordheim (FN) formalism (Chapter 1.4.2). For electrons tunneling through a triangular barrier in the presence of a high electric field, the current-voltage characteristics take the form [331]:

$$\mathrm{PC}\,(V) \propto V_{\mathrm{B}}^{2}\mathrm{exp}\left[-\frac{\beta}{V_{\mathrm{B}}}\right], \tag{5.4}$$

where

$$\beta = -\frac{4d\sqrt{2m}(\Phi_0 - h\nu/2)^{3/2}}{3e\hbar} \tag{5.5}$$

Here, m is the carrier effective mass in the barrier region, and the width d is determined by the hBN thickness.

The FN model exhibits several features that serve as fingerprints of a non-thermal carrier tunneling process, and can be compared directly with experiment. Eq. 5.4 suggests a linear relationship between ln(PC/V_{B}^2) and $1/V_{\mathrm{B}}$, with a bias-independent slope β. To examine the regime over which this behavior holds, we analyzed the PC-V_{B} data taken under supercontinuum laser excitation. Fig. 5.10a shows ln(PC/V_{B}^2) as a function of $1/V_{\mathrm{B}}$ at positive bias over a range of photon energies. At high bias or photon energy (Region B in Fig. 5.8b), we observed a linear relationship that breaks down at low $V_{\mathrm{B}}/h\nu$, where thermionic emission dominates (Region A). We extracted the slope (-β) from the linear fits, and found that $\beta^{2/3}$ scales linearly with the excitation photon energy $h\nu$, consistent with Eq. 5.5 (red dots in Fig. 5.10b). From fitting the data and comparing to Eq. 5.5, we estimate the barrier height from the x-axis intercept to be Φ_0 = 1.25 eV. Similar results were obtained at negative bias, with a slightly higher estimated barrier height Φ_0 = 1.31 eV (blue dots in Fig. 5.10b). These values agree well with the predicted potential barrier ($\sim$ 1.3 eV) between graphene and hBN by first-principle calculations [168], and confirm that the photocurrent is dominated by direct carrier tunneling at high $V_{\mathrm{B}}/h\nu$.

By adjusting the interlayer bias voltage and excitation photon energy, we can tune the interlayer transport process, thus allowing us to pinpoint the regime in which both processes occur on similar time scales. For direct carrier tunneling, the average lifetime of photoexcited carriers τ_{tun} can be estimated as $\tau_{\mathrm{tun}} = \tau/T(E) \sim h/\Delta E T(E)$, where $\tau \sim h/\Delta E$ is approximated from the uncertainty principle, h is Planck's constant, ΔE is the energy difference between initial and final states, and $T(E)$ is the WKB transmission probability [331, 332]. Both $T(E)$ and τ depend on the excitation energy and bias voltage, while $T(E)$ also contains information about the barrier height and effective mass in hBN. As a function of bias voltage and photon energy, this model predicts that the average lifetime remains constant over a series of lines in $h\nu$ vs. V_{B} space. Fig. 5.8b shows several of these lines (black dashed lines) and the corresponding times (τ_{tun} = 2, 7, 100 and 1000 fs). Carrier tunneling occurs faster at high $V_{\mathrm{B}}/h\nu$ than at low $V_{\mathrm{B}}/h\nu$, with τ_{tun} ranging from 1 fs to almost infinity (near zero bias voltage). Our estimate of τ_{tun} exhibits quite remarkable agreement with experiment. In particular, the contour at τ_{tun} = 7 fs effectively captures the main transition (blue to red) observed in Fig. 5.8b. Furthermore, the fit implies a carrier thermalization time on the order of 10 fs in graphene, which indeed matches well our results obtained in Chapter 4 ($\tau_{\mathrm{heat}} < 50$ fs) and the results of

other ultrafast experiments [95].

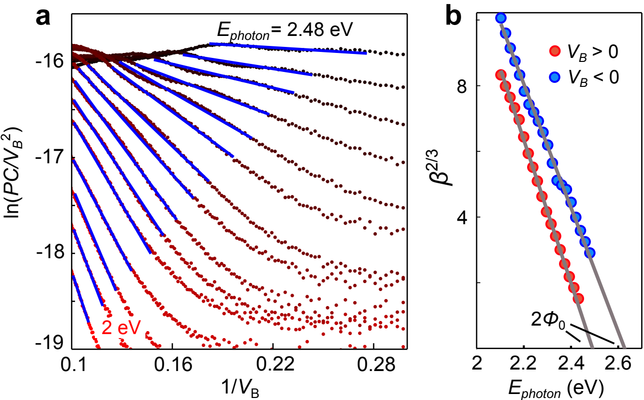

FIGURE 5.10: **Experimental signatures of direct Fowler-Nordheim carrier tunneling.** **a)** ln(PC/V_{B}^2) as a function of 1/V_{B} at different excitation photon energy $h\nu$ = 2.1 to 2.45 eV. The blue lines highlight the linear behavior at high bias, with slope of β. **b)** $\beta^{2/3}$ as a function of $h\nu$ at positive bias (red dots) and negative bias (blue dots). The lines are linear fits with x-intercepts at 2Φ_0, where Φ_0 = 1.25 and 1.31 eV correspond to the barrier height in the Fowler-Nordheim formula, Eq. 5.5 in the text. All measurements were carried out with a supercontinuum laser at T_0 = 100 K.

5.3 Conclusions and outlook

Summarizing, we explored the vertical interlayer transport of photoexcited carriers in various graphene-based heterostructures. In G/WSe_2/G heterostructures, sub-bandgap photons absorbed in graphene create a thermalized distribution of hot carriers, some of which have enough energy to overcome the G/WSe_2 Schottky barrier. The interlayer photocurrent generated through this mechanism, which we dubbed "photo-thermionic effect", is characterized by a superlinear power dependence and an exponential dependence on the Schottky barrier height Φ_{B}. This behaviour is well captured by our PTI model, which scales with $\exp(-\Phi_{\mathrm{B}}/k_{\mathrm{B}}T_{\mathrm{e}})$.

The PTI effect is also present in G/hBN/G heterostructures, but at larger interlayer bias and high photon energy excitation, an additional photocurrent mechanism emerges, which we identify as photon-assisted tunnelling. In this regime, photoexcited carriers in graphene tunnel through the hBN barrier before they thermalize with other carriers. An analysis of the competition between the two transport mechanisms indicates that the intralayer thermalization of photoexcited carrier in graphene occurs within $\sim$ 10 fs, in agreement with the results presented in Chapter 4.

Photodetectors based on the PTI effect presents several advantages. Like PTE-based devices, they can in principle work over an extremely broad wavelength range, including the mid-infrared and far-infrared (terahertz) regions, since they rely on the broadband absorption of graphene. They also hold potential for ultrafast photodetection given that their photo-switching time is governed by the picosecond cooling of hot electrons. Moreover, unlike in-plane graphene photodetectors where photocurrent is typically produce at 1D interfaces, vertical PTI devices have a scalable active area, which makes use of the entire graphene sheet, and can be easily integrated with conventional and flexible solid-state devices.

As discussed in Section 5.1.6, the relatively low IQE ($\sim$ 2%) measured in our heterostructures could be greatly improved, for instance, by reducing the thermal conductance Γ of hot carriers, further lowering the Schottky barrier height Φ_B or reducing the carrier injection time τ_{inj}. Future experimental and theoretical studies should therefore aim at understanding better the processes of interlayer heat or charge transfer in van der Waals heterostructure. Many questions remain to be answered: What is the impact of the electron momentum mismatch between adjacent layers on the PTI efficiency? Is PTI emission more efficient for Schottky barriers formed between graphene and conventional semiconductors like silicon? From a more fundamental viewpoint, what is the connection between the thermoelectric and thermionic effects? Is there a general theoretical framework to understand charge transport in van der Waals heterostructures? Interestingly, according to a recent theoretical study [311], the responsivity of PTI devices could exceed 1 A/W, resulting in EQE larger than 100% for $h\nu > 1$ eV. This encouraging prediction makes the photo-thermionic effect a promising mechanism not only for photodetection but also for energy harvesting.

Chapter 6

Picosecond photoresponse in TMD-based heterostructures

Two-dimensional crystals, such as graphene and transition metal dichalcogenides, present a collection of unique and complementary optoelectronic properties. Assembling different 2D materials in vertical heterostructures enables the combination of these properties in one device, thus creating multi-functional optoelectronic systems with superior performance. In this chapter, we demonstrate that graphene/WSe_2/graphene heterostructures ally the high photodetection efficiency of TMDs [50, 235] with a picosecond photoresponse comparable to that of graphene [31, 259, 268], thereby optimizing both speed and efficiency in a single photodetector. We follow in time the extraction of photoexcited carriers in these devices using time-resolved photocurrent measurements and demonstrate a photoresponse time as short as 5.5 ps, which we tune by applying a bias and by varying the TMD layer thickness. Our study provides direct insight into the physical processes governing the detection speed and quantum efficiency of these van der Waals heterostuctures, such as out-of-plane carrier drift and recombination. The observation and understanding of ultrafast and efficient photodetection demonstrate the potential of hybrid TMD-based heterostructures as a platform for future optoelectronic devices.

This chapter is based on:

- **Massicotte, M.**, Schmidt, P., Vialla, F., Schädler, K. G., Reserbat-Plantey, A., Watanabe, K., Taniguchi, T., Tielrooij, K.J. and Koppens, F.H.L. *Picosecond photoresponse in van der Waals heterostructures.* Nature Nanotech. 11, 5, 42-46 (2015)

6.1 Introduction

The optoelectronic response of 2D crystals is currently the subject of intense investigation [14, 15, 31, 32, 50, 69, 224, 227, 228, 233, 235, 238–241, 258, 259, 268, 296, 333] prompted by the need for next-generation photodetectors with superior performance in terms of efficiency, detection speed, as well as flexibility and transparency [7]. High photon absorption [50, 334, 335] and large photoconducting gain [224, 227, 228, 336] have been observed in devices based on semiconducting 2D crystals. Yet, the observed response time typically ranges from nanoseconds [233] to seconds [224, 227, 336], with faster devices often displaying lower responsivity [224]. Therefore, the main challenge is to develop and assess photodetectors based on 2D semiconductor crystals that simultaneously possess a large active area, high internal efficiency, and fast response time.

A promising approach to create such versatile devices is to sandwich a TMD layer between two graphene sheets serving as charge extraction contacts. In contrast to lateral photodetectors, such vertical van der Waals (vdW) heterostructures [25] have the advantage of possessing a large, scalable active area and an atomically short charge extraction channel, potentially enabling both efficient and fast photodetection. Whereas the quantum efficiency of these vdW devices [50, 235, 240] and the dynamics of photocarrier creation and relaxation in TMDs [148, 157, 165, 166, 216, 337–340] have been addressed (see Section 1.2.3), the response time of TMD-based photodetectors, as well as the dynamic processes governing their quantum efficiency remain elusive.

In this Chapter, we report on the intrinsic processes that limit the performance of photodetectors based on high-quality G/WSe_2/G (with G representing graphene) vdW heterostructures encapsulated in hBN [9]. We perform time-resolved photocurrent measurements [254, 268, 270, 341] on devices consisting of WSe_2 flakes with a range of thicknesses (monolayer and multilayers from 2.2 to 40 nm) and demonstrate a photoresponse time as short as 5.5 ps. This technique, which combines electronic detection with subpicosecond optical excitation, allows probing of the extraction (Fig. 6.1) and loss dynamics of the photoexcited charge carriers in the photoactive TMD layer. This provides direct insight into the physical processes governing the detection speed and quantum efficiency of these vdW heterostuctures and demonstrate their potential as a platform for future optoelectronic devices.

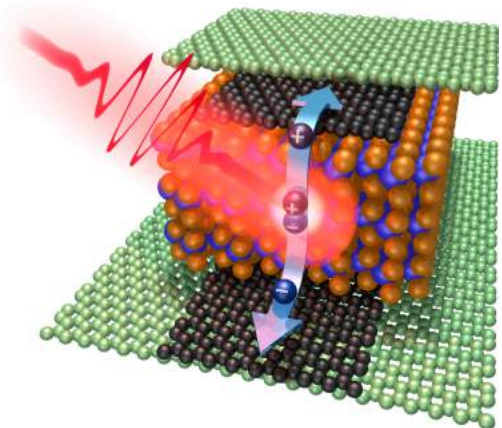

FIGURE 6.1: **Photocurrent generation in G/WSe2/G heterostructure.** Schematic representation of the photocurrent generation mechanism in a hBN/G/WSe_2/G/hBN heterostructure. Upon pulsed-laser excitation, excitons or electron-hole pairs are created, separated and transported to the graphene electrodes.

6.2 Graphene/WSe_2/Graphene devices

To perform this study, we use WSe_2 as the photoactive material because of its high optical quality [114, 238], and monolayer graphene flakes, placed below and above the TMD layer, as source and drain electrodes with gate-tunable work functions (Fig. 6.2a, see Section 3.2 for details on the fabrication)[1]. Fig. 6.2b shows an optical image of a typical device comprising a WSe_2 flake with a thickness of 2.2 nm (3 atomic layers). Unless otherwise specified, all measurements presented in Figs. 6.2 and 6.3 are obtained from this particular device.

We first characterize the photoresponse of our devices at room temperature using a scanning photocurrent microscope (see Section 2.5.1). The photocurrent map displayed in Fig. 6.2c shows that the photosensitive region corresponds to the area where the three main layers (G/WSe_2/G) are superimposed. The photocurrent spectrum (Figure 6.2d) measured in this area exhibits three main peaks (labeled A, B and A') whose positions match well with the exciton absorption peaks of WSe_2 [106, 107, 114]. This confirms that the photocurrent originates from the generation of photoexcited charge carriers upon light absorption in the WSe_2 layer, followed by the transfer of these charges to the graphene electrodes. The polarity and efficiency of the photocurrent are driven by the potential drop across the WSe_2 layer (ΔV), which can be tuned by applying a bias (V_B) or gate (V_G) voltage [50, 235] (see Sections C.1 and C.2).

[1]Most of these devices have also been used to study the PTI effect reported in Chapter 5

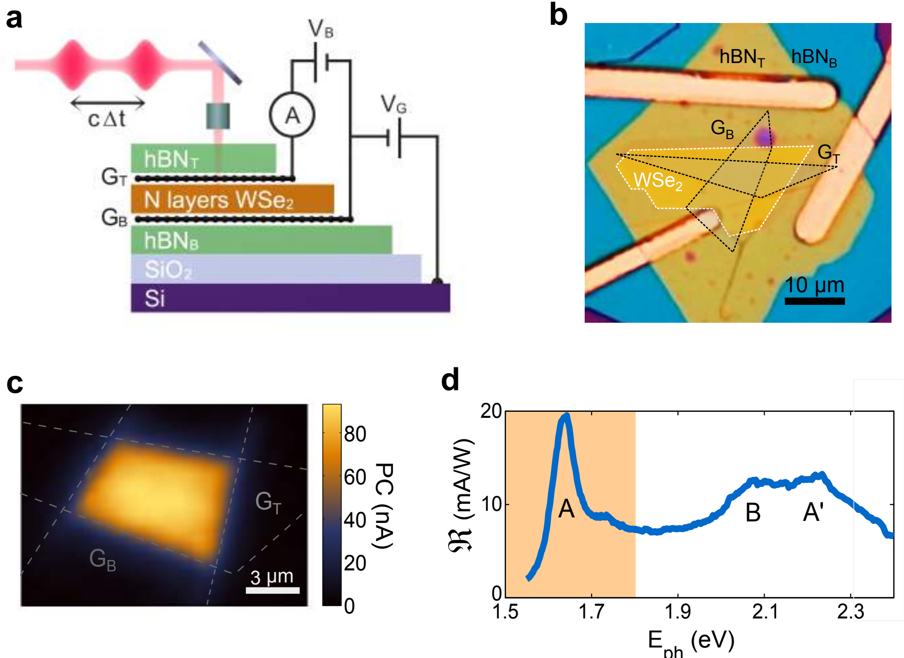

FIGURE 6.2: **Characterization of a G/WSe_2/G device. a)** Schematic illustrating the experimental time-resolved photocurrent setup and cross-sectional view of the device. Two ultrashort pulses, delayed by a controllable distance $c\Delta t$ (c denotes the speed of light), are focused on the device, which comprises a backgate (V_{G}). A bias voltage (V_{B}) can be applied between the top ($\mathrm{G_T}$) and bottom ($\mathrm{G_B}$) graphene layers through which photocurrent is measured. **b)** Optical image of a heterostructure comprising a 2.2 nm thick WSe_2 flake. The graphene and WSe_2 flakes are outlined and shaded for clarity. **c)** PC map obtained by scanning a focused laser beam with a wavelength λ = 759 nm and a power P = 5 μW on the device shown in **c** with V_{G} = 0 V and V_{B} = 0.4 V. The photocurrent is mainly generated in the region where graphene layers (delimited by gray dotted lines) overlap. **d)** Responsivity $\Re$ spectrum of the device shown in **b** measured at a constant power P = 5 μW, with V_{G} = 0 V and V_{B} = 0.4 V. The exciton peaks are labeled according to the convention of Wilson and Yoffe [107] for WSe_2 and confirm that the PC stems from the vertical extraction of carriers generated in the WSe_2 layer. The orange shading indicates the spectral range of the pulsed excitation (illustrated in **a**) employed for time-resolved measurements.

6.3 Measurement of the photoresponse time

In order to investigate the dynamics of the photoexcited charges, we perform time-resolved photocurrent measurements by exciting the photodetector with a pair of ultrashort pulses ($\sim$ 200 fs, centered at 1.55 eV) separated by a variable

time delay Δt (Fig. 6.2a, see Section 2.5.3). Also known as photocurrent autocorrelation measurements - in analogy to autocorrelation measurements using non-linear optical crystals - this technique exploits the nonlinear power dependence of the photocurrent to extract the photocurrent dynamics. Fig. 6.3a shows that this nonlinear power dependence is significant for average laser pulse intensities exceeding 10 kWcm^{-2}. The observed sublinearity likely originates from saturable absorption [148, 159, 342] (phase space filling), but we cannot exclude possible contributions from increased interactions between photocarriers (such as exciton-exciton annihilation [157, 338] and carrier-carrier scattering [148]), or from screening of the external bias [341]. In Chapter 7, we discuss in more detail the origin of this nonlinear response.

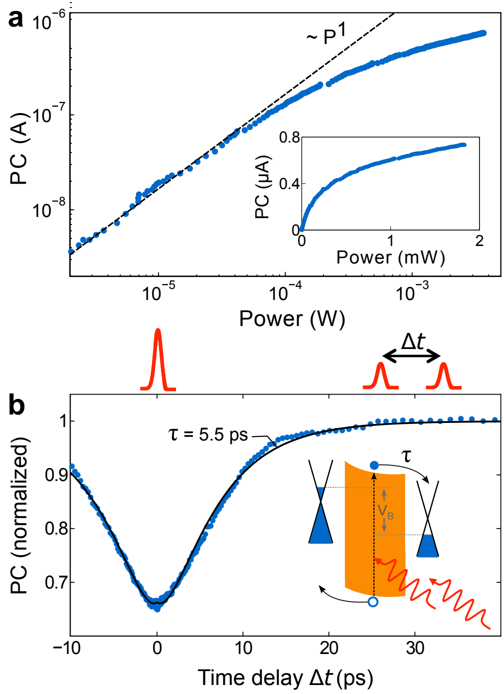

FIGURE 6.3: **Extraction of the photoresponse time of a G/2.2-nm WSe_2/G heterostructure by time-resolved photocurrent measurements. a)** Photocurrent vs. laser pulse power P for V_B = 0.2 V. The transition from the linear to sublinear regime takes place at $P \sim 100\ \mu$W ($\sim$ 10 kWcm^{-2}). Inset: the same data presented on a linear scale. **b)** Photocurrent as a function of time delay between two pulses (illustrated above the plot) with P = 300 μW, at V_B = 1.2 V (blue dots). The photocurrent is normalized by the value of the photocurrent saturating at long Δt. The solid black line is a fit to the data using Eq. 6.1, yielding a time constant τ = 5.5 $\pm$ 0.1 ps. Inset: Schematics of the photoresponse time in a G/WSe_2/G heterostructure, here represented by a band diagram with a bias voltage V_B applied between the graphene layers. The red sinusoidal arrows, blue dot and blue circle symbolize photons, photoexcited electron and hole, respectively. The photoresponse time τ, which corresponds to the time that photocarriers reside in the photoactive area, is represented by the black arrows.

As a result of this sublinearity, photocurrent autocorrelation measurements, such as the one presented in Figure 6.3b, exhibit a symmetric dip around $\Delta t = 0$. We ascribe the dynamics of the dip to depletion of photocarriers from the active region [270], which we can describe with a characteristic time constant τ that corresponds to the photoresponse time of our WSe_2-based photodetector.

The photoresponse time τ is obtained by fitting the time-resolved photocurrent signals using the following equation:

$$\frac{\mathrm{PC}(\Delta t)}{\mathrm{PC}(\Delta t \to \infty)} = 1 - C_1 \mathrm{exp}\left(\frac{-|\Delta t|}{\tau}\right) + C_2 \mathrm{exp}\left(\frac{-|\Delta t|}{\tau_\mathrm{G}}\right) \tag{6.1}$$

where amplitudes C_1 and C_2, and time constants τ and τ_G are the fitting parameters. We attribute the exponential term with time constant τ_G to the PTI response of the top and bottom graphene layers. As we observed in Section 5.1.3, the PTI is characterized by a superlinear power dependence, which gives rise to a positive photocurrent autocorrelation signal. In contrast, the sublinear power dependence of the WSe_2 photoresponse (Fig. 6.3a) leads to a negative autocorrelation contribution. This difference allows us to easily separate both response. We also note that graphene's contribution is slightly faster ($\tau_\mathrm{G} \sim$ 1-3 ps) and always smaller ($C_2 \ll C_1$) than the exponential term ascribed to the WSe_2 response.

We determine τ for five devices with different WSe_2 layer thicknesses L (Fig. 6.4a) and find that τ increases with L and varies by more than two orders of magnitude: from 10 ns (40 nm device) down to 5.5 ps (monolayer and 2.2 nm devices). Fig. 6.4b furthermore shows that τ scales quadratically with the thickness L (except the monolayer, which we discuss later). The highest response rate of $\Gamma = \tau^{-1}$ = (5.5 $\pm$ 0.1 ps)$^{-1}$, corresponding to a bandwidth of $f = 0.55/\tau$ = 100 GHz, is comparable to the intrinsic photo-switching speed of typical graphene detectors ($\sim$ 260 GHz) [268].

We note that in general ultrafast devices may have an operating speed limited by their resistance-capacitance (RC) time. In our devices the relevant capacitance is that of the WSe_2 channel and the resistance is the sum of the graphene resistance and graphene-metal contact resistance. We indeed expect the photoresponse time to be RC-limited to $\tau >$ 0.4 ns for the thinnest devices ($L <$ 10 nm, see Section C.3). Using real-time electronic measurements, we find an instrument-limited higher bound of $\sim$ 1.6 ns. This is already significantly faster than any TMD-based photodetectors reported to date [224, 227, 228, 235] and can further be improved by optimizing the circuit design, graphene resistance and contact resistance, up to the intrinsic limits that are reported in this work.

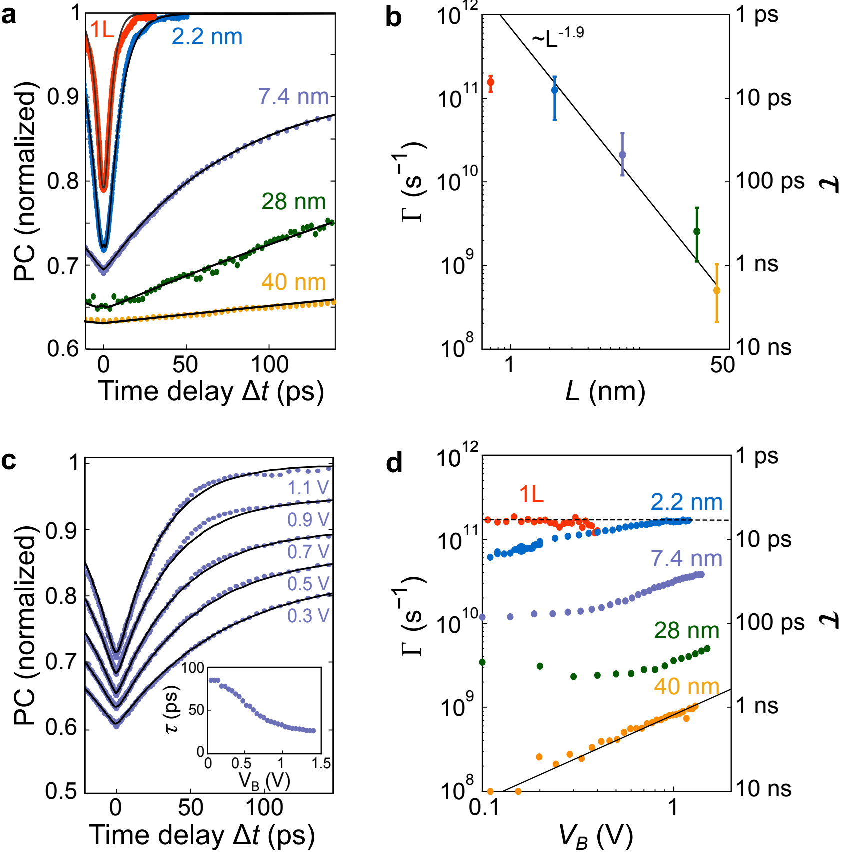

FIGURE 6.4: **Tuning of the photoresponse time by variation of the WSe_2 layer thickness and bias voltage. a)** Time-resolved photocurrent measurements on heterostructures with different L (curves are offset for clarity). All measurements are obtained using a laser pulse power $P \sim 300$ μW and a bias voltage $V_B = 0.5$ V, except the monolayer which was measured at $V_B = 0$ V. Solid black lines are fits to the data. **b)** Photoresponse rate $\Gamma = 1/\tau$ vs. L. Data points represent the averaged values of Γ for different V_B (typically from 0.1 to 1 V), whereas the error bars correspond to the minimum and maximum value of Γ. The solid black line is a power law fit (excluding the monolayer device), yielding $\Gamma \propto L^{-1.9\pm0.3}$. **c)** Time-resolved photocurrent measurements on a heterostructure with L = 7.4 nm at various bias voltages V_B and P = 300 μW (curves are offset for clarity). Inset: photoresponse time τ extracted from this heterostructure as a function of V_B. **d)** Photoresponse rate Γ as a function of V_B for various values of L. The solid black line corresponds to a linear relationship between Γ and V_B, whereas the dotted line labels the effective minimum response time τ = 5.5 ps.

6.4 Photocarrier dynamics in TMD-based heterostructures

To address the underlying physics governing the dynamics and efficiencies in more detail, we study the dependence of τ on the bias voltage V_B (Fig. 6.4c) and observe that τ decreases with V_B (Fig. 6.4c, inset), indicating that photocarriers escape the active region more quickly as the electric field across the WSe_2 layer increases. For devices made of a relatively thick WSe_2 layer ($L \geq 7.4$ nm), the response rate Γ depends linearly on V_B (Fig. 6.4d). This observation and the scaling of τ with L^2 suggests out-of plane drift-diffusive transport: to reach the graphene contact, photocarriers generated in the middle of the WSe_2 layer travel a distance $L/2$ with a drift velocity $v_\mathrm{d} = \mu E$ where μ is the out-of-plane photocarrier mobility and E is the electric field across the WSe_2 layer. Assuming that $E \approx V_\mathrm{B}/L$, the time τ_d it takes for photocarriers to drift out of the active region is $\tau_\mathrm{d} = L^2/2\mu V$. This simple expression, represented by the dotted line in Fig. 6.5a, captures the trend of Γ at low V_B/L^2 ($< 10^{-2}$ V/nm^2), yielding $\mu = 0.010 \pm 0.003$ cm^2/Vs. This value is similar to the one recently reported for thick MoS_2 flakes obtained from transport measurements [343], and is consistent with the strong conductivity anisotropy observed in TMDs (the in-plane conductivity is typically 2-3 orders of magnitude larger than the out-of-plane conductivity) [343].

Interestingly, for higher values of V_B/L^2 (> 0.1 V/nm^2) the response rate reaches a limit. For $L = 2.2$ nm (trilayer), this occurs for high V_B ($V_\mathrm{B} > 0.6$ V), whereas the monolayer device reaches this limit without any applied bias. This saturation behavior indicates the existence of an additional process that occurs in series with the drift process, thus prolonging the carrier extraction process. We find that the timescale τ_s of this additional process is bias-independent and is about 3-5 ps. This value is similar to the transfer time of photocarriers at the interface between WSe_2 and graphene (~ 1 ps) [216] and to the hot exciton dissociation time in few-layer MoS_2 (~ 0.7 ps) [340], which were both recently measured in all-optical pump-probe experiments. We thus argue that the response rate at high V_B/L^2 has a higher bound that is determined by these two processes rather than by drift (Fig. 6.5b); this constitutes an intrinsic limitation for this device geometry.

We also observe a lower bound for the response rate, occurring at low V_B, which we attribute to a loss mechanism that occurs in parallel to the photocurrent generation process (Fig. 6.5b). We find that this process presents a strong thickness dependence, with time constant τ_r ranging from 40 ps (2.2 nm device) up to $>$10 ns (40 nm device). We attribute this effect to radiative and non-radiative recombination of photocarriers [165, 166, 337, 339] and energy transfer via dipole-dipole interaction to the graphene sheets [344] - two processes that have been shown to depend on TMD layer thickness. The latter interpretation is corroborated by the quenching of the WSe_2 photoluminescence observed in the trilayer (10-fold quenching) and monolayer (300-fold quenching) devices (see

Section C.4).

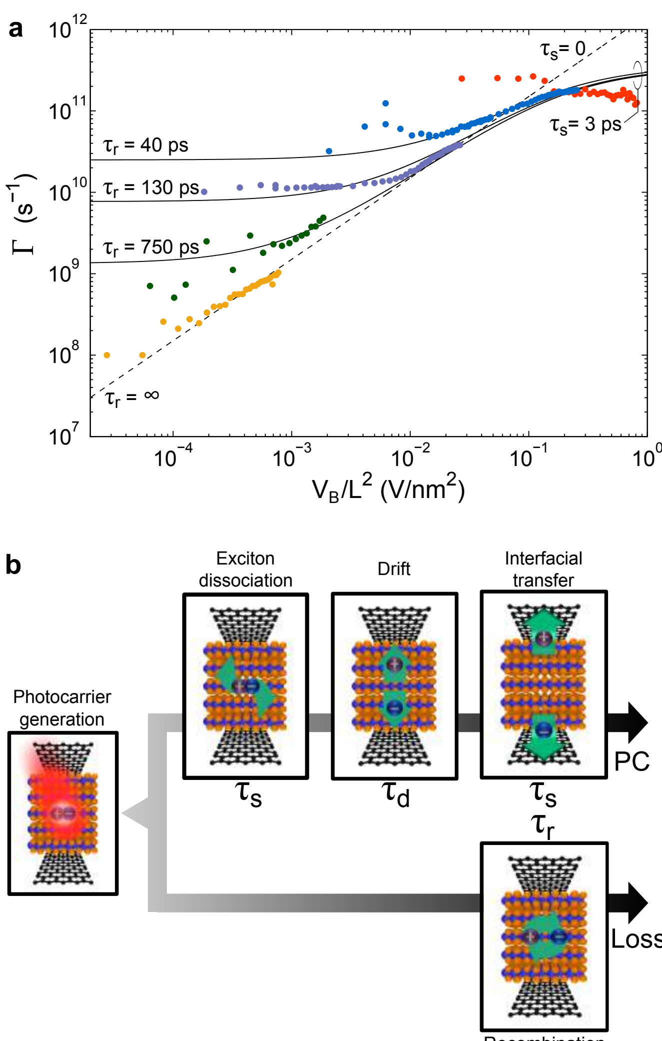

FIGURE 6.5: **Dynamic processes governing the photoresponse of G/WSe_2/G heterostructures. a)** Response rate $\Gamma = 1/\tau$ vs. V_B/L^2 (same data as Fig. 6.4d). The dotted line corresponds to the diffusive transport model discussed in the main text with photocarrier mobility $\mu = 0.010 \pm 0.003$ cm^2/Vs. The uncertainty in μ is estimated from the small variations in the mobility of each device, which, among other things, could stem from extrinsic factors (e.g. unintentional doping) or variations in the laser power employed to measure each device. The solid black lines correspond to the equation $\tau^{-1} = (\tau_d + \tau_s)^{-1} + \tau_r^{-1}$ with $\mu = 0.01$ cm^2/Vs, $\tau_s = 3$ ps and the values of τ_r indicated for each line. **b)** Schematic of the processes contributing to the response time. Radiative and non-radiative photocarrier recombination (τ_r) leads to losses, whereas photocurrent is generated by photocarrier drift (τ_d) in combination with exciton dissociation and/or charge transfer at the G/WSe_2 interface (τ_s).

6.5 Efficiency of G/WSe_2/G photodetectors

We now show that the internal quantum efficiency (IQE, defined as the ratio between the number of extracted photocarriers and the number of absorbed photons) of the photodetector is the direct result of the competition between the photocarrier extraction time ($\tau_d + \tau_s$) and recombination loss (τ_r). Fig. 6.6 shows the IQE as a function of ΔV (the potential drop across the WSe_2 layer) that can be controlled by both V_G and V_B (inset in Fig. 6.6). We find that the experimental IQE matches well the extraction efficiency $\tau_r/(\tau_d + \tau_s + \tau_r)$ derived from the dynamic model illustrated in Fig. 6.5b. This concordance confirms that the dynamic processes identified in our time-resolved study correspond to the relevant physical mechanisms that govern the photoresponse of the device in the linear response regime (low-power, quasi-continuous excitation). It further demonstrates that the high IQEs observed in TMD-based vertical photodetectors ($> 85\%$) [235] arise from the short extraction time of the photocarriers out of the thin TMD channel, thereby outcompeting the loss mechanisms.

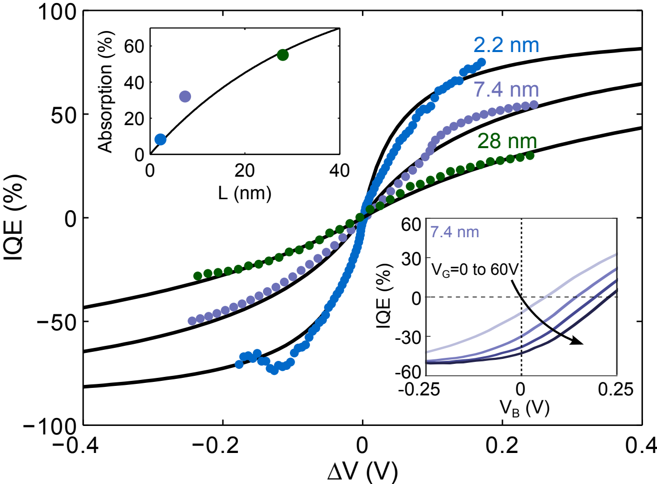

FIGURE 6.6: **Internal Quantum Efficiency of G/WSe_2/G heterostructures.** IQE as a function of the potential drop across the WSe_2 layer ΔV for devices with L = 2.2, 7.4 and 28 nm. The black lines correspond to the expression $\tau_r/(\tau_d + \tau_s + \tau_r)$, where $\tau_d = L^2/2\mu\Delta V$, using the values indicated in Fig. 6.5a. The experimental IQE (data points) is obtained by measuring the photocurrent generated at low power (P = 1 μW) with a quasi-continuous laser (λ = 759 nm) and by using the absorption as a fit parameter. The fitted absorption values are shown in the top left inset and compare well with the absorption expected from Beer-Lambert's law (solid black line) using the bulk absorption coefficient of WSe_2 (3×10^5 cm^{-1}) [106]. Bottom right inset: IQE vs V_B measured on the 7.4-nm-thick device under the same illumination conditions as the main panel, with V_G from 0 to 60 V in steps of 20 V.

This suggests that the IQE can be optimized by reducing the channel length, and thus minimizing the TMD thickness. Interestingly, for the most extreme case of a WSe_2 monolayer, we observe a very low IQE ($\sim$ 6%, assuming 5% absorption) despite of a very short response time. This indicates that the observed dynamics in this device, as opposed to thicker ones, correspond to the losses, rather than to the extraction of charges. This is supported by the observation that the response time is bias-independent. The two loss mechanisms mentioned previously (intrinsic recombination and energy transfer) should indeed both occur much faster for a monolayer: recombination is facilitated by the direct nature of the bandgap of monolayer WSe_2 [114] and loss through energy transfer exhibits a strong power law dependence with the inverse dipole-dipole distance [344].

6.6 Conclusion and outlook

We conclude that G/WSe_2/G devices made of trilayer WSe_2 (2.2 nm) offer the best compromise for optimizing the IQE as they exhibit both a fast photoresponse (down to 5.5 ps) and a high internal quantum efficiency ($>$ 70%). Moreover, the device can be efficiently operated at $V_B = 0$ without dark current (Fig. 6.6, bottom right inset), and thus with low noise level, by applying a large gate voltage and no bias voltage (Noise-equivalent Power down to $\sim 5\times10^{-12}$ W/Hz$^{1/2}$, see Section C.5). Further improvement of the external quantum efficiency (EQE = 7.3% in our 2.2-nm-thick device) can be achieved by enhancing the light-matter interaction in the TMD layer with, for instance, optical waveguides [259] and cavities or plasmonic nanostructures [50, 69]. Stacking multiple semiconducting 2D crystals with different bandgaps is also a promising way to extend the spectral absorption range [14] without compromising much the photoresponse time. Our comprehensive understanding of the photocurrent dynamics in G/TMD/G heterostructures paves the way for designing van der Waals heterostructures for fast and efficient optoelectronic applications, such as high-speed integrated data communication systems.

Chapter 7

Tunnel ionization of 2D excitons in monolayer WSe_2

The optoelectronic response of low-dimensional semiconducting systems is dominated by Coulomb-mediated many-body interactions, giving rise to excitons with high binding energies that are stable even at room temperature. While these nanomaterials are considered as promising building blocks for future optoelectronics applications, their ability to convert light into an electrical current is hindered by the difficulty of dissociating the strongly bound excitons into free carriers. In this chapter, we report on the tunnel ionization of excitons under high in-plane electric field in a monolayer WSe_2 p-n junction. We combine time- and spectrally-resolved photocurrent measurements to probe the field-induced exciton Stark shift and dissociation time and find excellent agreement with a theoretical model of 2D excitons with a binding energy of 170 meV. Our study provides crucial insight into the dynamic processes governing the performances of optoelectronic devices based on these 2D semiconductors.

This chapter is based on:

- **Massicotte, M.**, Vialla, F., Schmidt, P., Lundeberg, M. B., Latini, S., Haastrup, S., Danovich, M., Davydovskaya, D., Watanabe, K., Taniguchi, T., Fal'ko, V. I., Thygesen, K. S., Pedersen, T. G., Koppens, F. H. L., *Tunnel ionization of 2D excitons in monolayer WSe_2*. Submitted (2017)

7.1 Introduction

Understanding the behaviour of Coulomb-bound particles under high external electric field has been key to the early development of quantum mechanics and is now central to fields ranging from nuclear physics to attosecond science. As Johan Stark first observed in hydrogen atoms [345, 346], applying an electric field shifts the energy levels of the two-body system and eventually leads to its dissociation (Fig. 7.1a). In condensed matter physics, Wannier-Mott excitons display features analogous to those of hydrogen [123], but with the crucial difference that they recombine if they are not dissociated. Thermal energy is usually sufficient to ionize excitons in 3D semiconductors owing to their small binding energy E_B (typically a few meV). In contrast, quantum confinement effects and reduced Coulomb screening in low-dimensional materials give rise to large exciton binding energy ($E_\mathrm{B} > 100$ meV) [347, 348], which prevents thermal or spontaneous dissociation even at elevated temperatures and exciton densities.

In particular, monolayer transition metal dichalcogenides (TMDs) have aroused tremendous interest due to their unique optical properties governed by prominent excitonic features [14, 15, 34, 121] and spin- and valley- effects [118–120, 349, 350] (see Section 1.2.2). These 2D semiconductors provide an exciting testbed for probing the physics arising from many-body Coulomb interactions. Recently, all-optical experiments have revealed a wealth of physical phenomena such as exciton [150, 151], trion [140, 141] and biexciton [142] formation, bandgap renormalization [161] and exciton-exciton annihilation [154, 155, 157] (see Section 1.2.3). Optical probes also served to study excitons under high AC electric field, which led to the observation of the optical Stark effect [349, 350] and quasiparticle collisions [351] in TMDs. However, the inherent difficulty to discriminate between bound and unbound electron-hole pairs in optical spectroscopy limits the direct probing of the physics of exciton dissociation.

Photocurrent measurements, on the other hand, allow for quantitative assessment of the dissociation process since photocurrent directly stems from the conversion of excitons into free carriers. A large number of studies have investigated photodetection performances of 2D TMDs [31, 224, 238, 239, 241] and demonstrated their potential as photodetectors, but the discussion on the dissociation mechanism has been scarce [228]. Hence, despite theoretical studies suggesting that strong electric fields may provide the energy required to dissociate the excitons [138, 352, 353], the physics of exciton dissociation in 2D TMDs remains to be experimentally investigated.

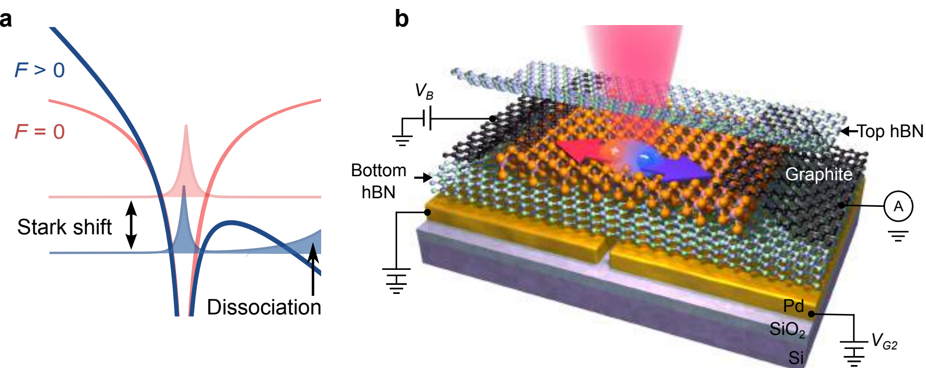

FIGURE 7.1: **Schematic of the exciton under high electric field and experimental concept. a)** Illustration of a Wannier-Mott exciton in the absence (red) and presence (blue) of a DC electric field. The exciton wave functions are represented by the shaded curves while the exciton potentials are shown by the thick solid lines. Applying an electric field shifts down the energy level of the exciton (Stark shift) and increases the leakage (via tunnelling) of the wave function to the continuum of states, which eventually leads to the dissociation of the exciton. **b)** Schematic of a monolayer WSe_2 device controlled by two local gates. Two graphite flakes (coloured in black) are placed on both sides of the WSe_2 layer (orange) and encapsulated between two hBN flakes (pale blue and green). The flakes are deposited on top of thin metallic (Pd) split gates, on a substrate of SiO_2/Si. We can apply gate voltages V_{G1} and V_{G2} on each local gate, as well as a bias voltage V_{B} between the two graphite flakes. The photocurrent resulting from the creation and dissociation of excitons (represented by a red hole and a blue electron) is measured through the graphite contacts.

In this chapter, we address this important issue by monitoring the exciton dissociation and subsequent transport of free carriers in a monolayer TMD p-n junction through spectrally and temporally resolved photocurrent measurements. Combining these two approaches allows us to assess and correlate two essential excitonic properties under high DC electric field, namely the Stark shift and the dissociation time. Further, we make use of the extreme thinness of 2D materials and their contamination-free assembly into heterostructures to reliably control the potential landscape experienced by the excitons. By placing the monolayer TMD (WSe_2) in close proximity to metallic split gates (Fig. 7.1b), we can generate high in-plane electric fields and drive a photocurrent (PC). We find that at low field the photoresponse time of our device is limited by the rate at which excitons tunnel into the continuum through the potential barrier created by their binding energy, a process known as tunnel ionization (Fig. 7.1a). Tuning the electric field inside the p-n junction further allows us to disentangle various dynamical processes of excitons and free carriers and to identify the kinetic bottlenecks that govern the performance of TMD-based optoelectronic devices.

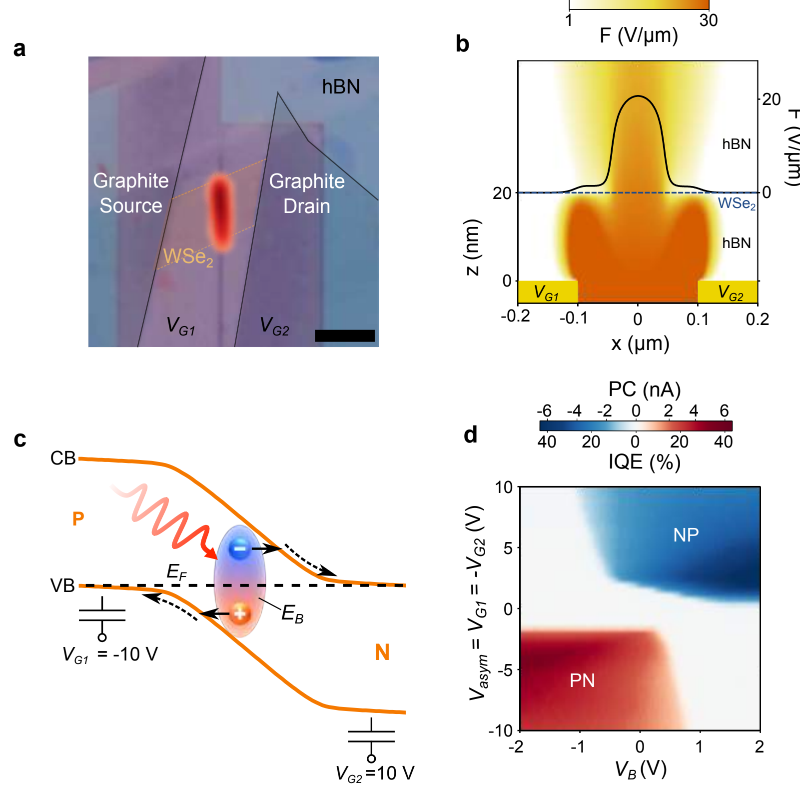

FIGURE 7.2: **Photocurrent generation in a monolayer WSe_2 p-n junction. a)** Optical image of a p-n junction device overlaid with a spatial PC map. The graphite and WSe_2 flakes are outlined and shaded for clarity. PC is measured at $V_{\mathrm{asym}} = V_{\mathrm{G1}} = -V_{\mathrm{G2}} = -10$ V and $V_{\mathrm{B}} = 0$ V, with a laser power $P = 1$ μW and a photon energy $h\nu = 1.65$ eV. The scale bar is 4 μm. **b)** Side view of the electric field distribution F across a device made of hBN (20 nm thick), monolayer WSe_2 (dotted blue line) and hBN (30 nm thick) atop metallic split gates separated by 200 nm (yellow rectangles). The field is calculated for $V_{\mathrm{asym}} = -10$ V and $V_{\mathrm{B}} = 0$ V. The colour bar above indicates the magnitude of $\log_{10}(F)$. The in-plane electric field $F(x)$ inside the WSe_2 is shown by the solid black line (right axis). **c)** Band diagram of the p-n junction between $x = -0.1$ and 0.1 μm calculated for $V_{\mathrm{asym}} = -10$ V and $V_{\mathrm{B}} = 0$ V. The solid orange lines represent the conduction (CB) and valence band (VB) and the black dotted line corresponds to the Fermi level (E_{F}). Following resonant optical excitation (red sinusoidal arrow), excitons (electron-hole pairs bound by a Coulomb energy E_{B}) are generated and dissociated via tunnel ionization (solid black arrows). The resulting free carriers drift out of the junction (dotted black arrows) and generate a photocurrent. **d)** PC measured at the junction as a function of V_{asym} and V_{B}, with a laser power $P = 0.5$ μW and a photon energy $h\nu = 1.65$ eV. The doping configuration (p-n or n-p) of the junction is indicated. The colour bar between above **d** displays the magnitude of the PC as well as the internal quantum efficiency, $IQE = \frac{PC}{e_0}\frac{h\nu}{A_{\mathrm{abs}}P}$, where $A_{\mathrm{abs}} = 5\%$ is the absorption coefficient.

7.2 Monolayer WSe_2 p-n junctions

Figs. 7.1b and 7.2a present a schematic and optical micrograph of our lateral p-n junction device made by assembling exfoliated flakes on metallic split gates (V_{G1} and V_{G2}) separated by 200 nm (see Section 3.2). Few-layer graphite flakes placed on both ends of a monolayer WSe_2 flake serve as ambipolar electrical contacts [180] that we use to apply a bias voltage V_B and collect the photogenerated charges. The lateral graphite-WSe_2-graphite assembly is fully encapsulated in hexagonal boron nitride, typically 20 nm thick, which provides a clean and flat substrate. Three devices were measured (see Section D.1), but unless otherwise specified, all measurements presented in this chapter are obtained at room temperature from the device shown in Fig. 7.2a.

Tuning of bias and gate voltages allows us to finely control the in-plane electric field F. Finite-element and analytical calculations of the electric field distribution in our device provide us with a precise estimate of F and the electrostatic doping inside the WSe_2 (see Section D.2 and Fig. 7.2b). Applying gate voltages of opposite polarity ($V_{\mathrm{asym}} = V_{G1} = -V_{G2} = -10$ V) leads to the formation of a sharp p-n junction (Fig. 7.2c) with an in-plane electric field reaching 21 V/μm (Fig. 7.2b). The photoresponse that we observed at the junction (Fig. 7.2a) follows a photodiode-like behaviour: PC is only generated in the p-n or n-p configuration (see Section D.1) and can be increased by applying a reverse bias voltage (Fig. 7.2d).

7.3 Field-dependent photocurrent spectroscopy

We probe the absorption spectrum in the photoactive region by measuring the PC as a function of photon energy $h\nu$ at a constant laser power P and in-plane electric field F. Fig. 7.3a shows the responsivity (PC/P) spectra of a device similar to the one presented in Fig. 7.2a, measured at various V_B and at low temperature (T = 30 K) in order to reduce thermal broadening. We observe a pronounced peak at a photon energy $h\nu$ = 1.73 eV, corresponding to the A exciton, and a step-like increase around 1.87 eV. For increasing electric field, this step-like feature broadens and an additional shoulder appears at 1.83 eV.

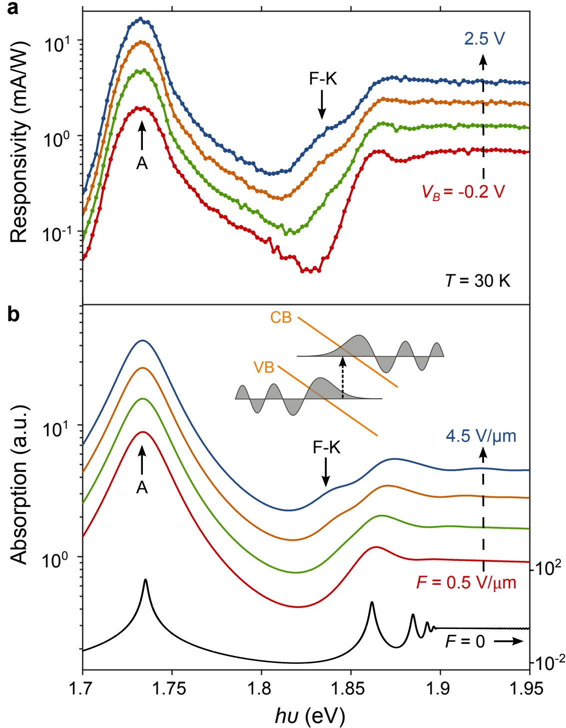

FIGURE 7.3: **Field-dependent photocurrent spectroscopy in monolayer WSe_2 p-n junctions.** **a)** Responsivity spectra measured at the p-n junction of Device 3 (Section D.1) for various $V_{\rm B}$, with a laser power $P = 1\ \mu$W and $T = 30$ K. The spectra are vertically shifted (by a factor of 1.5) for clarity. **b)** Absorption spectra calculated using a Wannier-Mott exciton model (Section D.3) for different in-plane electric fields F. The solid colored lines (left axis) were calculated with a phenomenological line shape broadening of 15 meV, while the black solid line (right axis) was calculated without broadening. All spectra are vertically shifted for clarity. Inset: Schematics illustrating the sub-bandgap, field-induced absorption increase due to the Franz-Keldysh effect. The application of an in-plane field tilts the conduction (CB) and valence band (VB) of the semiconductor (orange lines) and allows the wave functions of the free electrons and holes (gray shaded curves) to leak into the bandgap, which results in an increase of the sub-bandgap absorption (dotted arrow). The positions of the A exciton (A) and the absorption change attributed to the Franz-Keldysh (F-K) effect are indicated in **a** and **b**.

To identify the various spectral features, we compare the experimental spectra with those obtained from a model based on the 2D Wannier equation including the in-plane electric field (Section D.3). Screening by the TMD itself as well as the surrounding dielectric materials is described via the Keldysh potential for the electron-hole interaction. Fig. 7.3b shows calculated absorption spectra for different in-plane fields F. Excellent agreement between experiment and calculations is found assuming a bandgap of 1.9 eV, which yields a binding energy of $E_{\rm B} = 170$ meV for the A excitons consistent with the first-principles calculations. The unbroadened spectrum calculated at zero field (Fig. 7.3b, solid black line)

confirms the presence of multiple overlapping excited excitonic peaks below the bandgap. The calculated spectra for higher field reproduce remarkably well the field-induced increase of the sub-bandgap absorption observed experimentally. This is a manifestation of the Franz-Keldysh effect which results from the leakage of the free electron and hole wavefunctions into the bandgap (inset of Fig. 7.3b). We note that our experimental value of E_B agrees well with the one estimated from the diamagnetic shift of a monolayer WSe_2 encapsulated between silica and hBN [134]. Larger E_B has been observed in SiO_2-supported WSe_2 samples [131, 133, 135], underlining the role of the dielectric environment on the excitonic properties [130, 136].

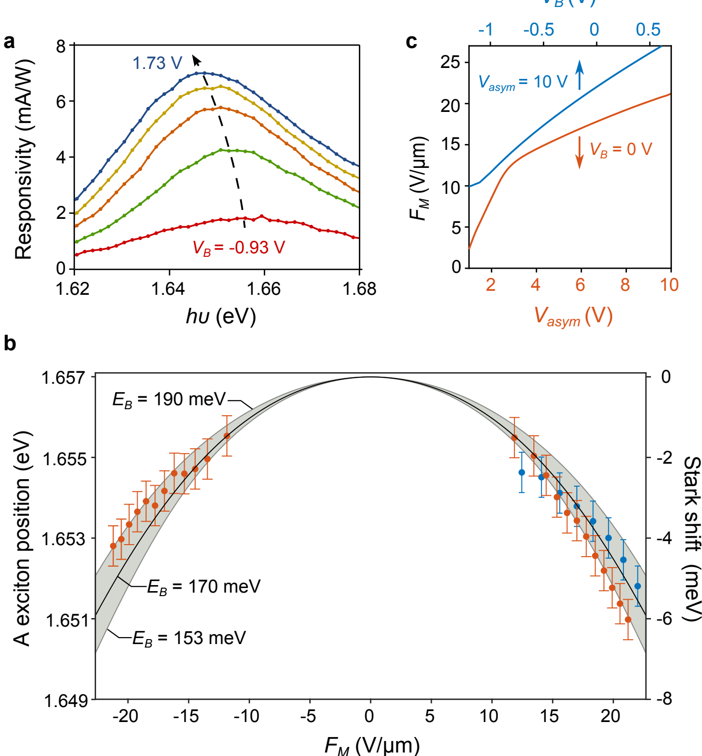

FIGURE 7.4: **DC Stack shift in a monolayer WSe_2. a)** Responsivity spectra (around the A exciton) measured on Device 1 (shown in Fig. 7.2a) at various V_B, with a laser power P = 0.5 μW, $V_{asym} = 10$ V and at room temperature. **d)** Position of the A exciton as a function of the calculated F_M for the same values of V_{asym} and V_B as the one shown in **e**. Orange data points correspond to different values of V_{asym} at $V_B = 0$ V, while blue data points represent different values of V_B at $V_{asym} = 10$ V. Error bars correspond to the spectral resolution of our measurements. The calculated Stark shifts (right axis) induced by the F_M are represented by the gray shaded curves ($E_B = 153$ and 190 meV) and black solid lines (E_B = 170 meV). **e)** Maximum in-plane electric field F_M calculated as a function of V_{asym} (with $V_B = 0$ V, solid orange line) and as a function of V_B (with $V_{asym} = 10$ V, solid blue line).

Turning our attention to the A exciton photocurrent peak, we observe a pronounced red-shift as V_{B} (Fig. 7.4a) and V_{asym} increase. We attribute this to the DC Stark effect. In first approximation, the Stark shift of a $1s$ exciton (without dipole moment) is given by $\Delta E = -1/2\alpha F^2$, where α is the in-plane polarizability. As shown in Fig. 7.4b, the A exciton energy shows a quadratic dependence with the maximum in-plane electric field F_{M} calculated for different values of V_{asym} and V_{B} (Fig. 7.4e), yielding a polarizability of $\alpha = (1 \pm 0.1) \times 10^{-6}$ Dm/V. This shift matches well with the predicted polarizability of $\alpha = 9.4^{-7}$ Dm/V for $E_{\mathrm{B}} = 170$ meV, thus supporting our previous spectral analysis. Interestingly, we note that the measured in-plane polarizability is two order of magnitude larger than the out-of-plane value recently obtained in PL experiments [353]. This strong anisotropy confirms the 2D nature of the A exciton and demonstrates the advantage of using in-plane electric fields for controlling the optical properties of TMDs [354].

7.4 Measurement of the photoresponse time

Along with the Stark shift, the application of a large in-plane electric field shortens the lifetime of excitons, which eventually decay into free electrons and holes (Fig. 7.1a). We probe these decay dynamics by assessing the photoresponse time τ of the device with time-resolved photocurrent measurements (TRPC, see section 2.5.3), banking on the nonlinear photoresponse of the WSe_2.

7.4.1 Nonlinear photoresponse

Figs. 7.5a,b show the strong sublinear power dependence of the photocurrent (and the corresponding responsivity) under resonant pulsed optical excitation ($h\nu = 1.65$ eV). As discussed in Section 6.3, many physical processes may be responsible for or contribute to the observed sublinearity, including phase space filling [159] and bandgap renormalization [160, 161]. However, recent time-resolved spectroscopy [154, 155] and photoluminescence [157] experiments indicate that in this exciton density regime ($N > 10^{11}$ cm^{-2}), exciton-exciton annihilation (EEA, or exciton Auger recombination) is the dominant nonradiative decay process for excitons in TMDs [153] (Section 1.2.3). To account for EEA in the rate equation governing the photocurrent, we add a loss term that scales quadratically with the exciton density (γN^2, where γ is the EEA rate). Assuming that each pulse generates an initial exciton population N_0, this model (see Section D.4) yields

$$PC \propto \ln(1 + \gamma\tau N_0), \tag{7.1}$$

which reproduces well the observed sublinear photoresponse (black lines in Figs. 7.5a,b). Moreover, the fits capture adequately the variation of the sublinear photoresponse with bias (Figs. 7.5a,b) and gate (Section D.4) voltages, from which

we extract the values of $1/\gamma\tau$ (Fig. 7.5c). Hence, these nonlinear measurements already offer an indirect way to probe the photoresponse time.

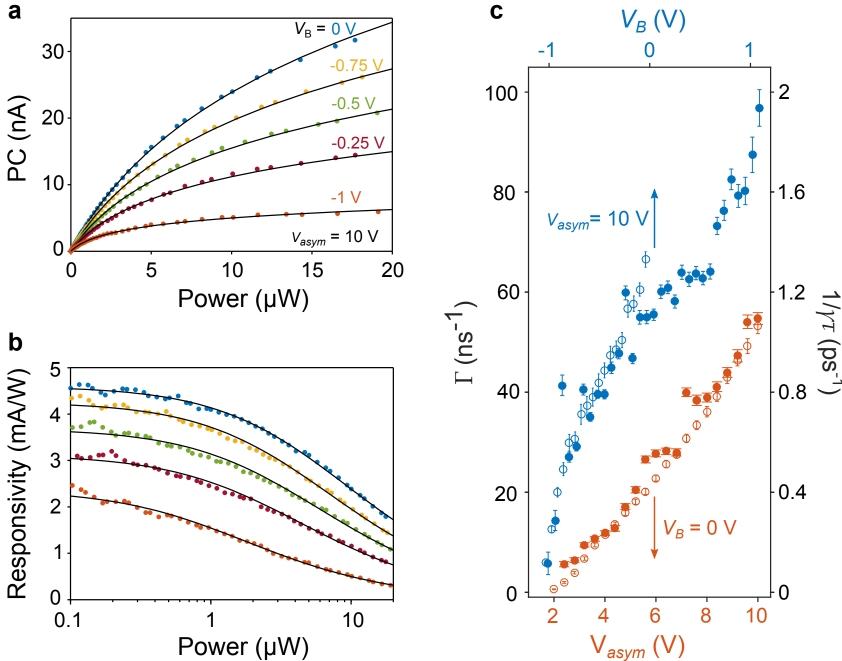

FIGURE 7.5: **Analysis of the nonlinear photoresponse due to exciton-exciton annihilation. a)** PC versus laser power P for various V_{B}, at $V_{\mathrm{asym}} = 10$ V and $h\nu = 1.65$ eV. **b)** Responsivity in the same conditions as **a**. The solid black lines in **a** and **b** are fits to the data using Eq. 7.1. **c)** Photoresponse rate $\Gamma = 1/\tau$ (filled circles, left axis) obtained from the TRPC measurements (shown in Fig. 7.6 and Section D.4) and $\Gamma/\gamma = 1/\gamma\tau$ (open circles, right axis) obtained from the power dependence measurements (shown in **a**, **b** and Section D.4) as a function of V_{asym} at $V_{\mathrm{B}} = 0$ V (orange, lower axis) and V_{B} at $V_{\mathrm{asym}} = 10$ V (blue, top axis). Good agreement between TPRC and nonlinear PC measurements is found for a EEA rate of $\gamma = 0.05$ cm^2/s. The error bars correspond to the standard deviations obtained from the fits.

7.4.2 Time-resolved photocurrent

In order to directly extract τ, we resonantly excite A excitons in the p-n junction with a pair of 200 fs-long laser pulses separated by a variable time delay Δt, for various values of V_{asym} (Fig. 7.6). Due to the sublinear power dependence, the photocurrent displays a symmetric dip when the two pulses coincide in time ($\Delta t = 0$). By extending our nonlinear photocurrent model to the case of two time-delayed pulses (Section D.4), we can show that the time dependence of this dip is dominated by an exponential time constant corresponding to the intrinsic photoresponse time τ of the device. The photoresponse rate $\Gamma = 1/\tau$ is extracted

from TRPC measurements at various values of V_{asym} (Figs. 7.6) and V_{B} (Section D.4) and presented in Fig. 7.5c. We observe that Γ increases markedly with gate and bias voltages, and remarkably follows the same trend as the values of $1/\gamma\tau$ obtained from the power dependence measurements. Comparing these two results, we obtain an EEA rate of $\gamma = 0.05$ cm^2/s, which is similar to those found in WSe_2 [155] and MoS_2 [154] using time-resolved spectroscopy. We also note that the shortest response time we measure, $\tau = 10.3 \pm 0.4$ ps, translates into a bandwidth of $f = 0.55/\tau \sim 50$ GHz, which compares with the fastest responses measured in TMD-based photodetectors [271] (see Section 6.3).

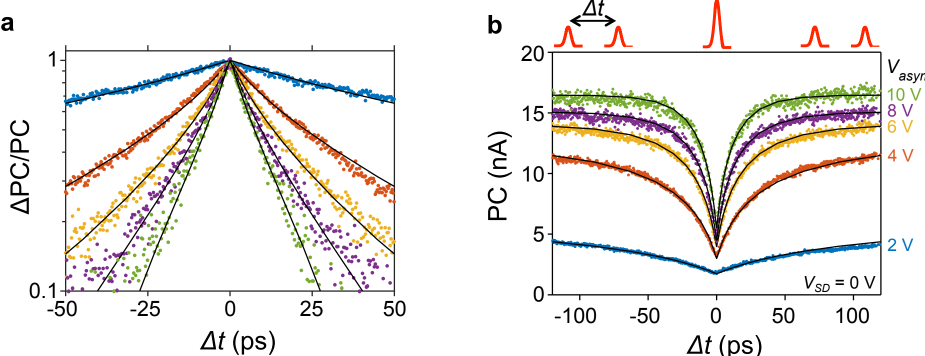

FIGURE 7.6: **Determination of the photoresponse τ by time-resolved photocurrent measurements.** **a)** PC as a function of time delay Δt between two pulses (illustrated above the plot) at various value of V_{asym}, with time-averaged $P = 100$ μW and $V_{\mathrm{B}} = 0$ V. **b)** Same data as in **d** but plotted with the normalized $\frac{\Delta PC}{PC} = \frac{PC(\Delta t \to \infty) - PC(\Delta t)}{PC(\Delta t \to \infty) - PC(\Delta t = 0)}$. The solid black lines in **a** and **b** are fits to the data using the model described in Section D.4. The photoresponse rate $\Gamma = 1/\tau$ extracted from these fits are shown in Fig. 7.5c.

7.5 Exciton dissociation and photocurrent dynamics in monolayer WSe_2

To directly address the exciton dissociation caused by the in-plane electric field F_{M}, we examine the dependence of the photoresponse rate Γ on F_{M} at the p-n junction (Fig. 7.7a). Clearly, two regimes can be distinguished. The rapid increase of Γ with F_{M} is attributed to dissociation by tunnel ionization. We verify this by comparing the measured Γ to the calculated tunnel ionization rate Γ_{diss}, obtained by introducing the complex scaling formalism in the 2D Wannier exciton model (Section D.3). According to this model, Γ_{diss} can be evaluated in first approximation by the product of the uncertainty-limited exciton lifetime $E_{\mathrm{B}}/\hbar$ and the exponential tunneling term $\exp(-E_{\mathrm{B}}/e_0 dF)$, where d is the exciton diameter (or Bohr radius). We find that the dependence of Γ at low field ($F_{\mathrm{M}} < 15$ V/μm) coincides well with the calculated dissociation rate of excitons with $E_{\mathrm{B}} = 170$ meV, in agreement with our photocurrent spectroscopy analysis.

More importantly, this shows that in the low-field regime the exciton dissociation process is the rate-limiting step governing the generation of photocurrent.

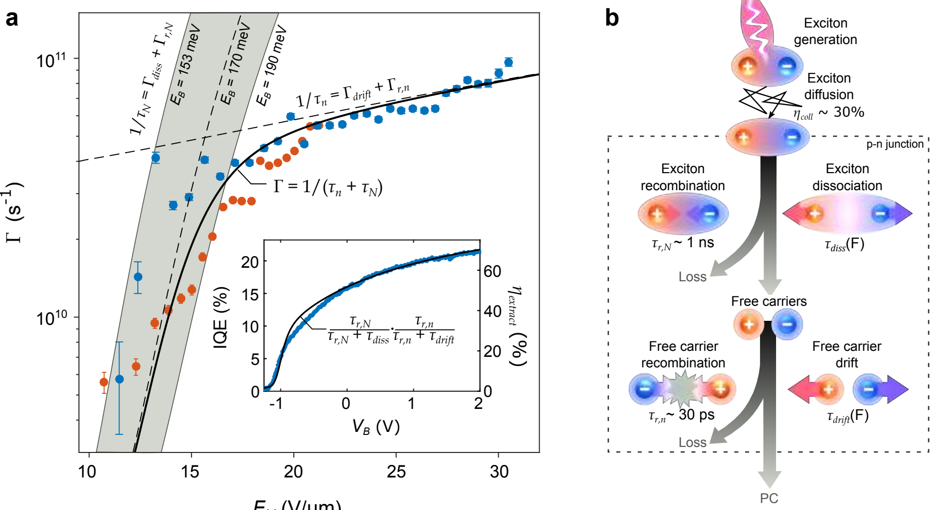

FIGURE 7.7: **Dynamic processes governing the photoresponse of monolayer WSe_2 p-n junctions.** **a)** Photoresponse rate $\Gamma = 1/\tau$ measured by TRPC (same data as Fig. 7.5c) versus maximum in-plane electric field F_{M} calculated for various values of V_{asym} (with $V_{\mathrm{B}} = 0$ V, orange points) and V_{B} (with $V_{\mathrm{asym}} = 10$ V, blue points). At low field ($F_{\mathrm{M}} < 15$ V/μm), the photoresponse is well described by the total exciton rate $\Gamma_N = 1/\tau_N = \Gamma_{\mathrm{diss}}(F_{\mathrm{M}}) + \Gamma_{\mathrm{r},N}$, where $\tau_{\mathrm{r},N} = 1/\Gamma_{\mathrm{r},N}$ is the exciton lifetime at zero field ($\tau_{\mathrm{r},N} \sim 1$ ns) and Γ_{diss} is the exciton dissociation rate predicted by the 2D Wannier exciton (SI) with a binding energy between $E_{\mathrm{B}} = 153$ and 190 meV (gray shaded curves) and $E_{\mathrm{B}} = 170$ meV (dotted black line). At high field ($F_{\mathrm{M}} > 20$ Vμm), the photoresponse is governed by the total free carrier rate $\Gamma_n = 1/\tau_n = \Gamma_{\mathrm{drift}}(F_{\mathrm{M}}) + \Gamma_{\mathrm{r},n}$ (dotted black line), where $\tau_{\mathrm{r},n} = 1/\Gamma_{\mathrm{r},n}$ is the free carrier lifetime at zero field ($\tau_{\mathrm{r},n} \sim 30$ ps) and Γ_{drift} is the rate at which carriers (with a mobility $\mu = 4$ cm^{2}V^{-1}s^{-1}) drift out of the junction (Section D.5). Since exciton dissociation and free carrier drift are consecutive processes, the total photoresponse rate of the device is $\Gamma \approx 1/(\tau_N + \tau_n)$ (black solid line). Inset: IQE versus V_{B} measured at $V_{\mathrm{asym}} = 10$ V extracted from Fig. 7.2d (left axis, blue data points). Extraction efficiency, $\eta_{\mathrm{extract}} = \frac{\tau_{\mathrm{r},n}}{\tau_{\mathrm{r},n}+\tau_{\mathrm{drift}}} \frac{\tau_{\mathrm{r},N}}{\tau_{\mathrm{r},N}+\tau_{\mathrm{diss}}}$, calculated with our model versus V_{B} (right axis, black solid line). **b)** Schematic of the processes contributing to the photoresponse of the device. Excitons are generated by resonant optical excitation and approximately 30% (η_{coll}) of them reach the p-n junction by diffusion during their lifetime $\tau_{\mathrm{r},N}$. Excitons entering the p-n junctions (black dotted box) may either recombine with a time constant $\tau_{\mathrm{r},N}$ or dissociate by tunnel ionization at a rate Γ_{diss}. The resultant free carriers generate a photocurrent as they as they drift out of the junction at a rate Γ_{drift}, but a fraction are also lost due to their finite lifetime $\tau_{\mathrm{r},n}$. Holes and electrons are represented by red and blue spheres.

At high electric field ($F_{\mathrm{M}} > 20$ V/μm), the response rate deviates from the

dissociation rate-limited model and enters a new regime characterized by a more moderate increase of Γ with F_{M}. The observed linear scaling of $\Gamma(F_{\mathrm{M}})$ suggests that, in this regime, the photoresponse rate is limited by the drift-diffusive transport of free carriers out of the p-n junction. By considering a carrier drift velocity $v_{\mathrm{drift}} = \mu F$, we estimate that carriers generated in the center of the junction of length $L = 200$ nm escape the junction at a rate $\Gamma_{\mathrm{drift}} = 2\mu F/L$. Comparing this simple expression (dotted line in Fig. 7.7a) to the measured Γ at high field, we find $\mu = 4 \pm 1$ cm^{2}V^{-1}s^{-1}, which is very similar to the room-temperature field-effect mobility that we measure in our sample ($\mu_{\mathrm{FE}} \sim 3$ cm^{2}V^{-1}s^{-1}, see Section D.1).

A complete photocurrent model is achieved by introducing competing loss mechanisms caused by the radiative and non-radiative recombination of excitons (Section 1.2.3). Good agreement with the experimental data is obtained by considering the finite lifetime of excitons ($\tau_{\mathrm{r},N} = 1/\Gamma_{\mathrm{r},N}$ ~1 ns [157, 162]) and free carriers ($\tau_{\mathrm{r},n} = 1/\Gamma_{\mathrm{r},n}$ ~30 ps [159]) at zero electric field. This complete picture of the dynamical processes (Fig. 7.7b) offers valuable insights into the internal quantum efficiency (IQE) of the photocurrent generation mechanism in this device. Indeed, the efficiency η of each photocurrent step depends on the competition between the PC-generating (τ_{drift}, τ_{diss}) and the loss $\tau_{\mathrm{r},N}$, $\tau_{\mathrm{r},n}$) pathways, such that $\eta_{\mathrm{diss/drift}} = \frac{\tau_{\mathrm{r},N/n}}{\tau_{\mathrm{r},N/n}+\tau_{\mathrm{diss/drift}}}$. In the inset of Fig. 7.7a, we compare the IQE measured at low power as a function of V_{B} with the total extraction efficiency $\eta_{\mathrm{extract}} = \eta_{\mathrm{drift}}\eta_{\mathrm{diss}}$ derived from the kinetic model shown in Fig. 7.7b. We find that η_{extract} captures very well the bias dependence of the IQE, indicating that we correctly identified the relevant PC-generating processes. The field-independent discrepancy of 30% is attributed to the collection efficiency η_{coll}, which we define as the ratio between the number of excitons reaching the p-n junction and the number of absorbed photons. This value coincides with our analysis of the measured photocurrent profile and with the prediction of our exciton diffusion model (see Section D.6).

7.6 Conclusion and outlook

In summary, our study offers an intuitive and coherent understanding of the behavior of excitons and free carriers in monolayer TMDs under strong in-plane electric field. We find that despite their large binding energy (170 meV), excitons can efficiently dissociate via tunnel ionization, thereby overcoming the kinetic bottleneck that limits the quantum efficiency and photodetection rate of these 2D semiconductors at low field. Further investigations of the exciton in the high-field regime might reveal new exciting phenomena such as impact ionization and excitation, which hold potential for boosting optoelectronic performances of TMDs. Our results demonstrate the potential of monolayer TMDs as a platform to study many-body physics and design future optoelectronic devices.

Conclusion

Research in optoelectronics bridges the fields of electronics and optics by studying and creating electronic systems that generate, detect and control light. One of the main objectives of optoelectronics is to understand how photons are converted into electricity in materials. This knowledge provides the basis for designing faster optical communications systems and more efficient solar energy conversion modules, two important scientific challenges of our time.

Summary

In this thesis we explored the potential of newly discovered 2D materials for photodetection by investigating their photocurrent generation mechanisms and probing the physical processes governing their photoresponse. To do so, we employed improved fabrication and measurement techniques, notably a versatile time-resolved photocurrent (TRPC) technique that enabled us to monitor the dynamic processes responsible for the photocurrent. We examined four different optoelectronic systems based on graphene, TMDs (WSe_2), hBN and their heterostructures. These systems can be categorized by their main photoactive material (graphene or TMD) and the direction (in-plane or out-of-plane) in which the photocurrent flows (Fig. 3). These categories provide an intuitive framework for understanding the photodetection mechanisms of each 2D material system.

The type of photoactive material (e.g., metallic, semiconductor) determines, to large extent, the form (electronic heat or potential energy) in which the excess energy deposited by light is stored. As discussed in Chapter 2, this excess electronic energy drives different photodetection mechanisms. Our investigation of graphene-based devices (Chapters 4 and 5) showed that light absorbed by graphene is rapidly and efficiently converted into a hot-carrier distribution. These hot carriers can generate a photocurrent via the photo-thermoelectric (Chapter 4) or photo-thermionic (Chapter 5) effect. In contrast, in Chapters 6 and 7, we found that in TMDs, this energy creates excess carriers, which, depending on the dielectric environment, can form strongly bound excitons. Once dissociated into free carriers, these charges can create a photocurrent by means of the photoconductive or photovoltaic effect.

The photodetection geometry (in-plane or out-of-plane) has important implications on the transport of the photoexcited carriers. Indeed, as observed in Chapters 4 and 7, intralayer (in-plane) transport is normally governed by drift

or diffusive processes, whereas interlayer (out-of-plane) transport often involves tunneling or interlayer transfer (emission) processes (Chapters 5 and 6). The geometry of the photodetector also affects the photon harvesting and carrier extraction efficiency. In the in-plane configuration, the photocurrent is usually produced at a quasi-1D interface which restricts the size of the photoactive area. Out-of-plane structures, however, can make use of the entire 2D plane of the photoactive material, and the extreme thinness of the materials potentially allows for rapid vertical extraction of the photocarriers.

More specifically, our effort to understand the optoelectronic response of various 2D materials and vdWHs led to the following achievements and findings:

In Chapter 4 we studied the photocurrent generated at different interfaces in in-plane graphene devices and demonstrated that in every case, photocurrent was driven by hot carriers via the photo-thermoelectric (PTE) effect. We further showed, for the first time, that the generation of a PTE photovoltage (due to carrier heating) in graphene is extremely fast ($\tau_{\mathrm{heat}} < 50$ fs). From the flat and broad spectral responsivity, we inferred that the carrier heating is fast enough to outcompete energy loss processes. These results confirm the great potential of graphene for ultrafast and broadband photodetector applications. Indeed, they indicate that the carrier heating process is not limiting the efficiency and photoresponse time of graphene photodetectors; rather, their performance is governed by the subsequent ps-long cooling of the carriers. The effect of the encapsulating material on this process requires further investigation.

In Chapter 5 we explored new ways to exploit the photodetection potential of graphene. With this in mind, we investigated the interlayer transport of photocarriers in various graphene-based heterostructures. Using G/WSe_2/G heterostructures, we first demonstrated the possibility of detecting infrared light by vertically extracting the hot carrier generated in graphene, a new mechanism that we called photo-thermionic emission. This process, which is characterized by a superlinear power dependence and a photoresponse time of ~ 1 ps, was also detected in G/hBN/G heterostructures. At a large interlayer bias and high photon energy excitation, an additional photocurrent mechanism emerged in these structures, identified as photon-assisted tunneling. In this regime, the interlayer tunneling process outcompetes the intralayer carrier thermalization in graphene, allowing us to estimate once more the carrier thermalization time ($\tau_{\mathrm{heat}} \sim 10$ fs, in agreement with Chapter 4). Our understanding of photon-induced interlayer transport in graphene has opened a promising avenue for optoelectronic applications that require size-scalable active areas, electrical tunability, broadband and ultrafast response.

In Chapter 6 we assessed the photodetection performance of G/WSe_2/G heterostructures (the same as those studied in Chapter 5) in the visible region, where the strong photoresponse of WSe_2 dominates. Varying the thickness of and the bias across the TMD layer allowed us to identify the dynamic processes

controlling the response time and efficiency of these devices, such as the out-of-plane drift, recombination and interlayer transfer of photocarriers. We showed that these photodetectors can simultaneously possess a high efficiency ($> 70\%$) and fast photoresponse on the order of 5 ps, translating into an intrinsic bandwidth of $\sim$ 100 GHz. Our observations and understanding of ultrafast and efficient photodetection demonstrate, for the first time, the potential of TMD-based heterostructures as a platform for high-speed optoelectronic applications.

In Chapter 7 we investigated the physics of 2D excitons and free carriers in monolayer TMDs under strong in-plane electric fields. Performance time- and spectrally-resolved photocurrent measurements allowed us to monitor the field-induced exciton Stark shift and dissociation time, as well as the Franz-Keldysh effect. In combination with theoretical calculations, these measurements demonstrate that at low field, the photoresponse time of our device is governed by the tunnel ionization rate of excitons, while at high field, the drift of free carriers is the main limiting process. These findings provide crucial insight into the physics of 2D excitons and the dynamic processes governing the performance of optoelectronic devices based on monolayer semiconductors.

2D materials for ultrafast photodetection

As a whole, these results clearly demonstrate the potential of 2D materials and vdWHs for ultrafast photodetection applications, such as on-chip high-speed optical communications. In Fig. 7.8 we compare the bandwidth(i.e., the 3 dB cutoff frequency) and responsivity of state-of-the-art, commercially available photodetectors (yellow stars) with those (measured or extrapolated) of the 2D material-based devices presented in this thesis (open circles and squares). For comparison, we also include some of the best high-speed photodetectors made of 2D materials that have been reported to date (filled dots).

From this figure, we conclude that the performance of 2D material-based photodetectors are comparable, and in some cases, superior to those of existing technologies made of Si and GaAs. This is already quite impressive considering that 2D materials are still in their infancy and devices have not yet been optimized or extensively engineered. Among the 2D materials, graphene appears to be that with the most potential for ultrafast photodetection, as its intrinsic bandwidth reaches almost 1 THz. However, its relatively weak absorption ($A_{\text{abs}} \approx 2.3\%$) results in low responsivity in our photo-thermoelectric and photo-thermionic devices. As ref. [48, 260] demonstrated (Fig. 7.8, red filled circles), this problem can be alleviated by combining graphene photodetectors with a silicon waveguide.

One of the main achievements of this thesis was to demonstrate, for the first time, the potential of TMD for fast detection. Fig. 7.8 shows the performances of G/WSe_2/G with different WSe_2 thicknesses as well as those of a monolayer

WSe_2 p-n junction. Due to their lower intrinsic absorption (compared to multilayer devices) and other limitations (exciton dissociation, recombination and interfacial energy transfer), devices made of monolayer WSe_2 typically display lower responsivities. As noted in Chapter 6, G/WSe_2/G devices made of trilayer WSe_2 offer the best compromise in terms of speed and responsivity, and compare very well with the best graphene photodetectors. Further work is needed to confirm the large 3 dB cutoff frequency of these devices, ideally using a waveguide-integrated structure.

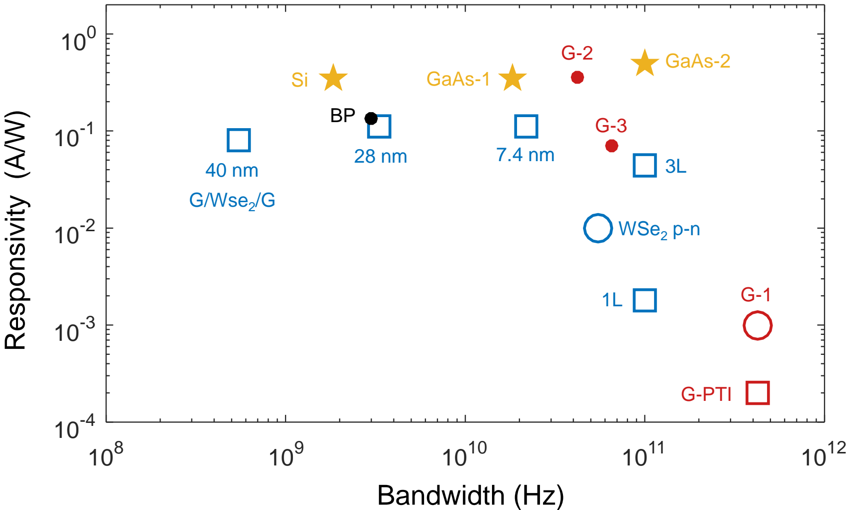

FIGURE 7.8: **Comparison of the performances of 2D materials and vdWHs for ultrafast photodetection.** Responsivity ($\Re = \text{PC}/P$) versus bandwidth (or, equivalently, 3 dB cutoff frequency f_c) for various commercial photodetectors and 2D material-based photodetectors. The photodetectors investigated in this thesis are represented by the open symbols. Their bandwidth is estimated from their measured photoresponse time τ using the formula $f_c = 0.55/\tau$. Red open circle (G-1): in-plane graphene p-n junction (Chapter 4). Red open square (G-PTI): G/WSe_2/G device in the infrared, based on the photothermionic effect (Chapter 5). Blue open squares (G/WSe_2/G): G/WSe_2/G in the visible, based on the photoconductive effect. The thickness (or layer number) of the WSe_2 layer is indicated in the figure. Blue open circle: p-n junction made of monolayer WSe_2 (Chapter 7). State-of-the-art photodetectors (integrated with silicon waveguides) made of 2D materials are represented by the filled circles. Black filled circle (BP): Black phosphorus-based photodetector [233]. Red filled circle: in-plane graphene photodetectors reported by Shiue *et al.* [260] (G-2) and Schuler *et al.* [48] (G-3). Commercially available photodetectors are represented by the filled yellow stars. Si: Silicon PIN photodiodes from Hamamatsu (S90055-01). GaAs-1: GaAs MSM photodetector from Hamamatsu (G4176). GaAs-2: 100 GHz waveguide-integrated photodiode from Finisar (XPDV412xR).

Outlook

Despite the remarkable performance of 2D materials and vdWHs photodetectors, many important challenges need to be overcome in order to turn these proof-of-concept devices into practical and marketable technologies [7, 355, 356]. First, the development synthesis method capable of producing large-scale, high-quality and low-cost 2D materials is imperative. Considerable progress has been made in the production of graphene [280, 357], and other 2D materials should soon follow [358, 359]. More efforts are also needed to develop fabrication (or synthesis) methods for the assembly (or growth) of large-scale vdWHs with precisely controlled chemical composition, layer thicknesses and relative crystallographic orientation [178, 179, 290, 360].

Besides these crucial technical issues, one of the major - if not the main – challenges for the commercialization of 2D material-based photodetectors (and other devices) is to find novel applications that exploit the unique properties and advantages of these materials. Indeed, as Herb Kroemer - Nobel laureate in Physics for his research on conventional heterostructures - wrote [361]: “The principal applications of any sufficiently new and innovative technology have always been - and will continue to be - applications created by that technology”. Finding radically new applications that fully unlock the potential of 2D materials and vdWHs, however, is an extraordinarily difficult task, which calls for a deeper understanding and broader exploration of the 2D material family.

The optoelectronics of 2D materials is a thriving field of research. Recent advances in the study of the valley pseudospin of graphene and TMDs have opened an entire subfield aiming to control this novel degree of freedom for information processing [119, 120]. Research is progressing at a fast pace, as evidenced by the recent demonstration of the valley Hall effect [118], valley-selective optical Stark effect [349, 350] and optical manipulation of the valley pseudospin [362]. The recent discovery of layered Weyl semimetals [363, 364], bulk materials that can be regarded as three-dimensional analogues of graphene, has also spurred a lot of interest and provides interesting opportunities to investigate and control Weyl fermions with light [364].

This might only be the tip of the iceberg. As these lines are being written, a new layered material, with new properties is undoubtedly being exfoliated and studied in one of the numerous research groups across the world. With an estimated ~ 100 stable 2D materials and endless stacking combinations, there is, as Feynman would say [1], “plenty of space at the bottom” of flatland.

Appendix A

Fabrication recipes

A.1 Layer assembly procedure

The following recipe explains in details how to assemble vdW heterostructures. For the clarity, Fig. A.1a presents a flowchart of the process and Figs. A.1b,c show images of the transfer setup used for the assembly process.

Exfoliation

1. Using tweezers, place a small piece of bulk layered crystal on a tape (e.g. R1011 from Ultron Systems) or commercial PDMS sheet (Gel-Pak®)
2. Fold and unfold the tape a few times until a sizable area ($\sim 2 \times 2$ cm) of the tape is covered with thin flakes.
3. Deposit flakes by pressing the tape on the desired substrate and peeling it slowly.
4. Identify the desired flakes under a microscope.

Polydimethylsiloxane (PDMS) preparation

1. Mix a 10:1 ratio of Sylgard® 184 Silcone elastomer (Dow Corning) base with the specific curing agent.
2. Stir vigorously for 3 minutes in a 14.5 cm-diameter petri dish and spread out evenly.
3. Sonicate for $\sim$ 4 minutes to remove bubbles.
4. Cover and cure overnight.

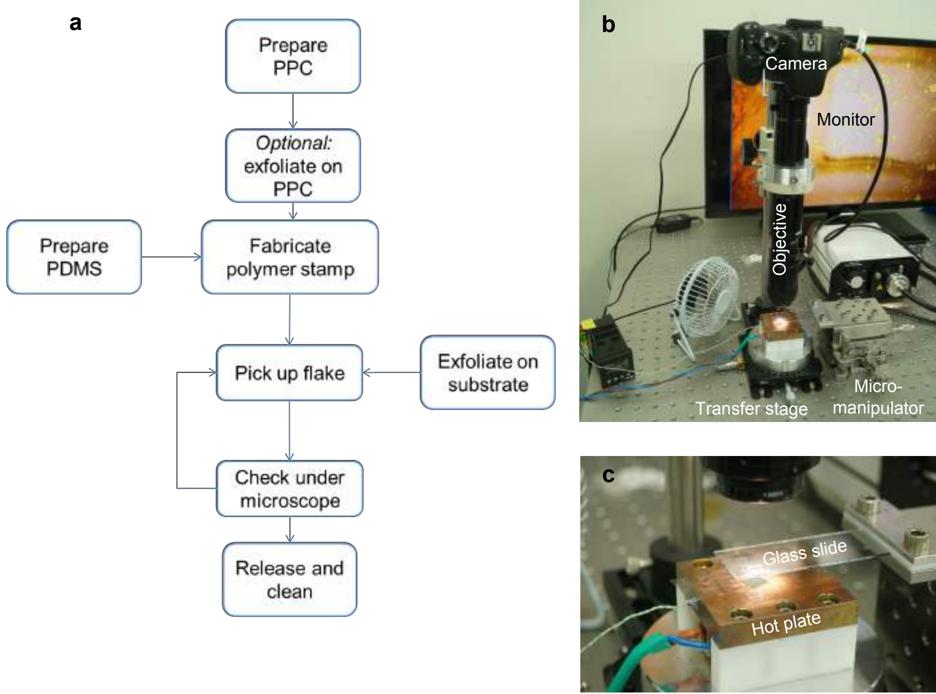

FIGURE A.1: **Flowchart of the layer assembly process and description of transfer setup. a)** Flowchart of the layer assembly process. **b** Photograph of the transfer setup used to assemble layers into vdW heterostructures. **c** Close-up on the transfer stage.

Polypropylene carbonate (PPC) preparation

1. Put PPC pellets (Sigma Aldrich) into anisole (99%, Sigma-Aldrich) to obtain a 15% (by weight) solution.
2. Sonicate until pellets are fully dissolved ($\sim$ 6 hours).

Fabrication of the transparent polymer stamp

1. Cut out a small piece (5$\times$5 mm) of PDMS from the petri dish.
2. Place the PDMS stamp on the extremity of a microscope glass slide.
3. Make sure that there are no bubble or contamination trapped at the glass-PDMS interface, and that the top of the PDMS surface is clean. If not, pressing and peeling a piece of Scotch Tape on the surface usually helps removing the dirt.
4. Spincoat PPC on a microscope slide (50 s at 1500 rpm)

5. Bake at $\sim$ 70°C for 2-3 minutes.
6. Optional: deposit exfoliated flakes on PPC using a commercial PDMS sheet cover with flakes. Peel extremely slowly. Find the desired flake.
7. Cut a small hole (slightly larger than the PDMS piece) in a piece of Scotch Tape with an X-acto knife.
8. Stick the Scotch Tape onto the PPC. In case flakes are exfoliated on the PPC, align the hole of the tape with the desired flake.
9. Peel the Scotch Tape. The PPC should detach from the substrate. Manipulate carefully to make sure that the suspended membrane of PPC remains intact.
10. Align the suspended PPC membrane and slowly deposit it on top of the small PDMS stamp. Keep the sticky side of the Sotch Tape face down such that it can adhere to the glass slide supporting the PDMS stamp.
11. Bake the glass slide covered with the PDMS/PPC stamp on a hot plate at $\sim$70°C for 1-2 minutes. This will make the PPC conform to the PDMS stamp.
12. Check under microscope that most of the PPC layer is clean and flat. If flakes were exfoliated on PPC, check that the desired flake is intact.

Pick up procedure

1. Stick the substrate supporting the flake to be picked up on the stage of the transfer setup using double-sided tape. Find the desired flake on the monitor by moving stage.
2. Install the glass slide supporting the polymer stamp on the micromanipulator with the stamp facing down towards the transfer stage.

   For picking up the first flake:

3. Lower down the PPC/PDMS stamp. Before bringing the stamp into contact with the flake on the substrate, make sure that the area of the PPC over the flake is clean.
4. Heat up the stage to 35-40°C and turn off the heater.
5. Once the stage has cooled down to room temperature, peel off the PPC from the substrate as slowly as possible by lifting up the glass slide with the micromanipulator.
6. If the desired flake has not been successfully picked up, rotate the stage to a different angle and repeat the pick-up process.

7. Inspect the picked-up flake.

   For picking up the next flake:

8. Find the picked-up flake(s) lying on the PPC by moving the glass slide with the micromanipulator.
9. Adjust the position and rotation of the (bottom) flake on the stage in order to align it with the picked-up flake(s)
10. Slowly bring the flakes into contact. Correct their positions as the glass slide is lowered down.
11. Heat up the stage to 35-40°C and turn off the heater.
12. Once the stage has cooled down to room temperature, peel off the PPC from the substrate as slowly as possible by lifting up the glass slide with the micromanipulator.
13. Inspect the picked-up flakes.

Release and cleaning procedure

The picked-up flakes can be released on a substrate or on another final flake. In both case the procedure is the same:

1. Stick the substrate supporting the flake to be picked up on the stage of the transfer setup using double-sided tape. Find the desired flake on the monitor by moving stage.
2. Install the glass slide supporting the polymer stamp and the picked-up flakes on the micromanipulator.
3. Bring the picked-up flakes into contact with the final substrate or flake.
4. Heat the transfer stage to 90°C. Note: Heating the stage before the flakes and substrate are brought into contact helps reducing the formation of contamination bubbles.
5. Slowly peel off the PPC from the PDMS stamp by lifting up the glass slide with the micromanipulator.
6. Put the substrate supporting the released heterostructure and PPC film in acetone for 2-3 minutes.
7. Dip the substrate in IPA and blow-dry it.

A.2 Laser writer

To perform this lithography step we employ a Laser writer system by MICROTEC (LW405).

1. Spin coat the sample with AZ5214 resist at 4000 rpm during 40 s.
2. Bake for 60 s at 100°C.
3. Draw the exposition pattern in-situ using the laser writer software.
4. Expose. Typical parameters are: lens = 5, gain = 11.5, filter = 3, d-step = 2.
5. Develop in a solution of AZ-351 B and water (1:4 volume ratio) for 30-50 s.

Appendix B

Complementary information: Photo-thermionic effect in G/WSe_2/G heterostructures

B.1 Cooling pathways of thermalized hot carriers in graphene

For our experiment, we consider the energy pathways illustrated in Fig. B.1a (see Section 1.1.3 for a more general discussion on these processes). Photons with an energy larger than twice the graphene Fermi level ($E_{\mathrm{photon}} > 2E_{\mathrm{F}}$) are absorbed in graphene due to interband transitions, creating photoexcited electrons and holes with energy $E = E_{\mathrm{photon}}/2$. This energy is transferred to the phonon and electron bath typically through optical phonon emissions or carrier-carrier scattering, respectively. These processes are characterized by the energy-loss rate of the photoexcited carrier due to optical phonon emission $\Gamma_{\mathrm{e-op}}$ and carrier-carrier scattering $\Gamma_{\mathrm{e-e}}$. Due to strong carrier-carrier interactions in graphene, carriers thermalize among themselves on ultrafast timescale (within 50 fs), which leads to a branching ratio between the two processes $\Gamma_{\mathrm{e-e}}/\Gamma_{\mathrm{e-op}}$ larger than 1 (see Chapter 4). This implies that most of the absorbed photon energy is redistributed to the electron bath. Hence, in our experiment we consider that $\eta_{\mathrm{heat}} = 70\%$ of the laser power absorbed in graphene is transferred to the electron bath [89], giving rise to a thermalized hot carrier distribution with temperature T_e.

Hot thermalized carriers subsequently cool down to equilibrate with the phonon (lattice) temperature T_{ph} and the ambient temperature T_0. This cooling can be due to various processes such as the emission of intrinsic acoustic phonons [98], disorder-enhanced supercollisions with acoustic phonons [76], interaction substrate phonons [79] and in-plane heat dissipation via diffusion of hot carriers. All these mechanisms exhibit a different dependence on T_{e}. To simplify, we assume that for low increase in electronic temperature ($\Delta T = T_{\mathrm{e}}–T_{\mathrm{ph}} \ll T_{\mathrm{ph}}$) the

cooling of hot carriers is proportional to ΔT with an electron-phonon coupling constant $\Gamma_{\mathrm{e-ph}}$. This coupling increases the phonon bath temperature T_{ph} and is finally dissipated through the substrate (at temperature T_0) at a rate Γ_0. Hence, we model the temperatures of the electron and phonon bath using the following equations:

$$C_{\mathrm{e}}\frac{\mathrm{d}T_e}{\mathrm{d}t} = P_{\mathrm{in}}(t) - \Gamma_{\mathrm{e-ph}}(T_{\mathrm{e}} - T_{\mathrm{ph}}) \tag{B.1}$$

$$C_{\mathrm{ph}}\frac{\mathrm{d}T_p h}{\mathrm{d}t} = \Gamma_{\mathrm{e-ph}}(T_{\mathrm{e}} - T_{\mathrm{ph}}) - \Gamma_0(T_{\mathrm{ph}} - T_0), \tag{B.2}$$

where C_{e} is the electronic heat capacity 1.1.1, $P_{\mathrm{in}}(t)$ is the laser power density that is absorbed by graphene (approximately 0.5% absorption considering the dielectric permittivity of the surrounding medium [326]) and transferred to the electronic bath. C_{ph} is the phonon heat capacity which we assume to be roughly 10^4 times larger than C_{e} [365].

The temperature dynamics predicted by Eqs. B.1 and B.2 largely depends on the rate-limiting relaxation step. Since the out-of-plane (c-axis) thermal conductivity of boron nitride is approximately 2 W/mK [366], we estimate $\Gamma_0 \sim 30$ MW/m^{2}K for our 70-nm-thick hBN substrate. This value is much larger than theoretical estimates of $\Gamma_{\mathrm{e-ph}}$, which are typically between 0.5 and 5 MW/m^{2}K [79]. Therefore, the electron-phonon cooling creates a "bottleneck" that confines the heat in the electron bath. We also note that since the in-plane electronic thermal conductivity κ_{e} is small ($\kappa_{\mathrm{e}} \sim 1$ W/mK), the cooling due to lateral diffusion of hot carriers ($\sim h\kappa_{\mathrm{e}}/A$, where $h = 0.3$ nm is the thickness of graphene and $A = 2.5$ μm^2 is the laser spot size) is negligible (i.e., $\Gamma_{\mathrm{e-ph}} \gg h\kappa_{\mathrm{e}}/A$) [73]. For steady-state conditions and $\Gamma_{\mathrm{e-ph}} \ll \Gamma_0$, Eqs. B.1 and B.2 simplify to

$$T_{\mathrm{e}} - T_0 \approx P_{\mathrm{in}}/\Gamma_{\mathrm{e-ph}}. \tag{B.3}$$

We use this relation to model the PTI effect in Section 5.1.5 and find that the data is best described with $\Gamma_{\mathrm{e-ph}} = 0.5 \pm 0.3$ MW/m^{2}K. This value is compatible with the calculated out-of-plane thermal conductance of G/hBN interfaces caused by electron coupling with SPP phonons [79]. It is also consistent with a disorder-enhanced supercollision cooling mechanism [83] which predicts $\Gamma_{\mathrm{e-ph}} \approx 3\Sigma T_{\mathrm{ph}}^2$ under steady-state conditions [76], where Σ is the supercollision rate coefficient (typically between 0.5 and 2 W/m^{2}K^3) [99].

To verify the validity of Eq. B.3 for our experimental conditions, we solve Eqs. B.1 and B.2 to exactly calculate the variation in temperature of the electron ($\Delta T_{\mathrm{e}} = T_{\mathrm{e}} - T_0$) and phonon ($\Delta T_{\mathrm{ph}} = T_{\mathrm{ph}} - T_0$) baths induced by a quasi-CW laser pulse similar to the one used in our experiment (pulse duration $dt = 100$ ps and repetition rate $f = 40$ MHz) with average laser power $P = 100$ μW, at T_0 =300 K and using $\Gamma_{\mathrm{e-ph}} = 0.5$ MW/m^{2}K and $\Gamma_0 = 30$ MW/m^{2}K. The calculations (Fig. B.1b) show that the T_{e} reaches a temperature that is much higher than T_{ph} (and T_0) and in quantitative agreement with Eq. B.3. Moreover, the temperature

closely follows the variation of the pulse intensity in time. This confirms the validity of the steady-state approximation, which is expected since the measured cooling time $\tau_{\rm cool}$ is much shorter than the pulse duration. More importantly, these calculations indicate that the electron bath is thermally decoupled from the phonon bath ($T_{\rm e} > T_{\rm ph}$) under (quasi-) steady-state conditions.

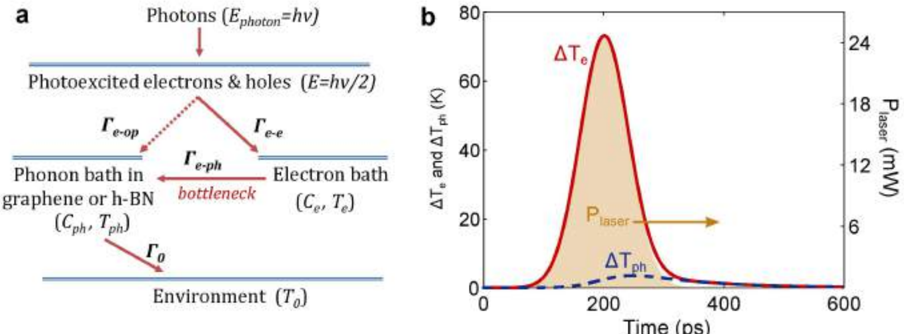

FIGURE B.1: **Heating and cooling pathways of hot carriers in graphene. a)** Schematics illustrating the cooling pathway of photoexcited carriers. Detailed descriptions are provided in the text. **b)** Time dependence of the rise in electron ($\Delta T_{\rm e} = T_{\rm e} - T_0$, red solid line) and phonon ($\Delta T_{\rm ph} = T_{\rm ph} - T_0$, blue dotted line) temperature calculated with the model illustrated in a under a quasi-CW pulse (full width at half maximum (FWHM) duration dt = 100 ps, average laser power P = 100 μW and repetition rate f = 40 MHz) at T_0 = 300 K, graphene Fermi level $E_{\rm F}$ = 0.2 eV. The pale yellow area represents the instantaneous laser power $P_{\rm laser}$ of a single pulse centered at 200 ps.

B.2 Devices with different WSe_2 thicknesses

We have varied the thickness L of the WSe_2 layer providing the energy barrier between the two graphene sheets. All the data shown in Section 5.1 come from a device containing WSe_2 layer with L = 28 nm. We also measured sub-bandgap photocurrent on devices with L = 2.2, 7.4 and 55 nm. These devices are made using the layer assembly technique described in Chapter 3, and are deposited on a Si/SiO_2 substrate that acts as a gate electrode. All devices display features in photocurrent that we attribute to the PTI effect. Figs. B.2a and B.3a show positive photocurrent autocorrelation peaks in devices with L = 2.2 and 7.4 nm (for details on the measurement technique see Section 2.5.3). As discussed in Section 5.1.3, the dynamics of this peak is characterized by a time constant $\tau_{\rm cool} \sim$ 1-2 ps which is on the order of the cooling time of the hot carriers in graphene. We also observe a superlinear power dependence of the photocurrent in these devices (Figs. B.2c and B.3c), which is characteristic of the PTI effect. Finally, the increase in photocurrent with gate voltage $V_{\rm G}$ (Figs. B.2d and B.3d) is consistent with the PTI effect, which depends exponentially on the Schottky barrier height $\Phi_{\rm B}$. This effect is also observed in the device with L = 55 nm. Importantly, we

note that the magnitude of the photocurrent does not vary significantly with the WSe_2 thickness L, indicating that tunneling effects (which depend exponentially on L) do not likely play a role in the photocurrent generation process. These observations further reinforce the conclusion that the PTI effect governs the photocurrent response of these heterostructures in this photon energy range.

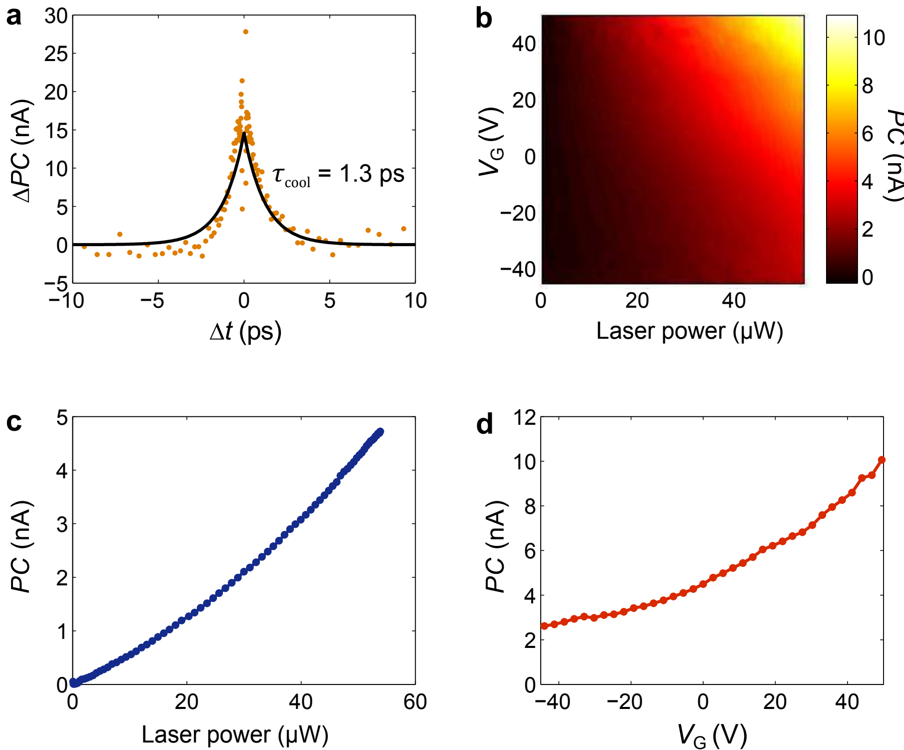

FIGURE B.2: **PTI photocurrent in G/2.2 nm WSe_2/G heterostructure a)** Photocurrent autocorrelation measurement performed with an average laser power P = 600 μW at T_0 = 30 K and bias voltage V_B = 0.5 V. The decay of ΔPC(Δt) = PC(Δt) - PC($\Delta t \rightarrow \infty$) is fitted with an exponential with time constant τ_{cool} =1.3 $\pm$ 0.1 ps (black solid line). **b)** PC vs. laser power and gate voltage V_G measured at bias voltage V_B = 0.7 V and T_0 = 30 K, with laser wavelength λ = 1300 nm. **c)** PC vs. laser power for V_G = 0 V and (**d**) PC vs. V_G for P = 50 μW taken from (**b**).

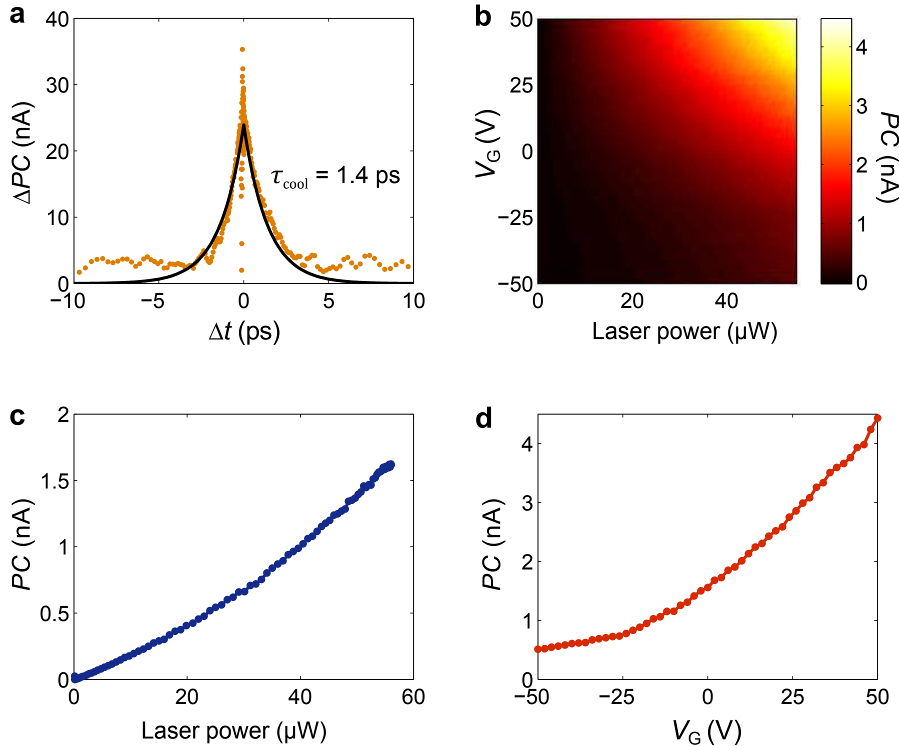

FIGURE B.3: **PTI photocurrent in G/7.4 nm WSe_2/G heterostructure a)** Photocurrent autocorrelation measurement performed with an average laser power P = 825 μW at T_0 = 300 K and bias voltage V_B = 0.06 V. The decay of $\Delta PC(\Delta t)$ = $PC(\Delta t)$ - $PC(\Delta t \to \infty)$ is fitted with an exponential with time constant τ_{cool} = 1.4 ± 0.1 ps (black solid line). **b)** PC vs. laser power and gate voltage V_G measured at V_B = 0.5 V and T_0 = 35 K, with laser wavelength λ = 1300 nm. **c)** PC vs. laser power for V_G = 0 V and (**d**) PC vs. VG for P = 50 μW taken from (**b**).

B.3 Internal photoemission in Au/WSe_2/Au heterostructures

In order to emphasize the difference between the internal photoemission (IPE) process typically observed at metal/semiconductor interface and the photo-thermionic (PTI) effect measured at graphene/WSe_2 junctions, we study the sub-bandgap photocurrent generated in Au/WSe_2/Au vertical heterostructures. Fig. B.4a shows such a device made with a 20-nm-thick WSe_2 layer and a 10-nm-thick Au top electrode (similar measurements were obtained on a Au/40-nm-thick WSe_2/Au device). The photocurrent map in Fig. B.4b shows that photocurrent is generated by sub-bandgap photons (λ = 1500 nm) in the region where

all three layers overlap. Interestingly, the magnitude of this photocurrent scales linearly with the laser power (Fig. B.4c), regardless of the bias voltage V_B. This observation is consistent with the IPE process (see Section 2.3.4), which predicts that the number of carriers emitted over the barrier scales linearly with the number of initial photoexcited carriers. Moreover, Fig. B.4d shows that the measured responsivity ($\Re$ = PC/P) satisfies the relation $\Re \propto (E_{\text{photon}} - \Phi_B)^2$ expected for the IPE process [249]. By projecting this relation to lower E_{photon}, we find a cut-off energy at $h\nu = \Phi_B \approx$ 0.4 - 0.5 eV. We also note that the IPE responsivity of the Au/WSe_2/Au is smaller than the PTI responsivity measured in G/WSe_2/G, especially at low photon energy. For instance, at $h\nu$ = 0.8 eV, the maximum responsivity measured in Au-based device is $\Re$ = 0.036 mAW^{-1}, whereas graphene-based devices can easily reach $\Re$ = 0.12 mAW^{-1}.

All these observations that we attribute to IPE (i.e., linear power dependence, strong dependence on E_{photon} and cut-off at Φ_B) clearly contrast with the main features of the PTI effects (superlinear power dependence and no dependence on E_{photon}). This raises the question of why IPE dominates the photoresponse of metal/WSe_2 while PTI governs the one of graphene/WSe_2. The answer is two-fold. First, as discussed in Section 5.1.1, carriers thermalize among themselves much more rapidly in graphene (approximately 10 fs) than in metal (approximately 100 fs) due to the stronger carrier-carrier interaction. This ultrafast thermalization process competes directly with the internal emission of initially photoexcited carriers (IPE). Assuming the timescale of this process to be equal for graphene and metal, we can conclude that IPE in graphene is suppressed by an order of magnitude compare to metal.

Secondly, we can explain why the PTI effect in graphene is larger than in metal from the result of the PTI model presented in Section 5.1.5. Indeed, under steady-state conditions (i.e. when the pulse duration is much longer than τ_{cool}, which is the case in our experiment except for time-resolved measurements), we can estimate the rise in electronic temperature as $\Delta T = P_{\text{in}}\Gamma$, where P_{in} is the incident power delivered to the carriers and Γ is a thermal conductance term which describe the rate-limiting heat dissipation mechanism from the electronic system to the phonon bath (see Section B.1). From the fit of our PTI model we obtain Γ_G = 0.5 $MWm^{-2}K^{-1}$ for graphene/WSe_2, while the electron-phonon coupling constant of Au, for instance, is Γ_{Au} = 2.6 x 10^{16} $Wm^{-3}K^{-1}$ [318]. Considering the 10-nm-thick Au electrode of the device shown in Fig. B.4a, this value corresponds roughly to a two-dimensional $\Gamma_{Au,2D}$ of 260 $MWm^{-2}K^{-1}$, which is two orders of magnitude larger than Γ_G. We conclude that for a given power P_{in}, the rise in electronic temperature ΔT is approximately 500 times larger in graphene than in gold (metals). This enhanced ΔT, along with the suppression of the IPE due to ultrafast thermalization of carriers in graphene, explains why the PTI effect, which depends exponentially on the carrier temperature, dominates the photoresponse of graphene/semiconductors junctions but not the one of metal/semiconductors interfaces.

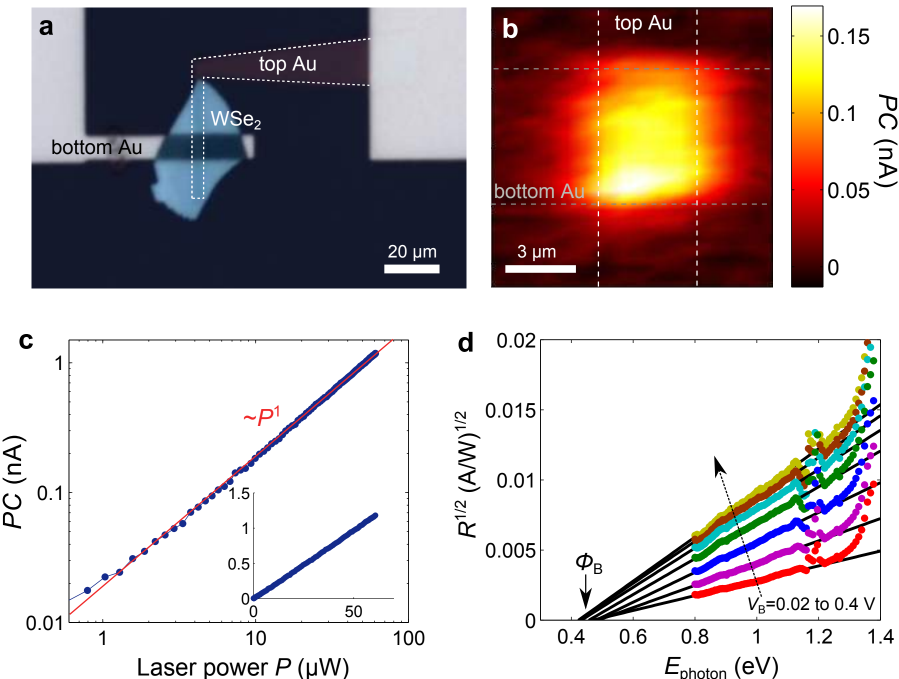

FIGURE B.4: **Photocurrent measurements in Au/20-nm-thick WSe_2/Au heterostructure.** **a)** Optical image of the device. **b)** Photocurrent map performed at $T_0 = 300$ K and $V_B = 0.2$ V, with a laser wavelength $\lambda = 1500$ nm and $P = 10$ μW. The position of the top and bottom Au electrodes is indicated by the white and gray dotted lines, respectively. **c)** Log-log plot of PC vs. laser power measured at $T_0 = 300$ K and $V_B = 0.2$ V, with $\lambda = 1500$ nm. The red solid line corresponds to a linear power dependence. Inset: same data on linear scale. **d)** Square root of the responsivity $\Re$ vs. photon energy $h\nu$ at V_B from 0.02 V (red) to 0.4 V (yellow). The black solid lines are linear fits to the data.

B.4 PTI model

To model the injection of hot carriers over the G/WSe_2 Schottky barrier, we consider the system shown in Fig. 5.1b, which consists of a single G_B/WSe_2 heterojunction. We note that this system does not include the top graphene layer. Indeed, as explained in Section 5.1.4, the contribution of the top graphene layer can be neglected when a positive interlayer bias V_B is applied. In these conditions, according to Landauer's transport theory [327, 367], the current density J flowing through the heterojunction (considered as the resistor channel) between the graphene and WSe_2 layers can be written as:

$$J = \frac{e_0}{\tau_{\text{inj}}} \int_{-\infty}^{\infty} T(E)D(E)\left[f_{\text{G}}(E) - f_{\text{WSe}_2}(E)\right] dE \tag{B.4}$$

where e_0 is the elementary charge, τ_{inj} is the time it takes for an electron to transfer through the junction, referred here as the charge injection time, $T(E)$ is the transmission probability, and $f_{\text{G}}(E)$ and $f_{\text{WSe}_2}(E)$ are the Fermi-Dirac function of graphene and WSe_2, respectively. $D(E)$ is the density of states of graphene, where $\hbar$ is the reduced Planck's constant and v_{F} is the graphene Fermi velocity.

We set the charge neutrality point of graphene to $E = 0$ (as illustrated in Fig. 5.1b) and assume the tunneling contribution to the photocurrent to be negligible (which is the case for the thick WSe_2 layer considered here) and a unity transmission for energies above the Schottky barrier. We obtain:

$$D(E) = 2|E|/\pi(\hbar v_{\text{F}})^2 \tag{B.5}$$

$$f_{\text{G}}(E) = 1/\left(e^{(E-\mu)/k_{\text{B}}T} + 1\right) \tag{B.6}$$

$$f_{\text{WSe}_2}(E) = 1/\left(e^{(E-\mu+e_0V_{\text{B}})/k_{\text{B}}T} + 1\right) \tag{B.7}$$

and

$$T(E) = \begin{cases} 1 & \text{for } E > \Phi_0 \\ 0 & \text{for } E \leq \Phi_0 \end{cases} \tag{B.8}$$

where μ is the Fermi energy of graphene, V_{B} is the voltage applied across the WSe_2 layer and Φ_0 is the offset between the WSe_2 conduction edge and graphene's Dirac point (Fig. 5.1b). In reverse bias condition (such that $f_{\text{G}}(E) \gg f_{\text{WSe}_2}(E)$ for $E > \Phi_0$), Eq. B.4 becomes:

$$J = \frac{2}{\pi}\frac{e_0}{\tau_{\text{inj}}}\frac{1}{(\hbar v_{\text{F}})^2}\int_{\Phi_0}^{\infty} |E| f_{\text{G}}(E) dE \tag{B.9}$$

Eq. B.9 can be solved analytically provided that $\Phi_{\text{B}} = \Phi_0 - \mu \gg k_{\text{B}}T$ and we obtain Eq. 5.1 that we used in Section 5.1.5 to model the PTI current.

B.5 Measurements at different ambient temperatures

Finally, to validate our model of the PTI effect, we repeat the measurement and analysis of PC vs. laser power P and gate voltage V_{G} at other ambient temperatures. At T_0 = 330 K (Figs. B.5a,b), the fit of the model gives a carrier injection

time τ_{inj} = 34 ± 10 ps and an out-of-plane interfacial thermal conductance Γ = 1 ± 0.6 MWm^{-2}K^{-1}, whereas at T_0 = 230 K (Figs. B.5c,d), we obtain τ_{inj} = 24 ± 10 ps and Γ = 0.6 ± 0.3 MWm^{-2}K^{-1}. We find a good agreement between the model and experiment for both temperatures, but a more detailed study is needed in order to examine and understand the possible dependence of τ_{inj} and Γ on temperature T_0.

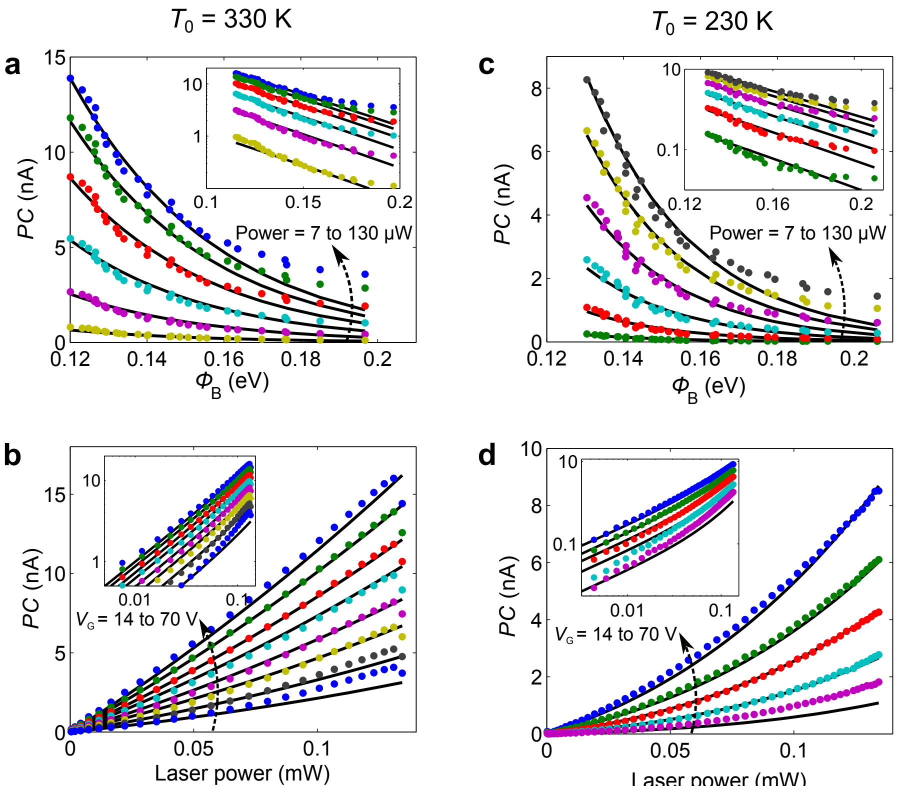

FIGURE B.5: **PTI response at different ambient temperature** Comparison between the PTI model and the experimental photoresponse measured at T_0 = 230 and 330 K, with λ = 1500 nm and V_B = 0.36 V in a G/28-nm-thick WSe_2/G heterostructure. **a,c)** PC vs. Φ_B at various laser powers P and (**b,d**) PC vs. laser power P at different gate voltages V_G measured at (**a,b**) T_0 = 330 K and (**a,b**) T_0 = 230 K. The data points correspond to the experiment and the solid lines to the model. Insets: Same experimental data and theoretical curves in logarithmic scale.

Appendix C

Complementary information: Picosecond photoresponse in TMD-based heterostructures

C.1 Steady-state photocurrent and IQE model

The photoresponse of our photodetectors can be well described by a photoconductor model where the driving electric field E is provided by the potential drop, ΔV, across the WSe2 of thickness L. As discussed in Chapter 1, the photocurrent density along the electric field direction is

$$j_{\mathrm{PC}}(\mathbf{r}) = 2e_0\mu\Delta n(\mathbf{r})\frac{\Delta V}{L} \tag{C.1}$$

where μ is the carrier mobility (we assume that the electron and hole mobility is the same) and $\Delta n(r)$ is the photoinduced carrier density. At low injection levels (in the linear power dependence regime), the steady-state excess carrier is

$$\Delta n(\mathbf{r}) = \Phi(\mathbf{r})\tau \tag{C.2}$$

As explained in the previous sections, τ is the average time that carriers reside in the WSe_2 before they either recombine or are extracted at the contacts, i.e., $\tau^{-1} = \tau_{\mathrm{r}}^{-1} + \tau_{\mathrm{ex}}^{-1}(E)$. Here, τ_{r} is the carrier recombination time and $\tau_{\mathrm{ex}}(E)$ is the field-dependent carrier extraction time. $\Phi(\mathbf{r})$ is the absorbed photon flux, which for simplicity, we assume to be uniform over the entire thickness of the WSe_2, such that

$$\Phi(\mathbf{r}) = \frac{A_{\mathrm{abs}}}{L}\frac{H(\mathbf{r})}{h\nu} \tag{C.3}$$

where A_{abs} is the optical absorption of the WSe_2 layer, $h\nu$ is the photon energy and $H(r)$ is the power density of the laser beam with total power P. The photocurrent can therefore be calculated as [236] :

$$\mathrm{PC} = \frac{1}{L}\int j_{\mathrm{PC}}(\mathbf{r})d^3r = 2e_0\mu\frac{\Delta V}{L^2}A_{\mathrm{abs}}\frac{P}{h\nu}\tau \tag{C.4}$$

Considering, as we argued in Section 6.4, that the carrier drift time is $\tau_{\mathrm{d}} = L^2/2\mu\Delta V$, we can rewrite the previous equation

$$\mathrm{PC} = e_0 A_{\mathrm{abs}}\frac{P}{h\nu}\frac{\tau}{\tau_{\mathrm{d}}} \tag{C.5}$$

And we obtain the expression that we used in Section 6.5 to evaluate the internal quantum efficiency

$$\mathrm{IQE} = \frac{\mathrm{PC}}{e_0}\frac{hv}{A_{\mathrm{abs}}P} = \frac{\tau}{\tau_{\mathrm{d}}} = \frac{\tau_{\mathrm{r}}}{\tau_{\mathrm{r}}+\tau_{\mathrm{d}}} \tag{C.6}$$

C.2 Electrostatic model for a $G/WSe_2/G$ heterostructure

Here, we demonstrate that the photocurrent is driven by the potential drop ΔV across the WSe_2 layer and that its magnitude is well predicted by the model described in the previous section. To evaluate ΔV, we develop an electrostatic model similar to the one used by Yu *et al.* [235], where the heterostruture is treated as multiple parallel plate capacitors. The schematic of the heterostructure and its band diagram depicted in Fig. C.1 show the relevant parameters for our model.

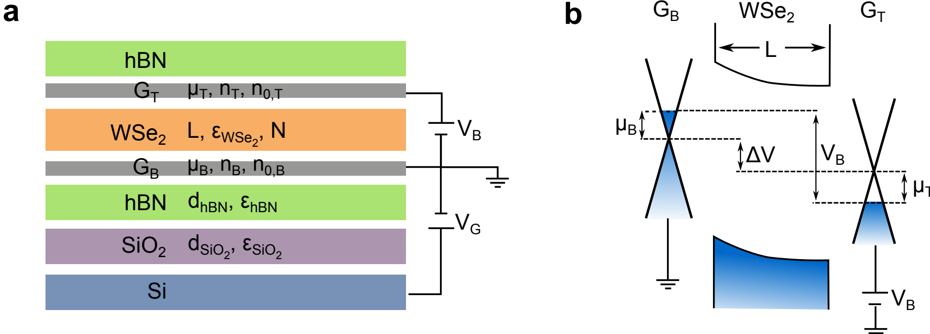

FIGURE C.1: **Schematic of the heterostructure and its band diagram. a)** We model the heterostructure as a series of plate capacitors. The parameters shown for each layer are described in the main text. **b)** Band diagram of the $G/WSe_2/G$ illustrating some of the main physical parameters of our electrostatic model.

According to Gauss's law, the charge densities in the top (n_T) and bottom (n_B) graphene are given by

$$e_0 n_\mathrm{B} = \epsilon_\mathrm{G} E_\mathrm{G} + \epsilon_{\mathrm{WSe}_2}\epsilon_0 E_\mathrm{B} \tag{C.7}$$

$$e n_\mathrm{T} = \epsilon_{\mathrm{WSe}_2}\epsilon_0 E_\mathrm{T}, \tag{C.8}$$

where E_B and E_T are the electric fields at the top and bottom graphene/WSe_2 interfaces, E_G is the field induced by the gate voltage, $\epsilon_{\mathrm{WSe}_2}$ = 7.2 is the relative permittivity of WSe_2 [322], ϵ_0 is the vacuum permittivity and ϵ_G is the permittivity of the gate dielectric. We note that the electron (hole) density is positive (negative).

The heterostructure is deposited onto a substrate made of two different dielectrics, the thermally grown SiO_2 with thickness d_{SiO_2} = 285 nm, and a hBN flake (15 nm $< d_\mathrm{hBN} <$ 50 nm). Since the permittivity of hBN and SiO_2 are very similar ($\epsilon_{\mathrm{SiO}_2}$ = 3.9 and ϵ_hBN = 4.2 [368]), we assume ϵ_G = 4 and the gate-induced electric field is $E_\mathrm{G} = V_\mathrm{G}/(d_{\mathrm{SiO}_2} + d_\mathrm{hBN})$.

Furthermore, by assuming that the WSe_2 layer is fully depleted, we find the following relationship between E_B and E_T:

$$E_\mathrm{T} = E_\mathrm{B} + \frac{N e_0 L}{\epsilon_{\mathrm{WSe}_2}}, \tag{C.9}$$

where N is the doping density in the WSe_2 and L is the thickness of WSe_2. From the electric fields we evaluate the potential drop ΔV across the WSe_2 layer as:

$$\mathit{\Delta} V = -\frac{1}{2}(E_\mathrm{B} + E_\mathrm{T})L. \tag{C.10}$$

We calculate the chemical potential in each of the two graphene flakes as

$$\mu = \hbar v_\mathrm{F}\sqrt{\pi|n + n_0|}, \tag{C.11}$$

where n_0 is the intrinsic charge density of the graphene flakes. Finally, when a bias voltage V_B is applied on the top graphene, the bands movement is governed by:

$$eV_\mathrm{B} = e_0 \mathit{\Delta} V + \mu_\mathrm{B} - \mu_\mathrm{T} \tag{C.12}$$

We now consider the device with L = 7.4 nm and compare its quasi-CW photoresponse with our photocurrent and electrostatic models. To calibrate our electrostatic model, we first look at the open-circuit voltage, V_OC, defined as the bias voltage V_B at which the photocurrent vanishes (Fig. C.2a). According to Eq. C.4, this occurs when $\Delta V(V_\mathrm{B}, V_\mathrm{G})$ = 0. A very good agreement between model

and measured V_{OC} is obtained by setting the $\mathrm{WSe_2}$ doping density to $N = 8 \times 10^{17}$ cm^{-3} and the initial doping of the bottom and top graphene to $n_{0,\mathrm{B}} = 8 \times 10^{11}$ cm^{-2} and $n_{0,\mathrm{T}} = 0$, respectively. Using these electrostatic parameters, we can now compare the photocurrent measured as a function of gate and bias (Fig. C.2b) with the one predicted by our photocurrent model. Fig. C.2c shows the photocurrent calculated using Eq. C.4 with the parameters obtained from the analysis of the time-resolved photocurrent measurements in Section 6.4, namely μ = 0.01 $\mathrm{cm^2/Vs}$, τ_{r} = 130 ps. The only fitting parameter here is the absorption which we estimate to A_{abs} = 20%, consistent with the absorption expected from Beer-lambet's law [106]. Overall, we find an excellent agreement between the measured and calculated photocurrent, thus validating our model and confirming that the potential drop ΔV inside $\mathrm{WSe_2}$ drives the photocurrent

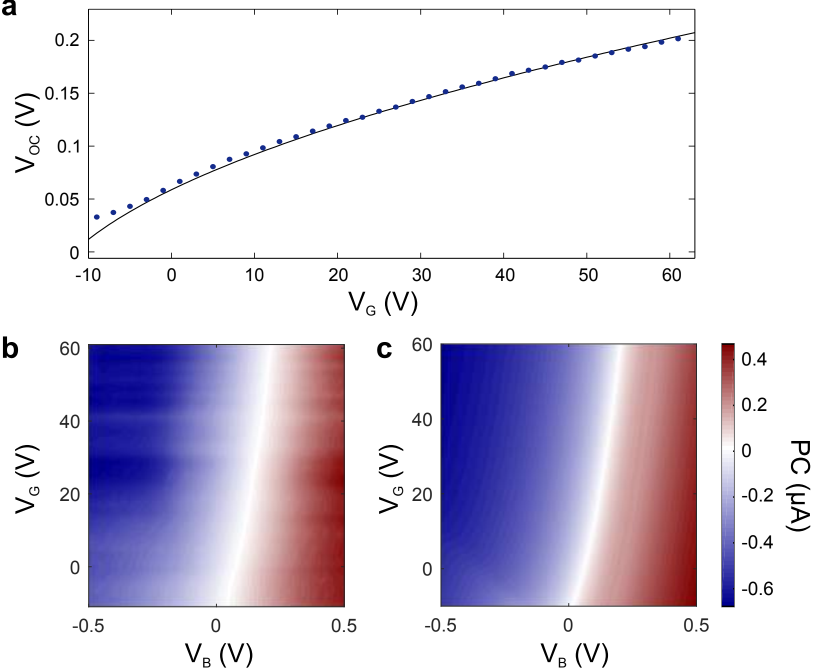

FIGURE C.2: **Comparison between measured and modelled photocurrent in a G/$\mathbf{WSe_2}$/G heterostructure. a)** Measured open-circuit voltage V_OC vs. backgate voltage V_{G}. The solid black line is a fit to the data obtained by setting $\Delta V(V_{\mathrm{B}}, V_{\mathrm{G}}) = 0$ in the electrostatic model presented in the text. **b)** Measured photocurrent as a function of bias V_{B} and backgate voltages V_{G} for the device with a $\mathrm{WSe_2}$ flake thickness $L = 7.4$ nm. The data was taken at a temperature of 26 K, with a laser wavelength λ = 575 nm and power P = 10 μW. **c)** Photocurrent calculated from the electrostatic and photocurrent models presented in the text, and witht the time constants extracted from the time-resolved photocurrent measurements in Section 6.4.

C.3 Real-time photoresponse and RC-time constant

We directly measure the photo-switching rate of our photodetectors by probing their response to a short light pulse in real time. Using a fast oscilloscope (Agilent MSO9404A, 4 GHz), we monitor the voltage across a 50 Ω load resistance (R_{L} in Figure C.3d). We find a similar bias-independent response time of 1.6 ns ($1/\tau \sim 0.6$ GHz) for both the 2.2 and 7.4 nm devices (Figure C.3a to c). These experimental values, which are limited by our electrical setup, give us a lower bound for the actual photo-switching rate of our devices, which we expect to lie in the GHz regime.

We can indeed evaluate the actual photo-switching rate of our detector. To this end, in addition to the photoresponse time discussed in Section 6.3, we have to take into account the resistance-capacitance (RC) time constant of the device equivalent circuit (Figure C.3d). In this vertical geometry, we expect that the RC time constant is largely determined by the large capacitance of the Gr/WSe_2/Gr heterostructure, $C_{\mathrm{WSe_2}} = \epsilon_0 \epsilon_{\mathrm{WSe_2}} A/L$, where A is the active area of the device. The resistance to take into account corresponds to the two graphene sheets and the following contacts and circuits (R_{S} in Figure C.3d). The high resistance of the WSe_2 channel $R_{\mathrm{WSe_2}}$ acts here as a shunt resistance so it does not affect the RC time constant. We estimate $R_{\mathrm{S}} = 1$ kΩ in our devices, yet this value can be further reduced by optimizating the circuit design, contact resitance and graphene charge density. These considerations give RC rates in the GHz regime, which is consistent with the instrument limited photo-switching rates observed experimentally and discussed previously (Figure C.3e). We finally note that for the reasonably optimized device we propose (smaller active area $A = 5$ μm^2 and lower graphene and contact resistance $R = 100$ Ω), we find much higher photo-switching rates which are RC limited only for thicknesses L lower than 2 nm.

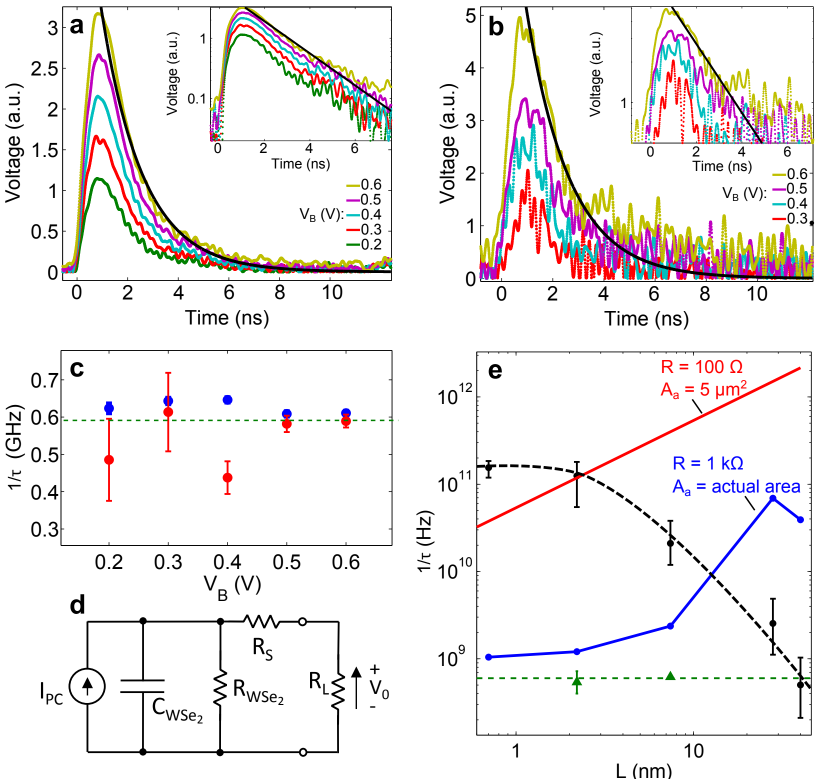

FIGURE C.3: **Real-time photocurrent response of G/WSe$_2$/G photodetectors. a,b)** Real-time traces of the photoresponse to a short optical pulse (55 ps pulse duration, $\lambda = 532$ nm) for different bias voltage V_B and devices with 7.4 **(a)** and 2.2 nm **(b)** thick WSe$_2$. The solid black lines are fits to the data corresponding to decay rates $1/\tau = 0.61$ and 0.59 GHz in a and b, respectively. Insets show the same data in semilog scale. **c)** Extracted decay rates of both devices (red for 2.2 nm and blue for 7.4 nm thick WSe$_2$) as function of bias voltage. **d)** Schematics of the equivalent circuit of our devices. **e)** Thickness dependence of the photoresponse rate (black, the data points are measured by time-resolved photocurrent – from Fig. 6.4b – and the dotted line is a guide to the eye), the RC time constant (evaluated for our actual devices in blue and for an optimized device in red) and the measured decay time limited by the probing setup (green, also shown in **c**).

C.4 Photoluminesence quenching

We perform spatial mapping of the photoluminescence (PL) from WSe$_2$ on the 1L and 3L devices on a different experimental setup than the one for photocurrent measurements. We use 532 nm excitation light (diffraction limited excitation spot with power $\sim 50\ \mu$W) and a detection with either a single photon counter

module (coupled with longpass filters) or a spectrometer (coupled to an EMCCD camera), in a confocal geometry. Spatial maps of the photoluminescence intensity are presented in Figure C.4, as well as corresponding photoluminescence spectra at given laser positions. Relative intensity and spectral lineshape from the two devices confirm the respective 1L and few-layer WSe_2 geometry [369].

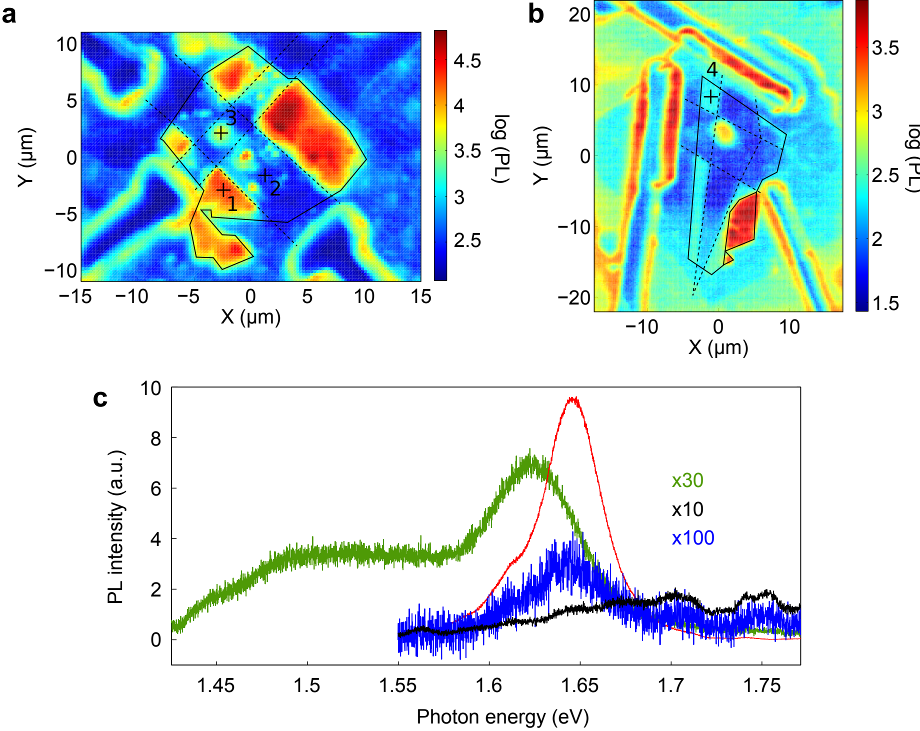

FIGURE C.4: **Photoluminescence quenching at G/WSe_2 interfaces.** Spatial maps of the photoluminescence (PL) intensity (in log scale) measured on devices with **(a)** monolayer WSe_2 and **(b)** 3-layer WSe_2 flakes (drawn with solid black lines). Strong quenching is observed in the area in contact with the graphene flakes (drawn with dashed lines). **(c)** PL spectra obtained on the marked spots in the maps, showing strong and spectrally narrow luminescence from the monolayer (1, red), quenched luminescence from the same monolayer (2, blue), scattering or luminescent defects (3, black) and spectrally broad luminescence from the 3-layer flake (4, green). We note the inclusion of a strongly luminescent monolayer flake on the bottom edge of the 3-layer flake.

We clearly observe a strong reduction of the luminescence from the areas where WSe_2 is in contact with the top and/or bottom graphene layers. This emission quenching is a strong evidence for an energy transfer from the WSe_2 to the graphene, by the addition of a highly efficient non-radiative relaxation pathway for the photogenerated excitons [344]. A quantitative evaluation of the quenching ratios shows on average a 300-fold and 10-fold reduction of the

luminescence in the 1L and 3L device respectively. This strong thickness dependence is indicative of an energy transfer mechanism. For instance in a Förster resonant energy transfer formalism, where dipole-dipole interaction between a point-like emitter and a plane is evaluated, the induced decay time of the emitter scales with the distance to the power of 4 [218, 344]. Moreover, the photoluminescence intensity being driven by the lifetime of the excitons in the WSe_2, the quenching ratio directly gives the ratio between the intrinsic lifetime (without graphene) and the reduced lifetime due to the energy transfer to graphene. Exciton lifetimes in WSe_2 have already been evaluated to be hundreds of ps from several optical pump-probe studies [337]. This gives reduced lifetimes of roughly tens of ps for the 3L device and a few ps for the 1L device. This timescale should correspond to the zero-bias photoresponse time of the device, introduced as τ_r in Section 6.4. It appears to be in good agreement with the values extracted from the time-resolved photocurrent measurements.

C.5 Characterization of the photodetectors

In this section we present an overall characterization of our devices as photodetectors at low injection levels (low laser power) by presenting their responsivity ($\Re$), external (EQE) and internal (IQE) quantum efficiency, noise equivalent power (NEP) and specific detectivity (D^*) in Table C.1. Defintions and equations for these parameters can be found in Chapter 1.

The EQE of the device with a WSe_2 flake thickness of $L = 7.4$ nm is presented as function of the bias voltage V_B and gate voltage V_G in Fig. C.5a. In the Table C.1, we note that higher values for responsivity and EQE can be reached for the device with $L = 40$ nm when applying very high bias and backgate voltages. However, we did not apply these high voltages in order to protect the device.

L (nm)	A_{abs} (%)	$\Re$ (mA/W)	EQE (%)	IQE (%)	NEP (W/Hz$^{1/2}$)	D^* (Hz$^{1/2}$cm/W)
Monolayer	5	1.8	0.29	6	1x10^{-10}	4x10^{6}
2.2	8	44	7.3	91	5x10^{-12}	1x10^{8}
7.4	30	110	18	60	1x10^{-12}	1x10^{9}
28	56	110	18	32	6x10^{-13}	6x10^{8}
40	70	>80	>13	>19	<1x10^{-14}	>5x10^{10}

TABLE C.1: Figures of merit for the different devices. Light excitation wavelength and power are 759 nm and 1 μW, respectively. Values of NEP and D^* are evaluated at $V_B = 0$ and $V_G = 30$ V.

We can optimize the NEP by taking advantage of the electrical tunability of our devices with bias V_B and gate voltage V_G. As seen in Fig. C.5a, applying

a gate voltage V_G increases the open circuit voltage. It is therefore possible to reach high photocurrent efficiency without applying any bias V_B. In this configuration, we minimize the dark current I_d and the noise of the detector is no longer dominated by the shot noise but only by the thermal contribution (Fig. C.5). For the device with $L = 7.4$ nm, we find values lower than 10^{-11} W/Hz$^{1/2}$ even at high bias where the highest efficiency is reached (Figure C.5d). Using a gate voltage $V_G = 30$ V, the NEP goes down to 10^{-12} W/Hz$^{1/2}$ at zero bias voltage while the IQE remains high (∼40%). These values of NEP are similar to those of typical commercial photodetectors.

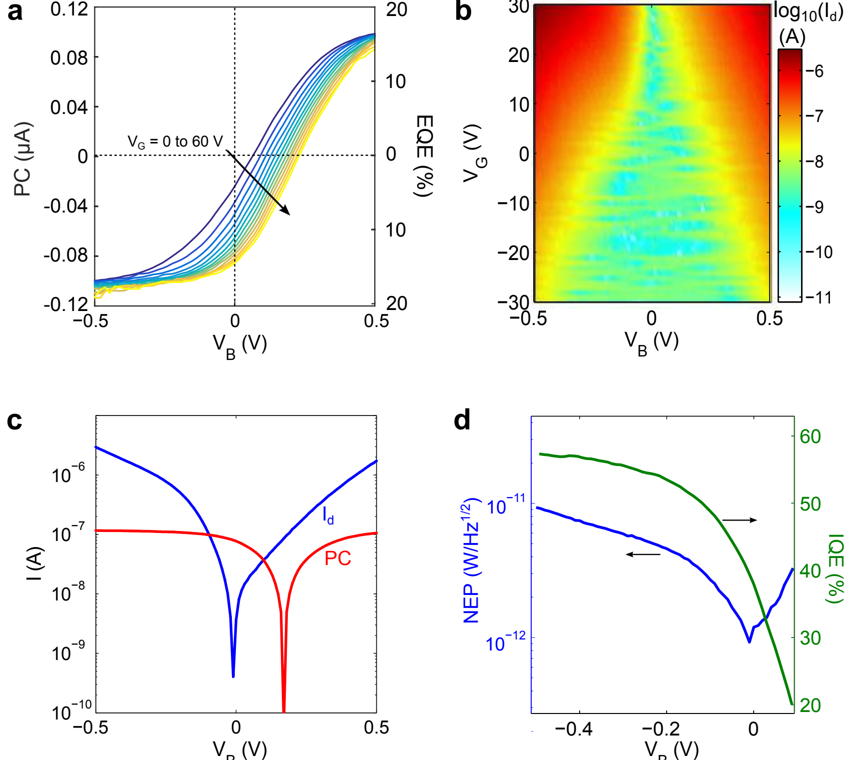

FIGURE C.5: **Performance of the G/7.4 nm WSe_2/G photodetector. a)** Photocurrent PC measured as a function of V_B for different values of backgate voltage V_G. The corresponding EQE is indicated on the right axis.**(b)** Bias and gate voltage dependence of the dark current I_d. **c)** Dark current (blue) and photocurrent (red) as function of bias voltage at $V_G = 30$ V. **(d)** Noise equivalent power (blue) and internal quantum efficiency (green) as function of bias voltage (same conditions as **c**). All data shown in this figure were taken at room temperature with an illumination wavelength $\lambda = 759$ nm and illumination power $P = 1$ μW.

Appendix D

Complementary information: Tunnel ionization of 2D excitons in monolayer WSe_2

D.1 Device characterization

Measurements shown in the previous sections mainly come from one device (Device 1, shown in Fig. 7.2a). Two other similar devices, Devices 2 and 3, have been measured. The photocurrent spectra of Device 3 measured at low temperature ($T = 30$ K) are shown in Fig. 7.3a. In this section we show additional measurements on Device 1 that demonstrate its proper electrical functioning, and we present a basic description and characterization of Devices 2 and 3.

Figs. D.1a,b shows the electrical behavior of Device 1 in the dark at room temperature. The dark current Id increases as the device is electrostatically doped with electrons ($V_{\mathrm{sym}} = V_{\mathrm{G1}} = V_{\mathrm{G2}} > 0$) and holes ($V_{\mathrm{sym}} < 0$), demonstrating ambipolar operation (Fig. D.1a). From this curve, we can estimate the 2-probe field-effect mobility μ_{FE} using the relation

$$\mu_{\mathrm{FE}} = \frac{L}{W} \frac{\mathrm{d}I_{\mathrm{d}}}{\mathrm{d}V_{\mathrm{sym}}} \frac{1}{CV_{\mathrm{B}}}, \tag{D.1}$$

where L and W are the channel length and width, respectively, C is the gate capacitance per unit area ($C = 2 \times 10^{-7}$ F/cm^2) and V_{B} is the bias voltage used for the measurement. We find that μ_{FE} reaches 3 cm^2/Vs at $V_{\mathrm{sym}} = -10$ V, in excellent agreement with the mobility extracted from the photoresponse rate measurements. This value also agrees with the field-effect mobilities reported in the literature ($\mu_{\mathrm{FE}} \sim 0.1$ to 100 cm^2/Vs) [14, 180].

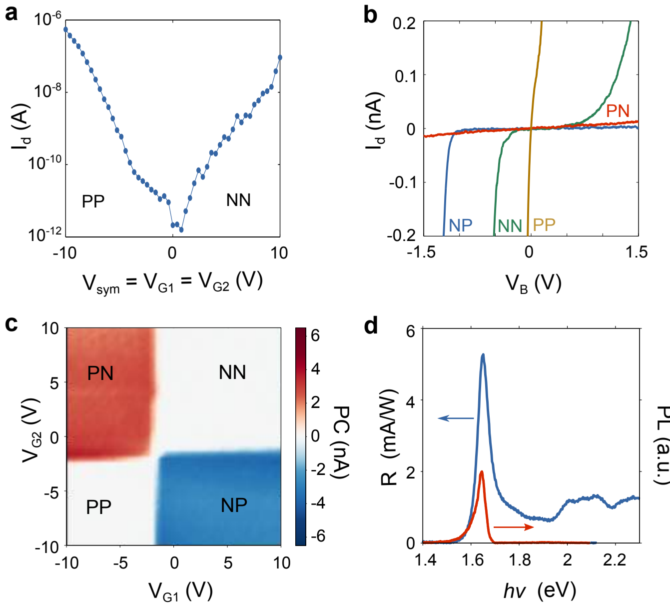

FIGURE D.1: **Characterization of device 1. a)** Variation of the dark current I_d as a function of $V_\text{sym} = V_\text{G1} = V_\text{G2}$ at $V_\text{B} = -1.5$ V. **b)** Dark IV curves measured under different gate voltage configurations: n-p (solid blue line; $V_\text{G1} = 10$ V, $V_\text{G2} = -10$ V), n-n (solid green line; $V_\text{G1} = 10$ V, $V_\text{G2} = 10$ V), p-p (solid yellow line; $V_\text{G1} = -10$ V, $V_\text{G2} = -10$ V), p-n (solid red line; $V_\text{G1} = -10$ V, $V_\text{G2} = 10$ V). **c)** PC measured at the junction as a function of gate voltages V_G1 and V_G2 at $V_\text{B} = 0$ V, laser power $P = 0.5$ μW and photon energy $h\nu = 1.65$ eV. Each region of the four-fold pattern is identify with the corresponding doping configuration. **d)** Solid blue line: Responsivity ($\Re = PC/P$) measured as a function phonon energy $h\nu$ at $V_\text{B} = 0$ V, $V_\text{asym} = 10$ V and $P = 0.5$ μW. Solid red line: Photoluminescence spectrum measured using a CW laser at $h\nu = 1.76$ eV, $V_\text{B} = 0$ V, $V_\text{asym} = 0$ V and $P = 200$ μW. .

Fig. D.1b shows that the rectifying behavior of the device can be increased by applying gate voltages of opposite polarity, thereby forming a p-n junction. The dependence of the photocurrent (PC) on the gate voltages displays a clear four-fold pattern corresponding to the four possible doping configurations (Fig. D.1c). The fact that photocurrent is measured only in the p-n and n-p configuration indicates that the device functions as a photodiode. Finally, the photoluminescence (PL) spectrum measured on the device confirms the monolayer nature of the WSe_2 flake (Fig. D.1d). The PL peak also matches well the A exciton peak observed in the PC spectrum.

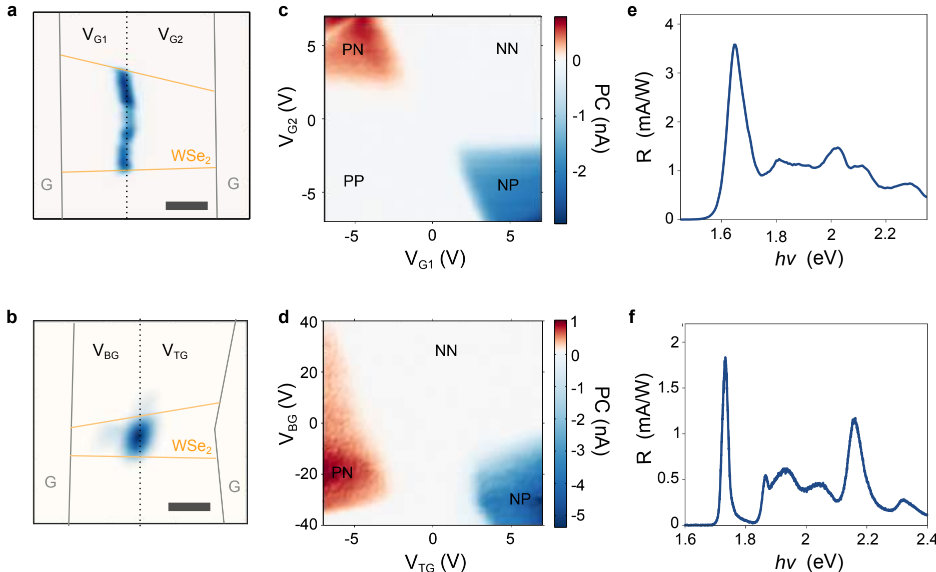

FIGURE D.2: **Characterization of Devices 2 and 3.** Device 2 is measured at room temperature (**a**, **c**, **e**) and Device 3 at$T = 30$ K (**b**, **d**, **f**). All PC measurements are performed at $P \sim 1$ μW. **a,b)** PC maps of (**a**) Device 2 ($V_{\text{asym}} = V_{\text{G1}} = -V_{\text{G2}} = 6$ V, $h\nu = 1.65$ eV) and (**b**) Device 3 ($V_{\text{TG}} = 7$ V, $V_{\text{BG}} = -30$ V, $h\nu = 1.72$ eV). The solid grey and orange lines correspond to the edge of the graphite and WSe_2 flakes, respectively. The dotted lines represent the edge of the top gates. The scale bars are 4 μm. **c,d)** PC measured at the junction versus (**c**) gate voltages V_{G1} and V_{G2} of Device 2 at $h\nu = 1.65$ eV and (**d**) top (V_{TG}) and bottom (V_{BG}) gate voltages of Device 3 at $h\nu = 1.73$ eV. Both measurements were performed at $V_{\text{B}} = 0$ V and each region of the four-fold patterns is identify with the corresponding doping configuration. **e,f)** Responsivity (R = PC/P) measured as a function phonon energy $h\nu$ at $V_{\text{B}} = 0$ V on (**e**) Device 2 ($V_{\text{asym}} = 7$ V) and (**f**) Device 3 ($V_{\text{TG}} = 7$ V, $V_{\text{BG}} = -30$ V).

Devices 2 and 3 are made out of the same hBN/1L-WSe_2/hBN stack, with bottom and top hBN flakes that are 22 and 57 nm thick, respectively. Device 2 is equipped with two top gates separated by $\sim 1\mu$m, while Device 3 only has one top gate covering half of the WSe_2 channel. In this case, we use the heavily doped silicon substrate as a global backgate to control the doping in the other half of the channel. We measured Device 2 at room temperature and Device 3 at $T = 30$ K. Figs. D.2a,b show the geometry and PC maps of both devices. Like Device 1, the photocurrent displays a characteristic four-fold pattern as gates voltages are varied (Figs. D.1c,d). Finally, the photocurrent spectra (Figs. D.1e,f) of both devices present similar features, but since Device 3 was measured at low temperature, its spectral features are narrower and the entire spectrum is blue shifted compared to the PC spectra of Devices 1 and 2.

D.2 Calculations of the electric field distribution

Electric field distributions are calculated by Thomas Garm Pederson using the "electrostatic" and "semiconductor" packages of the finite-element solver COMSOL. In the absence of source-drain bias, the field can be computed from Poisson's equation for a charge slab. For this we assume a temperature of 300 K, a band gap of 1.8 eV, effective masses $m_\mathrm{e} = 0.44m_0$ and $m_\mathrm{h} = 0.48m_0$, and undoped material. In the presence of a bias, a finite semiconductor thickness is required. We use a thickness of 5 nm and raise the temperature slightly to 350 K to achieve convergence. By comparison to the unbiased reference these approximations are found to reduce the maximum field by about 10%, for which we then correct all calculations made with source-drain bias. The field distributions for a range of V_B values and $V_\mathrm{asym} = 10$ V are shown in Fig. D.3.

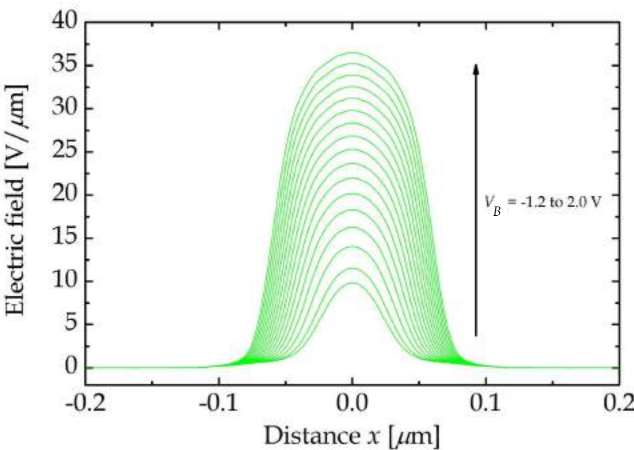

FIGURE D.3: **Finite-element calculations of the electric field at the p-n junction.** Distribution of the horizontal electric field vs. V_B for $V_\mathrm{asym} = 10$ V calculated using COMSOL.

D.3 Wannier-Mott exciton model

Thomas Garm Petersen developed the model for excitons in WSe_2 that we use in the previous section to analyse the Stark effect and the exciton ionization rate. This model is based on the Wannier equation, which, in the presence of an in-plane electric fields, reads as

$$\left\{-\frac{\hbar^2}{2\mu}\nabla^2 - w(r) + eFr\cos\theta + E_\mathrm{G}\right\}\psi_\mathrm{exc}(\vec{r}) = E_\mathrm{exc}\psi_\mathrm{exc}(\vec{r}), \tag{D.2}$$

where $\mu = m_\mathrm{e}m_\mathrm{h}/(m_\mathrm{e}+m_\mathrm{h})$ is the reduced in-plane exciton mass equal to $\mu = 0.23m_0$ with m_0 the free electron mass [370] and E_G is the band gap. The

potential $w(r)$ is the screened Coulomb attraction, which has a form similar to the Keldysh potential [137] presented in Section 1.2.2:

$$w(r) = \frac{\pi}{2r_0}\left[\mathrm{H}_0\left(\frac{\kappa r}{r_0}\right) - Y_0\left(\frac{\kappa r}{r_0}\right)\right]. \tag{D.3}$$

Here, $r_0 = 46.2$ Å is the screening length [370] and $\kappa = (\kappa_\mathrm{a} + \kappa_\mathrm{b})/2$ is the average of the dielectric constants of the surrounding materials above and beneath the sheet. For hBN we use an average between in-plane and out-of-plane dielectric constants [371] $\kappa_\mathrm{hBN} = (4.95 + 4)/2 \approx 4.5$. To simulate excitons with increased and decreased binding energies, we take $\kappa_\mathrm{hBN} = 4.0$ and 5.0 and obtain $E_\mathrm{B} = 190$ and 153 meV, respectively. We compute the exciton susceptibility in the Wannier approximation via the expression

$$\chi(\omega) = \chi_0 \sum_\mathrm{exc} \frac{|\psi_\mathrm{exc}(0)|^2}{E_\mathrm{exc}\left[E_\mathrm{exc}^2 - (\hbar\omega + i\hbar\gamma)^2\right]}, \tag{D.4}$$

where χ_0 is a material dependent constant. Also, the sum is over all exciton states with wave function $\psi_\mathrm{exc}(\vec{r})$ and energy E_exc relative to the ground state. Finally, $\hbar\gamma = 15$ meV is a phenomenological line shape broadening. Absorption is simulated as $\omega \mathrm{Im}\chi(\omega)$. The eigenstates are found by expanding in a Bessel function basis $J_m(\lambda_\mathrm{mn} r/R)\cos(m\theta)$, where J_m is the m'th Bessel function of the first kind and λ_mn is its n'th zero, i.e. $J_m(\lambda_\mathrm{mn}) = 0$. The parameter R is a large but finite confinement radius introduced to restrict the problem to a finite area. We use $R = 500$ in units of the effective exciton Bohr radius, a basis of 7 different angular momenta ($m = 0, \ldots, 6$), and 400 states ($n = 1, \ldots, 400$) for each value of m.

To calculate exciton ionization rates we use the complex scaling technique. This consists in substituting $\vec{r} \to e^{i\phi}\vec{r}$ in Eq. D.4, which then becomes non-Hermitian and has complex eigenvalues $E = E_0 + \Delta - \frac{i}{2}\Gamma$ with E_0 the unperturbed eigenvalue, Δ the Stark shift, and Γ the ionization rate. We take $\phi = 0.2$ and apply a Sturmian-Laguerre basis with $m = 0, \ldots, 6$ and $n = 1, \ldots, 150$. The ionization rate can be reliably computed for relatively large fields, i.e. $F \geq 15$ V/μm. To extrapolate to smaller fields, we fit computed values in the range 18 to 24 V/μm to the expected form for a two-dimensional material

$$\Gamma = aF^{-1/2}\exp(-F_0/F) \tag{D.5}$$

using a and F_0 as fitting parameters [138] (see Table D.1). Stark shifts and ionization rates for three different dielectric surroundings are shown in Fig. D.4.

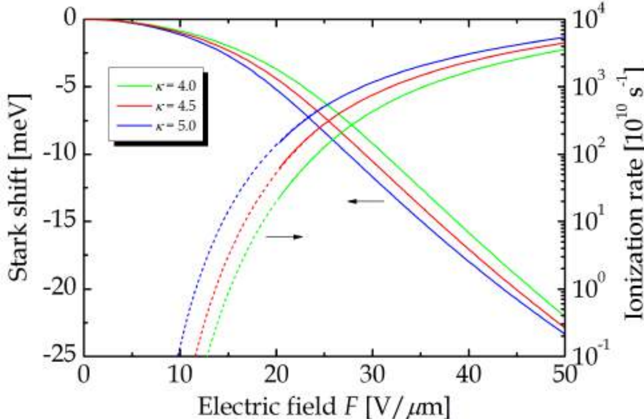

FIGURE D.4: **Calculated stark shifts and ionization rate for different dielectric encapsulations.** Solid lines are complex scaling calculations while dashed are fits to the analytical low-field form.

κ_{hBN}	E_{B} (meV)	a (μm$^{1/2}$/sV$^{1/2}$)	F_0 (V/μm)
4	190	1.62×10^{16}	196
4.5	170	1.82×10^{16}	179
5	153	8.46×10^{15}	144

TABLE D.1: Exciton binding energy (E_{B}) and fitting parameters (a and F_0) of the analytical ionization rate (Eq. D.5) obtained for different values of averaged dielectric constant in hBN (κ_{hBN}).

D.4 Nonlinear photoresponse model

D.4.1 Power dependence of the photocurrent

In order to simplify the analysis of the nonlinear photoresponse that we observe, we consider only one photoexcited specie (excitons) and introduce a quadratic loss term to the kinetic rate equation:

$$\frac{\mathrm{d}N}{\mathrm{d}t} = G(t) - \frac{N}{\tau} - \gamma N^2, \tag{D.6}$$

where N is the exciton density, $G(t)$ is the exciton generation rate, τ is the photoresponse time, γ is the time-independent exciton-exciton annihilation (EEA)

rate. Under pulsed excitation (e.i., $G(t) = N_0\delta(t)$, where N_0 is the initial exciton density), the solution to Eq. D.6 is :

$$N(t, N_0) = \frac{N_0 \exp\left(\frac{-t}{\tau}\right)}{1 + \gamma\tau N_0\left(1 - \exp\left(\frac{-t}{\tau}\right)\right)}. \tag{D.7}$$

In our experiment, the photocurrent we measure is proportional to the time-integrated excitons density:

$$PC(N_0) = \int_0^\infty N(t, N_0)dt \; = \frac{1}{\gamma}\ln(1 + \gamma\tau N_0) \tag{D.8}$$

As can be seen in Fig. D.5a (and Figs. 7.5a,b), this simple expression provides a good model for the sublinear power dependence of the photocurrent. We fit this Eq. D.8 to our data by assuming an initial exciton density is

$$N_0 = \frac{A_{\mathrm{abs}}}{f\pi r_L^2 h\nu} P, \tag{D.9}$$

where $A_{\mathrm{abs}} \sim 5\%$ is the absorption coefficient, P is the time-averaged laser power, $f = 40$ MHz is the laser repetition rate, $r_L = 0.7$ μm is the laser radius and $h\nu = 1.65$ eV is the photon energy. From these fits, we extract the value of $\gamma\tau$ as a function of V_{asym} and V_{B} shown in Fig. 7.5c.

D.4.2 Time-resolved photocurrent

We employ the TRPC technique (Section 2.5.3) to determine the absolute values of τ and γ, and thereby disentangle the contribution of the linear and nonlinear processes to the photoreponse of our device. This technique consists in measuring the photocurrent produced by two ultrashort ($\sim$ 200 fs) laser pulses with the same fluence as a function of the time delay Δt between the two pulses. In our experiment, one of the two pulses (the pump) is modulated by a mechanical chopper, such that the photocurrent (measured by lock-in) is:

$$PC(\Delta t) \propto \int_0^\infty N_{2\mathrm{P}}(t, N_0, \Delta t)\mathrm{d}t - \int_0^\infty N(t, N_0)\mathrm{d}t, \tag{D.10}$$

where $N(t, N_0)$ is the exciton density produced by a single pulse with initial exciton density N_0 (Eq. S14), and $N_{2\mathrm{P}}(t, N_0, \Delta t)$ is the exciton density produced by two pulses delayed by a time Δt. Assuming instantaneous (Dirac) pulses, this function can be written as

$$N_{2\mathrm{P}}\left(t, N_0, \Delta t\right) = \begin{cases} N\left(t, N_0\right) & \text{for } 0 < t < \Delta t \\ N\left(t-\Delta t, N_0 + N\left(\Delta t, N_0\right)\right) & \text{for } t > \Delta t \end{cases} \tag{D.11}$$

Fig. D.5b shows $N_{2\mathrm{P}}(t)$ and $N(t)$ calculated for N_0= 7×10^{12} cm^{-2}, Δt = 10 ps, τ = 25 ps and γ= 0.05 cm^2/s. We also calculate $N_{2\mathrm{P}}(t)$ produced by pulses with finite duration (200 fs) and find Eq. D.11 to be a good approximation. Using Eq. D.10 , we numerical solve $PC\left(\Delta t\right)$ for both finite duration pulses and Dirac delta-function pulses (Fig. D.5c) and observe no significant difference between both solutions.

In order to fit this model to our TRPC measurements, we develop an analytical expression that mimics the numerical solution. This expression takes into account the two limits of $PC\left(\Delta t\right)$:

$$PC\left(\Delta t \to \infty\right) \propto 2\int_0^\infty N\left(t, N_0\right)\mathrm{d}t - \int_0^\infty N\left(t, N_0\right)\mathrm{d}t = \frac{1}{\gamma}\ln\left(1+\gamma\tau N_0\right) \tag{D.12}$$

$$PC\left(\Delta t = 0\right) \propto \int_0^\infty N\left(t, 2N_0\right)\mathrm{d}t - \int_0^\infty N\left(t, N_0\right)\mathrm{d}t = \frac{1}{\gamma}\ln\left(1+\frac{\gamma\tau N_0}{1+\gamma\tau N_0}\right). \tag{D.13}$$

Interpolating between these two limits gives us the following analytical expression:

$$PC\left(\Delta t\right) \propto \ln\left[1+\frac{\gamma\tau N_0}{1+\gamma\tau N_0}\left(1+\gamma\tau N_0\left(1-\exp\left(\frac{-\Delta t}{\tau}\right)\right)\right)\right]. \tag{D.14}$$

We compare this expression to the numerical solutions of $PC\left(\Delta t\right)$ for the same set of parameters (Fig. D.5c) and observe very good agreement. Eq. D.14 also indicates that $PC\left(\Delta t\right)$ is governed by the exponential term $\exp\left(-\Delta t/\tau\right)$, which justifies the single exponential decay model often used to interpret TRPC measurements.

We employ this analytical expression (Eq. D.14) to fit our TRPC measurements and extract τ and other relevant parameters. The fitting parameters are then used to calculate the numerical solution of Eq. D.10 for pulses with finite duration. These numerical solutions are represented by the solid black lines in Figs. D.5d,e (and Figs. 7.6) and appear to match very well with the TRPC measurements.

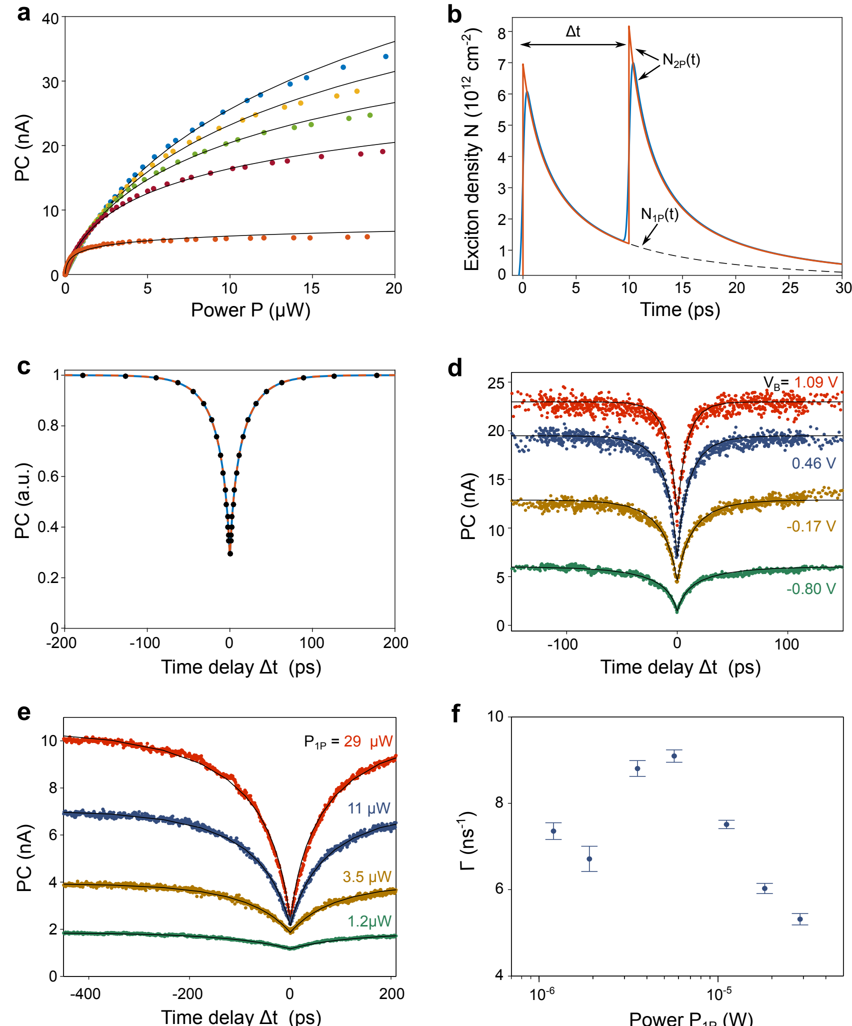

FIGURE D.5: **Additional analysis of the nonlinear and time-resolve photocurrent measurements. a)** Photocurrent versus laser power P measured at various gate voltages V_{asym} and $V_{\mathrm{B}} = 0$ V. The solid black lines are fit to the data using Eq. D.8. **b)** Temporal dependence of the calculated exciton density N_{2P} generated by 200 fs-long pulses (solid blue line) and Dirac delta-function pulses (solid red line). The black dotted line represents the single-pulse exciton density N_{1P}. Calculations are carried out using $N_0 = 7\times10^{12}$ cm^{-2}, Δt = 10 ps, τ = 25 ps and $\gamma = 0.05$ cm^2/s. **c)** Calculated PC as a function of the time delay Δt between pulses. The orange dotted line is computed using Dirac delta-function pulses (Eq. D.10 and D.11), the blue line is calculated using the analytic expression (Eq. D.14) and the black dots are computed numerically using 200 fs-long pulses. **d)** TRPC measurements at various bias voltages V_{B}, $V_{\mathrm{asym}} = 10$ V and single-pulse, time-averaged power $P_{\mathrm{1p}} = 100$ μW. **e)** TRPC measurements at different single-pulse power P_{1p} measured on Device 2 at $V_{\mathrm{asym}} = 6$ V and $V_{\mathrm{B}} = 0$ V. The solid black lines in (**d**) and (**e**) are fit to the data using the model presented in Section D.4.2. **f)** Photoresponse rate $\Gamma = 1/\tau$ extracted from the fit shown in (**e**) as a function of single-pulse power P_{1p}. Error bars correspond to the standard deviation obtained from these fits.

Finally, and importantly, we note that this model provides a way to determine the intrinsic value of τ independently of the laser power *P* employed for the TRPC measurements. Indeed, the model accounts for changes in the initial exciton density N_0 generated by a laser power *P* via Eq. D.9 . This represents a significant advantage over conventional models using a single exponential decay which typically yield power-dependent τ. Analysis of the TRPC measurements as a function of laser power using our model is shown in Figs. D.5e,f. No obvious trend between τ and *P* is observed when *P* is varied over more than one order of magnitude. We find however that the extracted value of τ varies by $\sim$40%, which might be a result of our fitting procedure.

D.5 Linear photoresponse model

Here we present the details of the photoresponse model that we introduced in Section 7.5 to explain the measured field-dependent photoresponse rate Γ and internal quantum efficiency (IQE). Our model describes the linear response of our device at low power excitation ($P \lesssim 1$ μW). In this regime, exciton-exciton annihilation and other nonlinear processes are negligeable. This assumption is justified since the values of Γ (extracted using the nonlinear model presented in the previous section) are disentangled from nonlinear effects and associated with linear processes. The linear response assumption also applies to the IQE because it was measured at low power ($P = 0.5$ μW).

As explained in Section 7.5, our model considers that excitons generated in (or diffusing to) the p-n junction at a rate *G* can either recombine at a field-independent rate$\Gamma_{\mathrm{r},N} = 1/\tau_{\mathrm{r},N}$ or dissociate by tunnel ionization at a rate $\Gamma_{\mathrm{diss}} = 1/\tau_{\mathrm{diss}}$. Prediction and calculations for Γ_{diss} as a function of in-plane electric field are presented in Section D.3 . Upon dissociation, free carriers drift out of the junction at a rate $\Gamma_{\mathrm{drift}} = 1/\tau_{\mathrm{drift}} = 2\mu F_{\mathrm{avg}}/L$, where μ is the free carrier mobility and *L* is the junction length. F_{avg}, the average electric field across the junction, is calculated from the field simulations presented in Section D.2. The drift process competes with the field-independent recombination of free carriers which occurs at a field-independent rate $\Gamma_{\mathrm{r},n} = 1/\tau_{\mathrm{r},n}$. Hence, the exciton density *N* and free carrier density *n* in the junction can be described by the following coupled rate equations:

$$\frac{\mathrm{d}N}{\mathrm{d}t} = G - \frac{N}{\tau_{\mathrm{diss}}} - \frac{N}{\tau_{\mathrm{r},N}} = G - \frac{N}{\tau_N} \tag{D.15}$$

$$\frac{\mathrm{d}n}{\mathrm{d}t} = \frac{N}{\tau_{\mathrm{diss}}} - \frac{n}{\tau_{\mathrm{drift}}} - \frac{n}{\tau_{\mathrm{r},n}} = \frac{N}{\tau_{\mathrm{diss}}} - \frac{n}{\tau_n}, \tag{D.16}$$

where $\Gamma_N = \frac{1}{\tau_N} = \frac{1}{\tau_{\mathrm{diss}}} + \frac{1}{\tau_{\mathrm{r},N}}$ and $\Gamma_n = \frac{1}{\tau_n} = \frac{1}{\tau_{\mathrm{drift}}} + \frac{1}{\tau_{\mathrm{r},n}}$ represent the total exciton and free carrier decay rates, respectively. The overall photoresponse rate

Γ of our device is determined by the slowest of these two rates and can therefore be approximately expressed as

$$\Gamma = \frac{1}{\tau} \approx \frac{1}{\tau_n + \tau_N}. \tag{D.17}$$

As we show in Fig. 7.7, Eq. D.18 captures well the field dependence of the measured photoresponse rate.

We now consider the efficiency of the photocurrent generation process predicted by our model. Under steady state conditions (i.e. CW illumination), the photocurrent produced is proportional to the rate at which free carriers drift out of the p-n junction, such that

$$PC \propto \frac{\mathrm{d}n_{\mathrm{extract}}}{\mathrm{d}t} = \frac{n}{\tau_{\mathrm{drift}}}, \tag{D.18}$$

where n_{extract} is the density of free carriers extracted out of the junction. Setting the time derivatives of Eqs. D.15 and D.16 to zero, we find the following relation between the rate at which excitons are created and the rate at which free carriers are extracted:

$$\frac{\mathrm{d}n_{\mathrm{extract}}}{\mathrm{d}t} = \frac{\tau_n}{\tau_{\mathrm{drift}}} \frac{\tau_N}{\tau_{\mathrm{diss}}} G = \eta_{\mathrm{extract}} G, \tag{D.19}$$

where η_{extract}, the extraction efficiency, can be rewritten as

$$\eta_{\mathrm{extract}} = \frac{\tau_{\mathrm{r},n}}{\tau_{\mathrm{r},n} + \tau_{\mathrm{drift}}} \frac{\tau_{\mathrm{r},N}}{\tau_{\mathrm{r},N} + \tau_{\mathrm{diss}}} = \eta_{\mathrm{drift}}\ \eta_{\mathrm{diss}}. \tag{D.20}$$

From this expression, it is clear that the extraction efficiency characterizes how efficiently exciton generated in (or diffusing to) the p-n junction dissociate into free carriers (η_{diss}), and how efficiently theses free carriers drift out of the junction (η_{drift}).

D.6 Collection efficiency

In this section we address the diffusion and collection excitons generated outside the junction. Indeed, in our experiment, a significant fraction of the total exciton population is generated away from the junction because the laser spot size we use is larger than the junction length. In order to contribute to the photocurrent, these excitons first need to diffuse to the junction. Those who reach the junction

then undergo the extraction process described in Section 6. The total IQE is therefore given by

$$\mathrm{IQE} = \eta_{\mathrm{coll}}\, \eta_{\mathrm{extract}}, \tag{D.21}$$

where η_{extract} is the extraction efficiency (see previous section), and η_{coll} , the collection efficiency, is define as the ratio between the number of excitons reaching the p-n junction and the total number of excitons generated (or photons absorbed) in the WSe_2. η_{coll} can be evaluated using the following equation :

$$\eta_{\mathrm{coll}} = \frac{\iint G(x,y)\;\, CP(x,y)\;\, \mathrm{d}x\mathrm{d}y}{\int G(x,y)\;\, \mathrm{d}x\mathrm{d}y}, \tag{D.22}$$

where $G(x,y)$ is the exciton generation rate and $CP(x,y)$, the collection probability, corresponds to the probability that an exciton generated in a certain region of the device has to reach the junction. In what follows, we evaluate η_{coll} in our experiment using two different approaches.

Experimental estimation of the collection efficiency

The first method consists in estimating the collection probability CP from the measured laser spot and photocurrent profile. Considering that the width of the junction (in they-direction) is much wider than the laser spot size, the photocurrent profile *PC(x)* obtained by scanning the laser position across the junction (in the *x*-direction) corresponds to the convolution of $G(x)$ and (x) :

$$PC(x) \propto \int G(x-x')\;\, CP(x')\, \mathrm{d}x'. \tag{D.23}$$

To simplify our analysis, we assume that both $G(x)$ and $CP(x)$ can be described by Gaussian profiles characterized by σ_{G} and σ_{CP}, respectively. Then, according to Eq. D.24 , the photocurrent also has a Gaussian profile with $\sigma_{\mathrm{PC}} = \sqrt{\sigma_{\mathrm{G}}^2 + \sigma_{\mathrm{CP}}^2}$.

Since the exciton generation rate is proportional to the intensity of the laser spot, we determine σ_{G} by measuring the reflection *R* of the laser as it is scans across the sharp junction made of two gates separated by 200 nm. Fitting the normalized Δ*R* with a Gaussian yields $\sigma_{\mathrm{G}} = 0.60 \pm 0.01$ μm, which translates into a FWHM of 1.4 μm (Fig. D.6a). Repeating this procedure with the measured $PC(x)$ gives $\sigma_{\mathrm{PC}} = 0.64 \pm 0.01$ μm, which implies that $\sigma_{\mathrm{CP}} = \sqrt{\sigma_{\mathrm{G}}^2 + \sigma_{\mathrm{PC}}^2} = 0.19 \pm 0.014$ μm. Using these values, we evaluate the collection efficiency with Eq. D.22 and find $\eta_{\mathrm{coll}} = 30 \pm 3\%$, which agrees very well with our IQE measurements and predictions for η_{extract} (see the inset Fig. 7.7a).

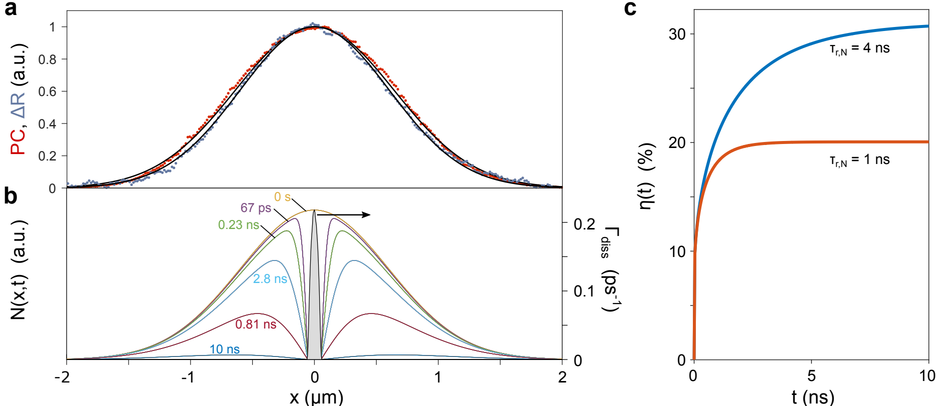

FIGURE D.6: **Experimental and numerical estimations of the collection efficiency. a)** Normalized photocurrent *PC(x)* (red data points) and reflection Δ*R(x)* (blue data points) profiles measured by scanning a focused laser beam ($h\nu$ = 1.65 eV, P = 4 μW) on Device 1 with $V_{\mathrm{B}} = 0$ V and $V_{\mathrm{asym}} = 10$ V. The black lines are Gaussian fits to the data, with standard deviations $\sigma_{\mathrm{PC}} = 0.64$ μm and $\sigma_{\Delta\mathrm{R}} = 0.60$ μm. **b)** Exciton density $N(x,t)$ calculated using Eq. D.25 for different times between t = 0 and 10 ns, assuming $\tau_{\mathrm{r},N} = 4$ ns. The junction is located at x = 0 and calculations are performed using the in-plane electric field simulated for $V_{\mathrm{B}} = 2$ V and $V_{\mathrm{asym}} = 10$ V. The dissociation rate $\Gamma_{\mathrm{diss}}(x,F) = 1/\tau_{\mathrm{diss}}(x,F)$ is calculated using the model presented in Section D.3 and represented by the solid black line with grey shading (right axis). **c)** Time evolution of η, the ratio between the number of dissociated excitons and the total number of excitons, calculated for $\tau_{\mathrm{r},N} = 1$ and 4 ns (solid red and blue lines, respectively).

D.6.1 Numerical estimation of the collection efficiency

We can also evaluate η_{coll} by including exciton diffusion to the linear photoresponse model described in the previous section. To model the dynamic of the exciton density $N(x,t)$ across the junction, we numerically solve the following partial differential equation:

$$\frac{\partial N(x,t)}{\partial t} = D_N \frac{\partial^2 N(x,t)}{\partial x^2} + G(x,t) - \frac{N(x,t)}{\tau_{\mathrm{diss}}(x,F)} - \frac{N(x,t)}{\tau_{\mathrm{r},N}}, \tag{D.24}$$

where D_N is the exciton diffusion constant, $G(x,t)$ is the exciton generation rate, $\Gamma_{\mathrm{diss}}(x,F) = 1/\tau_{\mathrm{diss}}(x,F)$ is the field-dependent exciton dissociation rate and $\Gamma_{\mathrm{r},N} = 1/\tau_{\mathrm{r},N}$ is the field-independent exciton recombination rate. We assume that excitons are generated by a Gaussian laser pulse, such that $G(x,t) \propto \delta(t) f(x, \sigma_{\mathrm{G}} = 0.60\ \mu\mathrm{m})$, where f represents a Gaussian function.

To evaluate η_{coll}, we calculate the total number of excitons that dissociate at the junction, $N_{\text{diss}}(t)$, and compute

$$\eta = \frac{N_{\text{diss}}\left(t \to \infty\right)}{\int G\left(x,y\right)\,\mathrm{d}x} = \eta_{\text{coll}}\eta_{\text{diss}}. \tag{D.25}$$

η_{coll} can be estimated by considering a case where the in-plane field *F(x)* is high, such that $\eta_{\text{diss}} \sim 1$ and $\eta \sim \eta_{\text{coll}}$. For this purpose, we use *F(x)* simulated for $V_{\text{B}} = 2$ V and $V_{\text{asym}} = 10$ V (see Section D.2) and calculate $\tau_{\text{diss}}(x, F)$ using the model presented in Section D.3 (Fig. D.6b).

Finally, D_N and $\tau_{\text{r},N}$ are set according to the values we extracted from our analysis of photoresponse time presented in Section 7.5. Specifically, the diffusion coefficient is evaluated using $D_N = \mu_N k_{\text{B}} T/e_0$, where μ_N is the exciton mobility, k_{B} is Boltzmann's constant, T = 300 K is the ambient temperature and e_0 is the elementary charge. For our simulations, we assume that μ_N is equal to the free carrier mobility (μ = 4 cm^2/Vs) determined experimentally. Since our measurements give a rather imprecise value of $\tau_{\text{r},N} \sim$ 1 ns, we evaluate η_{coll} for $\tau_{\text{r},N} = 1$ and 4 ns, corresponding to diffusion lengths $L_D = \sqrt{D_N\ \tau_{\text{r},N}} = 0.1$ and 0.2 μm, respectively.

The time evolution of $N(x,t)$ for $\tau_{\text{r},N}$ = 4 ns calculated by solving Eq. D.25 is shown in Fig D.6b. Fig. D.6c shows the increase of η as a function of time for both $\tau_{\text{r},N} = 1$ and 4 ns. From this last figure, we conclude that $\eta_{\text{coll}} \sim$ 20 - 30 %, for diffusion lengths of 0.1 and 0.2 μm, respectively. These values match well with the value of η_{coll} obtained with the experimental approach and the one deduced from our IQE measurements in Section 7.5 .

Publications

Publications covered in this thesis

- Tielrooij, K. J.*, **Massicotte, M.*** , Piatkowski, Woessner, A., Ma, Q., Jarillo-Herrero, P.,Van Hulst, N. F., and Koppens, F. H. L. *Hot-carrier photocurrent effects at graphene–metal interfaces*. J. Phys. Condens. Matter, 27, 16, 164207 (2015)
- Tielrooij, K. J., Piatkowski, L.*, **Massicotte, M.***, Woessner, A., Ma, Q., Lee, Y., Myhro, K. S.,Lau, C. N., Jarillo-Herrero, P., van Hulst, N. F. and Koppens, F. H. L. *Generation of Photovoltage in Graphene on a Femtosecond Timescale through Efficient Carrier Heating.* Nature Nanotech. 10, 5, 437–443 (2015)
- **Massicotte, M.**, Schmidt, P., Vialla, F., Schädler, K. G., Reserbat-Plantey, A., Watanabe, K., Taniguchi, T., Tielrooij, K.J. and Koppens, F.H.L. *Picosecond photoresponse in van der Waals heterostructures.* Nature Nanotech. 11, 5, 42-46 (2015)
- Ma, Q.*, Andersen, T.*, Nair, N.*, Gabor, N., **Massicotte, M.**, Lui, C. H., Young, A., Fang, W., Watanabe, K., Taniguchi, T., Kong, J., Gedik, N., Koppens F. H. L. and Jarillo-Herrero, P. *Ultrafast electron thermalization pathways in a van der Waals heterostructure.* Nature Phys. 12, 455-459 (2015)
- **Massicotte, M.**, Schmidt, P., Vialla, Watanabe, K., Taniguchi, T., Tielrooij, K. J. and Koppens, F. H. L. *Photo-thermionic effect in vertical graphene heterostructures*. Nat. Commun. 7, 12174 (2016)
- **Massicotte, M.**, Vialla, F., Schmidt, P., Lundeberg, M. B., Latini, S., Haastrup, S., Danovich, M., Davydovskaya, D., Watanabe, K., Taniguchi, T., Fal'ko, V. I., Thygesen, K. S., Pedersen, T. G., Koppens, F. H. L., *Tunnel ionization of 2D excitons in monolayer* WSe_2. Submitted (2017)

* These authors contributed equally to this work

Other publications by the author

- Tielrooij, K. J., Hesp, N., Principi, A., Lundeberg, M., Pogna, E., Banszerus, L, Mics, Z., **Massicotte, M.**, Schmidt, P., Davydovskaya, D., Taniguchi, T., Watanabe, K., Bonn, M., Turchinovich, D., Stampfer, C., Cerullo, G., Polini, M., Koppens, F. H. L., *Out-of-plane heat transfer in van der Waals stacks: electron-hyperbolic phonon coupling.* submitted (2017)
- Baudisch, M., Marini, A., Cox, J. D., Zhu, T., Silva, F., Teichmann, S., **Massicotte, M.**, Koppens, F. H. L., Levitov, L. S., Garcia de Abajo, F. G. , Biegert, J., *Petahertz optical response in graphene.* Submitted (2017)

Bibliography

1. Feynman, R. P. There's plenty of room at the bottom. *Engineering and Science* **25,** 22–36 (1960).
2. Alferov, Z. Nobel Lecture: The double heterostructure concept and its applications in physics, electronics, and technology. *Reviews of modern physics* **73,** 767–782 (2001).
3. Alferov, Z. Heterostructures for Optoelectronics: History and Modern Trends. *Proceedings of the IEEE* **101,** 2176–2182 (2013).
4. Weber, E. R. *Semiconductors and Semimetals: Imperfections in III/ V materials* (Academic Press Inc, 1993).
5. Novoselov, K. S. *et al.* Electric Field Effect in Atomically Thin Carbon Films. *Science* **306,** 666–669 (2004).
6. Novoselov, K. S. *et al.* Two-dimensional atomic crystals. *Proceedings of the National Academy of Sciences* **102,** 10451–10453 (2005).
7. Ferrari, A. C. *et al.* Science and technology roadmap for graphene, related two-dimensional crystals, and hybrid systems. *Nanoscale* **7,** 4598–4810 (2014).
8. Bolotin, K. *et al.* Ultrahigh electron mobility in suspended graphene. *Solid State Communications* **146,** 351–355 (2008).
9. Wang, L. *et al.* One-Dimensional Electrical Contact to a Two-Dimensional Material. *Science* **342,** 614–617 (2013).
10. Lee, C., Wei, X., Kysar, J. W. & Hone, J. Measurement of the Elastic Properties and Intrinsic Strength of Monolayer Graphene. *Science* **321,** 385–388 (2008).
11. Balandin, A. A. *et al.* Superior Thermal Conductivity of Single-Layer Graphene. *Nano Letters* **8,** 902–907 (2008).
12. Cassabois, G., Valvin, P. & Gil, B. Hexagonal boron nitride is an indirect bandgap semiconductor. *Nature Photonics* **10,** 262–266 (2016).
13. Giovannetti, G., Khomyakov, P. A., Brocks, G., Kelly, P. J. & van den Brink, J. Substrate-induced band gap in graphene on hexagonal boron nitride: Ab initio density functional calculations. *Physical Review B* **76,** 073103 (2007).
14. Wang, Q. H., Kalantar-Zadeh, K., Kis, A., Coleman, J. N. & Strano, M. S. Electronics and optoelectronics of two-dimensional transition metal dichalcogenides. *Nature Nanotechnology* **7,** 699–712 (2012).

15. Mak, K. F., Lee, C., Hone, J., Shan, J. & Heinz, T. F. Atomically thin MoS_2: A new direct-gap semiconductor. *Physical Review Letters* **105,** 136805 (2010).
16. Splendiani, A. *et al.* Emerging Photoluminescence in Monolayer MoS_2. *Nano Letters* **10,** 1271–1275 (2010).
17. Radisavljevic, B, Radenovic, A, Brivio, J, Giacometti, V & Kis, A. Single-layer MoS_2 transistors. *Nature Nanotechnology* **6,** 147–150 (2011).
18. Carvalho, A. *et al.* Phosphorene: from theory to applications. *Nature Reviews Materials* **1,** 16061 (2016).
19. Li, L. *et al.* Black phosphorus field-effect transistors. *Nature Nanotechnology* **9,** 372–377 (2014).
20. Xi, X. *et al.* Ising pairing in superconducting $NbSe_2$ atomic layers. *Nature Physics* **12,** 139–143 (2015).
21. Fei, Z. *et al.* Edge conduction in monolayer WTe_2. *Nature Physics.* arXiv: 1610.07924 (2017).
22. Huang, B. *et al.* Layer-dependent Ferromagnetism in a van der Waals Crystal down to the Monolayer Limit. arXiv: 1703.05892 (2017).
23. Dean, C. R. *et al.* Boron nitride substrates for high-quality graphene electronics. *Nature Nanotechnology* **5,** 722–726 (2010).
24. Wang, L. *et al.* One-Dimensional Electrical Contact to a Two-Dimensional Material. *Science* **342,** 614–617 (2013).
25. Geim, A. K. & Grigorieva, I. V. Van der Waals heterostructures. *Nature* **499,** 419–425 (2013).
26. Liu, Y. *et al.* Van der Waals heterostructures and devices. *Nature Reviews Materials* **1,** 16042 (2016).
27. Novoselov, K. S., Mishchenko, A, Carvalho, A & Castro Neto, A. H. 2D materials and van der Waals heterostructures. *Science* **353,** aac9439–aac9439 (2016).
28. Rasmussen, F. A. & Thygesen, K. S. Computational 2D Materials Database: Electronic Structure of Transition-Metal Dichalcogenides and Oxides. *The Journal of Physical Chemistry C* **119,** 13169–13183 (2015).
29. Lebègue, S., Björkman, T., Klintenberg, M., Nieminen, R. M. & Eriksson, O. Two-Dimensional Materials from Data Filtering and Ab Initio Calculations. *Physical Review X* **3,** 031002 (2013).
30. Ataca, C, Şahin, H. & Ciraci, S. Stable, Single-Layer MX_2 Transition-Metal Oxides and Dichalcogenides in a Honeycomb-Like Structure. *The Journal of Physical Chemistry C* **116,** 8983–8999 (2012).
31. Koppens, F. H. L. *et al.* Photodetectors based on graphene, other two-dimensional materials and hybrid systems. *Nature Nanotechnology* **9,** 780–793 (2014).
32. Bonaccorso, F, Sun, Z, Hasan, T & Ferrari, A. C. Graphene photonics and optoelectronics. *Nature Photonics* **4,** 611–622 (2010).

33. Xia, F., Wang, H., Xiao, D., Dubey, M. & Ramasubramaniam, A. Two-dimensional material nanophotonics. *Nature Photonics* **8,** 899–907 (2014).
34. Mak, K. F. & Shan, J. Photonics and optoelectronics of 2D semiconductor transition metal dichalcogenides. *Nature Photonics* **10,** 216–226 (2016).
35. Lou, Z., Liang, Z. & Shen, G. Photodetectors based on two dimensional materials. *Journal of Semiconductors* **37,** 091001 (2016).
36. Sun, Z., Martinez, A. & Wang, F. Optical modulators with 2D layered materials. *Nature Photonics* **10,** 227–238 (2016).
37. Withers, F. *et al.* Light-emitting diodes by band-structure engineering in van der Waals heterostructures. *Nature Materials* **14,** 301–306 (2015).
38. Chen, J. *et al.* Optical nano-imaging of gate-tunable graphene plasmons. *Nature,* 3–7 (2012).
39. Bao, Q. & Loh, K. P. Graphene Photonics, Plasmonics, and Broadband Optoelectronic Devices. *ACS Nano* **6,** 3677–3694 (2012).
40. Duan, X., Wang, C., Pan, A., Yu, R. & Duan, X. Two-dimensional transition metal dichalcogenides as atomically thin semiconductors: opportunities and challenges. *Chem. Soc. Rev.* **44,** 8859–8876 (2015).
41. Buscema, M. *et al.* Photocurrent generation with two-dimensional van der Waals semiconductors. *Chem. Soc. Rev.* **44,** 3691–3718 (2015).
42. Bablich, A., Kataria, S. & Lemme, M. Graphene and Two-Dimensional Materials for Optoelectronic Applications. *Electronics* **5,** 13 (2016).
43. Wang, Q., Lai, J. & Sun, D. Review of photo response in semiconductor transition metal dichalcogenides based photosensitive devices. *Optical Materials Express* **6,** 2313 (2016).
44. Nair, R. R. *et al.* Fine Structure Constant Defines Visual Transparency of Graphene. *Science* **320,** 1308–1308 (2008).
45. Gabor, N. M. *et al.* Hot Carrier-Assisted Intrinsic Photoresponse in Graphene. *Science* **334,** 648–652 (2011).
46. Mueller, T., Xia, F. & Avouris, P. Graphene photodetectors for high-speed optical communications. *Nature Photonics* **4,** 297–301 (2010).
47. Gan, X. *et al.* Chip-integrated ultrafast graphene photodetector with high responsivity. *Nature Photonics* **7,** 883–887 (2013).
48. Schuler, S. *et al.* Controlled Generation of a p–n Junction in a Waveguide Integrated Graphene Photodetector. *Nano Letters* **16,** 7107–7112 (2016).
49. Li, Y. *et al.* Measurement of the optical dielectric function of monolayer transition-metal dichalcogenides: MoS_2, $MoSe_2$, WS_2 and WSe_2. *Physical Review B* **90,** 205422 (2014).
50. Britnell, L *et al.* Strong Light-Matter Interactions in Heterostructures of Atomically Thin Films. *Science* **340,** 1311–1314 (2013).
51. Ceballos, F. & Zhao, H. Ultrafast Laser Spectroscopy of Two-Dimensional Materials Beyond Graphene. *Advanced Functional Materials* **27,** 1604509 (2017).

52. Wallace, P. The band theory of graphite. *Physical Review* **329** (1947).

53. Mermin, N. D. Crystalline Order in Two Dimensions. *Physical Review* **176,** 250–254 (1968).

54. Geim, A. K. Nobel Lecture: Random walk to graphene. *Reviews of Modern Physics* **83,** 851–862 (2011).

55. Dresselhaus, M. S. & Araujo, P. T. Perspectives on the 2010 Nobel Prize in Physics for Graphene. *ACS Nano* **4,** 6297–6302 (2010).

56. Castro Neto, A. H., Guinea, F, Peres, N. M. R., Novoselov, K. S. & Geim, A. K. The electronic properties of graphene. *Reviews of Modern Physics* **81,** 109–162 (2009).

57. Das Sarma, S., Adam, S., Hwang, E. H. & Rossi, E. Electronic transport in two-dimensional graphene. *Reviews of Modern Physics* **83,** 407–470 (2011).

58. Cooper, D. R. *et al.* Experimental Review of Graphene. *ISRN Condensed Matter Physics* **2012,** 1–56 (2012).

59. Banszerus, L. *et al.* Ballistic Transport Exceeding 28 μm in CVD Grown Graphene. *Nano Letters* **16,** 1387–1391 (2016).

60. Mak, K. F., Ju, L., Wang, F. & Heinz, T. F. Optical spectroscopy of graphene: From the far infrared to the ultraviolet. *Solid State Communications* **152,** 1341–1349 (2012).

61. Zhang, Y. B., Tan, Y. W., Stormer, H. L. & Kim, P. Experimental observation of the quantum Hall effect and Berry's phase in graphene. *Nature* **438,** 201–204 (2005).

62. Novoselov, K. S. *et al.* Two-dimensional gas of massless Dirac fermions in graphene. *Nature* **438,** 197–200 (2005).

63. Geim, A. K. & Novoselov, K. S. The rise of graphene. *Nature Materials* **6,** 183–191 (2007).

64. Mak, K. F. *et al.* Measurement of the Optical Conductivity of Graphene. *Physical Review Letters* **101,** 196405 (2008).

65. Li, Z. Q. *et al.* Dirac charge dynamics in graphene by infrared spectroscopy. *Nature Physics* **4,** 532–535 (2008).

66. Falkovsky, L. A. Optical properties of graphene. *Journal of Physics: Conference Series* **129,** 012004 (2008).

67. Mak, K. F., Shan, J. & Heinz, T. F. Seeing Many-Body Effects in Single- and Few-Layer Graphene: Observation of Two-Dimensional Saddle-Point Excitons. *Physical Review Letters* **106,** 046401 (2011).

68. Fang, H. *et al.* Quantum of optical absorption in two-dimensional semiconductors. *Proceedings of the National Academy of Sciences* **110,** 11688–11691 (2013).

69. Eda, G. & Maier, S. A. Two-Dimensional Crystals: Managing Light for Optoelectronics. *ACS Nano* **7,** 5660–5665 (2013).

70. Blake, P. *et al.* Making graphene visible. *Applied Physics Letters* **91,** 063124 (2007).

71. Breusing, M. *et al.* Ultrafast nonequilibrium carrier dynamics in a single graphene layer. *Physical Review B* **83,** 153410 (2011).
72. Castro Neto, A. H. The carbon new age. *Materials Today* **13,** 12–17 (2010).
73. Freitag, M., Low, T. & Avouris, P. Increased Responsivity of Suspended Graphene Photodetectors. *Nano Letters* **13,** 130305150920004 (2013).
74. George, P. a. *et al.* Ultrafast Optical-Pump Terahertz-Probe Spectroscopy of the Carrier Relaxation and Recombination Dynamics in Epitaxial Graphene. *Nano Letters* **8,** 4248–4251 (2008).
75. Gierz, I. *et al.* Snapshots of non-equilibrium Dirac carrier distributions in graphene. *Nature Materials* **12,** 1119–1124 (2013).
76. Graham, M. W., Shi, S.-F., Ralph, D. C., Park, J. & McEuen, P. L. Photocurrent measurements of supercollision cooling in graphene. *Nature Physics* **9,** 103–108 (2012).
77. Jensen, S. A. *et al.* Competing Ultrafast Energy Relaxation Pathways in Photoexcited Graphene. *Nano Letters* **14,** 5839–5845 (2014).
78. Johannsen, J. C. *et al.* Direct View of Hot Carrier Dynamics in Graphene. *Physical Review Letters* **111,** 027403 (2013).
79. Low, T., Perebeinos, V., Kim, R., Freitag, M. & Avouris, P. Cooling of photoexcited carriers in graphene by internal and substrate phonons. *Physical Review B* **86,** 045413 (2012).
80. Lui, C. H., Mak, K. F., Shan, J. & Heinz, T. F. Ultrafast Photoluminescence from Graphene. *Physical Review Letters* **105,** 127404 (2010).
81. Malic, E., Winzer, T., Wendler, F. & Knorr, A. Review on carrier multiplication in graphene. *physica status solidi (b)* **253,** 2303–2310 (2016).
82. Principi, A. *et al.* Super-Planckian Electron Cooling in a van der Waals Stack. *Physical Review Letters* **118,** 126804 (2017).
83. Song, J. C. W., Reizer, M. Y. & Levitov, L. S. Disorder-Assisted Electron-Phonon Scattering and Cooling Pathways in Graphene. *Physical Review Letters* **109,** 106602 (2012).
84. Song, J. C. W., Rudner, M. S., Marcus, C. M. & Levitov, L. S. Hot Carrier Transport and Photocurrent Response in Graphene. *Nano Letters* **11,** 4688–4692 (2011).
85. Song, J. C. W., Tielrooij, K. J., Koppens, F. H. L. & Levitov, L. S. Photoexcited carrier dynamics and impact-excitation cascade in graphene. *Physical Review B* **87,** 155429 (2013).
86. Song, J. C. W. & Levitov, L. S. Energy flows in graphene: hot carrier dynamics and cooling. *Journal of Physics: Condensed Matter* **27,** 164201 (2015).
87. Strait, J. H. *et al.* Very Slow Cooling Dynamics of Photoexcited Carriers in Graphene Observed by Optical-Pump Terahertz-Probe Spectroscopy. *Nano Letters* **11,** 4902–4906 (2011).
88. Tielrooij, K. J. *et al.* Out-of-plane heat transfer in van der Waals stacks : electron-hyperbolic phonon coupling, 1–24 (2017).

89. Tielrooij, K. J. *et al.* Photoexcitation cascade and multiple hot-carrier generation in graphene. *Nature Physics* **9,** 248–252 (2013).
90. Tse, W.-K. & Das Sarma, S. Energy relaxation of hot Dirac fermions in graphene. *Physical Review B* **79,** 235406 (2009).
91. Winnerl, S *et al.* Carrier Relaxation in Epitaxial Graphene Photoexcited Near the Dirac Point. *Physical Review Letters* **107,** 237401 (2011).
92. Winzer, T., Jago, R. & Malic, E. Experimentally accessible signatures of Auger scattering in graphene. *Physical Review B* **94,** 235430 (2016).
93. Winzer, T., Knorr, A. & Malic, E. Carrier Multiplication in Graphene. *Nano Letters* **10,** 4839–4843 (2010).
94. Winzer, T. & Malić, E. Impact of Auger processes on carrier dynamics in graphene. *Physical Review B* **85,** 241404 (2012).
95. Brida, D *et al.* Ultrafast collinear scattering and carrier multiplication in graphene. en. *Nature Communications* **4,** 1–9 (2013).
96. Gabor, N. M. Impact Excitation and Electron–Hole Multiplication in Graphene and Carbon Nanotubes. *Accounts of Chemical Research* **46,** 1348–1357 (2013).
97. Hwang, E. H., Hu, B. Y.-K. & Das Sarma, S. Inelastic carrier lifetime in graphene. *Physical Review B* **76,** 115434 (2007).
98. Bistritzer, R & MacDonald, A. H. Electronic Cooling in Graphene. *Physical Review Letters* **102,** 206410 (2009).
99. Betz, A. C. *et al.* Supercollision cooling in undoped graphene. *Nature Physics* **9,** 109–112 (2012).
100. Alencar, T. V., Silva, M. G., Malard, L. M. & de Paula, A. M. Defect-Induced Supercollision Cooling of Photoexcited Carriers in Graphene. *Nano Letters* **14,** 5621–5624 (2014).
101. Meric, I. *et al.* Current saturation in zero-bandgap, top-gated graphene field-effect transistors. *Nature Nanotechnology* **3,** 654–659 (2008).
102. Chen, J.-H., Jang, C., Xiao, S., Ishigami, M. & Fuhrer, M. S. Intrinsic and extrinsic performance limits of graphene devices on SiO2. *Nature Nanotechnology* **3,** 206–209 (2008).
103. Mattheiss, L. F. Band Structures of Transition-Metal-Dichalcogenide Layer Compounds. *Physical Review B* **8,** 3719–3740 (1973).
104. Grasso, V. *Electronic Structure and Electronic Transitions in Layered Materials* 42–43 (1987).
105. Kautek, W. Electronic mobility anisotropy of layered semiconductors: transversal photoconductivity measurements at n-$MoSe_2$. *Journal of Physics C: Solid State Physics* **15,** L519–L525 (1982).
106. Beal, A. R., Knights, J. C. & Liang, W. Y. Transmission spectra of some transition metal dichalcogenides. II. Group VIA: trigonal prismatic coordination. *Journal of Physics C: Solid State Physics* **5,** 3540–3551 (1972).

107. Wilson, J. & Yoffe, A. The transition metal dichalcogenides discussion and interpretation of the observed optical, electrical and structural properties. *Advances in Physics* **18,** 193–335 (1969).

108. Schmidt, H., Giustiniano, F. & Eda, G. Electronic transport properties of transition metal dichalcogenide field-effect devices: surface and interface effects. *Chem. Soc. Rev.* **44,** 7715–7736 (2015).

109. Podzorov, V., Gershenson, M. E., Kloc, C., Zeis, R. & Bucher, E. High-mobility field-effect transistors based on transition metal dichalcogenides. *Applied Physics Letters* **84,** 3301–3303 (2004).

110. Wurstbauer, U., Miller, B., Parzinger, E. & Holleitner, A. W. Light–matter interaction in transition metal dichalcogenides and their heterostructures. *Journal of Physics D: Applied Physics* **50,** 173001 (2017).

111. Kuc, A., Zibouche, N. & Heine, T. Influence of quantum confinement on the electronic structure of the transition metal sulfide TS_2. *Physical Review B* **83,** 245213 (2011).

112. Liu, G.-b. *et al.* Electronic structures and theoretical modelling of two-dimensional group-VIB transition metal dichalcogenides. *Chemical Society Reviews* **44,** 2643–2663 (2014).

113. Lebègue, S. & Eriksson, O. Electronic structure of two-dimensional crystals from ab initio theory. *Physical Review B* **79,** 115409 (2009).

114. Zhao, W. *et al.* Evolution of Electronic Structure in Atomically Thin Sheets of WS_2 and WSe_2. *ACS Nano* **7,** 791–797 (2013).

115. Zhao, W. *et al.* Origin of Indirect Optical Transitions in Few-Layer MoS_2 , WS_2 , and WSe_2. *Nano Letters* **13,** 5627–5634 (2013).

116. Xiao, D., Yao, W. & Niu, Q. Valley-Contrasting Physics in Graphene: Magnetic Moment and Topological Transport. *Physical Review Letters* **99,** 236809 (2007).

117. Xiao, D., Liu, G.-B., Feng, W., Xu, X. & Yao, W. Coupled spin and valley physics in monolayers of MoS_2 and other group-VI dichalcogenides. *Physical Review Letters* **108,** 196802 (2012).

118. Mak, K. F., McGill, K. L., Park, J. & McEuen, P. L. The valley Hall effect in MoS_2 transistors. *Science* **344,** 1489–1492 (2014).

119. Xu, X., Yao, W., Xiao, D. & Heinz, T. F. Spin and pseudospins in layered transition metal dichalcogenides. *Nature Physics* **10,** 343–350 (2014).

120. Schaibley, J. R. *et al.* Valleytronics in 2D materials. *Nature Reviews Materials* **1,** 16055 (2016).

121. Low, T. *et al.* Polaritons in layered two-dimensional materials. *Nature Materials* **16,** 182–194 (2016).

122. C., K. *Introduction to solid state physics* (eds Ltd, J. W. & Sons) (1953).

123. Koch, S. W., Kira, M, Khitrova, G & Gibbs, H. M. Semiconductor excitons in new light. *Nature Materials* **5,** 523–531 (2006).

124. Rosencher, E., Vinter, B. & Piva, P. G. *Optoelectronics* (Cambridge University Press, Cambridge, 2002).

125. Ramasubramaniam, A. Large excitonic effects in monolayers of molybdenum and tungsten dichalcogenides. *Physical Review B* **86,** 115409 (2012).

126. Qiu, D. Y., da Jornada, F. H. & Louie, S. G. Optical Spectrum of MoS_2: Many-Body Effects and Diversity of Exciton States. *Physical Review Letters* **111,** 216805 (2013).

127. Komsa, H.-P. & Krasheninnikov, A. V. Effects of confinement and environment on the electronic structure and exciton binding energy of MoS_2 from first principles. *Physical Review B* **86,** 241201 (2012).

128. Berkelbach, T. C., Hybertsen, M. S. & Reichman, D. R. Theory of neutral and charged excitons in monolayer transition metal dichalcogenides. *Physical Review B* **88,** 045318 (2013).

129. Thygesen, K. S. Calculating excitons, plasmons, and quasiparticles in 2D materials and van der Waals heterostructures. *2D Materials* (2017).

130. Latini, S., Olsen, T. & Thygesen, K. S. Excitons in van der Waals heterostructures: The important role of dielectric screening. *Physical Review B* **92,** 245123 (2015).

131. Chernikov, A. *et al.* Exciton binding energy and nonhydrogenic Rydberg series in monolayer WS_2. *Physical Review Letters* **113,** 076802 (2014).

132. Ye, Z. *et al.* Probing excitonic dark states in single-layer tungsten disulphide. *Nature* **513,** 214–218 (2014).

133. Ugeda, M. M. *et al.* Giant bandgap renormalization and excitonic effects in a monolayer transition metal dichalcogenide semiconductor. *Nature Materials* **13,** 1091–1095 (2014).

134. Stier, A. V., Wilson, N. P., Clark, G., Xu, X. & Crooker, S. A. Probing the Influence of Dielectric Environment on Excitons in Monolayer WSe_2 : Insight from High Magnetic Fields. *Nano Letters* **16,** 7054–7060 (2016).

135. He, K. *et al.* Tightly bound excitons in monolayer WSe_2. *Physical Review Letters* **113,** 026803 (2014).

136. Raja, A. *et al.* Coulomb engineering of the bandgap and excitons in two-dimensional materials. *Nature Communications* **8,** 15251 (2017).

137. Keldysh, L. V. Coulomb interaction in thin semiconductor and semimetal films. *Soviet Physics JETP* **29,** 658–660 (1979).

138. Pedersen, T. G., Mera, H. & Nikolić, B. K. Stark effect in low-dimensional hydrogen. *Physical Review A* **93,** 013409 (2016).

139. Zhang, X.-X., You, Y., Zhao, S. Y. F. & Heinz, T. F. Experimental Evidence for Dark Excitons in Monolayer WSe_2. *Physical Review Letters* **115,** 257403 (2015).

140. Ross, J. S. *et al.* Electrical control of neutral and charged excitons in a monolayer semiconductor. *Nature Communications* **4,** 1474 (2013).

141. Mak, K. F. *et al.* Tightly bound trions in monolayer MoS_2. *Nature Materials* **12,** 207–211 (2012).

142. You, Y. *et al.* Observation of biexcitons in monolayer WSe_2. *Nature Physics* **11,** 477–481 (2015).

143. Saigal, N., Sugunakar, V. & Ghosh, S. Exciton binding energy in bulk MoS_2 : A reassessment. *Applied Physics Letters* **108,** 132105 (2016).

144. Pedersen, T. G., Latini, S., Thygesen, K. S., Mera, H. & Nikolić, B. K. Exciton ionization in multilayer transition-metal dichalcogenides. *New Journal of Physics* **18,** 073043 (2016).

145. Amani, M. *et al.* Near-unity photoluminescence quantum yield in MoS_2. *Science* **350,** 1065–1068 (2015).

146. Moody, G., Schaibley, J. & Xu, X. Exciton dynamics in monolayer transition metal dichalcogenides. *Journal of the Optical Society of America B* **33,** C39 (2016).

147. Kozawa, D. *et al.* Photocarrier relaxation pathway in two-dimensional semiconducting transition metal dichalcogenides. *Nature Communications* **5,** 4543 (2014).

148. Nie, Z. *et al.* Ultrafast Carrier Thermalization and Cooling Dynamics in Few-Layer MoS_2. *ACS Nano* **8,** 10931–10940 (2014).

149. Thilagam, A. Exciton formation assisted by longitudinal optical phonons in monolayer transition metal dichalcogenides. *Journal of Applied Physics* **120,** 124306 (2016).

150. Ceballos, F., Cui, Q., Bellus, M. Z. & Zhao, H. Exciton formation in monolayer transition metal dichalcogenides. *Nanoscale* **8,** 11681–11688 (2016).

151. Steinleitner, P. *et al.* Direct Observation of Ultrafast Exciton Formation in a Monolayer of WSe_2. *Nano Letters* **17,** 1455–1460 (2017).

152. Kaindl, R. A., Carnahan, M. A., Hägele, D., Lövenich, R. & Chemla, D. S. Ultrafast terahertz probes of transient conducting and insulating phases in an electron–hole gas. *Nature* **423,** 734–738 (2003).

153. Danovich, M., Zólyomi, V., Fal'ko, V. I. & Aleiner, I. L. Auger recombination of dark excitons in WS_2 and WSe_2 monolayers. *2D Materials* **3,** 035011 (2016).

154. Sun, D. *et al.* Observation of Rapid Exciton–Exciton Annihilation in Monolayer Molybdenum Disulfide. *Nano Letters* **14,** 5625–5629 (2014).

155. Poellmann, C. *et al.* Resonant internal quantum transitions and femtosecond radiative decay of excitons in monolayer WSe_2. *Nature Materials* **14,** 889–893 (2015).

156. Murakami, Y. & Kono, J. Existence of an upper limit on the density of excitons in carbon nanotubes by diffusion-limited exciton-exciton annihilation: Experiment and theory. *Physical Review B* **80,** 035432 (2009).

157. Mouri, S. *et al.* Nonlinear photoluminescence in atomically thin layered WSe_2 arising from diffusion-assisted exciton-exciton annihilation. *Physical Review B* **90,** 155449 (2014).

158. Yuan, L. & Huang, L. Exciton dynamics and annihilation in WS_2 2D semiconductors. *Nanoscale* **7,** 7402–7408 (2015).

159. Aivazian, G. *et al.* Many-body effects in nonlinear optical responses of 2D layered semiconductors. *2D Materials* **4,** 025024 (2017).

160. Pogna, E. A. A. *et al.* Photo-Induced Bandgap Renormalization Governs the Ultrafast Response of Single-Layer MoS_2. *ACS Nano* **10,** 1182–1188 (2016).

161. Chernikov, A., Ruppert, C., Hill, H. M., Rigosi, A. F. & Heinz, T. F. Population inversion and giant bandgap renormalization in atomically thin WS_2 layers. *Nature Photonics* **9,** 466–470 (2015).

162. Palummo, M., Bernardi, M. & Grossman, J. C. Exciton Radiative Lifetimes in Two-Dimensional Transition Metal Dichalcogenides. *Nano Letters* **15,** 2794–2800 (2015).

163. Liu, G.-B., Xiao, D., Yao, Y., Xu, X. & Yao, W. Electronic structures and theoretical modelling of two-dimensional group-VIB transition metal dichalcogenides. *Chem. Soc. Rev.* **44,** 2643–2663 (2015).

164. Robert, C. *et al.* Exciton radiative lifetime in transition metal dichalcogenide monolayers. *Physical Review B* **93,** 205423 (2016).

165. Wang, H., Zhang, C. & Rana, F. Ultrafast Dynamics of Defect-Assisted Electron–Hole Recombination in Monolayer MoS_2. *Nano Letters* **15,** 339–345 (2015).

166. Shi, H. *et al.* Exciton Dynamics in Suspended Monolayer and Few-Layer MoS_2 2D Crystals. *ACS Nano* **7,** 1072–1080 (2013).

167. Wang, H., Zhang, C. & Rana, F. Surface Recombination Limited Lifetimes of Photoexcited Carriers in Few-Layer Transition Metal Dichalcogenide MoS_2. *Nano Letters* **15,** 8204–8210 (2015).

168. Kharche, N. & Nayak, S. K. Quasiparticle Band Gap Engineering of Graphene and Graphone on Hexagonal Boron Nitride Substrate. *Nano Letters* **11,** 5274–5278 (2011).

169. Britnell, L. *et al.* Electron Tunneling through Ultrathin Boron Nitride Crystalline Barriers. *Nano Letters* **12,** 1707–1710 (2012).

170. Lin, Y.-C. *et al.* Atomically thin resonant tunnel diodes built from synthetic van der Waals heterostructures. *Nature Communications* **6,** 7311 (2015).

171. Tran, T. T., Bray, K., Ford, M. J., Toth, M. & Aharonovich, I. Quantum Emission From Hexagonal Boron Nitride Monolayers. *Nature Nanotechnology* **11,** 37–41 (2015).

172. Dai, S. *et al.* Tunable Phonon Polaritons in Atomically Thin van der Waals Crystals of Boron Nitride. *Science* **343,** 1125–1129 (2014).

173. Xia, W. *et al.* Recent progress in van der Waals heterojunctions. *Nanoscale* **9,** 4324–4365 (2017).

174. Jariwala, D., Marks, T. J. & Hersam, M. C. Mixed-dimensional van der Waals heterostructures. *Nature Materials* **16,** 170–181 (2016).

175. Haigh, S. J. *et al.* Cross-sectional imaging of individual layers and buried interfaces of graphene-based heterostructures and superlattices. *Nature Materials* **11,** 764–767 (2012).

176. Polini, M. & Koppens, F. H. L. Graphene: Plasmons in moiré superlattices. *Nature Materials* **14,** 1187–1188 (2015).

177. Yankowitz, M. *et al.* Emergence of superlattice Dirac points in graphene on hexagonal boron nitride. *Nature Physics* **8,** 382–386 (2012).

178. Lin, Z. *et al.* 2D materials advances: from large scale synthesis and controlled heterostructures to improved characterization techniques, defects and applications. *2D Materials* **3,** 042001 (2016).

179. Robinson, J. A. Growing Vertical in the Flatland. *ACS Nano* **10,** 42–45 (2016).

180. Cui, X. *et al.* Multi-terminal transport measurements of MoS_2 using a van der Waals heterostructure device platform. *Nature Nanotechnology* **10,** 534–540 (2015).

181. Wierzbowski, J *et al.* Direct exciton emission from atomically thin transition metal dichalcogenide heterostructures near the lifetime limit. arXiv: 1705.00348v1 (2017).

182. Cadiz, F. *et al.* Excitonic linewidth approaching the homogeneous limit in MoS_2 based van der Waals heterostructures : accessing spin-valley dynamics. arXiv: 1702.00323 (2017).

183. Ajayi, O. *et al.* Approaching the Intrinsic Photoluminescence Linewidth in Transition Metal Dichalcogenide Monolayers. *2D Materials* **74,** 383–391 (2017).

184. Zhang, C. *et al.* Interlayer couplings, Moiré patterns, and 2D electronic superlattices in MoS_2 /WSe_2 hetero-bilayers. *Science Advances* **3,** e1601459 (2017).

185. Fang, H. *et al.* Strong interlayer coupling in van der Waals heterostructures built from single-layer chalcogenides. *Proceedings of the National Academy of Sciences* **111,** 6198–6202 (2014).

186. Woods, C. R. *et al.* Commensurate–incommensurate transition in graphene on hexagonal boron nitride. *Nature Physics* **10,** 451–456 (2014).

187. Wilson, N. R. *et al.* Determination of band offsets, hybridization, and exciton binding in 2D semiconductor heterostructures. *Science Advances* **3,** e1601832 (2017).

188. Mott, N. F. Note on the contact between a metal and an insulator or semiconductor. *Mathematical Proceedings of the Cambridge Philosophical Society* **34,** 568 (1938).

189. Anderson, R. L. Germanium-Gallium Arsenide Heterojunctions. *IBM Journal of Research and Development* **4,** 283–287 (1960).

190. Schottky, W. Halbleitertheorie der Sperrschicht. *Die Naturwissenschaften* **26,** 843–843 (1938).

191. Hill, H. M., Rigosi, A. F., Rim, K. T., Flynn, G. W. & Heinz, T. F. Band Alignment in MoS_2 /WS_2 Transition Metal Dichalcogenide Heterostructures Probed by Scanning Tunneling Microscopy and Spectroscopy. *Nano Letters* **16,** 4831–4837 (2016).

192. Kang, J., Tongay, S., Zhou, J., Li, J. & Wu, J. Band offsets and heterostructures of two-dimensional semiconductors. *Applied Physics Letters* **102,** 012111 (2013).

193. Le, N. B., Huan, T. D. & Woods, L. M. Interlayer Interactions in van der Waals Heterostructures: Electron and Phonon Properties. *ACS Applied Materials & Interfaces* **8,** 6286–6292 (2016).

194. Andersen, K., Latini, S. & Thygesen, K. S. Dielectric Genome of van der Waals Heterostructures. *Nano Letters* **15,** 4616–4621 (2015).

195. Coy Diaz, H. *et al.* Direct Observation of Interlayer Hybridization and Dirac Relativistic Carriers in Graphene/MoS_2 van der Waals Heterostructures. *Nano Letters* **15,** 1135–1140 (2015).

196. Simmons, J. G. Generalized Formula for the Electric Tunnel Effect between Similar Electrodes Separated by a Thin Insulating Film. *Journal of Applied Physics* **34,** 1793–1803 (1963).

197. Georgiou, T. *et al.* Vertical field-effect transistor based on graphene–WS_2 heterostructures for flexible and transparent electronics. *Nature Nanotechnology* **8,** 100–103 (2012).

198. Britnell, L. *et al.* Field-Effect Tunneling Transistor Based on Vertical Graphene Heterostructures. *Science* **335,** 947–950 (2012).

199. Fowler, R. H. & Nordheim, L. Electron Emission in Intense Electric Fields. *Proceedings of the Royal Society A: Mathematical, Physical and Engineering Sciences* **119,** 173–181 (1928).

200. Richardson. O. Thermionic phenomena and the laws which govern them. *Nobel Lecture* (1929).

201. Yu, W. J. *et al.* Vertically stacked multi-heterostructures of layered materials for logic transistors and complementary inverters. *Nature Materials* **12,** 246–252 (2012).

202. Moriya, R. *et al.* Influence of the density of states of graphene on the transport properties of graphene/MoS_2 /metal vertical field-effect transistors. *Applied Physics Letters* **106,** 223103 (2015).

203. Britnell, L *et al.* Resonant tunnelling and negative differential conductance in graphene transistors. *Nature Communications* **4,** 1794 (2013).

204. Mishchenko, a. *et al.* Twist-controlled resonant tunnelling in graphene/boron nitride/graphene heterostructures. *Nature Nanotechnology* **9,** 808–813 (2014).

205. Roy, T. *et al.* Dual-Gated MoS_2 /WSe_2 van der Waals Tunnel Diodes and Transistors. *ACS Nano* **9,** 2071–2079 (2015).

206. Yang, H. *et al.* Graphene Barristor, a Triode Device with a Gate-Controlled Schottky Barrier. *Science* **336,** 1140–1143 (2012).

207. Rigosi, A. F., Hill, H. M., Li, Y., Chernikov, A. & Heinz, T. F. Probing Interlayer Interactions in Transition Metal Dichalcogenide Heterostructures by Optical Spectroscopy: MoS_2 /WS_2 and $MoSe_2$ /WSe_2. *Nano Letters* **15,** 5033–5038 (2015).

208. Hong, X. *et al.* Ultrafast charge transfer in atomically thin MoS_2/WS_2 heterostructures. *Nature Nanotechnology* **9,** 682–686 (2014).

209. Ceballos, F., Bellus, M. Z., Chiu, H.-y. & Zhao, H. Ultrafast Charge Separation and Indirect Exciton Formation in a MoS_2 –$MoSe_2$ van der Waals Heterostructure. *ACS Nano* **8,** 12717–12724 (2014).

210. Rivera, P. *et al.* Observation of long-lived interlayer excitons in monolayer $MoSe_2$–WSe_2 heterostructures. *Nature Communications* **6,** 6242 (2015).

211. Nayak, P. K. *et al.* Probing Evolution of Twist-Angle-Dependent Interlayer Excitons in $MoSe_2$ /WSe_2 van der Waals Heterostructures. *ACS Nano* **11,** 4041–4050 (2017).

212. Rivera, P. *et al.* Valley-polarized exciton dynamics in a 2D semiconductor heterostructure. *Science* **351,** 688–691 (2016).

213. Fogler, M. M., Butov, L. V. & Novoselov, K. S. High-temperature superfluidity with indirect excitons in van der Waals heterostructures. *Nature Communications* **5,** 4555 (2014).

214. High, A. A. *et al.* Spontaneous coherence in a cold exciton gas. *Nature* **483,** 584–588 (2012).

215. Froehlicher, G., Lorchat, E. & Berciaud, S. Quantifying Photoinduced Charge Transfer in Graphene-Transition Metal Dichalcogenide van der Waals Heterostructures using Raman Spectroscopy. arXiv: 1703.05396 (2017).

216. He, J. *et al.* Electron transfer and coupling in graphene–tungsten disulfide van der Waals heterostructures. *Nature Communications* **5,** 5622 (2014).

217. Manolatou, C., Wang, H., Chan, W., Tiwari, S. & Rana, F. Radiative and nonradiative exciton energy transfer in monolayers of two-dimensional group-VI transition metal dichalcogenides. *Physical Review B* **93,** 155422 (2016).

218. Gaudreau, L. *et al.* Universal Distance-Scaling of Nonradiative Energy Transfer to Graphene. *Nano Letters* **13,** 2030–2035 (2013).

219. Kozawa, D. *et al.* Evidence for Fast Interlayer Energy Transfer in $MoSe_2$ /WS_2 Heterostructures. *Nano Letters* **16,** 4087–4093 (2016).

220. Kato, K., Kawano, K. & Kozen, A. Design of Ultrawide-Band, High-Sensitivity p-i-n protodetectors. *IEICE Transactions on Electronics* **E76-C,** 214–221 (1993).

221. Sze, S. & Ng, K. K. in *Physics of Semiconductor Devices* (John Wiley & Sons, Inc., Hoboken, NJ, USA, 2006).

222. Kim, J., Johnson, W., Kanakaraju, S, Calhoun, L. & Lee, C. Improvement of Dark Current Using InP/InGaAsP Transition Layer in Large-Area InGaAs MSM Photodetectors. *IEEE Transactions on Electron Devices* **51,** 351–356 (2004).

223. Tsai, D.-S. *et al.* Few-Layer MoS_2 with High Broadband Photogain and Fast Optical Switching for Use in Harsh Environments. *ACS Nano* **7,** 3905–3911 (2013).
224. Furchi, M. M., Polyushkin, D. K., Pospischil, A. & Mueller, T. Mechanisms of Photoconductivity in Atomically Thin MoS_2. *Nano Letters* **14,** 6165–6170 (2014).
225. Pradhan, N. R. *et al.* High Photoresponsivity and Short Photoresponse Times in Few-Layered WSe_2 Transistors. *ACS Applied Materials & Interfaces* **7,** 12080–12088 (2015).
226. Yin, Z. *et al.* Single-Layer MoS_2 Phototransistors. *ACS Nano* **6,** 74–80 (2012).
227. Lopez-Sanchez, O., Lembke, D., Kayci, M., Radenovic, A. & Kis, A. Ultrasensitive photodetectors based on monolayer MoS_2. *Nature Nanotechnology* **8,** 497–501 (2013).
228. Klots, A. R. *et al.* Probing excitonic states in suspended two-dimensional semiconductors by photocurrent spectroscopy. *Scientific Reports* **4,** 6608 (2015).
229. Zhang, W. *et al.* High-Gain Phototransistors Based on a CVD MoS_2 Monolayer. *Advanced Materials* **25,** 3456–3461 (2013).
230. Buscema, M. *et al.* Fast and Broadband Photoresponse of Few-Layer Black Phosphorus Field-Effect Transistors. *Nano Letters* **14,** 3347–3352 (2014).
231. Yuan, H. *et al.* Polarization-sensitive broadband photodetector using a black phosphorus vertical p–n junction. *Nature Nanotechnology* **10,** 707–713 (2015).
232. Guo, Q. *et al.* Black Phosphorus Mid-Infrared Photodetectors with High Gain. *Nano Letters* **16,** 4648–4655 (2016).
233. Youngblood, N., Chen, C., Koester, S. J. & Li, M. Waveguide-integrated black phosphorus photodetector with high responsivity and low dark current. *Nature Photonics* **9,** 249–252 (2015).
234. Freitag, M., Low, T., Xia, F. & Avouris, P. Photoconductivity of biased graphene. *Nature Photonics* **7,** 53–59 (2012).
235. Yu, W. J. *et al.* Highly efficient gate-tunable photocurrent generation in vertical heterostructures of layered materials. *Nature Nanotechnology* **8,** 952–958 (2013).
236. Song, J. C. W. & Levitov, L. S. Shockley-Ramo theorem and long-range photocurrent response in gapless materials. *Physical Review B* **90,** 075415 (2014).
237. Wu, C.-C. *et al.* Elucidating the Photoresponse of Ultrathin MoS_2 Field-Effect Transistors by Scanning Photocurrent Microscopy. *The Journal of Physical Chemistry Letters* **4,** 2508–2513 (2013).
238. Ross, J. S. *et al.* Electrically tunable excitonic light-emitting diodes based on monolayer WSe_2 p–n junctions. *Nature Nanotechnology* **9,** 268–272 (2014).

239. Pospischil, A., Furchi, M. M. & Mueller, T. Solar-energy conversion and light emission in an atomic monolayer p–n diode. *Nature Nanotechnology* **9,** 257–261 (2014).

240. Lee, C.-H. *et al.* Atomically thin p–n junctions with van der Waals heterointerfaces. *Nature Nanotechnology* **9,** 676–681 (2014).

241. Baugher, B. W. H., Churchill, H. O. H., Yang, Y. & Jarillo-Herrero, P. Optoelectronic devices based on electrically tunable p–n diodes in a monolayer dichalcogenide. *Nature Nanotechnology* **9,** 262–267 (2014).

242. Groenendijk, D. J. *et al.* Photovoltaic and Photothermoelectric Effect in a Double-Gated WSe_2 Device. *Nano Letters* **14,** 5846–5852 (2014).

243. Buscema, M., Groenendijk, D. J., Steele, G. a., van der Zant, H. S. J. & Castellanos-Gomez, A. Photovoltaic effect in few-layer black phosphorus PN junctions defined by local electrostatic gating. *Nature communications* **5,** 4651 (2014).

244. Hertz, H. Ueber einen Einfluss des ultravioletten Lichtes auf die electrische Entladung. *Annalen der Physik und Chemie* **267,** 983–1000 (1887).

245. Einstein, A. Über einen die Erzeugung und Verwandlung des Lichtes betreffenden heuristischen Gesichtspunkt. *Annalen der Physik* **322,** 132–148 (1905).

246. Scales, C. & Berini, P. Thin-Film Schottky Barrier Photodetector Models. *IEEE Journal of Quantum Electronics* **46,** 633–643 (2010).

247. Fowler, R. H. The Analysis of Photoelectric Sensitivity Curves for Clean Metals at Various Temperatures. *Physical Review* **38,** 45–56 (1931).

248. Yan, R. *et al.* Determination of graphene work function and graphene-insulator-semiconductor band alignment by internal photoemission spectroscopy. *Applied Physics Letters* **101,** 022105 (2012).

249. Sze, S. M., Crowell, C. R. & Kahng, D. Photoelectric Determination of the Image Force Dielectric Constant For Hot Electrons in Schottky Barriers. *Journal of Applied Physics* **35,** 2534–2536 (1964).

250. Goykhman, I. *et al.* On-Chip Integrated, Silicon-Graphene Plasmonic Schottky Photodetector with High Responsivity and Avalanche Photogain. *Nano Letters* **16,** 3005–3013 (2016).

251. Amirmazlaghani, M., Raissi, F., Habibpour, O., Vukusic, J. & Stake, J. Graphene-Si Schottky IR Detector. *IEEE Journal of Quantum Electronics* **49,** 589–594 (2013).

252. Wang, X., Cheng, Z., Xu, K., Tsang, H. K. & Xu, J.-B. High-responsivity graphene/silicon-heterostructure waveguide photodetectors. *Nature Photonics* **7,** 888–891 (2013).

253. Goupil, C., Seifert, W., Zabrocki, K., Miller, E. & Snyder, G. J. Thermodynamics of thermoelectric phenomena and applications. *Entropy* **13,** 1481–1517 (2011).

254. Sun, D. *et al.* Ultrafast hot-carrier-dominated photocurrent in graphene. *Nature Nanotechnology* **7,** 114–118 (2012).

255. Xu, X., Gabor, N. M., Alden, J. S., van der Zande, A. M. & McEuen, P. L. Photo-Thermoelectric Effect at a Graphene Interface Junction. *Nano Letters* **10,** 562–566 (2010).

256. Buscema, M. *et al.* Large and tunable photothermoelectric effect in single-layer MoS_2. *Nano Letters* **13,** 358–363 (2013).

257. Low, T., Engel, M., Steiner, M. & Avouris, P. Origin of photoresponse in black phosphorus phototransistors. *Physical Review B* **90,** 081408 (2014).

258. Xia, F., Mueller, T., Lin, Y.-m., Valdes-Garcia, A. & Avouris, P. Ultrafast graphene photodetector. *Nature Nanotechnology* **4,** 839–843 (2009).

259. Schall, D. *et al.* 50 GBit/s Photodetectors Based on Wafer-Scale Graphene for Integrated Silicon Photonic Communication Systems. *ACS Photonics* **1,** 781–784 (2014).

260. Shiue, R. J. *et al.* High-Responsivity Graphene-Boron Nitride Photodetector and Autocorrelator in a Silicon Photonic Integrated Circuit. *Nano Letters* **15,** 7288–7293 (2015).

261. Hwang, E. H., Rossi, E. & Das Sarma, S. Theory of thermopower in two-dimensional graphene. *Physical Review B* **80,** 235415 (2009).

262. Bulusu, A. & Walker, D. G. Review of electronic transport models for thermoelectric materials. *Superlattices and Microstructures* **44,** 1–36 (2008).

263. Yan, J. *et al.* Dual-gated bilayer graphene hot-electron bolometer. *Nature Nanotechnology* **7,** 472–478 (2012).

264. Engel, M., Steiner, M. & Avouris, P. Black Phosphorus Photodetector for Multispectral, High-Resolution Imaging. *Nano Letters* **14,** 6414–6417 (2014).

265. Graham, R & Yu, D. Scanning Photocurrent Microscopy in Semiconductor Nanostructures. *Modern Physics Letters B* **27,** 1330018 (2013).

266. Haynes, J. R. & Shockley, W. Investigation of Hole injection in transistor action. *Physical Review* **75,** 691 (1949).

267. Ubrig, N., Jo, S., Berger, H., Morpurgo, A. F. & Kuzmenko, A. B. Scanning photocurrent microscopy reveals electron-hole asymmetry in ionic liquid-gated WS_2 transistors. *Applied Physics Letters* **104** (2014).

268. Urich, A., Unterrainer, K. & Mueller, T. Intrinsic Response Time of Graphene Photodetectors. *Nano Letters* **11,** 2804–2808 (2011).

269. Son, B. H. *et al.* Imaging ultrafast carrier transport in nanoscale field-effect transistors. *ACS nano* **8,** 11361–8 (2014).

270. Gabor, N. M., Zhong, Z., Bosnick, K. & McEuen, P. L. Ultrafast Photocurrent Measurement of the Escape Time of Electrons and Holes from Carbon Nanotube P-i-N Photodiodes. *Physical Review Letters* **108,** 087404 (2012).

271. Wang, H., Zhang, C., Chan, W., Tiwari, S. & Rana, F. Ultrafast response of monolayer molybdenum disulfide photodetectors. *Nature Communications* **6,** 8831 (2015).

272. Stormer, H. L., Tsui, D. C. & Gossard, A. C. The fractional quantum Hall effect. *Reviews of Modern Physics* **71,** S298–S305 (1999).

273. Novoselov, K. S. Electric Field Effect in Atomically Thin Carbon Films. *Science* **306,** 666–669 (2004).

274. Liang, X. *et al.* Toward clean and crackless transfer of graphene. *ACS Nano* **5,** 9144–9153 (2011).

275. Goossens, A. M. *et al.* Mechanical cleaning of graphene. *Applied Physics Letters* **100,** 98–101 (2012).

276. Lin, Y. C. *et al.* Graphene annealing: How clean can it be? *Nano Letters* **12,** 414–419 (2012).

277. Moser, J., Barreiro, A. & Bachtold, A. Current-induced cleaning of graphene. *Applied Physics Letters* **91,** 1–4 (2007).

278. Bolotin, K. I., Sikes, K. J., Hone, J., Stormer, H. L. & Kim, P. Temperature-dependent transport in suspended graphene. *Physical Review Letters* **101,** 1–4 (2008).

279. Dean, C. R. *et al.* Multicomponent fractional quantum Hall effect in graphene. *Nature Physics* **7,** 693–696 (2011).

280. Li, X. *et al.* Large-area synthesis of high-quality and uniform graphene films on copper foils. *Science* **324,** 1312–1314 (2009).

281. Hernandez, Y. *et al.* High yield production of graphene by liquid phase exfoliation of graphite. *Nature Nanotechnology* **3,** 563–8 (2008).

282. Blake, P. *et al.* Making graphene visible. *Applied Physics Letters* **91,** 89–92 (2007).

283. Agraït, N, Castellanos-Gomez, A., Agrat, N. & Rubio-Bollinger, G. Optical identification of atomically thin dichalcogenide crystals. *Applied Physics Letters* **96,** 2–5 (2010).

284. Ferrari, A. C. & Basko, D. M. Raman spectroscopy as a versatile tool for studying the properties of graphene. *Nat Nanotechnol* **8,** 235–246 (2013).

285. Ferrari, A. C. *et al.* Raman spectrum of graphene and graphene layers. *Physical Review Letters* **97,** 187401 (2006).

286. Neumann, C. *et al.* Raman spectroscopy as probe of nanometre-scale strain variations in graphene. *Nature Communications* **6,** 8429 (2015).

287. Castellanos-Gomez, A. *et al.* Deterministic transfer of two-dimensional materials by all-dry viscoelastic stamping. *2D Materials* **1,** 011002 (2014).

288. Allain, A., Kang, J., Banerjee, K. & Kis, A. Electrical contacts to two-dimensional semiconductors. *Nature Materials* **14,** 1195–1205 (2015).

289. Kretinin, A. V. *et al.* Electronic properties of graphene encapsulated with different two-dimensional atomic crystals. *Nano Letters* **14,** 3270–3276 (2014).

290. Pizzocchero, F. *et al.* The hot pick-up technique for batch assembly of van der Waals heterostructures. *Nature Communications* **7,** 11894 (2016).

291. Dorgan, V. E., Bae, M. H. & Pop, E. Mobility and saturation velocity in graphene on SiO2. *Applied Physics Letters* **97,** 082112 (2010).

292. Massicotte, M., Yu, V., Whiteway, E., Vatnik, D. & Hilke, M. Quantum Hall effect in fractal graphene: growth and properties of graphlocons. *Nanotechnology* **24,** 325601 (2013).

293. Lee, E., Balasubramanian, K., Weitz, R., BurkHard, M. & Kern, K. Contact and edge effects in graphene devices. *Nature nanotechnology* **3,** 486–90 (2008).

294. Xia, F. *et al.* Photocurrent imaging and efficient photon detection in a graphene transistor. *Nano Letters* **9,** 1039–1044 (2009).

295. Park, J., Ahn, Y. H. & Ruiz-Vargas, C. Imaging of photocurrent generation and collection in single-layer graphene. *Nano Letters* **9,** 1742–1746 (2009).

296. Pospischil, A. *et al.* CMOS-compatible graphene photodetector covering all optical communication bands. *Nature Photonics* **7,** 892–896 (2013).

297. Accanto, N. *et al.* Phase control of femtosecond pulses on the nanoscale using second harmonic nanoparticles. *Light: Science & Applications* **3,** e143 (2014).

298. Ma, Q. *et al.* Competing channels for hot-electron cooling in graphene. *Physical Review Letters* **112,** 5 (2014).

299. Rakic, a. D., Djurisic, A. B., Elazar, J. M. & Majewski, M. L. Optical properties of metallic films for vertical-cavity optoelectronic devices. *Appl. Optics* **37,** 5271–5283– (1998).

300. Echtermeyer, T. J. *et al.* Photothermoelectric and photoelectric contributions to light detection in metal-graphene-metal photodetectors. *Nano Letters* **14,** 3733–3742 (2014).

301. Badioli, M. *et al.* Phonon-mediated mid-infrared photoresponse of graphene. *Nano Letters* **14,** 6374–6381 (2014).

302. Freitag, M. *et al.* Substrate-sensitive mid-infrared photoresponse in graphene. *ACS Nano* **8,** 8350–8356 (2014).

303. Lemme, M. C. *et al.* Gate-activated photoresponse in a graphene p-n junction. *Nano Letters* **11,** 4134–4137 (2011).

304. Mueller, T., Xia, F., Freitag, M., Tsang, J. & Avouris, P. Role of contacts in graphene transistors: A scanning photocurrent study. *Physical Review B - Condensed Matter and Materials Physics* **79,** 245430 (2009).

305. Grüneis, A. *et al.* Inhomogeneous optical absorption around the k point in graphite and carbon nanotubes. *Physical Review B* **67,** 1–7 (2003).

306. Mittendorff, M. *et al.* Anisotropy of excitation and relaxation of photogenerated charge carriers in graphene. *Nano Letters* **14,** 1504–1507 (2014).

307. Kim, M. *et al.* Polarization dependence of photocurrent in a metal-graphene-metal device. *Applied Physics Letters* **101,** 1–4 (2012).

308. Wu, S. *et al.* Multiple hot-carrier collection in photo-excited graphene Moire superlattices. *Science Advances* **2.** arXiv: 1603.04934 (2016).

309. Liang, S. J. & Ang, L. K. Electron thermionic emission from graphene and a thermionic energy converter. *Physical Review Applied* **3,** 014002 (2015).

310. Svetovoy, V. B. & Palasantzas, G. Graphene-on-Silicon Near-Field Thermophotovoltaic Cell. *Physical Review Applied* **2,** 1–6 (2014).

311. Rodriguez-Nieva, J. F., Dresselhaus, M. S. & Song, J. C. W. Enhanced Thermionic-Dominated Photoresponse in Graphene Schottky Junctions. *Nano Letters* **16,** 6036–6041 (2016).

312. Rodriguez-Nieva, J. F., Dresselhaus, M. S. & Levitov, L. S. Thermionic emission and negative dI/dV in photoactive graphene heterostructures. *Nano Letters* **15,** 1451–1456 (2015).

313. Peters, D. D. An infrared detector utilizing internal photoemission. *Proceedings of the IEEE* **55,** 704–705 (1967).

314. Brongersma, M. L., Halas, N. J. & Nordlander, P. Plasmon-induced hot carrier science and technology. *Nature Nanotechnology* **10,** 25–34 (2015).

315. Clavero, C. Plasmon-induced hot-electron generation at nanoparticle/metal-oxide interfaces for photovoltaic and photocatalytic devices. *Nature Photonics* **8,** 95–103 (2014).

316. Goykhman, I, Desiatov, B, Khurgin, J & Shappir, J. Locally Oxidized Silicon Surface-Plasmon Schottky Detector for Telecom Regime. *Nano Letters* **11,** 2219–2224 (2011).

317. Knight, M. W., Sobhani, H, Nordlander, P & Halas, N. J. Photodetection with Active Optical Antennas. *Science* **332,** 702–704 (2011).

318. Qiu, T. Q. & Tien, C. L. Heat Transfer Mechanisms During Short-Pulse Laser Heating of Metals. *Journal of Heat Transfer* **115,** 835 (1993).

319. Ross, R. T. & Nozik, A. J. Efficiency of hot-carrier solar energy converters. *Journal of Applied Physics* **53,** 3813–3818 (1982).

320. Voisin, C & Plaçais, B. Hot carriers in graphene. *Journal of Physics: Condensed Matter* **27,** 160301 (2015).

321. Tielrooij, K. J. *et al.* Generation of photovoltage in graphene on a femtosecond timescale through efficient carrier heating. *Nature nanotechnology* **10,** 437–43 (2015).

322. Kim, K. *et al.* Band alignment in WSe_2-graphene heterostructures. *ACS Nano* **9,** 4527–4532 (2015).

323. Massicotte, M *et al.* Picosecond photoresponse in van der Waals heterostructures. *Nature Nanotechnology* **11,** 42–46 (2015).

324. Zhang, S. *et al.* Direct observation of degenerate two-photon absorption and its saturation in WS_2 and MoS_2 Monolayer and few-wayer films. *ACS Nano* **9,** 7142–7150 (2015).

325. Chen, W., Wang, Y. & Ji, W. Two-Photon Absorption in Graphene Enhanced by the Excitonic Fano Resonance. *Journal of Physical Chemistry C* **119,** 16954–16961 (2015).

326. Stauber, T., Peres, N. M. R. & Geim, A. K. Optical conductivity of graphene in the visible region of the spectrum. *Physical Review B* **78,** 085432 (2008).

327. Sinha, D. & Lee, J. U. Ideal graphene/silicon schottky junction diodes. *Nano Letters* **14,** 4660–4664 (2014).

328. Schwede, J. W. *et al.* Photon-enhanced thermionic emission for solar concentrator systems. *Nature materials* **9,** 762–7 (2010).

329. Schwede, J. W. *et al.* Photon-enhanced thermionic emission from heterostructures with low interface recombination. *Nature communications* **4,** 1576 (2013).

330. Zhu, X. Exceeding the limit in solar energy conversion with multiple excitons. *Accounts of Chemical Research* **46,** 1239–1241 (2013).

331. Wolf, E. L. *Principles of Electron Tunneling Spectroscopy:Second Edition* 616 (Oxford University Press, 2011).

332. J. J. Sakurai. *Modern Quantum Mechanics* (ed Addison-Wesley) (1994).

333. Furchi, M. M., Pospischil, A., Libisch, F., Burgdörfer, J. & Mueller, T. Photovoltaic Effect in an Electrically Tunable van der Waals Heterojunction. *Nano Letters* **14,** 4785–4791 (2014).

334. Bernardi, M., Palummo, M. & Grossman, J. C. Extraordinary sunlight absorption and one nanometer thick photovoltaics using two-dimensional monolayer materials. *Nano Letters* **13,** 3664–3670 (2013).

335. Carvalho, A., Ribeiro, R. M. & Castro Neto, A. H. Band nesting and the optical response of two-dimensional semiconducting transition metal dichalcogenides. *Physical Review B* **88,** 115205 (2013).

336. Roy, K. *et al.* Graphene-MoS_2 hybrid structures for multifunctional photoresponsive memory devices. *Nature nanotechnology* **8,** 826–830 (2013).

337. Cui, Q., Ceballos, F., Kumar, N. & Zhao, H. Transient Absorption Microscopy of Monolayer and Bulk WSe_2. *ACS Nano* **8,** 2970–2976 (2014).

338. Sun, D. *et al.* Observation of rapid exciton-exciton annihilation in monolayer molybdenum disulfide. *Nano Letters* **14,** 5625–5629 (2014).

339. Strait, J. H., Nene, P. & Rana, F. High intrinsic mobility and ultrafast carrier dynamics in multilayer metal-dichalcogenide MoS_2. *Physical Review B* **90,** 245402 (2014).

340. Borzda, T. *et al.* Charge photogeneration in few-layer MoS_2. *Advanced Functional Materials* **25,** 3351–3358 (2015).

341. Griebel, M. *et al.* Tunable subpicosecond optoelectronic transduction in superlattices of self-assembled ErAs nanoislands. *Nature materials* **2,** 122–126 (2003).

342. Wang, K. *et al.* Ultrafast saturable absorption of two-dimensional MoS_2 nanosheets. *ACS Nano* **7,** 9260–9267 (2013).

343. Li, D. *et al.* Electric-field-induced strong enhancement of electroluminescence in multilayer molybdenum disulfide. *Nature Communications* **6,** 7509 (2015).

344. Swathi, R. S. & Sebastian, K. L. Resonance energy transfer from a dye molecule to graphene. *Journal of Chemical Physics* **129,** 054703 (2008).

345. Stark, J. Observation of the Separation of Spectral Lines by an Electric Field. *Nature* **92,** 401–401 (1913).

346. Kox, A. J. The discovery of the Stark effect and its early theoretical explanations. *Annalen der Physik* **525,** A63–A66 (2013).

347. Scholes, G. D. & Rumbles, G. Excitons in nanoscale systems. *Nature Materials* **5,** 920–920 (2006).

348. Wang, F. The Optical Resonances in Carbon Nanotubes Arise from Excitons. *Science* **308,** 838–841 (2005).

349. Kim, J. *et al.* Ultrafast generation of pseudo-magnetic field for valley excitons in WSe_2 monolayers. *Science* **346,** 1205–1208 (2014).

350. Sie, E. J. *et al.* Valley-selective optical Stark effect in monolayer WS_2. *Nature Materials* **14,** 290–294 (2014).

351. Langer, F. *et al.* Lightwave-driven quasiparticle collisions on a subcycle timescale. *Nature* **533,** 225–229 (2016).

352. Haastrup, S., Latini, S., Bolotin, K. & Thygesen, K. S. Stark shift and electric-field-induced dissociation of excitons in monolayer MoS_2 and hBN/MoS_2 heterostructures. *Physical Review B* **94,** 041401 (2016).

353. Scharf, B. *et al.* Excitonic Stark effect in MoS_2 monolayers. *Physical Review B* **94,** 245434 (2016).

354. Pedersen, T. G. Exciton Stark shift and electroabsorption in monolayer transition-metal dichalcogenides. *Physical Review B* **94,** 125424 (2016).

355. Novoselov, K. S. *et al.* A roadmap for graphene. *Nature* **490,** 192–200 (2012).

356. Zurutuza, A. & Marinelli, C. Challenges and opportunities in graphene commercialization. *Nature Nanotechnology* **9,** 730–734 (2014).

357. Wu, T. *et al.* Fast growth of inch-sized single-crystalline graphene from a controlled single nucleus on Cu–Ni alloys. *Nature Materials* **15,** 43–47 (2015).

358. Song, L. *et al.* Large Scale Growth and Characterization of Atomic Hexagonal Boron Nitride Layers. *Nano Letters* **10,** 3209–3215 (2010).

359. Kang, K. *et al.* High-mobility three-atom-thick semiconducting films with wafer-scale homogeneity. *Nature* **520,** 656–660 (2015).

360. Das, S., Robinson, J. A., Dubey, M., Terrones, H. & Terrones, M. Beyond Graphene: Progress in Novel Two-Dimensional Materials and van der Waals Solids. *Annual Review of Materials Research* **45,** 1–27 (2015).

361. Kroemer, H. Nobel Lecture: Quasielectric fields and band offsets: teaching electrons new tricks. *Reviews of Modern Physics* **73,** 783–793 (2001).

362. Ye, Z., Sun, D. & Heinz, T. F. Optical manipulation of valley pseudospin. *Nature Physics* **13,** 26–29 (2016).

363. Lv, B. Q. *et al.* Experimental Discovery of Weyl Semimetal TaAs. *Physical Review X* **5,** 031013 (2015).

364. Ma, Q. *et al.* Direct optical detection of Weyl fermion chirality in a topological semimetal. arXiv: 1705.00590 (2017).

365. Benedict, L. X., Louie, S. G. & Cohen, M. L. Heat capacity of carbon nanotubes. *Solid State Communications* **100,** 177–180 (1996).

366. Simpson, A. & Stuckes, A. D. The Thermal Conductivity of Highly Oriented Pyrolytic Boron Nitride. *Journal of Physics C: Solid State Physics* **4,** 1710–1718 (1971).

367. Datta, S. in *Lessons from Nanoelectronics* New Jersey, 1–121 (World Scientific, 2012).

368. Cai, Y., Zhang, L., Zeng, Q., Cheng, L. & Xu, Y. Infrared reflectance spectrum of BN calculated from first principles. *Solid State Communications* **141,** 262–266 (2007).

369. Zeng, H. *et al.* Optical signature of symmetry variations and spin-valley coupling in atomically thin tungsten dichalcogenides. *Scientific Reports* **3,** 1608 (2013).

370. Olsen, T., Latini, S., Rasmussen, F. & Thygesen, K. S. Simple Screened Hydrogen Model of Excitons in Two-Dimensional Materials. *Physical Review Letters* **116,** 056401 (2016).

371. Geick, R, Perry, C. H. & Rupprecht, G. Normal Modes in Hexagonal Boron Nitride. *Physical Review* **146,** 543–547 (1966).